

# Time-Resolved Spectroscopy of Organometallic Alkane and Silane Intermediates



The University of  
**Nottingham**

Edward Bowman MSci

School of Chemistry

University of Nottingham

*Thesis submitted to the University of Nottingham for the degree of Doctor of Philosophy*

September 2023

## Declaration

I hereby declare all the work within this thesis is my own, except where stated otherwise.



Edward Bowman

September 2023

## Acknowledgements

I'd like to thank my supervisors, Professor Mike George, Dr Andy Dent, and Dr Stu Bartlett, for their dedication, guidance, and support throughout my time working on this Thesis, which has helped me through a myriad of difficulties.

I'd also like to thank Professor Nick Besley, for the enthusiasm, kindness, and insight he offered and which I missed deeply after his passing. The groundwork he laid is an indelible part of this Thesis and a small fraction of his legacy as a brilliant scientist.

In working across two separate facilities, I've had the pleasure of being part of two different communities, both full of friends and colleagues who have advised, assisted, collaborated with and trained me throughout my time. I would especially like to thank Dr Genevieve Garwood, who was fantastic company both at Nottingham and abroad.

To the George Group at Nottingham, I'd like to say thank you, especially to Dr Ashely Love and Dr David Tiemessen for their guidance. I would also like to thank my colleagues at Diamond, especially Dr Gabriel Karras and Dr Anne Fitzpatrick for their mastery of all things laser-related, and Dr. Joshua Elliott for stepping in and providing computational expertise when I was in need.

Finally, I'd like to thank my parents, without whom I would have never started this path, let alone got this far.

## Abbreviations

ADZP	Augmented Double Zeta Polarization
APD	Avalanche Photodiode
A.U.	Arbitrary Units
CIF	Crystallographic Information File
Cp	Cyclopentadienyl
Cp'	Methylcyclopentadienyl
DCM	Dichloromethane
DFT	Density Functional Theory
ECP	Effective Core Potential
Et	Ethyl
EXAFS	Extended X-ray Absorption Fine Structure
FDMNES	Finite Difference Method Near Edge Structure
FTIR	Fourier Transform Infrared
FWHM	Full Width Half Maximum
IR	Infrared
NMR	Nuclear Magnetic Resonance
OPA	Optical Parametric Amplifier
R-space	Reciprocal Space
TRIR	Time-Resolved Infrared
UV/vis	Ultraviolet / Visible
XANES	X-ray Absorption Near-Edge Structure
XAFS	X-ray Absorption Fine Structure

XAS X-ray Absorption Spectroscopy

XFEL X-ray Free Electron Laser

$\Delta$ Abs Change in Absorbance

## Abstract

### Chapter 1

In this Chapter, the history of time-resolved spectroscopic methods is reviewed, with particular focus on IR spectroscopy and XAS spectroscopy. The study of metal carbonyl intermediates, the family of complexes investigated in this Thesis, and the previous investigation of their photochemistry is also reviewed.

### Chapter 2

In this Chapter, experimental techniques and spectroscopic apparatus used to perform TRXAS at the APS and to take TRIR measurements at the University of Nottingham are described. Computational methods used to process and produce data in other Chapters of this Thesis are also detailed.

### Chapter 3

This Chapter details the development and implementation of a time resolved XAS system on the I18 beamline of the Diamond Light Source synchrotron, including details of the components and adaptation of the setup across multiple experiments. The impact of setup design on signal is described, with quality of the jet, the collinearity of the laser and x-ray beams, and the proximity of the avalanche photodiode (APD) found to be of great importance to producing quality signal.

## Chapter 4

In this Chapter, the photolysis of  $\text{CpRe}(\text{CO})_3$  in alkane and alkyl silane solvents is explored with TRIR and TRXAS. The kinetics of  $\text{CpRe}(\text{CO})_3$  photolyzed in *n*-heptane doped with triethyl silane are measured with TRIR.

EXAFS data was used to measure the Re- $\text{C}_{\text{alkane}}$  bond lengths of  $\text{CpRe}(\text{CO})_2(\textit{n}\text{-hexane})$  ( $2.61 \pm 0.37 \text{ \AA}$ ) and  $\text{CpRe}(\text{CO})_2(\text{cyclohexane})$  ( $2.52 \pm 0.11 \text{ \AA}$ ). The Re-Si bond length for  $\text{CpRe}(\text{CO})_2(\text{HSiEt}_3)$  was also evaluated, and was found to be  $2.45 \pm 0.05 \text{ \AA}$  for the 0 to 10  $\mu\text{s}$  timeframe and  $2.42 \pm 0.05 \text{ \AA}$  at the 10 to 30  $\mu\text{s}$  timeframe. These values are within error of computational calculations, but measuring detail sufficient to conclusively determine the activation of C-H or Si-H bonds will require both more extensive calculations and higher quality data than have been obtained in this Thesis.

## Chapter 5

This Chapter examines TRIR and TRXAS data for the photolysis of  $\text{CpMn}(\text{CO})_3$  in alkane and alkyl silane solvents. TRIR has been used to determine the photoproducts of  $\text{CpMn}(\text{CO})_3$  in *n*-heptane doped with triethyl silane and established the relationship between the conversion of  $\text{CpMn}(\text{CO})_2(\textit{n}\text{-heptane})$  to  $\text{CpMn}(\text{CO})_2(\text{HSiEt}_3)$  and the doped concentration of triethyl silane.

TRXAS has been used to characterize the difference K-edge manganese data arising from photolysis of  $\text{CpMn}(\text{CO})_3$  to form both an alkane-bound and silane-bound structure. We found evidence that  $\text{CpMn}(\text{CO})_2(\textit{n}\text{-heptane})$  exists in both the primary carbon bound and secondary carbon bound isomers, and identified characteristic features of carbon binding in a silane-doped alkane solution.

The XANES modelling abilities of both FDMNES and QChem were tested, with both software packages being found to produce qualitatively comparable spectra. This allowed the assignment of select features in the experimental data to alkane or silane binding, illustrating the use of theoretical modelling even in early development.

## Appendix I

This Appendix contains graphs of smoothed and unsmoothed k-space data obtained from analysis of the rhenium L<sub>III</sub> edge data collected at the APS in Chicago, in order to demonstrate the degree of effectiveness of smoothing on removing noise while retaining signal.

## Contents

<b>Time-Resolved Spectroscopy of Organometallic Alkane and Silane Intermediates .....</b>	<b>i</b>
Declaration.....	ii
Acknowledgements.....	iii
Abbreviations.....	iv
Abstract.....	vi
Chapter 1.....	vi
Chapter 2.....	vi
Chapter 3.....	vi
Chapter 4.....	vii
Chapter 5.....	vii
Appendix I.....	viii
<b>Chapter 1 – Introduction.....</b>	<b>1</b>
1.1 – Spectroscopy of Reactive Intermediates.....	2
1.1.1 – Pump-Probe and Time Resolved Spectroscopy.....	3
1.1.2 – TRIR of Organometallic Intermediates.....	8
1.1.3 – Introduction to XAS.....	10
1.2 – Organometallic Complexes and Photolysis.....	17
1.2.1 – Metal-Ligand Bonding.....	18
1.2.2 – Trends in Stability.....	19
1.2.3 – Bond Activation.....	20
1.3 – DFT and Computational Chemistry.....	21
1.3.1 – Kohn-Sham DFT.....	21
1.3.2 – Basis Sets and ECPs.....	22
1.3.3 – Computational Modelling of XAS.....	23
1.4 – References.....	23

<b>Chapter 2 – Experimental and Theoretical Methods .....</b>	<b>30</b>
2.1 – Materials .....	30
2.2 – TRIR Sample Preparation .....	30
2.3 – Ultrafast TRIR Apparatus.....	31
2.4 – TRXAS Sample Preparation. ....	32
2.5 – Advanced Photon Source TRXAS.....	33
2.6 – Analysis of XAS Data.....	36
2.6.1 – Generating a Difference Fit.....	36
2.6.2 – Scan Selection .....	37
2.6.3 – Backgrounding .....	38
2.6.4 – Calculating R and Quality of Fit.....	40
2.7 – FTIR Spectroscopy .....	41
2.8 – DFT Calculations.....	41
2.9 – References.....	42
<b>Chapter 3 – Development of Experimental TRXAS at Diamond.....</b>	<b>44</b>
3.1 – Introduction .....	44
3.2 – Aims.....	45
3.3 – Experimental Development .....	45
3.3.1 – The Flow Cell .....	47
3.3.2 – The Pump System.....	51
3.3.3 – X-ray Detection .....	54
3.3.4 – PORTO .....	55
3.4 – Conclusion .....	57
3.5 – References.....	57
<b>Chapter 4 – Probing Organometallic Re-alkane and Re-silane complexes with Time- resolved XAFS .....</b>	<b>59</b>

4.1 – Introduction .....	59
4.1.1 – Rhenium-alkane complexes .....	61
4.1.2 – Rhenium-silane complexes .....	63
4.2 – Aims.....	66
4.3 – Results .....	67
4.3.1 – TRIR of CpRe(CO) <sub>3</sub> in neat triethyl silane .....	67
4.3.2 – TRIR of CpRe(CO) <sub>3</sub> in n-heptane doped with triethyl silane .....	71
4.3.3 – XAS Investigations of CpRe(CO) <sub>3</sub> .....	75
4.3.3.1 – XANES Difference Analysis .....	81
4.3.3.2 – EXAFS of CpRe(CO) <sub>3</sub> in <i>n</i> -hexane.....	83
4.3.3.3 – EXAFS of CpRe(CO) <sub>3</sub> in cyclohexane.....	89
4.3.3.4 – EXAFS of CpRe(CO) <sub>3</sub> in triethyl silane .....	95
4.3.3.5 – Linear Combination Fitting of CpRe(CO) <sub>3</sub> in triethyl silane .....	107
4.4 – Conclusions .....	109
4.5 – References.....	110
<b>Chapter 5 – Manganese-solvent interactions .....</b>	<b>113</b>
5.1 – Introduction .....	113
5.1.1 – Manganese-Alkane Complexes.....	114
5.1.2 – Manganese-Silane Complexes .....	116
5.2 – Aims.....	119
5.3 – Results .....	120
5.3.1 – TRIR of CpMn(CO) <sub>3</sub> in neat triethyl silane.....	120
5.3.2 – TRIR of CpMn(CO) <sub>3</sub> in n-heptane doped with triethyl silane.....	123
5.3.3 – XANES of CpMn(CO) <sub>3</sub> in neat <i>n</i> -heptane .....	127
5.3.4 – XANES of CpMn(CO) <sub>3</sub> in neat triethyl silane .....	139
5.3.5 – XANES of CpMn(CO) <sub>3</sub> in n-heptane doped with tributyl silane .....	143

5.4 – Conclusions .....	152
5.5 – References.....	152
<b>Appendix I – Unsmoothed Rhenium Difference Data.....</b>	<b>155</b>

# Chapter 1 – Introduction

The elucidation of the mechanisms of a process is crucial for a full understanding of a chemical reaction.<sup>1</sup> One key aspect of this exploration involves the detection and characterization of reaction intermediates, which are the transient species that play a pivotal role in determining reaction pathways and overall outcomes of chemical reactions.<sup>2</sup> The importance of studying intermediates is because of their role in determining the reaction pathways and rate of reactions. The identification and characterisation of short-lived species allows insight into bonding and the transformation of intermediates during the reaction. Such knowledge is key for designing efficient catalysts, optimizing reaction conditions, and developing new synthetic strategies. Monitoring intermediates can additionally lead to a deeper comprehension of reaction kinetics and the prediction and control of reaction rates. Several experimental approaches are employed to detect and characterize reaction intermediates. Spectroscopic techniques such as UV-Visible, IR and NMR spectroscopy offer invaluable insights into molecular structures and electronic states. Time-resolved spectroscopic approaches can be undertaken on timescales from femtosecond to minutes and provides snapshots into ultrafast processes and transient species. Such measurements are supported by computational methods including density functional calculations (DFT) and molecular dynamics simulations and these approaches enable intermediate structures and energies to be predicted. In this work we aim to apply both time-resolved infrared and X-ray techniques to provide structural information regarding reaction intermediates particularly focused on organometallic reactions.

Organometallic bonding is an area that promises a wealth of interesting reaction pathways, where metal-ligand interactions can be exploited to great use in catalysis and photocatalysis<sup>3-5</sup> and organic synthesis<sup>6</sup> as well as in more recent areas such as the synthesis and applications of metal-organic frameworks.<sup>7</sup> One particular aspect being explored in modern chemistry is the understanding of ligand binding in these complexes, particularly as such knowledge is a prerequisite to developing new complexes to provide an efficient catalytic pathway such as C-H, Si-H and C-C bond activation.<sup>4, 8 9</sup>

However, the bond formation and dissociation behaviour of these complexes is not yet well understood, with factors such as the steric bulk of other ligands, orbital overlap, and electronegativity all potentially contributing. Understanding this behaviour is key to utilising it to achieve C-H bond activation or other desired pathways, and to investigate these mechanisms scientists have used IR spectroscopy, including time-resolved IR spectroscopy<sup>10, 11</sup>, neutron diffraction<sup>12</sup>, both solid state and solution NMR<sup>13-16</sup>, UV/visible spectroscopy<sup>17</sup>,<sup>18</sup>, and mass spectroscopy.<sup>19</sup>

This Thesis explores the use of Time-resolved X-ray Absorption Spectroscopy (TRXAS) as a novel tool for probing the structures of short-lived organometallic intermediates coupled with more traditional methods of spectroscopy such as time-resolved IR Spectroscopy (TRIR). This Chapter describes the background and theory relevant to the rest of this Thesis.

## 1.1 – Spectroscopy of Reactive Intermediates

As stated above, spectroscopy provides a broad range of investigative probes for the toolbox but not all of them are suited to the investigation of short-lived intermediates which are the subject of the work in this Thesis as the species of interest have lifetimes ranging from nanoseconds to milliseconds. Certain techniques such as NMR cannot easily be applied to interrogate such transients even though NMR provides key structural insight on these short time-scales.

Matrix isolation, developed by Pimentel in 1954, pioneered the investigation of such short-lived species by preserving them in inert media at low temperatures<sup>20</sup>, and the preservation of samples at low temperatures has allowed intermediates to be investigated mainly with spectroscopic tools such as UV/visible and IR spectroscopy.<sup>21</sup> Studies characterising unique new molecules (such as organometallic alkane complexes relevant to this Thesis) have led to subsequent work which allowed characterisation with more conventional structural probes such as NMR<sup>16</sup>, and X-ray diffraction<sup>22</sup>. While both of these techniques are powerful structural probes, the requirement of long-lived intermediates and low temperatures for

NMR studies and solid-state samples for X-ray diffraction have prevented the more widespread analysis of these intermediates *in situ* using these direct structural techniques.

UV/vis spectroscopy has been used to probe both excited states and untangle complex dynamics between states as well as unravelling the formation and dynamics of reactive intermediates. This approach is often used to provide kinetic information on the decay and formation of those species.<sup>17, 18</sup> The comparatively broad and featureless peaks of UV/vis spectroscopy limit its usefulness to systems with very pronounced changes, so it is much less useful in for providing structural insight than TRIR, described below.<sup>17</sup>

### 1.1.1 – Pump-Probe and Time Resolved Spectroscopy

The technique of flash photolysis was developed by Norrish and Porter in 1949<sup>23, 24</sup>, and it remains a cornerstone of modern time-resolved techniques: by instigating a photochemical reaction with a single brief pulse, the kinetics of that reaction can be examined via the use of fast spectroscopic methods on the excited sample. Figure 1.1 shows an illustration of the pump-probe process.

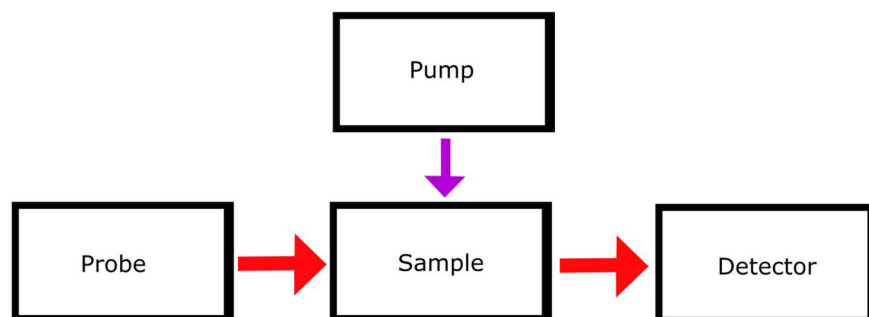


*Figure 1.1: Scheme showing the pump- probe principle: a pump (typically a pulsed UV laser) initiates a chemical reaction in the sample, which is then monitored with a probe beam and detector.*

The time resolution of pump-probe techniques has steadily improved with the advance of laser and detector technology, with modern lasers now offering femtosecond-level measurements.<sup>25</sup> TRIR remains one of the most widely used versions of time-resolved spectroscopy<sup>26</sup>, with high structural sensitivity that is well-suited to monitoring the changes of organometallics.<sup>27</sup> TRIR can also be performed by using a moving mirror to scan through IR wavelengths on a short timescale, a technique called rapid-scan FTIR that is limited by the velocity of the mirror. Mirror speeds typically limit scan times to 45-100 ms on an advanced FTIR spectrometer.<sup>28</sup> Point by point TRIR can, monitor timeframes as small as a few nanoseconds and is limited by the risetime of IR detectors. In this version of the technique each wavenumber is probed in turn across the experiment's timescale before pumping the sample again and monitoring at the next wavenumber, thus constructing the extended spectrum point-by-point. This necessitates having repeatable reaction conditions and is also a significantly more time-intensive technique, due to the number of repetitions that must be performed to construct the spectrum. Step-scan FTIR is a less time-intensive variant that utilises a broadband IR source and moving a mirror stepwise to generate a series of time dependent interferograms. Changes in the spectrum are then extracted by Fourier transform of the interferograms.<sup>29</sup>

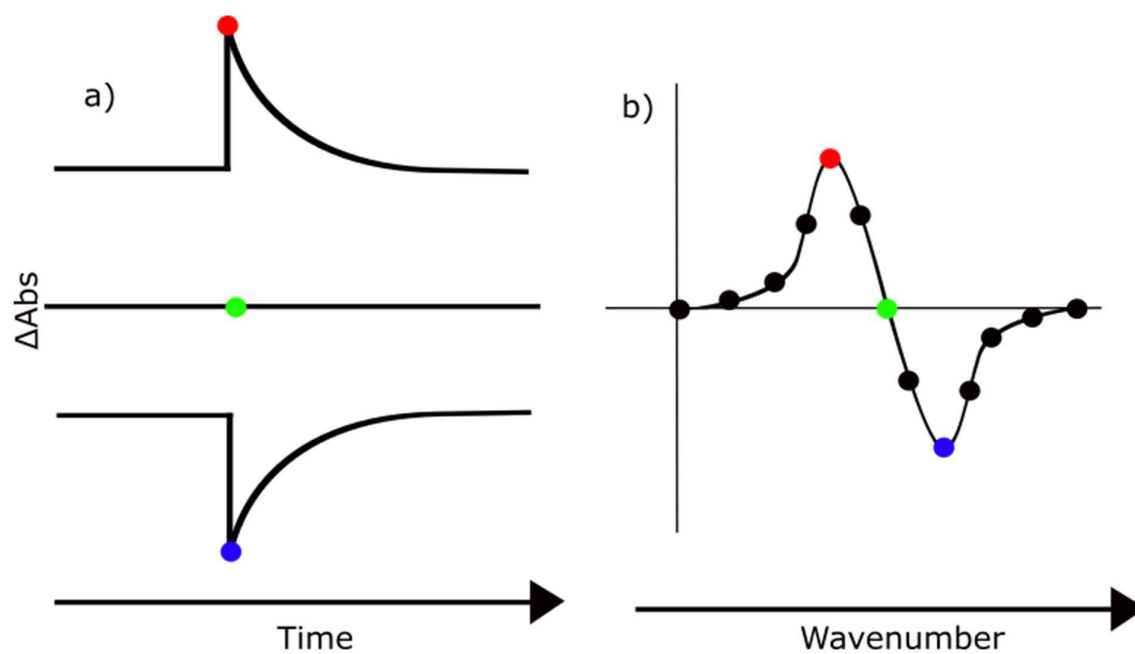
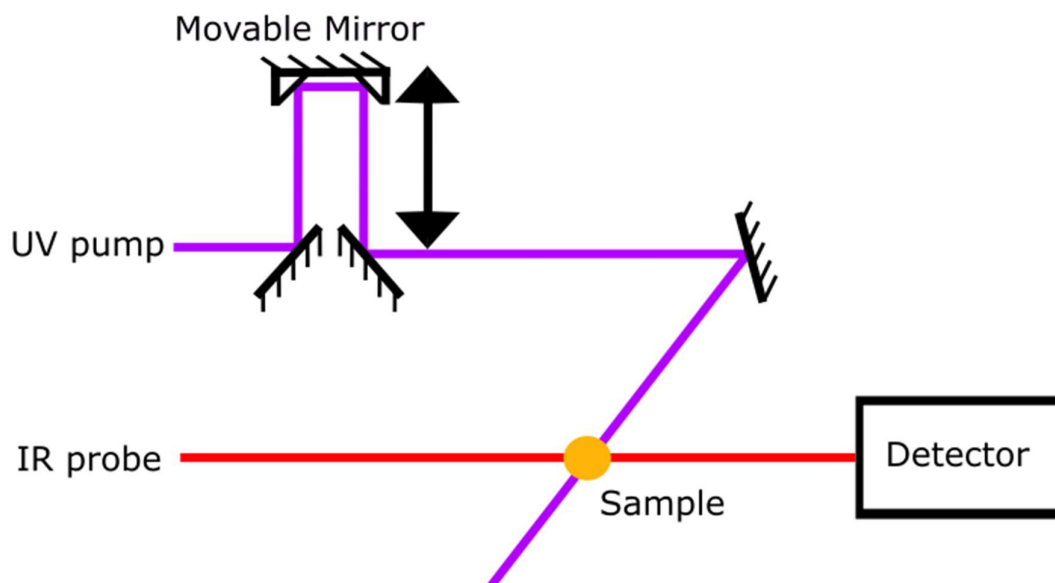


Figure 1.2: Illustration of step-scan TRIR process, with a) the change in absorbance monitored at different wavelengths, and b) the resulting plot of change in absorbance vs wavenumber that arises from those points.

Ultrafast TRIR can be achieved by using broadband pulsed IR lasers which are employed with an optical parametric amplifier (OPA) and a delay line is used to control the interval between the pump and probe pulse and can achieve femtosecond-level resolution.<sup>30</sup> The main limitations of the TRIR approach the need for strongly absorbing IR bands to monitor structural changes, and strong solvent absorptions can hinder the signal-to-noise in such measurements. The TRIR apparatus used in this Thesis is detailed in Chapter 2.



*Figure 1.3: Scheme of a delay line for pump-probe spectroscopy. The movable mirror's motion in the direction of the arrows alters the path length of the pump pulse, adjusting the time delay between the pump and probe reaching the sample.*

Time-resolved resonance Raman spectroscopy has also been employed to investigating organometallics<sup>31</sup>, and allows investigation via otherwise weak Raman bands to reveal structural information.<sup>32</sup> Hammonds et al. recently investigated the charge transfer mechanism of ruthenium(II) trisbipyridine, and confirm its photoinduced reaction pathway with methyl viologen.<sup>33</sup> Figure 1.4 shows their use of time-resolved resonance Raman spectroscopy in this analysis. However, resonance Raman spectroscopy is limited to observing totally symmetric vibrations, and broad solvent bands can obscure vital sections of the spectrum.

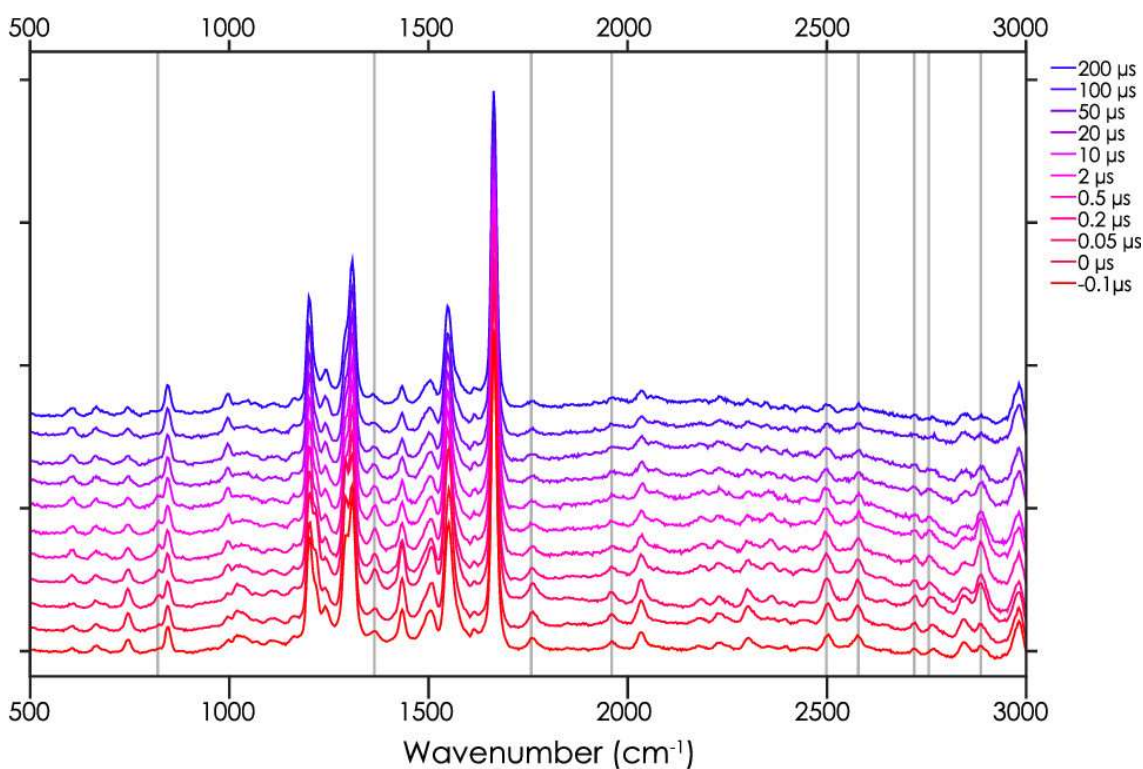


Figure 1.4: Time-resolved Resonance Raman spectra of aqueous  $[Ru(bpy)_3]^{2+}$  and  $MV^{2+}$ , taken at microsecond-time scale intervals following excitation. Replicated from Hammonds et al.<sup>33</sup>

As mentioned above this Thesis focuses on using TRXAS to interrogate reaction intermediates. Various X-ray based techniques have been combined with pump-probe and other time resolved methods to provide novel insights into intermediates, such as with small-angle scattering.<sup>34</sup> X-ray crystallography can elucidate molecular structures with sub-Angstrom accuracy, and with recent advances in x-ray pulse generation has been used to study a variety of fast time-resolved processes.<sup>35</sup> This technique has been reviewed<sup>36</sup> and can be used to monitor important structural changes such as probing protein structural transitions.<sup>37</sup> The technique requires systems that express long-range order to determine structure, and so cannot probe solution-phase reactions.

X-ray Absorption Spectroscopy (XAS) is a powerful technique due to its element-selectivity and sensitivity to both structural and electronic properties and a detailed introduction to the technique is given below. However, time-resolved XAS experiments require high levels of flux that restrict the capacity to perform them to synchrotrons and other high intensity

sources. Some early examples of TRXAS experiments were performed by Dent *et al.*<sup>38</sup>, investigating the structural rearrangements of organometallic complexes on a several-hour timescale, and by Mills *et al.*<sup>39</sup> to investigate the recombination of carbon monoxide and myoglobin following laser photolysis. As synchrotron technology improved, faster and more precise experimentation became possible, and the opportunities of using XAS in conjunction with ultrafast lasers were anticipated.<sup>40</sup>

The rise of 3<sup>rd</sup> generation synchrotrons<sup>41</sup> offered stable, high-flux, high repetition rate sources and has enabled an array of time-resolved studies, which have enabled the development of several TRXAS experimental regimes<sup>42</sup> and opened the way to study metal co-ordination<sup>43</sup> and catalysis<sup>44</sup>. The arrival of (X-ray Free Electron Lasers) XFELs has similarly broadened the horizons of TRXAS<sup>45</sup>, and has been used to investigate the excited state properties of  $[\text{Fe}(\text{dcpp})_2]^{2+}$  (dcpp = 2,6- (dicarboxypyridyl)pyridine).<sup>46</sup>

TRXAS has surged in use in investigating photochemical systems<sup>47</sup>, and shows its versatility in investigations of metal-ligand bond geometry<sup>48</sup>, excited state transitions<sup>49</sup>, and even the investigation of mixed-metal complexes.<sup>50</sup>

### 1.1.2 – TRIR of Organometallic Intermediates

TRIR of organometallic intermediates has been performed extensively<sup>14, 18, 27, 51</sup> due to the technique's high suitability to investigating their properties using a powerful structural probe.<sup>26</sup> Relevant to the work in this Thesis, the high absorbance of carbonyl ligands in the 1700 - 2200  $\text{cm}^{-1}$  region allows them to be clearly observed in a variety of solvents, and their sensitivity to electron density at the metal centre causes those bands to shift substantially with the chemical changes of the metal complex.

The technique has been applied extensively to the area from its inception, with early successes in the characterisation of metal carbonyl intermediates<sup>52</sup> and their isomers<sup>53</sup> followed by later use in the identification of excited states.<sup>10</sup>

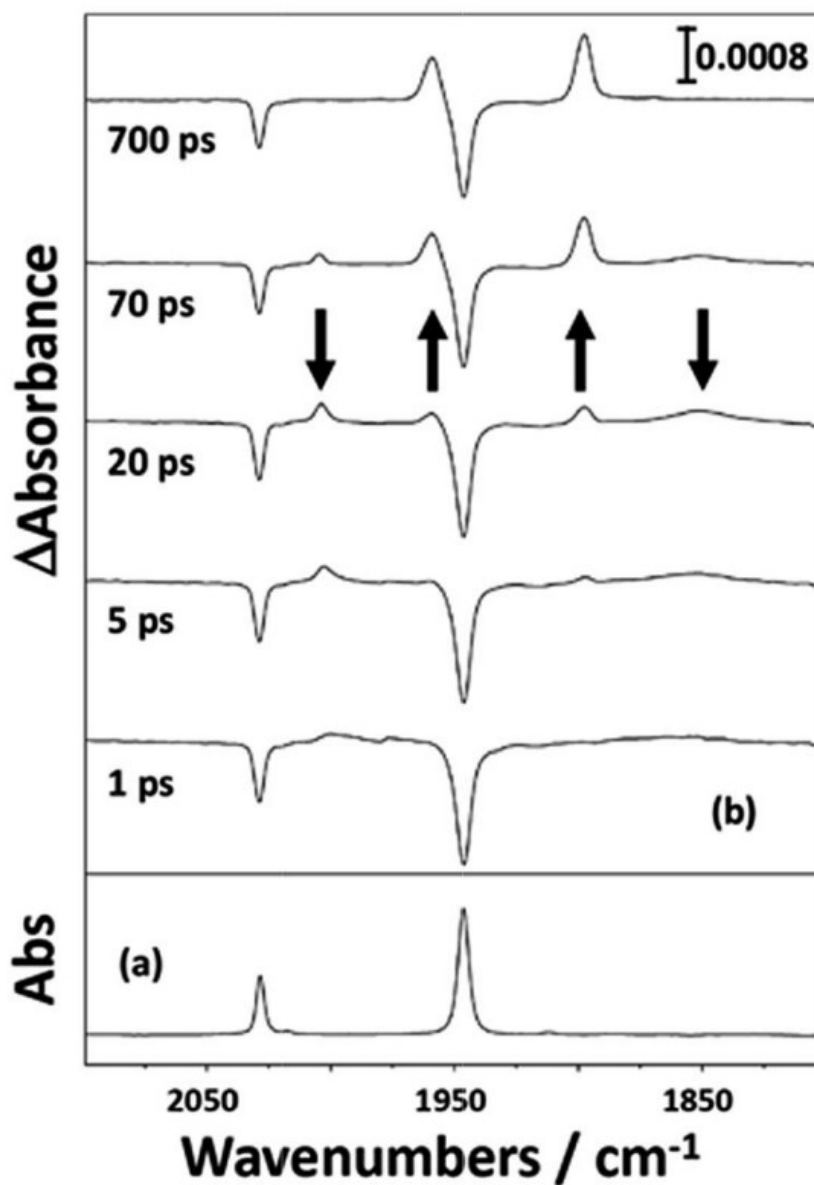


Figure 1.5: Example IR spectrum of  $\text{CpMn(CO)}_3$  in *n*-heptane including a) the original spectrum of the parent and b) the time-resolved difference spectrum at selected intervals post-photolysis. Replicated from ref.<sup>54</sup>

Figure 1.5 shows an example of TRIR spectroscopy performed on  $\text{CpMn(CO)}_3$  in neat *n*-heptane. The base spectrum (a) shows the peaks of the parent species, while the difference spectra (b) show new bands appearing on the picosecond timescale after photolysis of the solution. This shows the degree of peak shift that can be provoked from simple loss of a ligand and the subsequent changes that can be resolved through the growth and decay of

peaks. The TRIR spectrum obtained 1 ps after excitation shows that the parent  $\nu(\text{C-O})$  bands are bleached and two new broad  $\nu(\text{C-O})$  bands are formed. These new  $\nu(\text{C-O})$  bands sharpen to 2004 and 1849  $\text{cm}^{-1}$  over the first few picoseconds following excitation. This shift is consistent with vibrational cooling of the initially formed transient. These bands were assigned to  ${}^3\text{CpMn}(\text{CO})_2$  by comparison with the previous TRIR and matrix isolation studies,  ${}^3\text{CpMn}(\text{CO})_2$  decays to form the organometallic alkane complex,  ${}^1\text{CpMn}(\text{CO})_2(n\text{-C}_7\text{H}_{16})$ . In the modern day TRIR continues to be a powerful form of analysis, being utilised in the growing field of ultrafast chemistry<sup>55</sup> for purposes such as investigating nitrogen fixation.<sup>56</sup>

### 1.1.3 – Introduction to XAS

As XAS is a major part of this Thesis a more detailed introduction is needed, especially as such time-resolved measurements are new at Nottingham. XAS monitors the change in absorption of a sample as the energy of incident x-rays is varied. The attenuation of the sample is given by Equation 1.1:

$$I = I_0 e^{-\mu t} \quad (1.1)$$

Where  $I$  is the transmitted intensity,  $I_0$  is the incident intensity,  $\mu$  is the absorption coefficient, and  $t$  is the thickness of the sample.

In the general case,  $\mu$  can be approximated with Equation 1.2:

$$\mu \approx \frac{\rho Z^4}{AE^3} \quad (1.2)$$

Where  $\rho$  is the density,  $Z$  is the atomic number,  $A$  is the atomic mass, and  $E$  is the incident x-ray energy. Thus, the X-ray absorption of a sample declines sharply with increasing photon energy as the penetration of the radiation increases but exhibits sharp increases at energies corresponding to the ionisation energy of core-shell electrons. These sharp features are appropriately called edges. The XAFS is the information-rich pattern in the x-ray absorption of an atom above and below an edge, arising from the modulation of  $\mu$ . A general scheme for this pattern is shown in Figure 1.6 below.

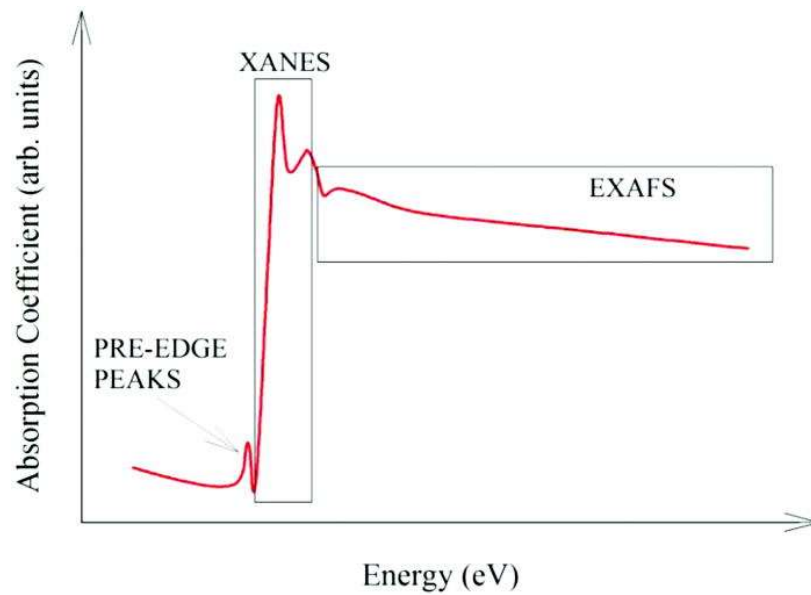


Figure 1.6: XAFS spectrum indicating the general location of the XANES and EXAFS regions, reproduced from ref.<sup>57</sup>

Edges are labelled by their corresponding shell, with the K-edge arising from excitation from the 1s energy level, and the L<sub>I</sub>-edge from excitation of the 2s level, and the L<sub>II</sub> and L<sub>III</sub>-edges from the 2p<sup>1/2</sup> and 2p<sup>3/2</sup> levels, and so on. As these edges vary in energy based on the nuclear charge, they are highly element-specific features.

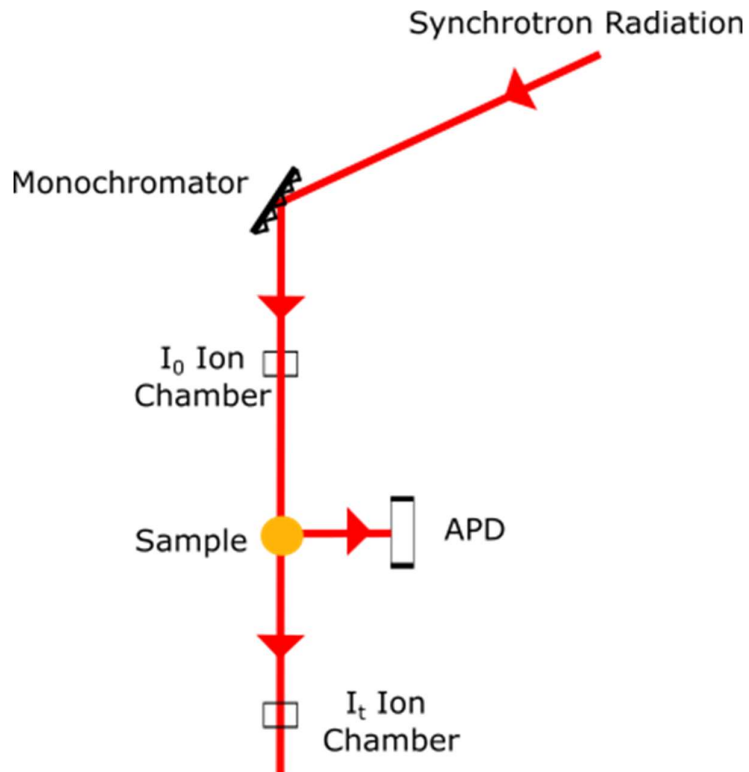


Figure 1.7: Diagram of XAS data collection, showing the X-ray beam path in red.

Figure 1.7 shows a general example of the collection of XAS data: a synchrotron or other sufficiently high flux source provides X-ray radiation which is filtered to a selected energy by a monochromator. Ion chambers positioned before and after the sample measure  $I_0$  and  $I_t$  respectively, while an APD or other sensor positioned at  $90^\circ$  to the X-ray path can measure fluorescence radiation.

Following the excitation of an electron, the system can de-excite by two main types of emission: Auger emission or fluorescence. In fluorescence, a higher-energy electron emits radiation as it descends to the lower energy level, while in the Auger effect one electron descends to the empty core hole while another electron is ejected with the excess energy. It is therefore possible to measure the absorption of a sample through its transmission, fluorescence, or Auger emission. Of these, fluorescence is more commonly used as Auger emission is typically limited to surface measurements.

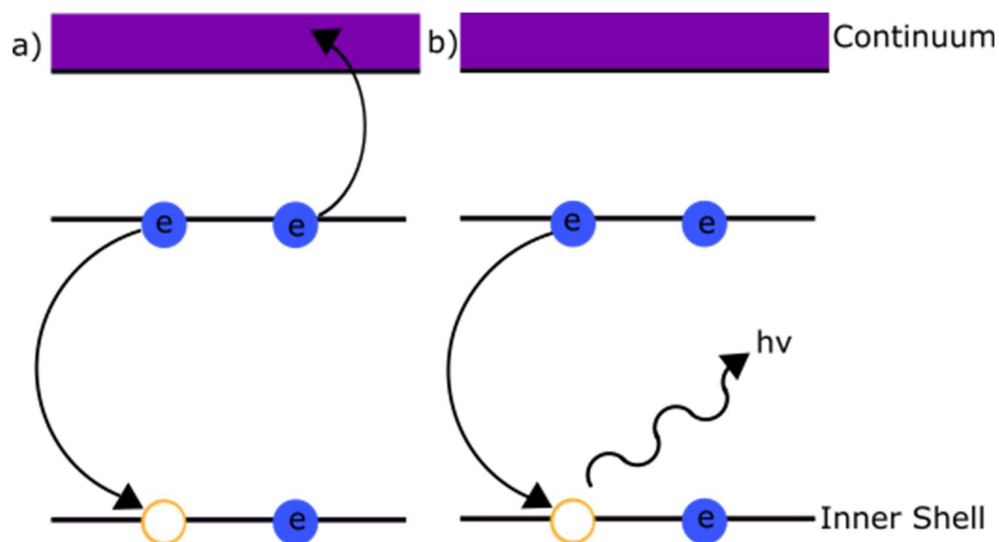


Figure 1.8: Diagram of a) Auger emission and b) fluorescence arising from an inner shell vacancy.

The XAFS arises from several factors, and it is generally split into two regions where different contributions dominate: the X-ray Absorption Near-Edge Structure (XANES), typically defined as the region from about 10eV below the absorption edge to 50eV above it, and the Extended X-ray Absorption Fine Structure (EXAFS), usually taken as the section above the XANES upper energy limit. While the theory of EXAFS has been investigated since the early 1930s<sup>58, 59</sup>, it has been challenging to develop a theory that provides quantitative agreement with experiment. An accurate formula derived from theoretical principles was worked towards over several decades. This process saw several competing theories explored and contrasted, including debate over whether the phenomenon was dictated by long-range or short-range effects.<sup>60</sup> With steady work from the community, a functional mathematical model was developed and applied successfully to experimental data.<sup>61, 62</sup>

The short-range order (SRO) theory can be used to rationalise EXAFS in terms of a non-classical phenomenon. When a photoelectron is produced by an incident X-ray upon an atom, its wavelike nature causes it to scatter off nearby features in the molecule. The reflected waves from nearby atoms interfere constructively or destructively with the original photoelectron wave. This interference in turn affects the transition strength of the X-ray induced transition, and thus the probability of that transition occurring.

By taking the formula for the de Broglie wavelength of the photoelectron (considered in the non-relativistic limit here for simplicity),

$$\lambda = \frac{h}{mv} \quad (1.3)$$

and considering the phase difference of a reflected wave from a point that is a distance  $r$  away,

$$\Phi = 2\pi \left[ \left[ \frac{2r}{\lambda} \right] \right] \quad (1.4)$$

where  $\left[ \left[ \frac{2r}{\lambda} \right] \right]$  is the non-integer component of  $\frac{2r}{\lambda}$ . We can see that the degree of interference depends on both the wavelength of the photoelectron (which will decrease as the energy of the incident X-ray increases) and the distance between the origin atom and the scattering atom. Therefore, in a system with stationary bond lengths and a spectrum of incident X-rays, it would be expected that the absorption above the photoexcitation threshold would vary with a sinusoidal pattern as this phase difference changed with photon energy.

The SRO theory has been largely enshrined as a good theory for understanding EXAFS through the formula first given by Sayers et al. in 1971.<sup>63</sup> The formula (Equation 1.5 below) consistently predicts and describes EXAFS features and has been used since its development to quantify XAS data.

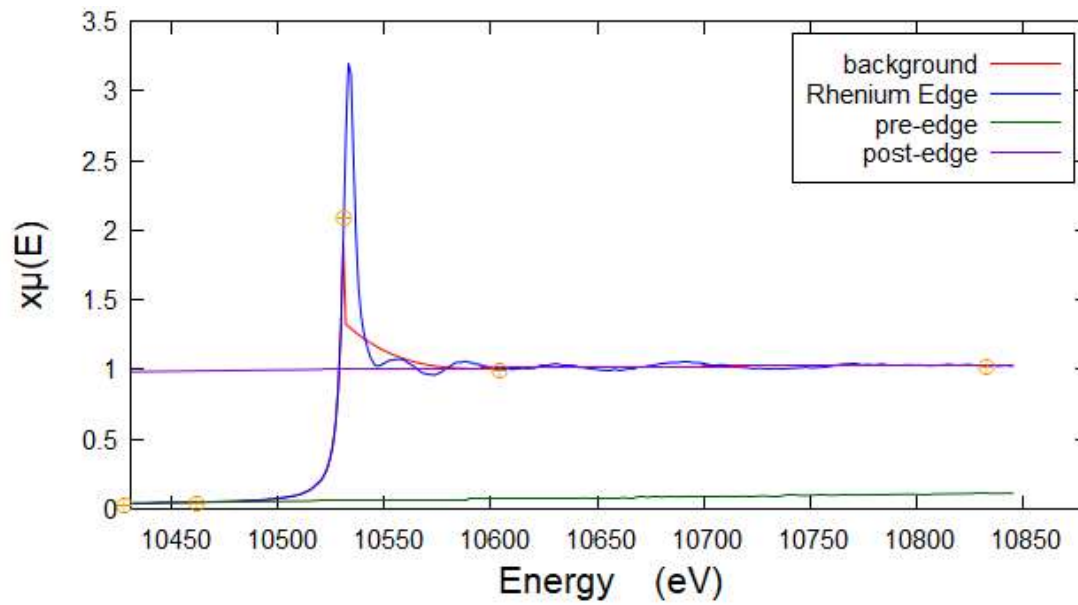


Figure 1.9: Plot of rhenium  $L_{III}$  edge data showing pre-edge and post-edge lines used to construct the background.

Figure 1.9 shows an example of EXAFS data for the  $L_{III}$  edge of rhenium. By constructing a background that accounts for the signal before the edge and the excitation at the edge itself the contributions from scattering effects can be isolated and put through a Fourier transform to produce a set of oscillations which can be plotted in reciprocal space, as shown in Figure 1.10. These oscillations can then be described with the parameters of Equation 1.5.

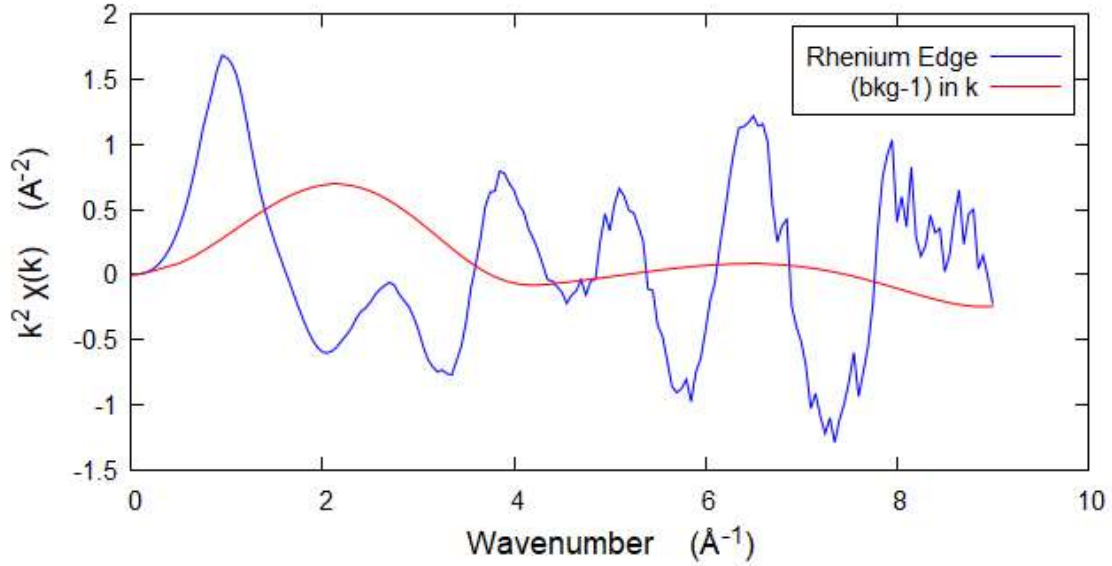


Figure 1.10:  $k$ -space spectrum derived from Re  $L_{III}$  edge data (blue) and excluded background component (red).

$$\chi(k) = \sum_R S_0^2 N_R \frac{|f(k)|}{kR^2} \sin(2kR + 2\delta_c + \Phi) e^{\frac{-2R}{\lambda(k)}} e^{-2\sigma^2 k^2} \quad (1.5)$$

The formula gives the dependence of the normalised XAFS spectrum  $\chi$  with respect to the photoelectron momentum index,  $k$ . In this case  $\chi$  is the profile of the edge with the removal of the ‘background’ energy contribution of the edge itself. The index  $k = \sqrt{\hbar\omega - |E_c|}$  is a form familiar to quantum chemistry. The parameters  $R$  are the interatomic distances,  $N_R$  is the co-ordination number of the atom, and  $\sigma$  is the rms bond length fluctuation.  $\lambda(k)$  is the XAFS mean free path.  $\delta_c$  is the central atom partial-wave phase shift of the final state. The phase factor  $\Phi$  arises from the quantum mechanical nature of the wavefunction, and the term  $S_0^2$  is the amplitude reduction factor.

Unlike the EXAFS, XANES is not described by a widely accepted formula, though computational methods for generating XANES spectra are being developed and employed.<sup>64</sup>  
<sup>65</sup> In the energy range of the XANES, multiple photoelectron scattering is a significant contribution to the absorption function, which contributes to the complexity of the system

but also allows more geometric information to be extracted. While the strength of these scattering events involving two or more reflections decay quickly, they are still significant in the XANES region. Figure 1.11 illustrates the difference between single and multiple scattering.

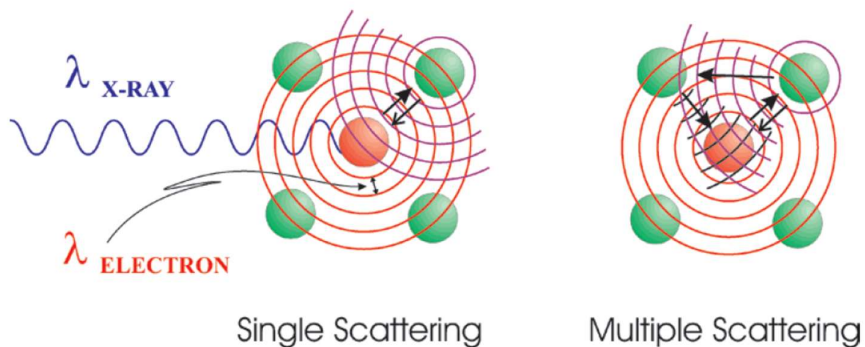


Figure 1.11: Diagram of photoelectron wave scattering phenomena replicated from ref.<sup>66</sup>

XANES spectra also show features due to excitations to low-lying excited states, where the core electron receives enough energy to jump to a state that lies close to the free energy continuum. As these electrons are still bound to the complex, they do not exhibit the same interference patterns from local structure.

## 1.2 – Organometallic Complexes and Photolysis

The following section discusses the importance of the metal ligand interactions which are important in this thesis, with particular focus on metal carbonyls, Organometallic Alkane Complexes and the general details of their photochemistry showing common trends in their behaviour, as well as briefly reviewing the history of their study.

### 1.2.1 – Metal-Ligand Bonding

Metal-ligand bonding is a complex relationship between the metal centre and the ligand, with the movement of electron density between metal and ligand giving rise to a number of subtle effects that can impact the bonding of the ligand itself and the metal's bonds to other ligands. The nature of ligand informs the types of bonding it can instigate. This includes both large ligands which bond to the metal centre at multiple sites, such as  $\text{Tp}^*\text{Rh}(\text{CO})_2$  ( $\text{Tp}^* = \text{HB-Pz}_3^*$ ,  $\text{Pz}^* = 5,3,5\text{-dimethylpyrazolyl}$ )<sup>67</sup>, and multiple atoms involved in bonding at a single site, such as with  $\eta^2\text{-CO}_2$  bonding.<sup>68</sup> Bridging ligands can bond to two separate metals, a property that allows the construction of metal-organic frameworks.<sup>7</sup> This Thesis focuses on nominally more simple systems, where the ligands of interest are formally regarded to be bonding at a single site.

The process of photoexcitation in metal carbonyls has been explored both experimentally and computationally<sup>69</sup>, but the result of that photoexcitation is well-known and widely utilised.<sup>70</sup> A metal carbonyl is ejected from the complex, leaving a vacant coordination site.

Upon removal of a ligand from a stable organometallic complex, a highly reactive unsaturated intermediate is created, and another available moiety will often bind to the vacant site, as shown in Figure 1.12.

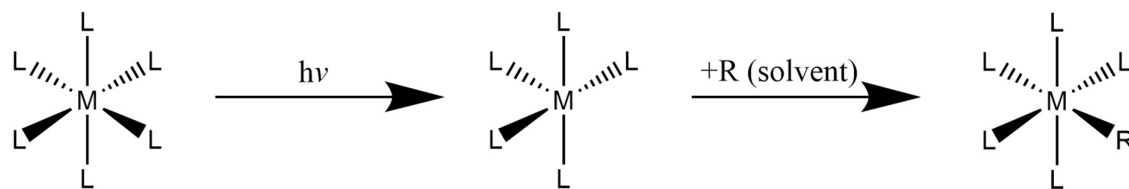


*Figure 1.12: Scheme of a typical metal-ligand loss and occupation of the empty site by a solvent molecule.*

Due to the reactivity of this unsaturated complex, even classically 'inert' species like noble gases may be accepted to the complex.<sup>71</sup> This bonding can take various forms based on the properties of the solvent molecule, the metal centre, and the surrounding ligands. One form of bonding is the sigma complex, where the  $\sigma$ -bond of a molecule donates its electron

density to the metal to create a 3-centre-2-electron bond. The range of  $\sigma$  complexes is quite broad, with examples of H-H<sup>72</sup>, B-H<sup>73</sup>, Si-H<sup>74</sup> and C-H<sup>75</sup>  $\sigma$  bonds being known.

### 1.2.2 – Trends in Stability

The earliest metal carbonyl intermediates investigated were metal-noble gas complexes derived from hexacarbonyls.<sup>76</sup> Following studies established a difference in rate based on the metal centre, with Cr and Mo reacting more quickly than W.<sup>18</sup>

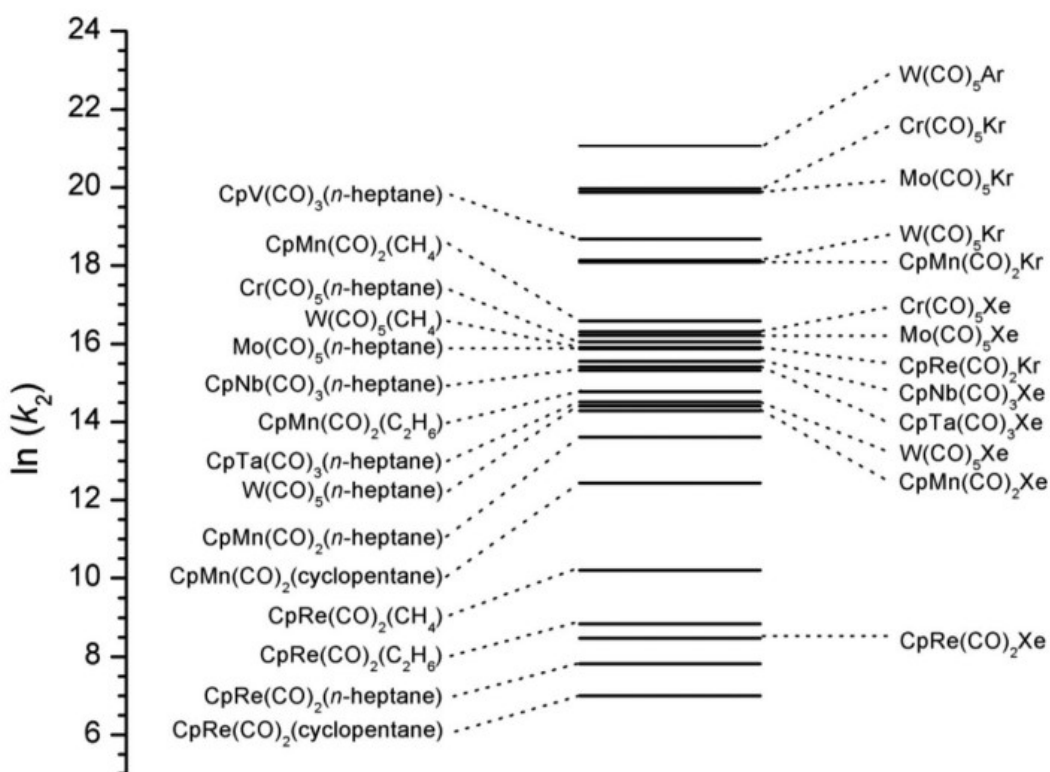


Figure 1.13: Reaction rates of alkane and noble gas complexes, reproduced from ref.<sup>77</sup>

Investigations expanded the range of metals and complexes investigated, and found rhenium to give rise to the most stable metal-alkane complexes investigated yet, with CpRe(CO)<sub>2</sub>(cyclopentane) being the longest-lived metal-alkane complex found so far.<sup>78</sup>

These data have been compiled across decades of work to produce an extensive list of metal-alkane and metal- noble gas intermediates and their rates of reaction, as shown in Figure 1.13.<sup>77</sup> These studies determined that cyclic alkane complexes were more stable than their linear counterparts, and that for Group V-VII metals stability is increased moving down and right along the groups.

### 1.2.3 – Bond Activation

One of the major ambitions for organometallic catalysis is the development of efficient, economic methods of C-H and Si-H bond activation, which would allow for conversion of chemical feedstocks such as methane into more useful reagents, e.g., methanol. The exploration of  $\sigma$ -alkane complexes as a route to C-H bond activation is an ongoing endeavour<sup>79</sup>, and transition metal hydrides<sup>80</sup> and silane bond cleavage<sup>81</sup> have also been explored as powerful potential uses for organometallic complexes.

In the process of binding to a metal centre, the  $\sigma$ -bond of the C-H moiety is donated from the alkane, and this system is stabilised by  $\pi$  backbonding from the metal d-orbitals. With sufficient backdonation to the antibonding orbital, the C-H bond can be activated, leading to an alkane-metal-hydride complex forming.<sup>3</sup>

The full details of why a metal alkane system will or will not undergo C-H activation are not yet known; an osmium-methane complex can express significant distortion of the methane ligand without activation<sup>82</sup>, while evidence of activation is seen for specific rhenium alkane complexes.<sup>83</sup> There have been a number of computational studies of sigma-alkane complexes<sup>6</sup>, including an exploration of the promising subcategory of rhodium  $\sigma$ -alkane complexes.<sup>84</sup>

## 1.3 – DFT and Computational Chemistry

The advance of computational chemistry has led to the capability to model and determine a species' structure and spectral fingerprints, in addition to various other quantities of interest.<sup>85-87</sup> This is achieved through quantum chemistry calculations, specifically the solution of the Schrödinger equation for atoms and molecules. The Schrödinger equation cannot be solved exactly for systems of more than one electron which necessitates the use of approximate models that have an associated level of error, and much of the development of the field is associated with finding methods that achieve more accurate results, either generally or for specific classes of systems. While there are many different software packages that have been used to model chemical structures, this Thesis focuses specifically on the application of QChem, which can model a range of properties using DFT, and FDMNES, a program specifically for modelling XANES structures.

### 1.3.1 – Kohn-Sham DFT

DFT is the process of modelling an electronic system via the electron density, rather than the many electron wavefunction. Most DFT calculations adopt the formalism of Kohn and Sham<sup>88</sup>. In Kohn-Sham DFT the electron density is described as:

$$\rho(\mathbf{r}) = \sum_{i=1}^N |\psi_i(\mathbf{r})|^2 \quad (1.6)$$

Within Kohn-Sham DFT it is not known how to exactly model the exchange correlation term, which is estimated by a further functional. This is shown in the following equation:

$$E[\rho] = V_{ne}[\rho] + T_s[\rho] + J[\rho] + E_{XC}[\rho] \quad (1.7)$$

where  $E[\rho]$  is the total energy,  $V_{ne}[\rho]$  is the electron-nucleus interaction energy,  $T_s[\rho]$  is the kinetic energy of non-interacting electrons, and  $J[\rho]$  is Coulomb repulsion between electrons.  $E_{XC}[\rho]$  represents the exchange correlation. In Kohn-Sham DFT the density is

determined by minimising the energy in a Self-Consistent Field (SCF) approach, which is an iterative method of solving and checking for convergence as illustrated in Figure 1.14.

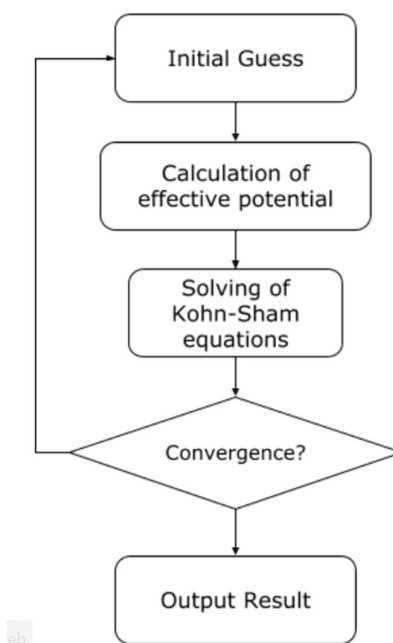


Figure 1.14: Flow chart of an SCF method utilising Kohn-Sham DFT.

### 1.3.2 – Basis Sets and ECPs

Basis sets comprise sets of functions used to describe the orbitals in the system, and the majority of basis sets use Gaussian functions. As a general rule, larger basis sets are more accurate, but increasing the size of the basis set also increases the computational expense. Similarly, the number of points used in the grid to model the integral generally increase the accuracy of the calculation with size at the expense of computational cost. For particularly large atoms with many filled shells of electrons, it is often beneficial to reduce the computational burden by employing ECPs. This involves the approximation of modelling the innermost orbital of heavier atoms as a pseudopotential, which describes the effect of the orbitals on the outer orbitals without explicitly including them in the calculation. While ECPs are often a useful approximation, the nature of XAS makes them incompatible with modelling the XAFS.

### 1.3.3 – Computational Modelling of XAS

The XANES is one of the many physical characteristics that can now be modelled with DFT<sup>89</sup>, with computations now being applied to ultrafast systems.<sup>64</sup> The development of software to simulate the XAFS is derived from the extensive theoretical understanding of the phenomenon, and is a considered compromise between approximations and computational costs.<sup>61</sup> A variety of software packages are available to scientists in the modern day, with FDMNES<sup>90</sup>, FEFF9<sup>91</sup>, and the Demeter Suite<sup>92</sup> being well-known examples. FDMNES employs a DFT-LSDA code to predict edge structure and is used to model XANES and EXAFS spectra.<sup>65</sup> FEFF9 employs a real-space Green's function to create a computationally cheap system of modelling, and is an adept tool for evaluating the XANES.<sup>93</sup>

The Demeter Suite utilises the IFEFFIT package<sup>94</sup> to calculate XAS features, and provides the Athena program to process and background XAS data, as well as the Artemis program to fit parameters such as bond lengths to EXAFS data.<sup>95</sup> It is also possible to model the XANES with QChem by computing the excited states of the core electrons, an option that is tested in this Thesis. At present QChem lacks a sophisticated treatment of the relativistic correction, so the systems that can be analysed with it are somewhat limited. This Thesis makes use of the Demeter suite for investigating EXAFS data and compares the strengths of both FDMNES and QChem for modelling the XANES.

## 1.4 – References

1. D. Astruc, *New Journal of Chemistry*, 2005, **29**, 42-56.
2. N. E. Leadbeater, *Comments on Inorganic Chemistry*, 1998, **20**, 57-82.
3. R. H. Crabtree, *Journal of Organometallic Chemistry*, 2004, **689**, 4083-4091.
4. F. J. Song, T. Gou, B. Q. Wang and Z. J. Shi, *Chemical Society Reviews*, 2018, **47**, 7078-7115.
5. B. Zhang and L. Sun, *Chemical Society Reviews*, 2019, **48**, 2216-2264.

6. D. L. Davies, S. A. Macgregor and C. L. McMullin, *Chemical Reviews*, 2017, **117**, 8649-8709.
7. L. Hanna and J. V. Lockard, *Journal of Physics-Condensed Matter*, 2019, **31**, 20.
8. K. R. Sawyer, J. F. Cahoon, J. E. Shanoski, E. A. Glascoe, M. F. Kling, J. P. Schlegel, M. C. Zoerb, M. Hapke, J. F. Hartwig, C. E. Webster and C. B. Harris, *Journal of the American Chemical Society*, 2010, **132**, 1848-1859.
9. A. A. Shteinman and M. Mitra, *Inorganica Chimica Acta*, 2021, **523**, 13.
10. J. M. Butler, M. W. George, J. R. Schoonover, D. M. Dattelbaum and T. J. Meyer, *Coordination Chemistry Reviews*, 2007, **251**, 492-514.
11. D. I. Grills, Doctor of Philosophy, University of Nottingham, 1999.
12. T. F. Koetzle, P. M. B. Piccoli and A. J. Schultz, *Nuclear Instruments & Methods in Physics Research Section a-Accelerators Spectrometers Detectors and Associated Equipment*, 2009, **600**, 260-262.
13. G. E. Ball, T. A. Darwish, S. Geftakis, M. W. George, D. J. Lawes, P. Portius and J. P. Rourke, *Proceedings of the National Academy of Sciences of the United States of America*, 2005, **102**, 1853-1858.
14. J. A. Calladine, O. Torres, M. Anstey, G. E. Ball, R. G. Bergman, J. Curley, S. B. Duckett, M. W. George, A. I. Gilson, D. J. Lawes, R. N. Perutz, X. Z. Sun and K. P. C. Vollhardt, *Chemical Science*, 2010, **1**, 622-630.
15. S. B. Duckett, M. W. George, O. S. Jina, S. L. Matthews, R. N. Perutz, X.-Z. Sun and K. Q. Vuong, *Chemical Communications*, 2009, 1401 - 1403.
16. D. J. Lawes, S. Geftakis and G. E. Ball, *Journal of the American Chemical Society*, 2005, **127**, 4134-4135.
17. D. C. Grills, K. W. Huang, J. T. Muckerman and E. Fujita, *Coordination Chemistry Reviews*, 2006, **250**, 1681-1695.
18. X. Z. Sun, M. W. George, S. G. Kazarian, S. M. Nikiforov and M. Poliakoff, *Journal of the American Chemical Society*, 1996, **118**, 10525-10532.
19. J. Kopyra, P. Maciejewska and J. Maljkovic, *Beilstein Journal of Nanotechnology*, 2017, **8**, 2257-2263.
20. E. Whittle, D. A. Dows and G. C. Pimentel, *Journal of Chemical Physics*, 1954, **22**, 1943-1943.
21. J. S. Shirk, *Journal of the American Chemical Society*, 1983, **105**, 5180-5180.

22. A. J. Bukvic, A. L. Burnage, G. J. Tizzard, A. J. Martinez-Martinez, A. I. McKay, N. H. Rees, B. E. Tegner, T. Kramer, H. Fish, M. R. Warren, S. J. Coles, S. A. Macgregor and A. S. Weller, *Journal of the American Chemical Society*, 2021, **143**, 5106-5120.
23. R. G. W. Norrish and G. Porter, *Discussions of the Faraday Society*, 1954, 40-46.
24. R. G. W. Norrish and G. Porter, *Nature*, 1949, **164**, 658-658.
25. P. M. Donaldson, G. M. Greetham, C. T. Middleton, B. M. Luther, M. T. Zanni, P. Hamm and A. T. Krummel, *Accounts of Chemical Research*, 2023, 10.
26. A. Mezzetti, J. Schnee, A. Lapini and M. Di Donato, *Photochemical & Photobiological Sciences*, 2022, **21**, 557-584.
27. M. K. Kuimova, W. Z. Alsindi, J. Dyer, D. C. Grills, O. S. Jina, P. Matousek, A. W. Parker, P. Portius, X. Z. Sun, M. Towrie, C. Wilson, J. X. Yang and M. W. George, *Dalton Transactions*, 2003, 3996-4006.
28. B. H. Weiller, *Journal of the American Chemical Society*, 1992, **114**, 10910-10915.
29. X. Z. Sun, S. M. Nikiforov, J. Yang, C. S. Colley and M. W. George, *Applied Spectroscopy*, 2002, **56**, 31-39.
30. M. Towrie, D. C. Grills, J. Dyer, J. A. Weinstein, P. Matousek, R. Barton, P. D. Bailey, N. Subramaniam, W. M. Kwok, C. S. Ma, D. Phillips, A. W. Parker and M. W. George, *Applied Spectroscopy*, 2003, **57**, 367-380.
31. P. G. Bradley, N. Kress, B. A. Hornberger, R. F. Dallinger and W. H. Woodruff, *Journal of the American Chemical Society*, 1981, **103**, 7441-7446.
32. S. K. Sahoo, S. Umapathy and A. W. Parker, *Applied Spectroscopy*, 2011, **65**, 1087-1115.
33. M. Hammonds, T. T. Tran, Y. H. H. Tran, M. H. Ha-Thi and T. Pino, *Journal of Physical Chemistry A*, 2020, **124**, 2736-2740.
34. D. Keefer, S. M. Cavaletto, J. R. Rouxel, M. Garavelli, H. Yong and S. Mukamel, *Annual Review of Physical Chemistry*, 2023, **74**, 73-97.
35. P. Coppens, J. Benedict, M. Messerschmidt, I. Novozhilova, T. Graber, Y.-S. Chen, I. Vorontsov, S. Scheins and S.-L. Zheng, *Acta Crystallographica Section A*, 2010, **66**, 179-188.
36. T. Schnappinger, D. Jadoun, M. Gudem and M. Kowalewski, *Chemical Communications*, 2022, **58**, 12763-12781.

37. S. Pandey, R. Bean, T. Sato, I. Poudyal, J. Bielecki, J. Cruz Villarreal, O. Yefanov, V. Mariani, T. A. White, C. Kupitz, M. Hunter, M. H. Abdellatif, S. Bajt, V. Bondar, A. Echelmeier, D. Doppler, M. Emons, M. Frank, R. Fromme, Y. Gevorkov, G. Giovanetti, M. Jiang, D. Kim, Y. Kim, H. Kirkwood, A. Klimovskaia, J. Knoska, F. H. M. Koua, R. Letrun, S. Lisova, L. Maia, V. Mazalova, D. Meza, T. Michelat, A. Ourmazd, G. Palmer, M. Ramilli, R. Schubert, P. Schwander, A. Silenzi, J. Sztuk-Dambietz, A. Tolstikova, H. N. Chapman, A. Ros, A. Barty, P. Fromme, A. P. Mancuso and M. Schmidt, *Nature Methods*, 2020, **17**, 73-78.
38. A. J. Dent, L. J. Farrugia, A. G. Orpen and S. E. Stratford, *Journal of the Chemical Society-Chemical Communications*, 1992, 1456-1457.
39. D. M. Mills, A. Lewis, A. Harootunian, J. Huang and B. Smith, *Science*, 1984, **223**, 811-813.
40. H. Stiel, M. Schnurer, H. Legal, W. Malzer, L. Anklamm, C. Schlesiger, K. A. Janulewicz, M. Iqbal and P. V. Nickles, San Diego, CA, 2013.
41. D. H. Bilderback, P. Elleaume and E. Weckert, *Journal of Physics B: Atomic, Molecular and Optical Physics*, 2005, **38**, S773.
42. A. M. March, A. Stickrath, G. Doumy, E. P. Kanter, B. Krassig, S. H. Southworth, K. Attenkofer, C. A. Kurtz, L. X. Chen and L. Young, *Review of Scientific Instruments*, 2011, **82**, 8.
43. M. Rentschler, S. Iglesias, M.-A. Schmid, C. Liu, S. Tschierlei, W. Frey, X. Zhang, M. Karnahl and D. Moonshiram, *Chemistry (Weinheim an der Bergstrasse, Germany)*, 2020, **26**, 9527-9536.
44. T. Ressler, J. Wienold, R. E. Jentoft, T. Neisius and M. M. Gunter, *Topics in Catalysis*, 2002, **18**, 45-52.
45. D. Rolles, *Advances in Physics-X*, 2023, **8**, 27.
46. A. Britz, W. Gawelda, T. A. Assefa, L. L. Jamula, J. T. Yarranton, A. Galler, D. Khakhulin, M. Diez, M. Hardee, G. Doumy, A. M. March, E. Bajnoczi, Z. Nemeth, M. Papai, E. Rozsalyi, D. S. Szemes, H. Cho, S. Mukherjee, C. Liu, T. K. Kim, R. W. Schoenlein, S. H. Southworth, L. D. Young, E. Jakubikova, N. Huse, G. Vanko, C. Bressler and J. K. McCusker, *Inorganic Chemistry*, 2019, **58**, 9341-9350.
47. M. Fracchia, P. Ghigna, A. Vertova, S. Rondinini and A. Minguzzi, *Surfaces*, 2018, **1**, 138-150.

48. J. X. Zhang, X. Y. Zhang, K. Suarez-Alcantara, G. Jennings, C. A. Kurtz, L. M. L. Daku and S. E. Canton, *Acs Omega*, 2019, **4**, 6375-6381.
49. G. Smolentsev, K. M. van Vliet, N. Azzaroli, J. A. van Bokhoven, A. M. Brouwer, B. de Bruin, M. Nachtegaal and M. Tromp, *Photochemical & Photobiological Sciences*, 2018, **17**, 896-902.
50. D. Hayes, L. Kohler, R. G. Hadt, X. Zhang, C. Liu, Karen L. Mulfort and L. X. Chen, *Chemical Science*, 2018, **9**, 860-875.
51. O. S. Jina, X. Z. Sun and M. W. George, *Dalton Transactions*, 2003, 1773-1778.
52. G. C. Pimentel and K. C. Herr, *Journal De Chimie Physique Et De Physico-Chimie Biologique*, 1964, **61**, 1509-1516.
53. G. R. Dobson, P. M. Hodges, M. A. Healy, M. Poliakoff, J. J. Turner, S. Firth and K. J. Asali, *Journal of the American Chemical Society*, 1987, **109**, 4218-4224.
54. X. Wu, Z. Liu, T. S. Murphy, X. Z. Sun, M. W. D. Hanson-Heine, M. Towrie, J. N. Harvey and M. W. George, *Faraday Discussions*, 2019, **220**, 86-104.
55. B. Wezislá, J. Lindner, U. Das, A. C. Filippou and P. Vöhringer, *Angewandte Chemie International Edition*, 2017, **56**, 6901-6905.
56. J. B. Eastwood, L. A. Hammarback, M. T. McRobie, I. P. Clark, M. Towrie, I. J. S. Fairlamb and J. M. Lynam, *Dalton Transactions*, 2020, **49**, 5463-5470.
57. A. O. Er, J. Chen and P. M. Rentzepis, *Journal of Applied Physics*, 2012, **112**, 16.
58. R. D. Kronig, *Zeitschrift Fur Physik*, 1932, **75**, 191-210.
59. R. D. Kronig, *Zeitschrift Fur Physik*, 1931, **70**, 317-323.
60. L. V. Azaroff, *Reviews of Modern Physics*, 1963, **35**, 1012-&.
61. J. J. Rehr and R. C. Albers, *Reviews of Modern Physics*, 2000, **72**, 621-654.
62. E. A. Stern, *Physical Review B*, 1974, **10**, 3027-3037.
63. D. E. Sayers, E. A. Stern and F. W. Lytle, *Physical Review Letters*, 1971, **27**, 1204-&.
64. T. Northey, J. Norell, A. E. A. Fouda, N. A. Besley, M. Odelius and T. J. Penfold, *Physical Chemistry Chemical Physics*, 2020, **22**, 2667-2676.
65. M. M. Syrokvashin, E. V. Korotaev, I. Y. Filatova, S. V. Trubina and S. B. Erenburg, *Spectrochimica Acta Part a-Molecular and Biomolecular Spectroscopy*, 2018, **205**, 593-596.
66. C. Bressler and M. Chergui, *Chemical Reviews*, 2004, **104**, 1781-1812.

67. S. E. Bromberg, H. Yang, M. C. Asplund, T. Lian, B. K. McNamara, K. T. Kotz, J. S. Yeston, M. Wilkens, H. Frei, R. G. Bergman and C. B. Harris, *Science*, 1997, **278**, 260-263.
68. K. K. Pandey, *Coordination Chemistry Reviews*, 1995, **140**, 37-114.
69. P. Hummel, J. Oxgaard, W. A. Goddard and H. B. Gray, *Inorganic Chemistry*, 2005, **44**, 2454-2458.
70. J. J. Turner, M. W. George, M. Poliakoff and R. N. Perutz, *Chemical Society Reviews*, 2022, **51**, 5300-5329.
71. J. J. Turner, J. K. Burdett, R. N. Perutz and M. Poliakoff, *Pure and Applied Chemistry*, 1977, **49**, 271-285.
72. G. J. Kubas, *Journal of Organometallic Chemistry*, 2001, **635**, 37-68.
73. G. Alcaraz and S. Sabo-Etienne, *Coordination Chemistry Reviews*, 2008, **252**, 2395-2409.
74. T. Komuro, S. Okawara, K. Furuyama and H. Tobita, *Chemistry Letters*, 2012, **41**, 774-776.
75. B. Chan and G. E. Ball, *Journal of Chemical Theory and Computation*, 2013, **9**, 2199-2208.
76. R. N. Perutz and J. J. Turner, *Journal of the American Chemical Society*, 1975, **97**, 4791-4800.
77. J. A. Calladine, K. Q. Vuong, X. Z. Sun and M. W. George, *Pure and Applied Chemistry*, 2009, **81**, 1667-1675.
78. G. I. Childs, C. S. Colley, J. Dyer, D. C. Grills, X.-Z. Sun, J. Yang and M. W. George, *Journal of the Chemical Society, Dalton Transactions*, 2000, 1901-1906.
79. A. S. Weller, F. M. Chadwick and A. I. McKay, in *Advances in Organometallic Chemistry*, ed. P. J. Pérez, Academic Press, 2016, vol. 66, pp. 223-276.
80. G. S. McGrady and G. Guilera, *Chemical Society Reviews*, 2003, **32**, 383-392.
81. J. Y. Corey, *Chemical Reviews*, 2011, **111**, 863-1071.
82. P. J. Sempsrott, B. B. Trinh, C. F. Lovitt, N. E. Capra and G. S. Girolami, *Science Advances*, **9**, eadg8130.
83. A. J. Cowan, P. Portius, H. K. Kawanami, O. S. Jina, D. C. Grills, X.-Z. Sun, J. McMaster and M. W. George, *Proceedings of the National Academy of Sciences*, 2007, **104**, 6933-6938.

84. A. G. Algarra, A. L. Burnage, M. Iannuzzi, T. Krämer, S. A. Macgregor, R. E. M. Pirie, B. Tegner and A. S. Weller, in *21st Century Challenges in Chemical Crystallography II: Structural Correlations and Data Interpretation*, eds. D. Michael P. Mingos and P. R. Raithby, Springer International Publishing, Cham, 2020, pp. 183-228.
85. J. McMaster, P. Portius, G. E. Ball, J. P. Rourke and M. W. George, *Organometallics*, 2006, **25**, 5242-5248.
86. S. Y. Ketkov, E. A. Rychagova, S. Y. Tzeng and W. B. Tzeng, *Physical Chemistry Chemical Physics*, 2018, **20**, 23988-23997.
87. R. Sahnoun and C. Mijoule, *Journal of Physical Chemistry A*, 2001, **105**, 6176-6181.
88. W. Kohn and L. J. Sham, *Physical Review*, 1965, **140**, 1133-&.
89. P. Ravindran, R. Vidya, P. Vajeeston, A. Kjekshus and H. Fjellvag, *Journal of Solid State Chemistry*, 2003, **176**, 338-374.
90. O. Bunau and Y. Joly, *Journal of Physics-Condensed Matter*, 2009, **21**, 11.
91. J. J. Rehr, J. J. Kas, F. D. Vila, M. P. Prange and K. Jorissen, *Physical Chemistry Chemical Physics*, 2010, **12**, 5503-5513.
92. B. Ravel and M. Newville, *Journal of Synchrotron Radiation*, 2005, **12**, 537-541.
93. S. Rojsatien, A. Mannodi-Kanakkithodi, T. Walker, T. Nietzold, E. Colegrove, B. Lai, Z. Cai, M. Holt, M. K. Y. Chan and M. I. Bertoni, *Radiation Physics and Chemistry*, 2023, **202**, 110548.
94. M. Newville, *Journal of Synchrotron Radiation*, 2001, **8**, 322-324.
95. S. A. Bartlett, N. A. Besley, A. J. Dent, S. Diaz-Moreno, J. Evans, M. L. Hamilton, M. W. D. Hanson-Heine, R. Horvath, V. Manici, X. Z. Sun, M. Towrie, L. J. Wu, X. Y. Zhang and M. W. George, *Journal of the American Chemical Society*, 2019, **141**, 11471-11480.

# Chapter 2 – Experimental and Theoretical Methods

This Chapter will describe the established methods used in the course of this Thesis, which were implemented without significant changes from previously established methodologies. The development of the TRXAS setup at Diamond is detailed more extensively in Chapter 3.

## 2.1 – Materials

The solvents *n*-heptane (>99%), *n*-hexane, cyclohexane (extra dry, >99.5%), and dichloromethane (DCM) were all purchased from Sigma Aldrich. Triethyl silane (extra dry, >99%) was purchased from Sigma Aldrich or Fisher Scientific dependent on availability.

The metal complexes  $\text{CpMn}(\text{CO})_3$ , and  $\text{Cp}'\text{Mn}(\text{CO})_3$  ( $\text{Cp}' = \text{methylcyclopentadienyl}$ ) were purchased from Sigma Aldrich and used without further purification. The metal complex  $\text{CpRe}(\text{CO})_3$  was purchased from Strem Chemicals. 3 Å molecular sieves ( $\text{K}_n\text{Na}_{12-n}[(\text{AlO}_2)_{12}(\text{SiO}_2)_{12}] \cdot x\text{H}_2\text{O}$ ) were purchased from Sigma Aldrich. Purchased chemicals were used without further purification.

## 2.2 – TRIR Sample Preparation

To prepare samples for TRIR analysis for all experiments, a Schlenk line was used with dry and degassed solvents under an argon atmosphere. Metal carbonyl was weighed out into an airtight flask and dissolved in 25 mL of solvent. The solution was then degassed via three cycles of freeze-pump-thaw.

Concentrations were kept between 5 -6 mmol, and path lengths adjusted accordingly to give absorbances of less than 1 for bands of interest. An infrared cell (Harrick Corp.) with CaF<sub>2</sub> windows was used with a path length between 0.3-1.0 mm as suited each experiment. The flask and cell were connected via Teflon tubing, with a peristaltic pump used to circulate solution through the system.

## 2.3 – Ultrafast TRIR Apparatus

The TRIR setup was used to perform nanosecond and picosecond TRIR. The construction of the system is described in detail in literature<sup>1</sup> but is summarised here. Experiments were undertaken in collaboration with Drs Genevieve Garwood and Surajit Kayal.

The apparatus uses a tuneable Ti: sapphire oscillator (MaiTai, SpectraPhysics) in conjunction with a regenerative amplifier (Spitfire Pro, Spectra Physics). The initial laser pulses (140 fs) have a wavelength of 800 nm, an energy of 2.3 mJ, and a repetition rate of 1 kHz, and are split into 2 separate beams. One beam is directed into a TP-1 harmonic generator (TimePlate Tripler, Minioptic Technology Inc.) which produces 400 or 267 nm UV pulses. This is used as the pump beam to excite the sample for picosecond timescale measurements. A translation stage (Aerotech) is used to delay the pulse by up to 3ns before being focused on the sample with a quartz lens. For nanosecond timescale measurements, a Q-switched Nd: YVO laser (600 ps, Advanced Optical Technology, UK) is used to generate the pump pulse, with a delay from 0.5ns to 100  $\mu$ s controlled by a pulse generator (DG535, Stanford Research System). The Nd: YVO outputs at 1064nm, which is frequency quadrupled to produce a 266 nm beam or tripled to produce a 355 nm pulse.

The second beam is directed to a TOPAS-C OPA (Light Conversion) with a DFG (difference frequency generator) unit to produce a tuneable mid-IR pulse. The spectral bandwidth of the pulse is 180  $\text{cm}^{-1}$ , and its pulse energy is 2  $\mu$ J at 2000  $\text{cm}^{-1}$ . This IR beam is then split further between a beam incident on a single element MCT (Kolmar Technology) used as a reference detector, and a probe beam incident on the sample at an angle of 54.7° to the pump pulse. The probe signal is measured with a 128-element MCT detector (Infrared

Associates) positioned after a 250mm IR monochromator (DK240, Spectra Product). The signals from the MCT are increased with a 144-channel amplifier and digitized by a 16-bit analogue-to-digital converter.

Half of the pump pulses are removed with a chopper, resulting in a pump-off signal that is ratioed with the pump-on signal to derive the change in absorbance. The probe beam ( $\sim 200 \mu\text{m}$ ) is significantly smaller than the pump beam ( $\sim 500 \mu\text{m}$ ) such that there will be uniform excitation across the probed solution. The cell is rastered in the x-y plane with a motorised mount in order to prevent overheating and degradation of the sample.

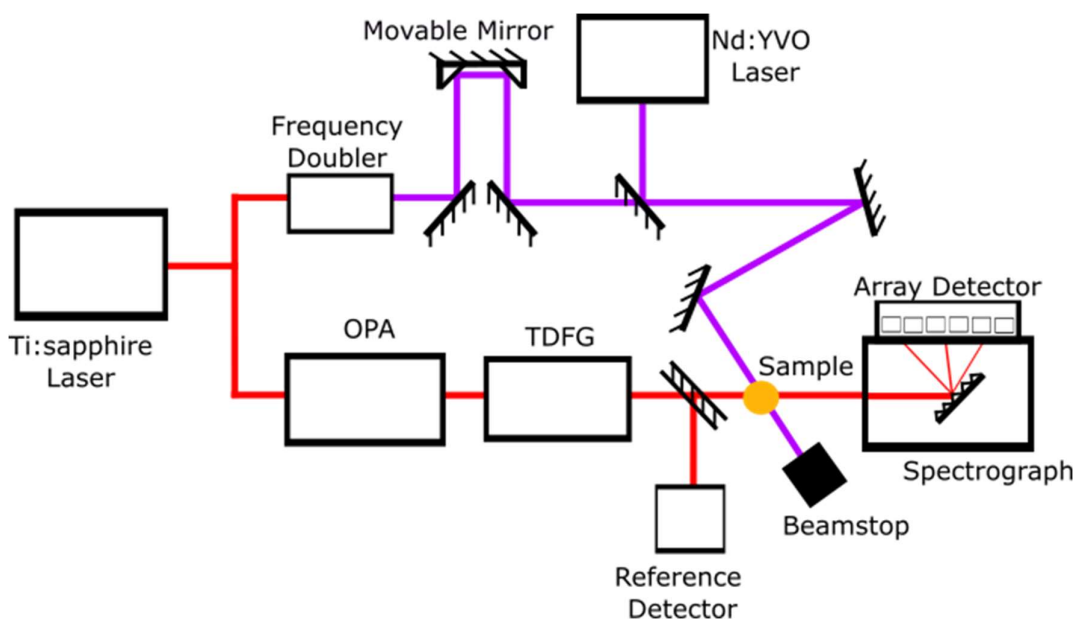


Figure 2.1: Schematic of fast TRIR setup used at the University of Nottingham.

## 2.4 – TRXAS Sample Preparation.

To prepare samples for TRXAS analysis in all chapters, a Schlenk line was used with dry and degassed solvents and kept under an argon atmosphere. Metal carbonyl was weighed out into a 1L airtight flask prepared with activated molecular sieves, which was then sealed and

degassed, then refilled with argon. Degassing and refilling with argon was repeated twice more to ensure removal of oxygen.

Concentrations were kept between 5 -6 mmol to give absorbances strong enough to give good XAFS signal while allowing sufficient penetration for the X-ray attenuation to be significant across the width of the jet. Dry solvent was then transferred directly from the bottle (with dryness maintained via a rubber seal) into the flask via cannula, with a pressure applied via argon flow into the solvent bottle. Preparation was conducted on site and samples stored in darkness under argon for no more than 24 hours before measurement.

## 2.5 – Advanced Photon Source TRXAS

The APS beamline setup was recreated from the previous TRXAS experiments performed, which are recorded in literature.<sup>2</sup> Measurements were conducted at the 11-ID-D beamline of the Advance Photon Source at Argonne National Laboratory, Illinois, USA. Measurements were made in fluorescence mode, at the Re  $L_{III}$  edge.

The fourth harmonic of a Ti: sapphire regenerative laser with a repetition rate of 10 kHz is used to produce 266 nm pulses with a FWHM of 500 fs. X-ray pulses are produced by the synchrotron in 24-bunch mode, for a 153 ns interval between pulses. These are coordinated with the laser pulses as shown in Figure 2.2.

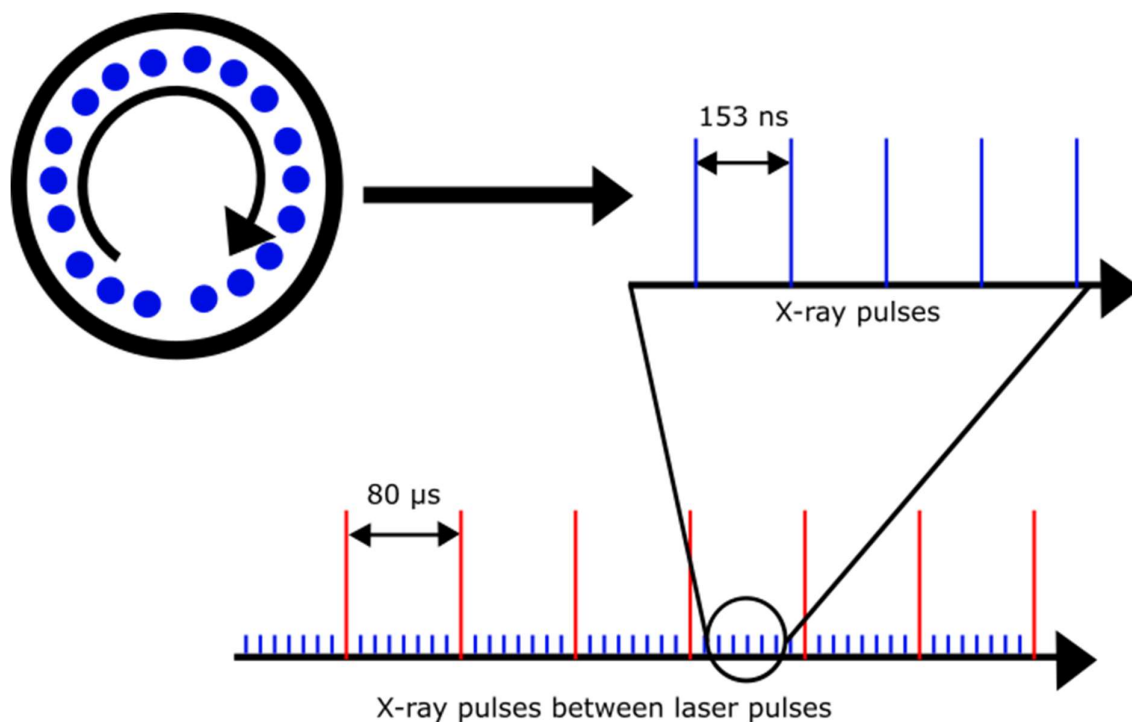


*Figure 2.2: Scheme of bunch path around the synchrotron producing X-ray pulses at 153 ns intervals, which are synchronised with the laser pulses to give consistent intervals of data collection post-photolysis.*

The solution to be measured is pumped via a peristaltic pump through a stainless-steel nozzle to produce a roughly 500 μm wide jet. A t-piece connects a sealed pipe with an argon bubble to the system to act as a shock absorber, reducing pulsing in the solution from the pump's action. An APD is positioned at 90° to the X-ray beam path on either side of the jet to collect the fluorescence signal. Soller slits and tungsten foil were placed between the jet and the APDs to filter scattering radiation out of the signal.

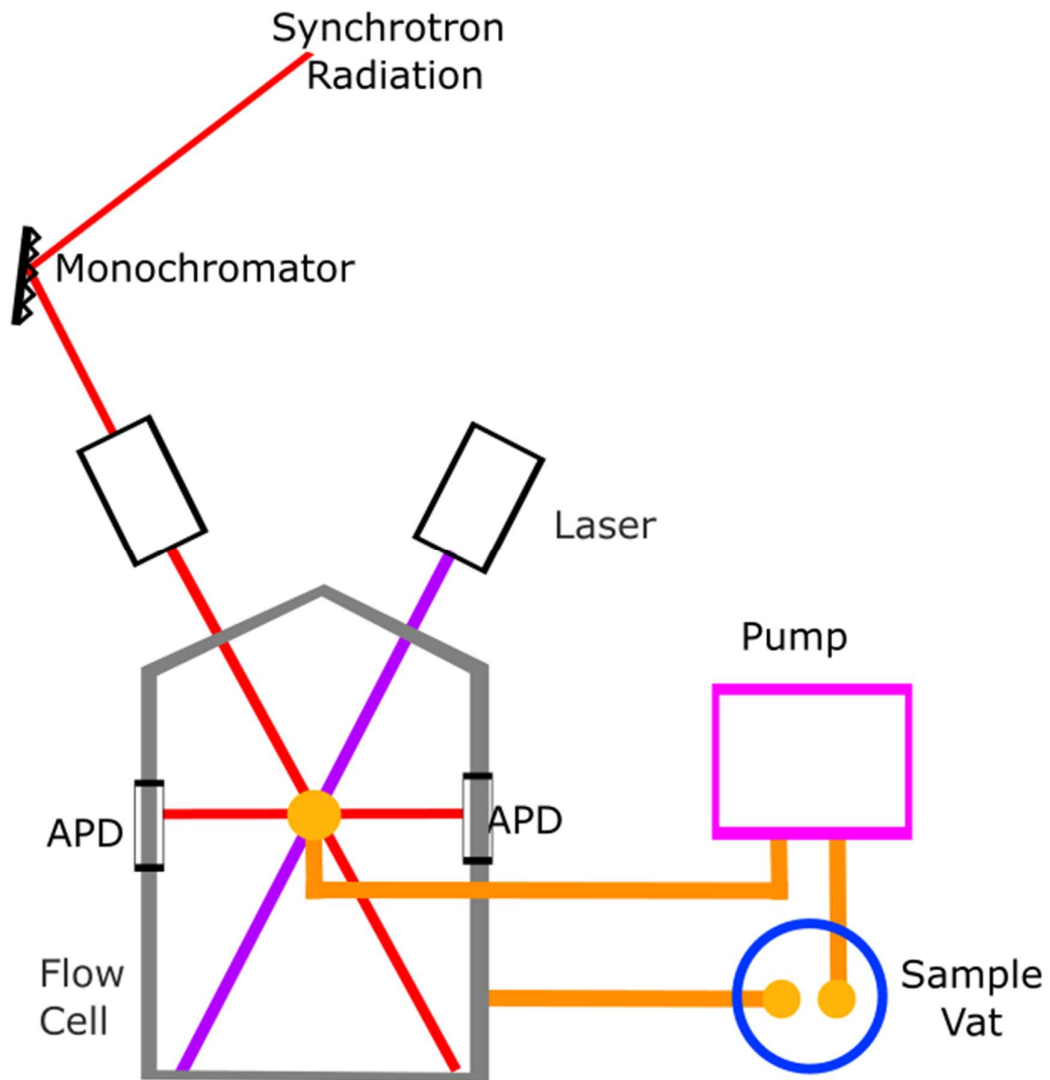


*Figure 2.3: Top-down scheme of APS flow cell, showing the vertical sample jet's intersection with the laser and X-ray beams.*

Difference data was obtained by taking the average signal from bunches at the end of the cycle when the excited solution has been flushed from the jet as the 'laser off' signal and subtracting it from the 'laser on' signal, the bunches in the window of interest.

## 2.6 – Analysis of XAS Data

EXAFS data collected at the APS was processed with the Demeter suite software packages Artemis and Athena. These programs are used to interpret and fit backgrounds to XAS data, and to derive parameters from EXAFS spectra, including Debye-Waller factors and path lengths. In order to extract structures from difference spectra, static pre-photolysis data is first processed to generate a set of parameters for the parent species; the bond lengths and associated Debye Waller factors, and the energy shift of the species are determined. These parameters are then applied as a fixed negative factor to the difference spectra investigated, while parameters for the product species are fitted to the resultant spectrum.

### 2.6.1 – Generating a Difference Fit

The difference fit is generated via Equation 2.1:

$$\Delta\chi = \chi_{Lon} - \chi_{Loff} \quad (2.1)$$

Where  $\Delta\chi$  is the difference spectrum,  $\chi_{Lon}$  is the contribution from the modelled photoproduct, and  $\chi_{Loff}$  is the factors of the pre-fitted parent species. This method is derived from previously established methods to fit experimental parameters from theoretical models<sup>3</sup>.

This method incorporates an amplitude reduction factor,  $S_0^2$ , that adjusts the magnitude of the fit to match the difference data. This factor kept constant for the parent and product contributions under each fit, which assumes that the loss of parent is equal to the gain of product, and thus that the contribution to the signal from each process is almost equal in magnitude. This holds true if the conversion of photolyzed parent to product is 1:1, an approximation which is not completely accurate in all systems tested.

## 2.6.2 – Scan Selection

XAS is not a noiseless measurement, and the degree of noise is greatly increased in time-resolved XAS by the much smaller signal that is the difference (often only 1-2% of the original). This is mitigated by collecting several scans over the course of hours and filtering out anomalous scans that have been caused by jet disruption, sample destruction causing later scans in a run to fail, and other factors. Visually inspecting and removing scans is impractical with the amount of data collected, so it is performed algorithmically instead.

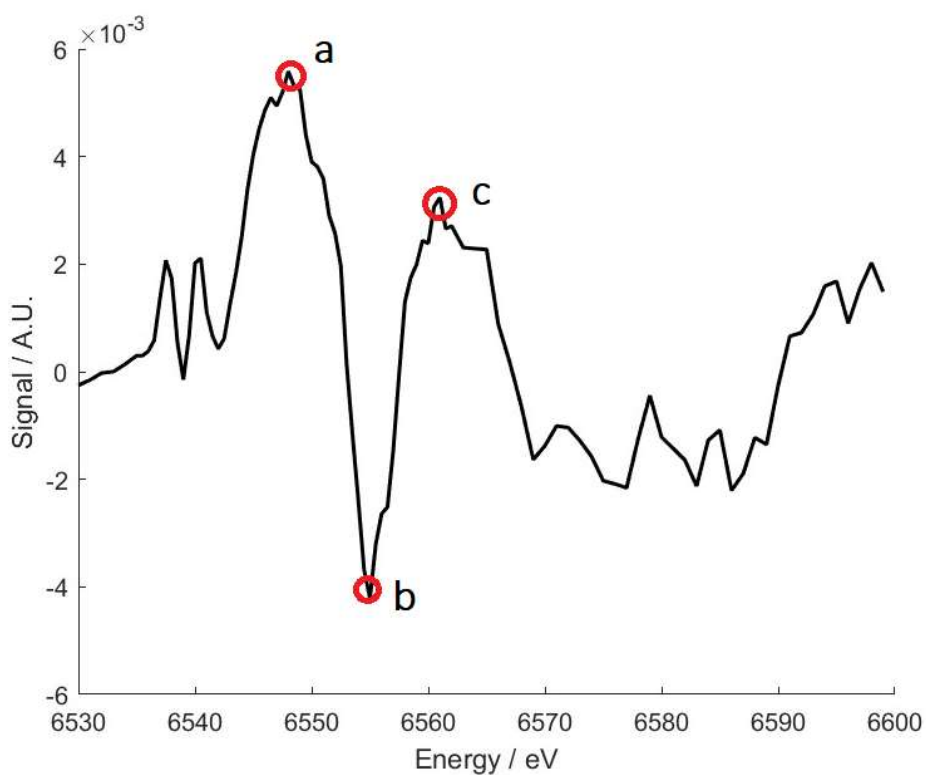


*Figure 2.4: Difference XAFS data for  $\text{CpMn}(\text{CO})_3$  photolyzed in neat  $n$ -heptane. Points a, b and c are the positions where the measured signal is used to determine the values of A, B and C in Equation 2.2.*

As shown in Figure 2.4, the XANES difference systems examined in this work are characterised by a sharp rise just below the edge and a drop at the edge. These major

features are the criteria used to evaluate the quality of the signal, with a value being derived through the use of Equation 2.2:

$$S = B - A - \left(\frac{A - C}{2}\right) \quad (2.2)$$

Where  $S$  is the estimated signal strength,  $A$  is the average of the 7 points around point a on Figure 2.4, and  $B$  and  $C$  are the corresponding averages for points b and c.  $S$  is then compared to a threshold value, and if less than the threshold the scan is excluded from averaging as having insufficient signal.

### 2.6.3 – Backgrounding

Backgrounding was performed in Athena, with the contribution of the edge removed from the spectrum before performing a Fourier transform to construct the k-space interference pattern. This is modelled from a pre-edge and post-edge function to describe the 'base' X-ray absorption before and after the edge, and with a selected value for the edge itself. This is shown in Figure 2.5 below. The edge energy is taken as the peak of the derivative of the data.

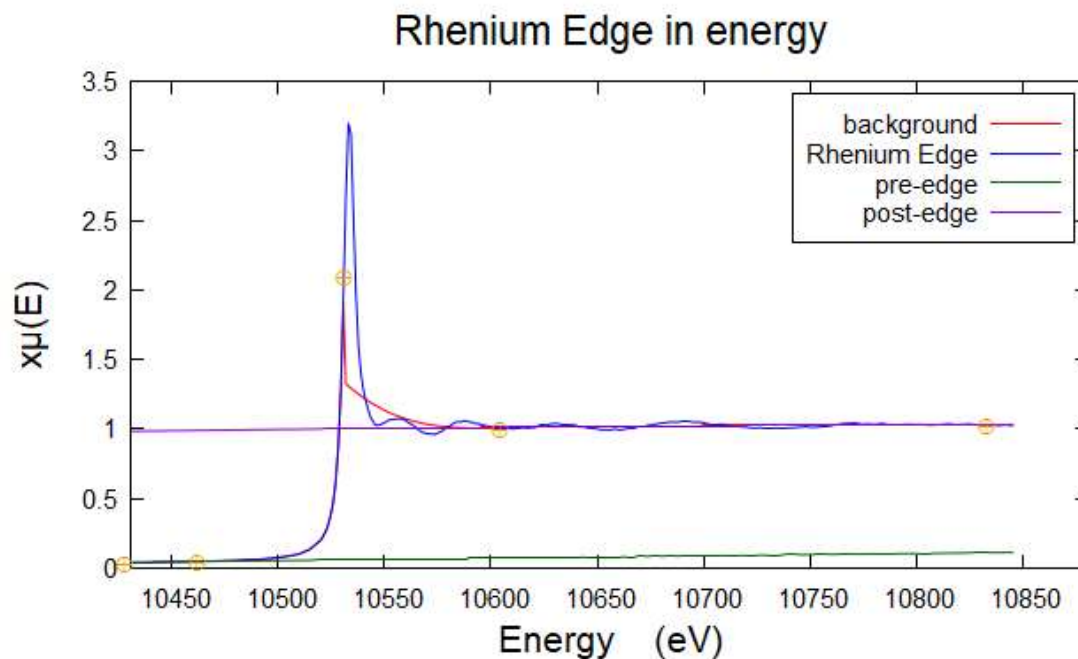


*Figure 2.5: Plot of rhenium data showing pre-edge and post-edge lines used for backgrounding.*

This process is slightly more complicated for difference data, which does not have the same edge step as normal XAS data. In this case the edge step is assumed to be effectively 0, and the pre-edge and post-edge functions are virtually identical.

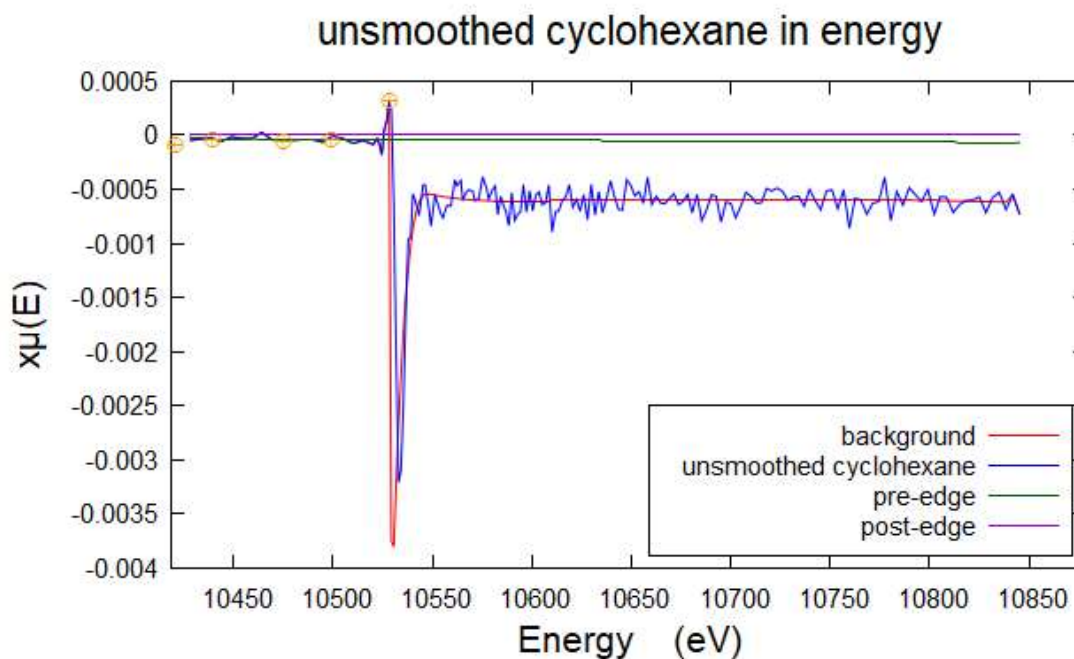


Figure 2.6: Difference data for  $\text{CpRe}(\text{CO})_3$  photolyzed in neat cyclohexane

While there is sometimes an apparent step, this is attributed to a difference in post-edge oscillations and a component of the EXAFS.

#### 2.6.4 – Calculating R and Quality of Fit

The fitting procedure and analysis used are those provided in the IFEFFIT software, detailed in published literature.<sup>4</sup> To summarise, the theoretical spectrum is compared to the experimental spectrum in R-space, and a difference function,  $f$ , is calculated at each point across the spectra within the bounds of the fit.

$$f(R_i) = \text{Re}[\tilde{\chi}(R_i|data) - \tilde{\chi}(R_i|theory)] + \text{Im}[\tilde{\chi}(R_i|data) - \tilde{\chi}(R_i|theory)] \quad (2.3)$$

$$R_{fac} = \frac{\sum_{i=1}^N f(R_i)^2}{\sum_{i=1}^N ([Re(\tilde{\chi}(R_i|data))]^2 + [Im(\tilde{\chi}(R_i|data))]^2)} \quad (2.4)$$

From this a value for how tightly the theoretical spectrum overlays the data is obtained; the smaller the value of  $R_{fac}$ , the less divergence between the two. By reducing this value through a non-linear minimisation that varies the fit parameters, bond lengths and other factors can be adjusted to find the values that produce an improved match to experimental data.

This evaluation does not factor in how accurate any of the theoretical parameters are, and so must be used in concert with a measured evaluation of the feasibility of the structure produced.

## 2.7 – FTIR Spectroscopy

FTIR spectra were collected with a Nicolet iS50 FTIR Spectrometer. An infrared cell (Harrick Corp.) with  $\text{CaF}_2$  windows was used with a path length of 0.3- 1.0 mm depending on how optically dense the species of interest was.

## 2.8 – DFT Calculations

DFT calculations were performed to find the optimised geometries of metal complexes and to simulate harmonic frequencies and XAFS features. Calculations to optimise geometries of structures carried out at the University of Nottingham were performed with the QChem software package<sup>5</sup> using the M06 functional.<sup>6</sup> For the calculation of  $\text{CpRe}(\text{CO})_2(\text{X})$  structures, the 6-311G(d,p)++ basis set was used for H, C, O, and Si while the LANL08 basis set was used for Re. The LANL08 ECP was also applied for modelling Re.

For the calculation of  $\text{CpMn}(\text{CO})_2(\text{X})$  structures, which were performed in cooperation with Dr Joshua Elliot, the structure was optimised with the B3LYP functional and the Jorge-ADZP basis set.

Excited state calculations for XANES analysis of manganese complexes were performed with QChem at the University of Nottingham, from geometric structures optimised with the above specifications. The excited state calculations then proceeded with the same basis set. The lower level of theory used helped offset the increased computational cost incurred by not being able to use ECPs.

XANES simulations for manganese complexes were also performed with FDMNES. FDMNES is a DFT-LSDA based program written to simulate XANES spectra.<sup>7</sup> A radius of 3 Å was used for an initial evaluation before performing a second run with an extended radius of 7 Å to produce a final prediction. The 'convolution' 'relativism' 'dipole' and 'quadrupole' keywords were employed. The 'convolution' keyword instructs the program to apply a convolution to the Lorentzian peaks, while the 'relativism' keyword instructs it to perform a calculation that includes relativistic components. The 'dipole' and 'quadrupole' keywords instruct the program to calculate the dipolar and quadrupolar components respectively.

## 2.9 – References

1. P. Brennan, M. W. George, O. S. Jina, C. Long, J. McKenna, M. T. Pryce, X. Z. Sun and K. Q. Vuong, *Organometallics*, 2008, **27**, 3671-3680.
2. S. A. Bartlett, N. A. Besley, A. J. Dent, S. Diaz-Moreno, J. Evans, M. L. Hamilton, M. W. D. Hanson-Heine, R. Horvath, V. Manici, X. Z. Sun, M. Towrie, L. J. Wu, X. Y. Zhang and M. W. George, *Journal of the American Chemical Society*, 2019, **141**, 11471-11480.
3. C. F. J. Konig, J. A. van Bokhoven, T. J. Schildhauer and M. Nachttegaal, *Journal of Physical Chemistry C*, 2012, **116**, 19857-19866.

4. B. Ravel, in *X-Ray Absorption and X-Ray Emission Spectroscopy: Theory and Applications*, ed. C. L. Jeroen A. Van Bokhoven, John Wiley and Sons, Ltd, 2016, ch. 11, pp. 281-302.
5. Y. Shao, Z. Gan, E. Epifanovsky, A. T. B. Gilbert, M. Wormit, J. Kussmann, A. W. Lange, A. Behn, J. Deng, X. Feng, D. Ghosh, M. Goldey, P. R. Horn, L. D. Jacobson, I. Kaliman, R. Z. Khaliullin, T. Kuś, A. Landau, J. Liu, E. I. Proynov, Y. M. Rhee, R. M. Richard, M. A. Rohrdanz, R. P. Steele, E. J. Sundstrom, H. L. Woodcock, P. M. Zimmerman, D. Zuev, B. Albrecht, E. Alguire, B. Austin, G. J. O. Beran, Y. A. Bernard, E. Berquist, K. Brandhorst, K. B. Bravaya, S. T. Brown, D. Casanova, C.-M. Chang, Y. Chen, S. H. Chien, K. D. Closser, D. L. Crittenden, M. Diedenhofen, R. A. DiStasio, H. Do, A. D. Dutoi, R. G. Edgar, S. Fatehi, L. Fusti-Molnar, A. Ghysels, A. Golubeva-Zadorozhnaya, J. Gomes, M. W. D. Hanson-Heine, P. H. P. Harbach, A. W. Hauser, E. G. Hohenstein, Z. C. Holden, T.-C. Jagau, H. Ji, B. Kaduk, K. Khistyayev, J. Kim, J. Kim, R. A. King, P. Klunzinger, D. Kosenkov, T. Kowalczyk, C. M. Krauter, K. U. Lao, A. D. Laurent, K. V. Lawler, S. V. Levchenko, C. Y. Lin, F. Liu, E. Livshits, R. C. Lochan, A. Luenser, P. Manohar, S. F. Manzer, S.-P. Mao, N. Mardirossian, A. V. Marenich, S. A. Maurer, N. J. Mayhall, E. Neuscamman, C. M. Oana, R. Olivares-Amaya, D. P. O'Neill, J. A. Parkhill, T. M. Perrine, R. Peverati, A. Prociuk, D. R. Rehn, E. Rosta, N. J. Russ, S. M. Sharada, S. Sharma, D. W. Small, A. Sodt, T. Stein, D. Stück, Y.-C. Su, A. J. W. Thom, T. Tsuchimochi, V. Vanovschi, L. Vogt, O. Vydrov, T. Wang, M. A. Watson, J. Wenzel, A. White, C. F. Williams, J. Yang, S. Yeganeh, S. R. Yost, Z.-Q. You, I. Y. Zhang, X. Zhang, Y. Zhao, B. R. Brooks, G. K. L. Chan, D. M. Chipman, C. J. Cramer, W. A. Goddard, M. S. Gordon, W. J. Hehre, A. Klamt, H. F. Schaefer, M. W. Schmidt, C. D. Sherrill, D. G. Truhlar, A. Warshel, X. Xu, A. Aspuru-Guzik, R. Baer, A. T. Bell, N. A. Besley, J.-D. Chai, A. Dreuw, B. D. Dunietz, T. R. Furlani, S. R. Gwaltney, C.-P. Hsu, Y. Jung, J. Kong, D. S. Lambrecht, W. Liang, C. Ochsenfeld, V. A. Rassolov, L. V. Slipchenko, J. E. Subotnik, T. Van Voorhis, J. M. Herbert, A. I. Krylov, P. M. W. Gill and M. Head-Gordon, *Molecular Physics*, 2015, **113**, 184-215.
6. Y. Zhao and D. G. Truhlar, *Journal of Chemical Physics*, 2006, **125**, 18.
7. O. Bunau and Y. Joly, *Journal of Physics-Condensed Matter*, 2009, **21**, 11.

# Chapter 3 – Development of Experimental TRXAS at Diamond

## 3.1 – Introduction

This Chapter will describe the techniques used to perform TRXAS at the I18 beamline at Diamond Light Source and how they were developed over the course of this work, including discussing the faults found in each beamtime they were used in and the subsequent improvements that were made to the setup.

As discussed in Chapter 1, TRXAS has developed considerably as the technology to produce tighter pulsed radiation has enabled the probing of smaller timeframes. While laboratory-based time resolved XAS is a developing field of its own<sup>1</sup>, the flux requirements to achieve good signal in fast and ultrafast experiments still restrict many sensitive experiments to synchrotrons and XFELs. Not only are solution samples often relatively dilute (in part due to solubility of the metal complex in the solvent as well as due to laser penetration constraints) but the excited fraction is then itself only a smaller part of that low number.

A number of time-resolved pump-probe laser / X-ray systems have been developed<sup>2-5</sup> and applied to study various systems, such as photoexcitation in titanium oxide<sup>6</sup> and structural changes cooling silica<sup>7</sup>, using synchrotron radiation on the ultrafast timescale. These experimental arrays require specific beamlines with their own dedicated laser array, which limits the accessibility of these facilities.

More recently TRXAS has been used to investigate organometallic excited states<sup>8</sup>, resolve small changes in ligand bond lengths<sup>9</sup>, and organometallic alkane complexes<sup>10</sup>, which was the foundational investigation from which this thesis was conceived.

This setup was mainly modelled after the APS flow cell system described in Chapter 2, with alterations to make a setup compatible with the PORTO laser's portable nature and the other specifics of the I18 beamline.

## 3.2 – Aims

Pump-probe laser / X-ray TRXAS requires dedicated facilities with high X-ray flux and is currently only available in a few select facilities. This project was undertaken to take advantage of PORTO: a laser system that could be moved between beamlines, allowing experiments requiring laser use to be conducted on multiple established beamlines.

- (i) To construct a functional setup where PORTO could be used on the I18 beamline with a flow system to conduct *in situ* solution-phase time resolved experiments.
- (ii) To iteratively improve upon this setup and achieve maximal signal from time-resolved systems.
- (iii) To use this setup to collect accurate TRXAS data on the microsecond timescale.

## 3.3 – Experimental Development

While the TRXAS setup was modified and reassembled several times in the course of its development, the basic layout remained the same. A schematic of this setup is shown below in Figure 3.1, illustrating a bird's eye view of the setup.

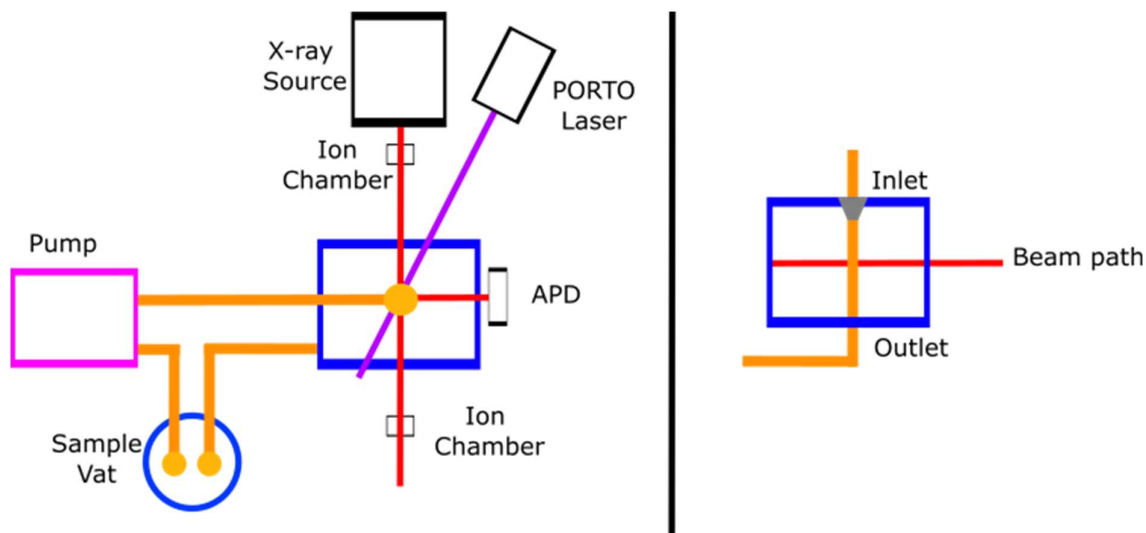


Figure 3.1: Scheme of the general layout of the TRXAS setup assembled on I18. Left is a 'top down' view of the flow cell and surrounding setup, while right is a 'side on' view of the cell.

The system is constructed around the I18 hutch's X-ray beam path, with a motorised mount holding the flow cell in that path. The flow cell connects to a reservoir of solution and a pump to circulate the solution, while PORTO is mounted next to the beamline and the laser directed to the sample with an optical array constructed around the X-ray beam path. An APD is mounted next to the flow cell at 90° to the X-ray beam to collect the fluorescence signal. Ion chambers before and after the setup are used to measure X-ray intensity at those points.

The pulsing of the laser creates intervals of data collection, with X-ray fluorescence data being collected for each microsecond after the pulse out to approximately 40  $\mu$ s. With a laser repetition rate ranging between 40 and 80 microseconds collection of this time-resolved data can be repeated with fresh solution continuously for each X-ray energy across the range, allowing a picture of the sample's attenuation to be built point by point.

The synchrotron ring operated with X-ray pulses at a frequency of 500 kHz which were synchronised with the laser pulses equivalently to operations at the APS (see Figure 2.2)

### 3.3.1 – The Flow Cell

The original flow cell body was constructed from machined stainless steel and includes windows for the X-ray path, laser path, and APDs. The detachable roof has a fixture for an input pipe to be attached, with a screw mounting on the underside with which to attach the jet nozzle. This is positioned to lie directly over the outflow hole in the base of the cell when attached, which likewise connects with an outflow pipe to the reservoir. This has since been replaced with a 3D-printed version that is more compact and allows for more alterations and adaptability.

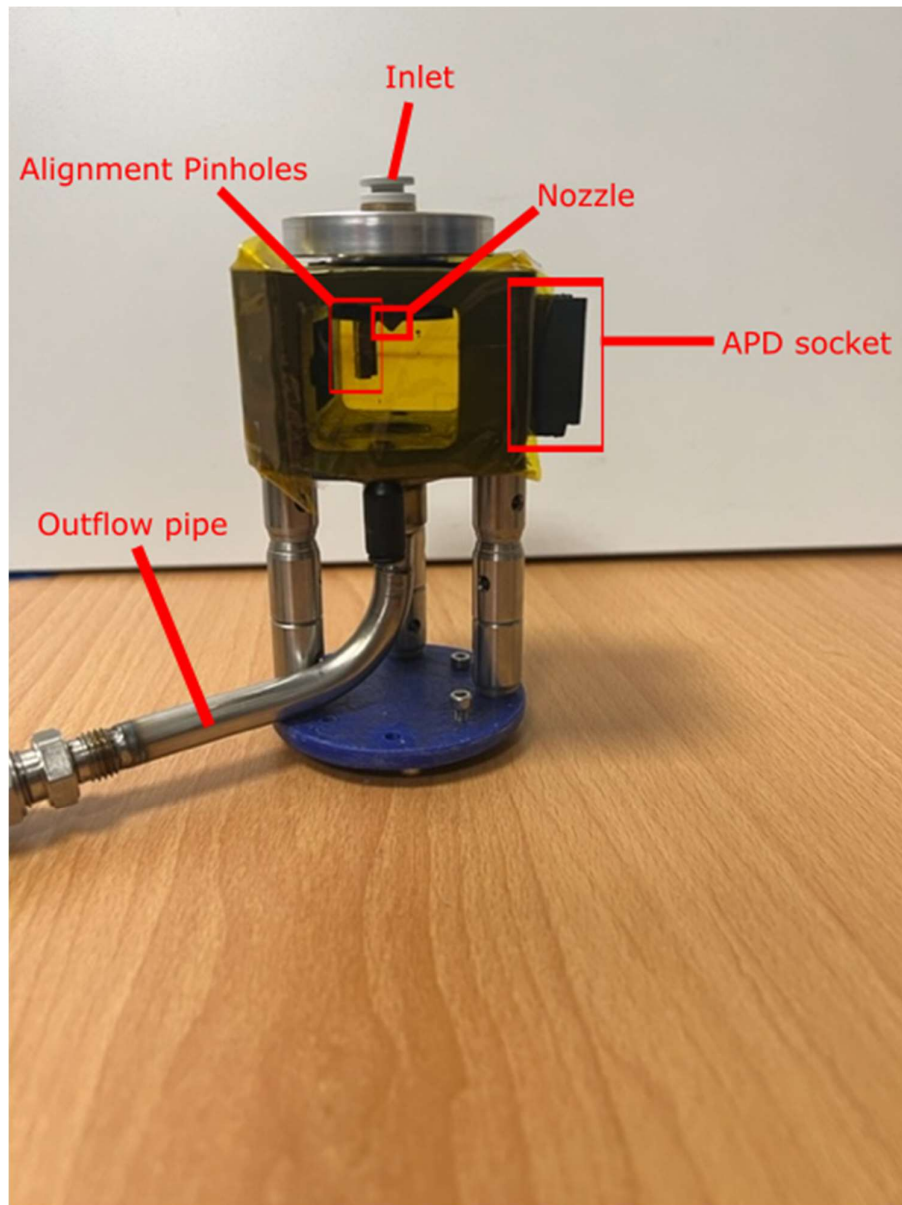


*Figure 3.2: Image of 3D printed flow cell. The inlet, nozzle, and alignment pinholes are all connected to a single freely rotating component that allows the pinholes to be rotated out of the way for jet measurement without removing the cell.*

The side-facing windows are removable fused silica pieces with an original thickness of 5 mm. Originally the front laser access window was also covered with one of these windows, but observation of the system in low lighting revealed a dull red glow indicative of filamentation effects where the laser passed through the window. This reduced power

applied to the sample jet and led to a burning of the window, which further exacerbated the issue.

In order to combat this, thinner windows of 1 mm and 0.5 mm thickness were employed to reduce the power loss, but they were still susceptible to being burned by the laser at high powers. While both sets of windows were tested, filamentation was still found to be a problem at higher laser powers. This was later circumvented by replacing the quartz window with transparent Kapton tape, which could then have a small hole burned in it with the laser to create a minimal opening that would not impede the laser. The flow of helium applied in the cell was confirmed via manual monitoring of the breeze from the hole to be sufficient to keep the environment under a positive pressure of inert gas.

Originally, filed needles were glued into nuts to form jet nozzles of consistent width, but tests showed that this method did not reliably produce vertical jets. Significant deflections, visibly not vertical, but coming out at an acute angle were a consistent problem for alignment and producing new nozzles and testing them was unsustainable.

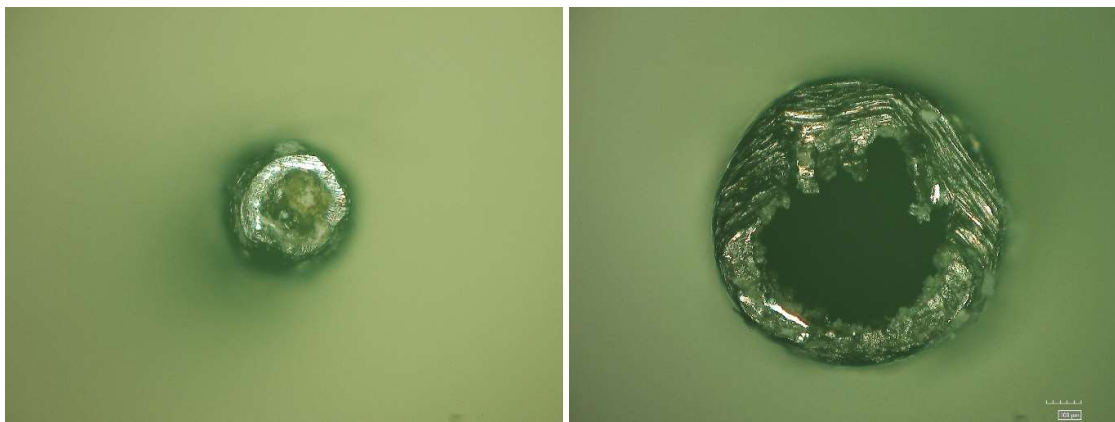


*Figure 3.3: File-cut needles, showing jagged and uneven ends.*

To create smoother, higher-quality nozzles the needles were instead cut with PORTO itself, leading to a flatter, more level cutoff. The difference between these two methods can be seen in Figures 3.3 and 3.4, and much smaller deflections were observed and the accuracy of the method in producing viable nozzles was drastically improved.

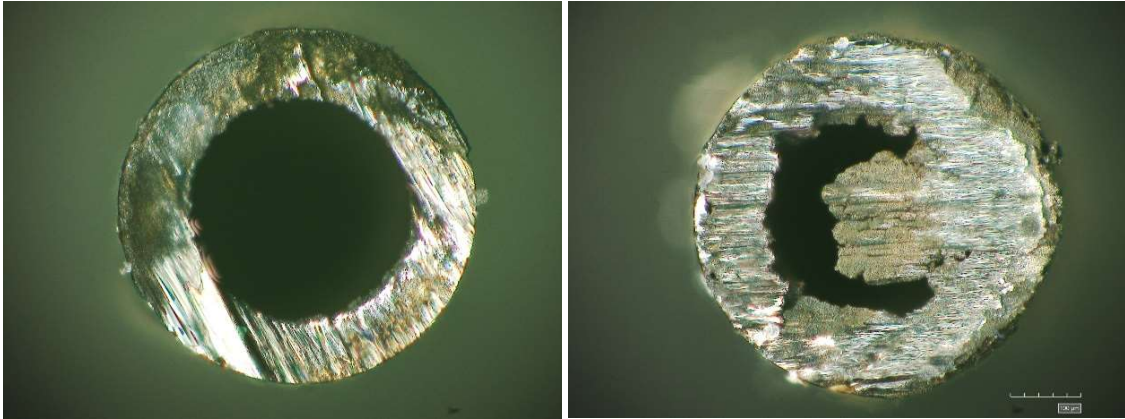


*Figure 3.4: Laser-cut needles, showing smooth ends but with some imperfect bores.*

As can be seen from Figure 3.4, this improved cutting did not guarantee the needles themselves were uniform, and subsequent needles were inspected for defects after cutting to avoid further deflection problems.

Unfortunately, later experiments showed another key limitation of these internally developed nozzles: the glue seal. At higher pressures the setup would begin to exhibit a dripping alongside the jet, which was found to result from the glue seal between the needle and the nut failing.

Ultimately this was resolved by purchasing machined nozzles from RS Components, which were found to give reliable, well-aligned jets.



*Figure 3.5: Image of brass nozzle (400  $\mu\text{m}$  internal diameter) used in improved flow cell design.*

### 3.3.2 – The Pump System

Preliminary tests of the flow cell with a peristaltic pump revealed defects in the collected data that were attributed to pulsing in the jet. In order to overcome this issue a new pump was purchased: a Tacmina Q series Smoothflow pump. This pump has the advantage of providing a smoother output flow but has a more limited range of flow rates it can output at, from approximately 1 to 80 mL/min.

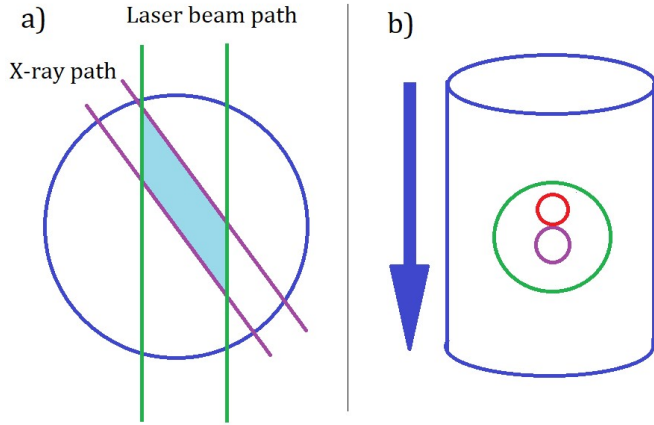


Figure 3.6: diagram of the overlap of the X-ray and laser beams in the sample jet (a), and the progression of the excited fraction of solution through the X-ray beam path. The green circle indicates the volume of the jet excited by the laser, while the purple circle indicates the initial volume probed by the X-ray beam, and the red circle indicates the volume probed by the X-ray beam at a later time.

As can be seen in Figure 3.6, the relative cross-sections of the X-ray and laser beams affect the duration for which photolyzed solution remains in the X-ray path. Assuming the X-ray beam is vertically centred in the laser beam, with beam diameters of  $d_x$  and  $d_l$  respectively, and defining our jet velocity as  $v$ , we can calculate the time photolyzed solution remains in the X-ray beam path as:

$$t_{photo} = \frac{(d_l - d_x)}{2v} \quad (3.1)$$

The pulse rate for the laser can then be set in relation to  $t_{photo}$  so that the next jet section is photolyzed a short period after the initial photolyzed section leaves the X-ray beam path, allowing fresh data to be taken continuously over several hours.

The jet velocity can be calculated from the flow rate set by the pump as:

$$v = \frac{4f}{\pi(d_j)^2} \quad (3.2)$$

Where  $f$  is the flow rate and  $d_j$  is the jet diameter.

In the experiment a pulse rate of either 25 or 12.5 kHz was used, with a laser beam diameter of 50  $\mu\text{m}$ . The X-ray beam has a vertical diameter of 8.5  $\mu\text{m}$ . The jet diameter is taken as the internal diameter of the nozzle used, at 0.400 mm, and the flow rate was set to 15 mL/minute. This gives a jet velocity of  $2.0 \text{ m s}^{-1}$  and gives a value of 10.4  $\mu\text{s}$  for  $t_{photo}$ . This is an approximate value, as the alignment method used could not determine how well-centred the beams were.

As a further consideration the jet solutions are by design highly absorbing of the laser radiation, and so care must be taken with the concentration of the solution to achieve a system that attenuates the laser radiation semi-consistently through the width of the jet. This ensures that the area of overlap will still contain a decent proportion of photoproduct even if that area of overlap is further into the jet. With a too high concentration the intervening solution would absorb most of the laser pulse. This problem is minimised by ensuring a good match between the jet size and the laser beam size and having highly colinear X-ray and laser beams. An absorbance of approximately 0.5 was calculated for our jet width, laser frequency and concentration from comparison to previous UV/vis measurements (see Figure 3.7).

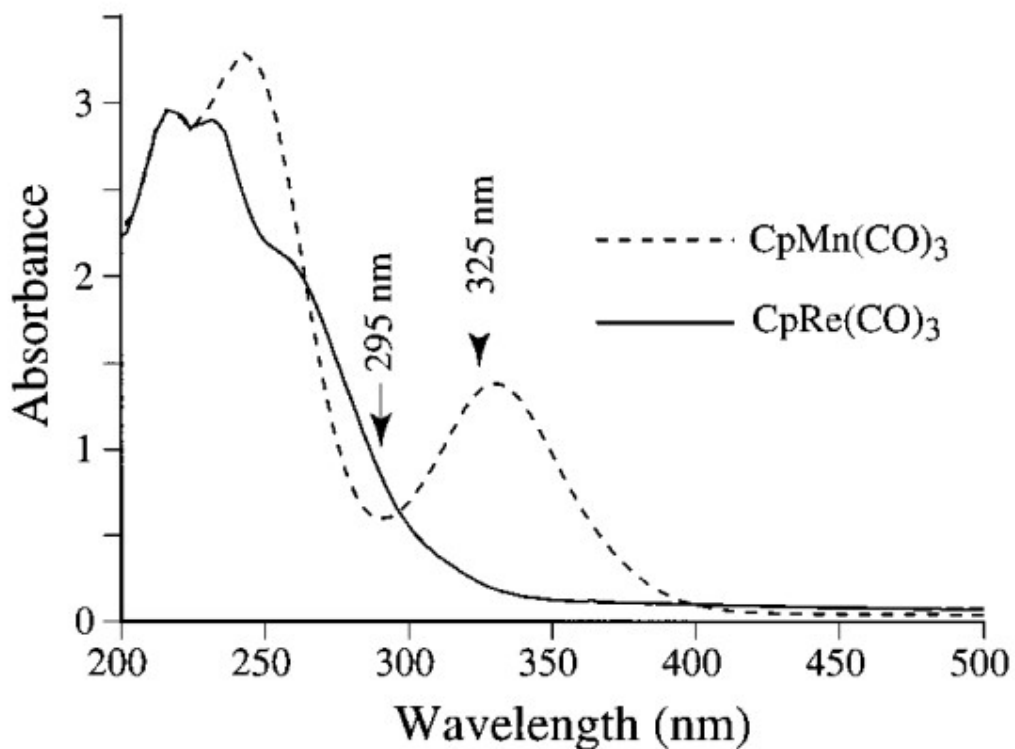


Figure 3.7: UV/vis spectra of  $\text{CpMn}(\text{CO})_3$  at 25mM and a 400  $\mu\text{m}$  path length and  $\text{CpRe}(\text{CO})_3$ , demonstrating variance in absorbance between species and exciting wavelength. Replicated from ref.<sup>11</sup>

The pump system was flushed with solvent between runs to remove precipitate and traces of the previous solution. Some attempts were made with DCM to remove more stubborn precipitate, but it was not observed to be of significant improvement over a standard solvent flush. Some precipitate could only be removed with thorough cleaning involving the disassembly of the flow system.

### 3.3.3 – X-ray Detection

The APD used for detection was a 10 mm by 10 mm sensor purchased from FMB Oxford. For the first flow cell used the APD was clamped in position next to the cell, but with the

remade cell a slot was built into the design so the APD could be secured closer to the cell for improved signal. Soller slits<sup>12</sup> and a Z-1 metal foil were used to filter data and improve the signal to noise ratio.

### 3.3.4 – PORTO

The PORTO laser facility was initiated at the Diamond light source with the aim of have five enabling roles:

- (i) PORTO will be used for laser-pump/X-ray probe experiments at beamlines of Diamond, providing the capability of structurally sensitive time-resolved experiments with 40 ps temporal resolution in hybrid mode. In low alpha operational mode this can be reduced to 10 ps, albeit with a significant sacrifice of photon flux.
- (ii) PORTO will provide a test facility for designing experiments for X-ray free electron lasers. This is critical if UK research groups are to remain at the forefront of time-resolved X-ray field and wish to retain realistic chances of being part of the community exploring these highly competitive 4th generation light sources.
- (iii) PORTO will provide off-line optimization of the irradiation and sampling conditions, such as concentrations of precious samples, of intermediates, flux, fluence and optical pathlengths. This is crucial for maximising the output of time-resolved X-Ray experiments at Diamond.
- (iv) PORTO will complement existing systems at ULTRA as it can be used to monitor excited state dynamics on the time scale  $> 10$  ps matching the synchrotron capability, which does not require  $\sim 50$  fs ULTRA laser pulses, thus dramatically increasing the facilities' throughput in underpinning time-resolved X-ray experiments.
- (v) PORTO may be moved to other storage ring facilities (e.g. the ESRF) for pump-probe experiments available at those sites.

PORTO is a mobile laser apparatus that consists of a rack containing the safety interlock control, power supply, and chiller control; and a table housing the lasers themselves. While PORTO contains a tuneable OPA, this was not used for the work described in this thesis. The PHAROS single-unit femtosecond laser system was used in conjunction with an automated harmonics generator, both from Photonic Solutions.

PORTO's laser pulses were synchronised with the X-ray pulses of the synchrotron with a timeframe generator (TFG), with the RF frequency from the ring used to trigger the laser.

Originally, the laser was directed from PORTO's output gate over the beamline via a periscopic arm, where a further series of mirrors directed it into the flow cell through a separate window to the X-ray beam. This gave it an incidence angle with the X-ray path of about 45°.

This was in part attributed to the burning out of windows in the periscopic arm, which was discovered after the beamtime, but having failed to reliably produce good signal even at high power earlier on the beamtime, it was apparent that alignment and not laser power was the limiting factor on improving signal in the setup. This was supported by the presence of dark precipitate in solutions after testing on the beamline, showing evidence that the solution was reacting under the laser. Such changes were not observed in solutions stored for equivalent times before being tested on the beamline.

Once it became apparent that poor signal was being obtained, and the silica windows had been discarded in favour of Kapton, the laser path was reworked to come in more colinearly with the X-ray beam, through the same window. This reduced the angle to approximately 20°, but still resulted in little to no signal above noise in the beamtime.

For the July 2023 beamtime a revised mirror setup excluded the periscopic arm and reduced the incidence angle to ~3°. It now also incorporates a motorised mirror with a model 8742 picomotor controller (New Focus). This allows for the laser path to be rastered from the control room while both laser and X-ray beams were active inside the hutch, enabling optimisation of signal much more easily. With improved collinearity and alignment, a sustained good quality signal was achieved in these experiments that was vastly improved from earlier attempts.

### 3.4 – Conclusion

A setup capable of collecting time-resolved XAS data has been constructed at Diamond, enabling difference data collection on the microsecond timescale. In the course of creating and improving this setup the main limiting factors on the quality of the data were found to be the quality of the jet, the collinearity of the laser and X-ray beams, and the proximity of the APD. The setup constructed can now produce a usable data set within 8 hours of probing and is likely ready to be used by non-specialists. Further assembly of the setup should now be rote and require minimal further alteration.

### 3.5 – References

1. H. Stiel, M. Schnurer, H. Legal, W. Malzer, L. Anklamm, C. Schlesiger, K. A. Janulewicz, M. Iqbal and P. V. Nickles, San Diego, CA, 2013.
2. A. Bartels, F. Hudert, C. Janke, T. Dekorsy and K. Kohler, *Applied Physics Letters*, 2006, **88**, 3.
3. A. M. March, A. Stickrath, G. Doumy, E. P. Kanter, B. Krassig, S. H. Southworth, K. Attenkofer, C. A. Kurtz, L. X. Chen and L. Young, *Review of Scientific Instruments*, 2011, **82**, 8.
4. F. J. Wuilleumier and M. Meyer, *Journal of Physics B-Atomic Molecular and Optical Physics*, 2006, **39**, R425-R477.
5. W. Gawelda, C. Bressler, M. Saes, M. Kaiser, A. N. Tarnovsky, D. Grolimund, S. L. Johnson, R. Abela and M. Chergui, *Physica Scripta*, 2005, **T115**, 102-106.
6. M. H. Rittmann-Frank, C. J. Milne, J. Rittmann, M. Reinhard, T. J. Penfold and M. Chergui, *Angewandte Chemie International Edition*, 2014, **53**, 5858-5862.
7. L. B. Skinner, C. J. Benmore, J. K. R. Weber, M. C. Wilding, S. K. Tumber and J. B. Parise, *Physical Chemistry Chemical Physics*, 2013, **15**, 8566-8572.

8. G. Smolentsev, K. M. van Vliet, N. Azzaroli, J. A. van Bokhoven, A. M. Brouwer, B. de Bruin, M. Nachtegaal and M. Tromp, *Photochemical & Photobiological Sciences*, 2018, **17**, 896-902.
9. J. X. Zhang, X. Y. Zhang, K. Suarez-Alcantara, G. Jennings, C. A. Kurtz, L. M. L. Daku and S. E. Canton, *Acs Omega*, 2019, **4**, 6375-6381.
10. S. A. Bartlett, N. A. Besley, A. J. Dent, S. Diaz-Moreno, J. Evans, M. L. Hamilton, M. W. D. Hanson-Heine, R. Horvath, V. Manici, X. Z. Sun, M. Towrie, L. J. Wu, X. Y. Zhang and M. W. George, *Journal of the American Chemical Society*, 2019, **141**, 11471-11480.
11. H. Yang, M. C. Asplund, K. T. Kotz, M. J. Wilkens, H. Frei and C. B. Harris, *Journal of the American Chemical Society*, 1998, **120**, 10154-10165.
12. B. Bewer, *Journal of Synchrotron Radiation*, 2012, **19**, 185-190.

# Chapter 4 – Probing Organometallic Re-alkane and Re-silane complexes with Time-resolved XAFS

## 4.1 – Introduction

Traditional binding of ligands to transition metals occurs via donation of an electron pair either as a dative covalent bond or by a  $\pi$ -bond. A less common interaction is formed by a simple  $\sigma$ -bond between a pair of atoms acting as a donor to a metal center in so called  $\sigma$ -complexes.<sup>1</sup> The original  $\sigma$ -bond ligand discovered by Kubas is  $H_2$ .<sup>2</sup> Examples can also be found with alkanes, silanes, boranes and germanes. They typically exhibit  $\eta^1$ - or  $\eta^2$ -E-H geometries (E=H, C, B, Si, Ge) and are unsupported by other bonds to the metal. The first examples of organometallic alkane complexes were observed by spectroscopic data arising from matrix isolation experiments at 12 K,<sup>3</sup> and since then both fast time-resolved spectroscopic studies<sup>4</sup> and low temperature studies with NMR<sup>5</sup> have been used to characterise these complexes in solution. A breakthrough for characterisation of organometallic alkanes occurred with the transformation of single crystals of  $[(iBu_2PCH_2CH_2P^iBu_2)Rh(NBD)][BAR^F_4]$  (NBD = norbornadiene,  $C_7H_8$ ;  $Ar^F = 3,5-(CF_3)_2C_6H_3$ ),  $[1-NBD][BAR^F_4]$ , into  $[(iBu_2PCH_2CH_2P^iBu_2)Rh(NBA)][BAR^F_4]$  (NBA = norbornane,  $C_7H_{12}$ ),  $[1-NBA][BAR^F_4]$ .<sup>6</sup> This was achieved by the addition of  $H_2$  gas to the crystals, which hydrogenates NBD to NBA. When performed at room temperature, this allows a metal-alkane complex to be formed *in situ* in solid state and can be preserved with rapid cooling to obtain a sufficient lifetime to perform single-crystal X-ray diffraction.

This technique has now allowed an array of metal-alkane complexes to be characterised with X-ray diffraction, with the species of interest being formed via solid/gas hydrogenation of alkene precursors, often in single-crystal-to-single-crystal (SC-SC) transformations.<sup>7</sup>

Of the various organometallic alkane metal carbonyl systems that have been investigated in solution, rhenium carbonyls have been found to be some of the longest lived<sup>8,9</sup>. The effect was so pronounced that it enabled a characterisation of the  $\text{CpRe}(\text{CO})_2(\text{cyclopentane})$  complex via low-temperature NMR<sup>5</sup>, and further rhenium complexes have been utilised to study organometallic alkane complexes exploiting the stability of these complexes<sup>10,11</sup>. The long lifetime of such species makes them ideal systems for investigating the bonding and interaction of the metal centre with Si-H and C-H bonds. In this Chapter the reactivity of the piano-stool complex  $\text{CpRe}(\text{CO})_3$  is investigated in various solvents to further understanding of bonding and reactivity of the Si-H bond in organometallic silane complexes and its interaction with the C-H bond for alkane solvents in organometallic alkane complexes.

In both cases the metal centre and ligand form a 3-centre-2-electron sigma complex as an intermediate step in the activation of the bond. The geometry of this bonding has been probed theoretically to determine its nature, and is largely agreed to proceed via an  $\eta^2$  H, C binding before  $\pi$  back-donation to the  $\sigma^*$  orbital breaks the C-H bond, as illustrated in Figure 4.1.<sup>12</sup>

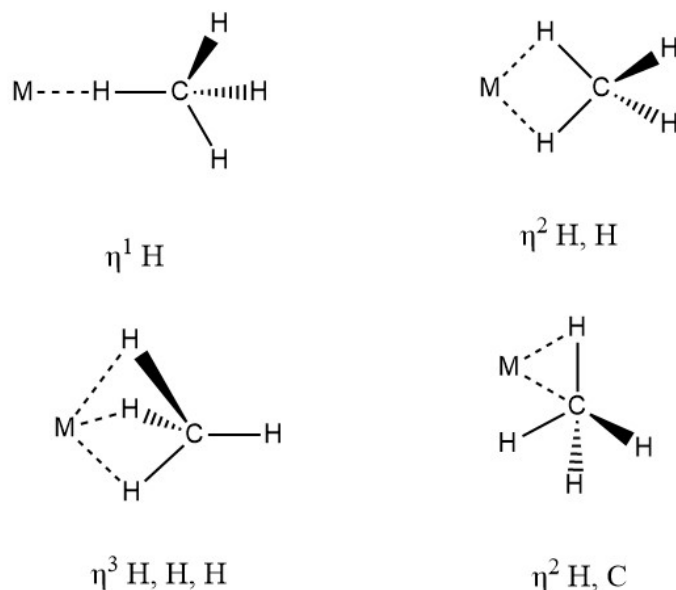


Figure 4.1: Possible binding modes of methane to a metal centre.

What is less well-defined is whether an  $\eta^1$  binding exists beforehand, with the C-H approaching the metal hydrogen first, rather than side on. Theoretical studies support an approach that places the hydrogen closer before moving to a more  $\eta^2$  type arrangement.<sup>13</sup> While computational studies in this area are consistent, conclusive experimental evidence of  $\eta^1$  binding in these structures has not yet been found.

#### 4.1.1 – Rhenium-alkane complexes

While initially considered unfeasible, stable metal- alkyl complexes have been known for a while, to the great advantage of metathesis.<sup>14</sup> Examples of stable metal- alkane complexes are decidedly more elusive. Perutz et al. identified methane-metal complexes through matrix isolation<sup>15</sup>, while other early examples of metal centre interactions with C-H bonds were reported by Roe *et al.* in 1972<sup>16</sup>, and examples of C-H activation via metal- alkane complexes were promptly searched for and investigated.<sup>17</sup> Today various metal complexes are utilised in the search for efficient and selective C-H activation mechanisms.<sup>18</sup>

Rhenium-alkane complexes were found to be incredibly long-lived in comparison to other metal carbonyls.<sup>19</sup> Investigation of the activation of alkanes by  $\text{CpRe}(\text{CO})_3$  and other piano stool rhenium complexes was investigated by TRIR for short alkanes, observing that a substituted ring could exert considerable influence over the process.<sup>20</sup>

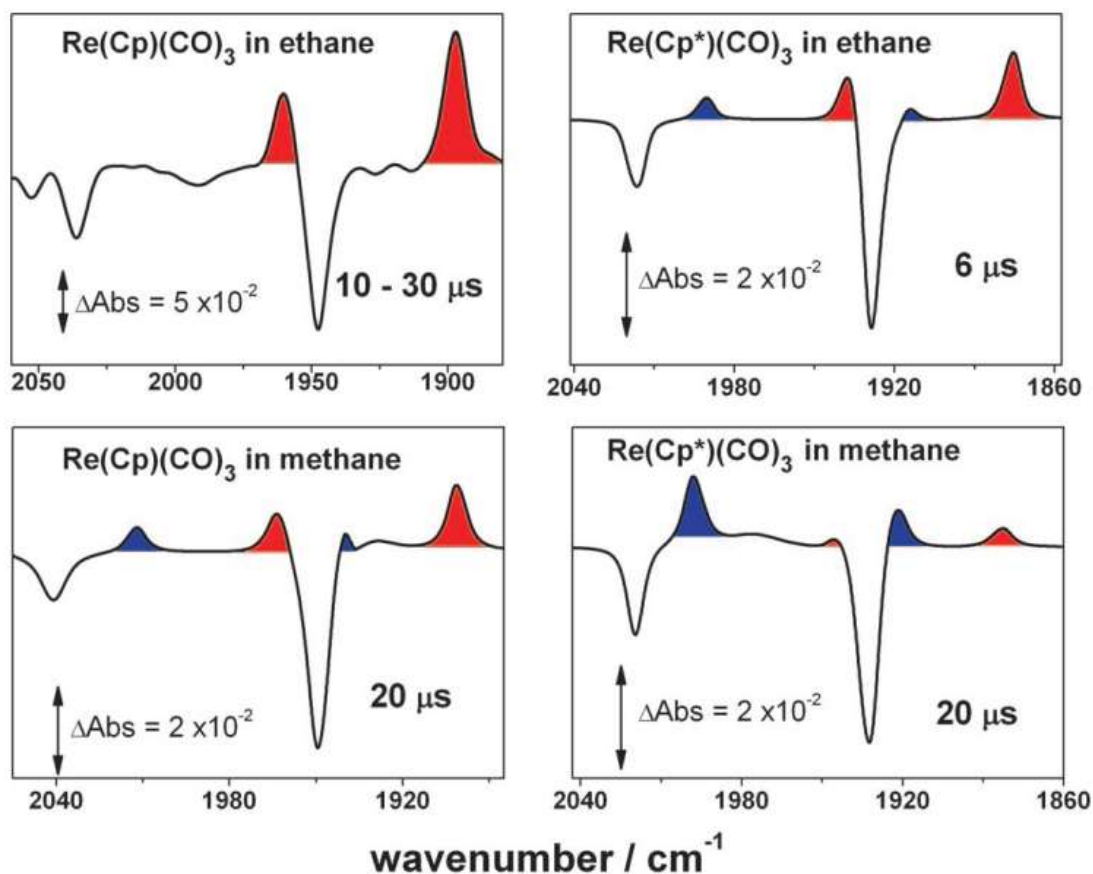


Figure 4.2: TRIR spectra showing peaks due to unactivated (red) and activated (blue) rhenium-alkane complexes. Replicated from ref.<sup>20</sup>

Figure 4.2 shows this change in activation: the change from Cp to Cp\* leads to the complex activating the ethane bond and dramatically increases the rate of activation of the methane bond. Of import to this work, they observed that these shorter alkanes were activated much more readily than their longer-chain relatives. From this result we anticipate activation of longer chain alkanes by  $\text{CpRe}(\text{CO})_3$  is very unlikely.

#### 4.1.2 – Rhenium-silane complexes

The photochemical reaction of transition metal carbonyl complexes with silanes was investigated in 1971, and a number of organometallics tested and found to produce silyl metal hydrides.<sup>21</sup> This included  $\text{CpMn}(\text{CO})_3$ , which remains a subject of study today, as described in Chapter 5. Yang et al. performed a femtosecond to nanosecond investigation of the photolysis of  $\text{CpRe}(\text{CO})_3$  in 1998, and proposed a reaction scheme based on their observations, reproduced here in Figure 4.3.<sup>22</sup>

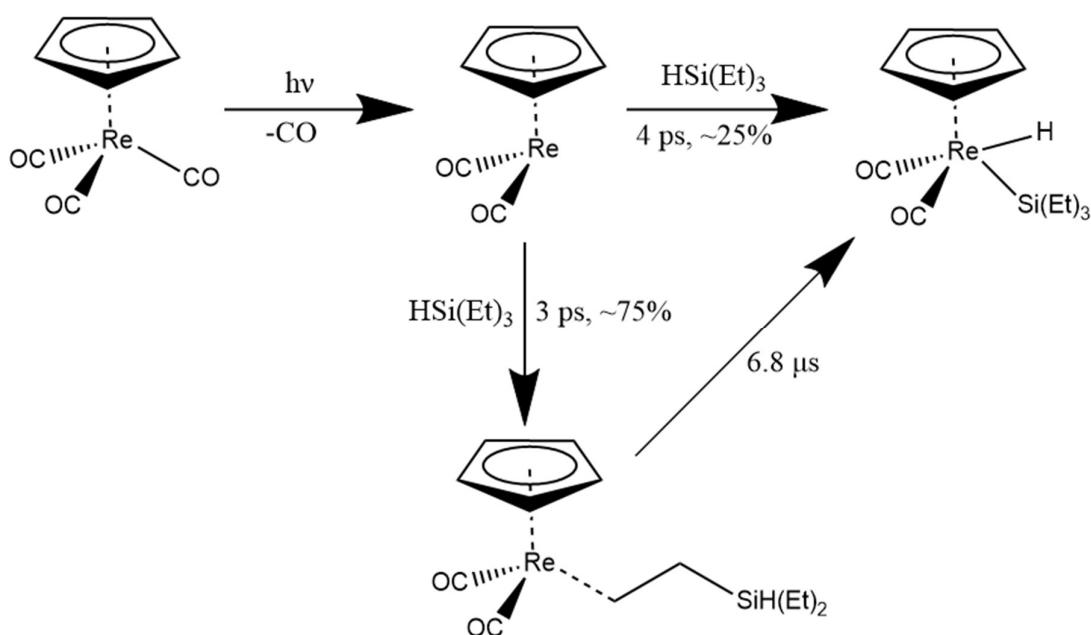


Figure 4.3: Reaction mechanism for photolysis of  $\text{CpRe}(\text{CO})_3$  in triethyl silane as proposed by Yang et al.<sup>22</sup>

Of relevance to this work is their assignment of 2 distinct pathways for the formation of the activated rhenium silyl complex: one via solvation through the ethyl moiety before rearranging to activate the silane bond, occurring on a scale of microseconds, and another via direct solvation of the silyl moiety, occurring on a picosecond timescale. Yang et al. estimated an inequality in the two modes of solvation, with 25% solvation via the silyl moiety and 75% solvation via an ethyl moiety. Thus a 3:1 ratio of ethyl-bound intermediate

to silyl-bound intermediate is predicted to exist within the first few nanoseconds of the reaction.

Later computational calculations of this system were performed by Zhang and Su<sup>23</sup>, who found that computational modelling led to consistent results for the activity observed in the rhenium system.

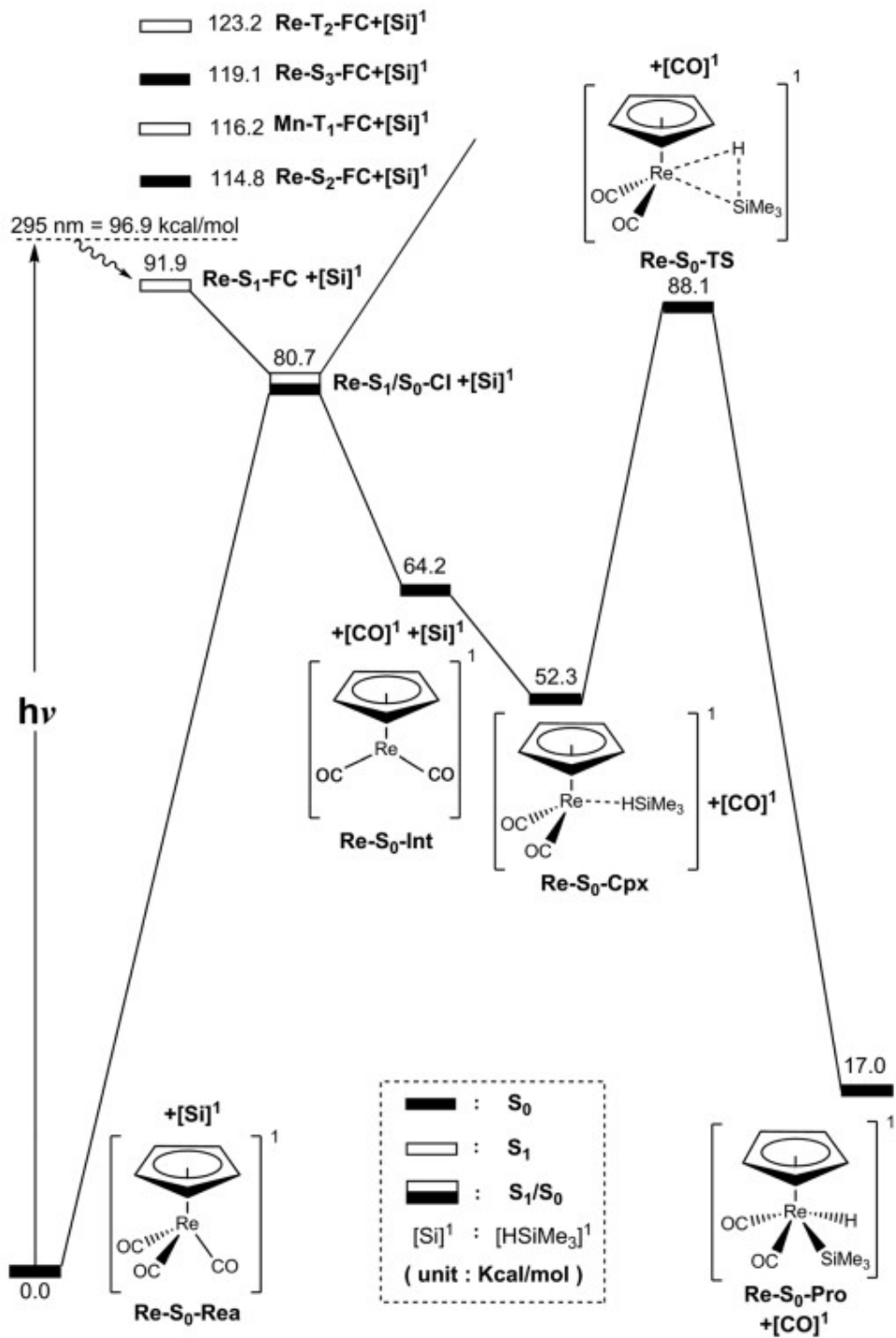


Figure 4.4: Calculated energy profiles for the photoexcitation reactions of  $\text{CpRe}(\text{CO})_3$  with energies given in  $\text{kcal mol}^{-1}$ . Reproduced from ref.<sup>23</sup>

Zhang and Su predict a relatively simple progression from excitation to loss of a CO ligand and attachment of the silane, with the transition to the activated state being past an energy barrier. This rearrangement involves movement from a more  $\eta^1$  H binding type structure to a side-on  $\eta^2$  H, Si geometry before the H-Si distance increases as the bond breaks.<sup>23</sup>

## 4.2 – Aims

Cyclopentadienyl Rhenium complexes produce some of the longest-lived alkane and silane complexes, making them some of the most suitable species to be studied in time-resolved XAS. There is also existing literature investigating TRIR of those systems which can provide a basis of expectation to work from. Following from the investigation of Cyclopentadienyl Rhenium systems on the picosecond and nanosecond timescales with TRIR, we investigate further with TRIR and utilise TRXAS to investigate on the microsecond timescale. The aims of this Chapter are as follows:

- (i) To re-investigate the photolysis of  $\text{CpRe}(\text{CO})_3$  in alkane and silane solvents with TRIR in order to establish the kinetics required under TRXAS conditions and to investigate some anomalies in the early TRIR data.
- (ii) To investigate the photolysis of  $\text{CpRe}(\text{CO})_3$  in both neat alkane and silane solvents with TRXAS, informed by the findings from TRIR experiments to explore whether TRXAS can see structural differences in these different solvents.
- (iii) To estimate the geometry and electronic structure as well as kinetics of the photoproducts from the TRXAS of those reactions.
- (iv) To carry out of photolysis of  $\text{CpRe}(\text{CO})_3$  in alkane doped with silane to distinguish between different photoproducts via XAFS analysis as the  $\text{CpRe}(\text{CO})_2(\text{alkane})$  intermediate interconverts to the  $\text{CpRe}(\text{CO})_2(\text{silane})$  product.

For aim (i) TRIR was performed at the University of Nottingham. These experiments were based upon the experiments reported by Yang et al.<sup>22</sup>, which observed nanosecond and picosecond dynamics. The following work focused on the microsecond timescale in order to

examine the lifetimes of the solvent-bound intermediates. Identifying the species that exist on that timescale and their rate of decay is the foundational work for modelling and identifying the features of those species in TRXAS.

For aims (ii) through (iv), TRXAS was performed at the Advanced Photon Source of the Argonne National Laboratory, Illinois, USA. These experiments sought to establish further evidence for the reaction schemes derived from IR data and investigate the geometries of those intermediates and their conversions. These TRIR and TRXAS investigations were performed in collaboration with Dr Garwood.

## 4.3 – Results

Solutions of  $\text{CpRe}(\text{CO})_3$  in various solvents were prepared under an inert atmosphere and excited with 266 nm UV radiation in a pump-probe TRIR experiment, as described in Chapter 2. The concentration of  $\text{CpRe}(\text{CO})_3$  was between 5 and 6 mM in each sample.

### 4.3.1 – TRIR of $\text{CpRe}(\text{CO})_3$ in neat triethyl silane

The photolysis of  $\text{CpRe}(\text{CO})_3$  in neat triethyl silane results in 2 depletion peaks forming within the first 100 ns from the bleaching of the parent.

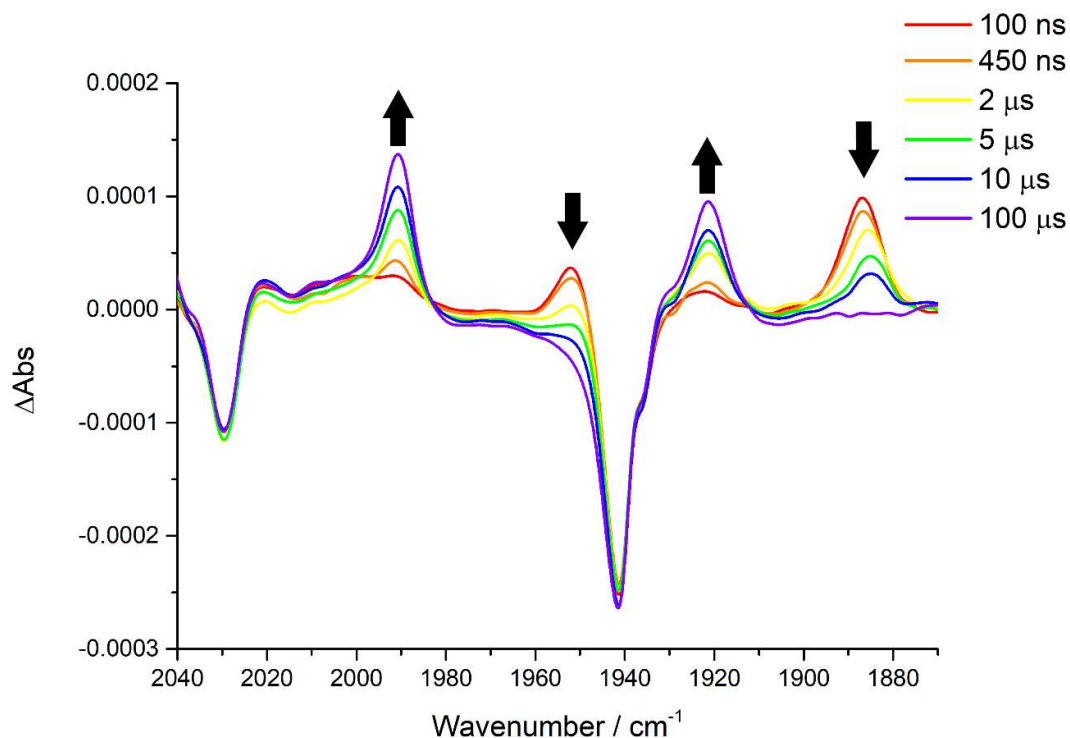


Figure 4.5: TRIR of  $\text{CpRe}(\text{CO})_3$  in neat triethyl silane, photolyzed at 266nm.

As shown in Figure 4.5, the initial product peaks grow in at wavenumbers of 1952 and 1885  $\text{cm}^{-1}$ , and the secondary product peaks occur at 1989 and 1921  $\text{cm}^{-1}$ . The first pair of product peaks grow in within 100 ns before decaying away over the next 100  $\mu\text{s}$ , matching the growth of the second pair of peaks. These primary product peaks are consistent with those previously observed by Yang et al.'s and assigned to  $\text{CpRe}(\text{CO})_2(\text{Et}_3\text{SiH})$ , where the silane is bonding to the Re moiety via a C-H moiety of the ethyl tail. Similarly, the secondary product peaks are consistent with the previously observed product which was assigned to  $\text{CpRe}(\text{CO})_2(\text{H})(\text{SiEt}_3)$ .<sup>22</sup> That assignment is based upon theoretical expectations, but given the predictions of computational studies<sup>23</sup> it is possible that the Si-H bond is only partially activated, without enough energy to overcome the barrier to complete cleavage. Where that previous work focuses on the picosecond timescale, we observe these peaks' behaviour on the scale of nanoseconds and microseconds.

Analysis of the kinetics of the bands led to the observation of a bi-exponential trend in the decay of  $\text{CpRe}(\text{CO})_2(\text{Et}_3\text{SiH})$  to  $\text{CpRe}(\text{CO})_2(\text{H})(\text{SiEt}_3)$ . This trend is shown in Figure 4.6 and was

unexpected as previous literature reported a mono-exponential decay<sup>22</sup>. A single exponential component is consistent with a model of one reaction pathway for the conversion of  $\text{CpRe}(\text{CO})_2(\text{EtSiHEt}_2)$  to  $\text{CpRe}(\text{CO})_2(\text{H})(\text{SiEt}_3)$ , so some explanations for this difference have been considered.

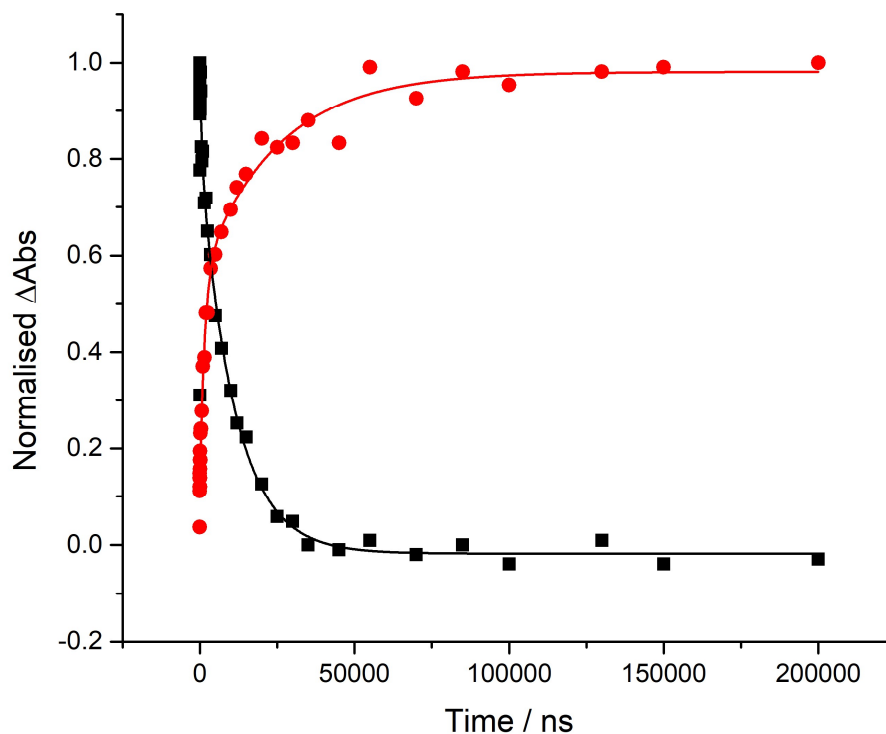


Figure 4.6: Normalised decay and growth of peak at  $1885\text{ cm}^{-1}$  (black) and peak at  $1921\text{ cm}^{-1}$  (red) for  $\text{CpRe}(\text{CO})_3$  photolyzed in neat triethyl silane with biexponential fit shown.

The factors are both on the microsecond timescale, which makes either component being due to a vibrational cooling unlikely, with such factors being observed to resolve on a picosecond timescale.<sup>22</sup>

The biexponential could also be due to a contaminant providing a secondary reaction pathway, but with the cleaning and degassing techniques used to avoid impurities, this is considered highly unlikely. Laser drift is another possible explanation, but as the same effect is not observed in the parent peaks has also been discounted as an explanation.

The biexponential fit gives a slow component (11.7  $\mu\text{s}$ ) and a fast component (1.4  $\mu\text{s}$ ). We attribute the slow component to conversion from ethyl-bound to silyl-bound  $\text{CpRe}(\text{CO})_2(\text{Et}_3\text{SiH})$ , with the fast component being currently unassigned by this work.

Further independent TRIR experiments were conducted independently by Dr Garwood following observation of a slight shift in IR peak position of the initial photoproduct observed in both alkane and silane solvents. Her study found that this peak shift was most likely due to 2 species with almost entirely overlapping peaks, with one species decaying in as the other grew to create the shift effect.

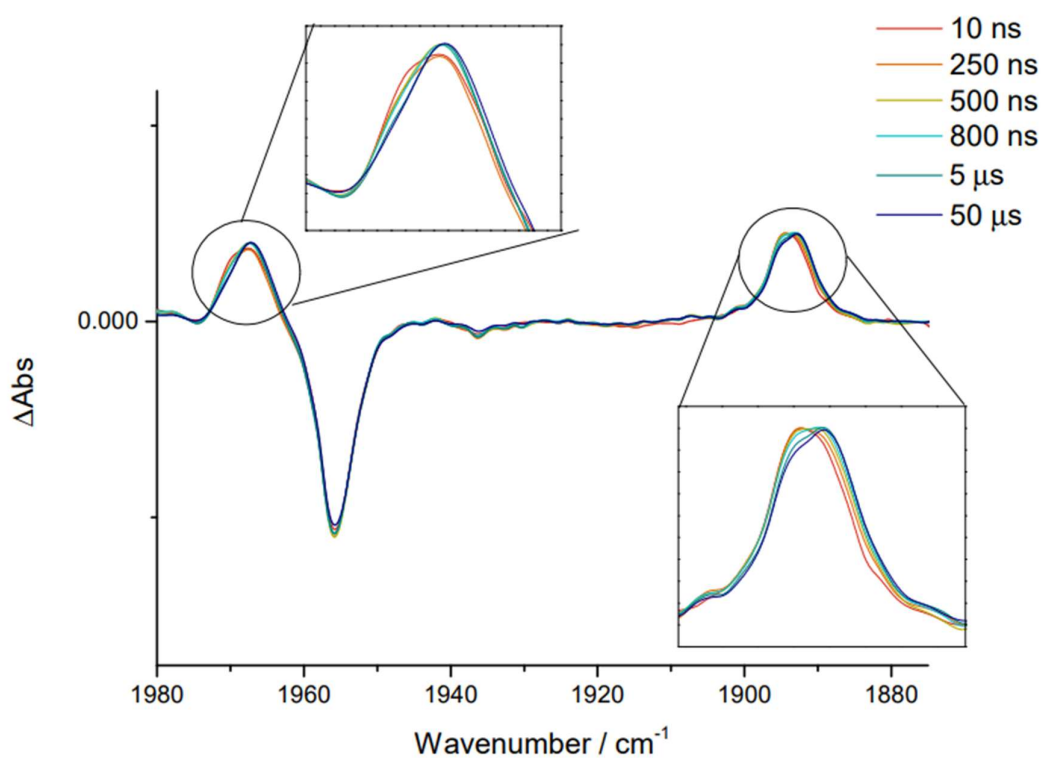


Figure 4.7: TRIR trace of  $\text{CpMn}(\text{CO})_3$  photolyzed in neat *n*-heptane. Reproduced from ref.<sup>24</sup>

This shift can be seen in Figure 4.7, and when fitted as two overlapping species was analysed to derive a lifetime of 0.88  $\mu\text{s}$  for the transition between species.

The nature of these two species, while almost certainly isomers of  $\text{CpRe}(\text{CO})_2(\text{n-heptane})$ , is unclear. One proposed possibility is that the species correspond to an  $\eta^1$  Re-H binding mode and an  $\eta^2$  Re-H-C 3-centre-2-electron binding mode or vice versa, which would match well

with a model of the heptane moiety approaching hydrogen-first before bending into a more electronically favourable shape. Thus, for the experiments in neat silane the early time kinetics are due to  $\eta^1$  Re-H binding mode and an  $\eta^2$  Re-H-C 3-centre-2-electron binding mode or vice versa of the  $\text{CpRe}(\text{CO})_2(\text{EtSiHEt}_2)$  moiety.

An alternative explanation for both the experiments producing  $\text{CpRe}(\text{CO})_2(\text{silane})$  and  $\text{CpRe}(\text{CO})_2(\text{alkanes})$  is that the shift represents the binding site moving along the alkane chain, from primary to secondary carbon. While there is evidence for such alkane chain-walking in analogous systems, the theory proposed thus far is that these isomers exist in a dynamic equilibrium rather than forming in sequence.<sup>25, 26</sup> However, this is unlikely because there is not a significant alkane in the silane case and it would be surprising that similar spectroscopic shifts and kinetics would be observed between these two species.

#### 4.3.2 – TRIR of $\text{CpRe}(\text{CO})_3$ in n-heptane doped with triethyl silane

Previous investigation in the University of Nottingham group found that for 0.25 M tributyl silane doped in n-heptane, only one photoproduct was produced on the timescale of the experiment (1 ms). This was attributed to the high stability of the  $\text{CpRe}(\text{CO})_2(n\text{-heptane})$  photoproduct. In order to observe the kinetics of the displacement of the heptane moiety by triethyl silane, much higher concentrations of silane were used.

$\text{CpRe}(\text{CO})_3$  was dissolved in n-heptane doped with varying quantities of triethyl silane. Solutions were doped to give 2 to 5 M concentrations of silane. At higher concentrations, the volume of silane used was in excess of the original volume of heptane employed, so the term 'doped with silane' is only partially accurate.

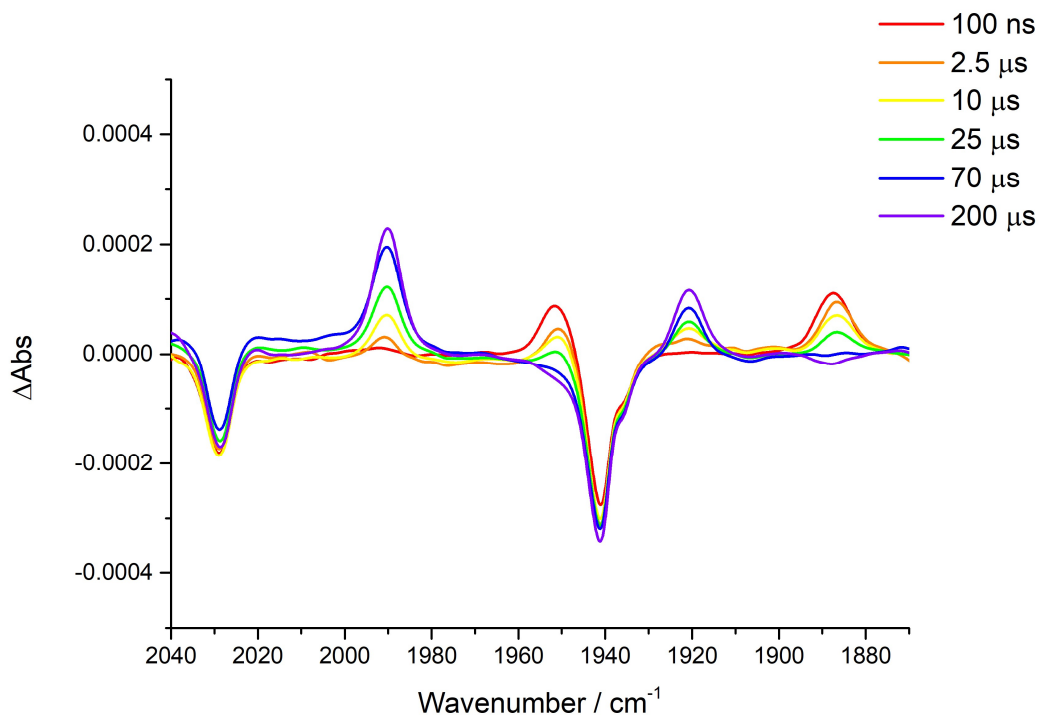


Figure 4.8:  $\text{CpRe}(\text{CO})_3$  in heptane doped with 2 M triethyl silane, photolyzed at 266 nm.

From Figure 4.8 it can be seen that there are once again 2 parent depletion bands and 4 product bands. Of the product bands, an initial pair form within the first 100 ns and then decay commensurately to the other 2 that grow in over 200  $\mu\text{s}$ .

The parent peaks are observed at 2029 and 1941  $\text{cm}^{-1}$ , consistent with their position in neat n-heptane. The primary photoproduct's peaks are at 1952 and 1888  $\text{cm}^{-1}$ , and the secondary product peaks grow in at 1990 and 1921  $\text{cm}^{-1}$ .

Previous work<sup>22</sup> describes the reaction of photolyzed  $\text{CpRe}(\text{CO})_3$  in neat triethyl silane as producing  $\text{CpRe}(\text{CO})_2(\text{H})(\text{SiEt}_3)$ , as the system cleaves the activated H-Si bond. The shift we observe above can therefore be tentatively attributed to the Re metal centre activating the Si-H bond.

In addition to this observable shift in the secondary product's peaks, the growth of those peaks and decay of the primary product peaks fit more closely to a second order exponent than a first order exponent as shown in Figure 4.9, as was seen for the conversion rate in neat triethyl silane.

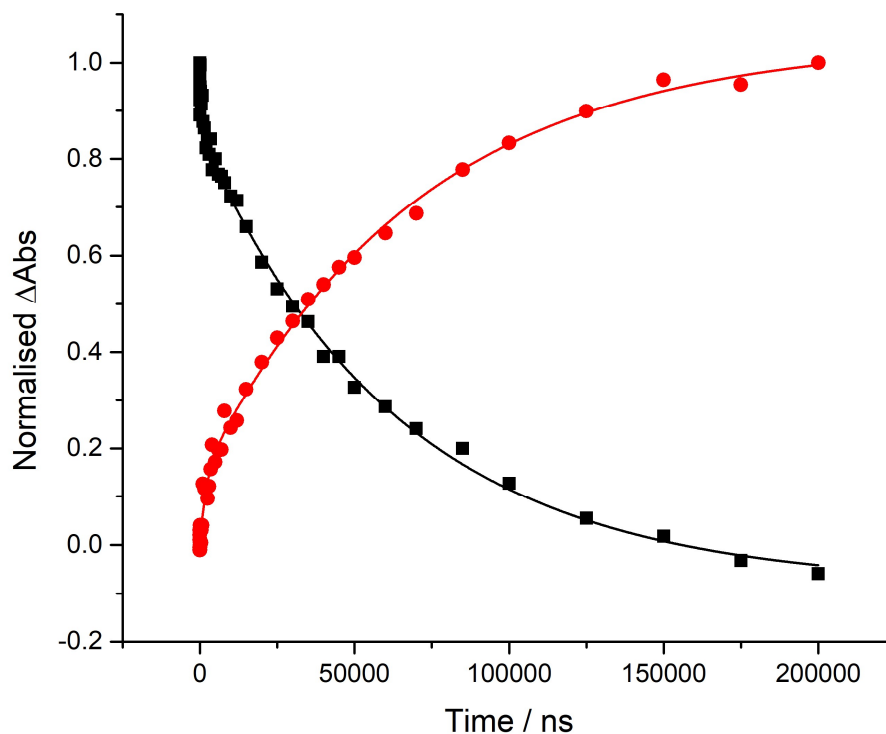


Figure 4.9: Decay and growth of absorbance peak at  $1887\text{ cm}^{-1}$  (black) and  $1992\text{ cm}^{-1}$  (red) for  $\text{CpRe}(\text{CO})_3$  photolyzed at  $266\text{ nm}$  in heptane doped with  $2.0\text{ M}$  triethyl silane.

This is unlikely to be due to an extension of the lifetime of the ethyl-solvated species, as the second order exponential fit also works for the data from  $\text{CpRe}(\text{CO})_3$  in neat triethyl silane. This is instead a significant indication that the reaction is no longer pseudo-first order.

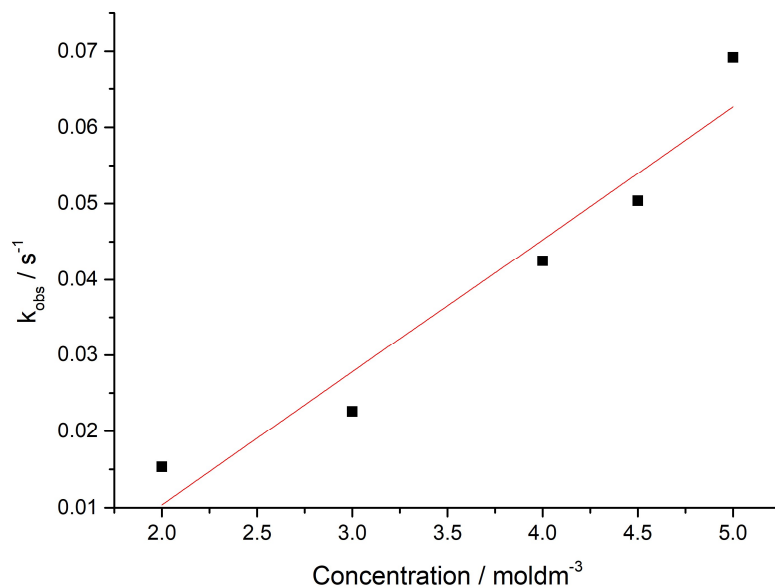


Figure 4.10: Stern-Volmer plot of observed rate constant against concentration of triethyl silane for  $\text{CpRe}(\text{CO})_3$  in *n*-heptane and triethyl silane. A linear fit is used to model a pseudo-first order relationship, which is sufficiently accurate for the rate predictions needed.

The rate of conversion was measured in 5 different concentrations of triethyl silane in *n*-heptane, with the resulting data shown in a Stern-Volmer plot in Figure 4.10 and numerically in Table 4.1. The pseudo-first order rate constant was taken as the gradient, calculated as  $k = 0.0174 \pm 0.0026 \text{ mol}^{-1} \text{ dm}^3 \text{ s}^{-1}$ .

Table 4.1: Derived rates for selected concentrations of triethyl silane.

Silane Concentration / M	Rate, $k_{\text{obs}} / \text{s}^{-1}$
2.0	$1.54 \times 10^4$
3.0	$2.26 \times 10^4$
4.0	$4.25 \times 10^4$
4.5	$5.04 \times 10^4$
5.0	$6.92 \times 10^4$

This rate constant gives a half-life for the silane-bound complex on the order of a few milliseconds, which is too long to work with the flow rates required in the pumped solution TRXAS and observe both intermediates.

From these observations we determined that a neat solution of triethyl silane would provide a system where  $\text{CpRe}(\text{CO})_2(\text{Et}_3\text{SiH})$  would persist in solution for a reasonable timeframe of several microseconds before the significant population of photoproduct became  $\text{CpRe}(\text{CO})_2(\text{HSiEt}_3)$ , allowing an adequate window to observe the ethyl-bound species via TRXAS.

#### 4.3.3 – XAS Investigations of $\text{CpRe}(\text{CO})_3$

Following on from TRIR investigations of the photolysis of  $\text{CpRe}(\text{CO})_3$ , a series of investigations were conducted as part of beamtime at the APS, Chicago. The method used is detailed in Chapter 2.  $\text{CpRe}(\text{CO})_3$  was photolyzed in neat cyclohexane, n-hexane, and triethyl silane, with EXAFS data collected for each system.

While performing a comparison between cycloheptane and n-heptane's behaviour as solvents would be desirable, the use of cyclohexane was preferred for the higher-priority goal of comparing n-alkane bond lengths with the metal centre to cycloalkane bond lengths. This is because in 2019 evidence was found for chain-walking between the primary and secondary carbons of n-heptane bound to tungsten pentacarbonyl.<sup>25</sup> That investigation found the EXAFS provided a metal-alkane bond length well-matched to the weighted average of computational predictions for the metal-primary carbon and metal-secondary carbon bonding. A cycloalkane, by virtue of having only secondary alkanes, should therefore produce a more consistent match to theoretical models. Cycloheptane's ring is large enough that it was anticipated to exhibit conformers that could present significantly different carbon environments to the metal centre, so cyclohexane was used instead.

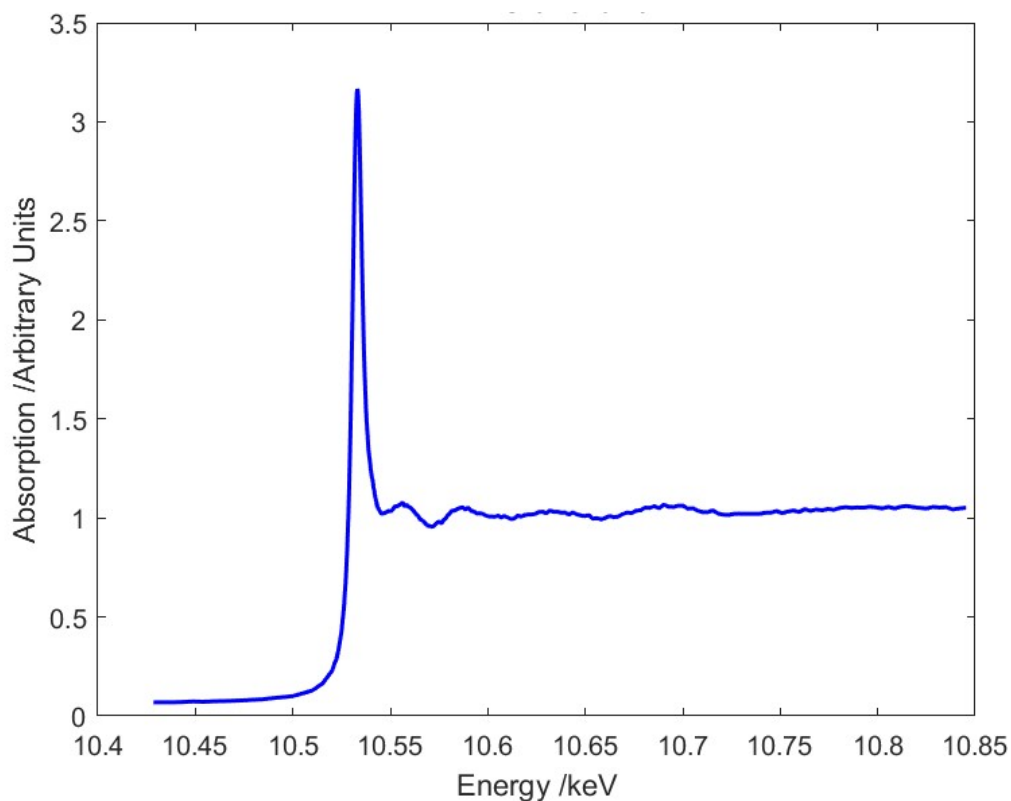


*Figure 4.11: EXAFS spectrum of L<sub>III</sub> edge of Rhenium for CpRe(CO)<sub>3</sub> in triethyl silane solution.*

As shown in Figure 4.11, the Rhenium L<sub>III</sub> edge is characterised by a sharp rise at 10.53 keV. This profile is common to each solvent system, as just being solvated in different compounds does not have a pronounced effect on the structure of the organometallic complex around the metal centre or the position of the edge.

From this data we can produce a transform in both k-space and R-space, allowing us to interrogate the structure of the molecule and derive path lengths by fitting a model of the expected scattering paths to the experimental data.

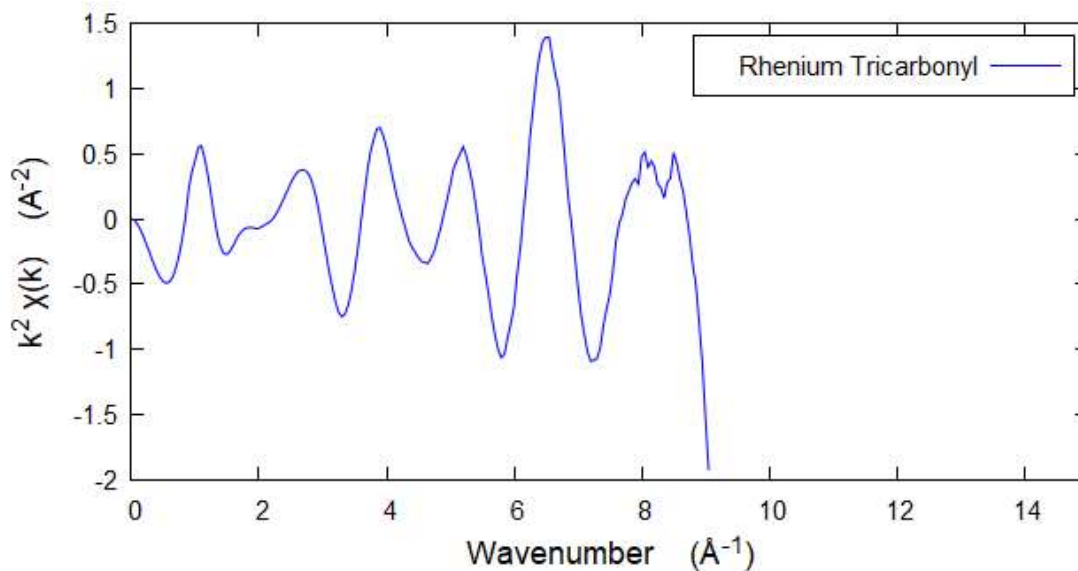


Figure 4.12: *k*-space spectrum of CpRe(CO)<sub>3</sub> in neat triethyl silane.

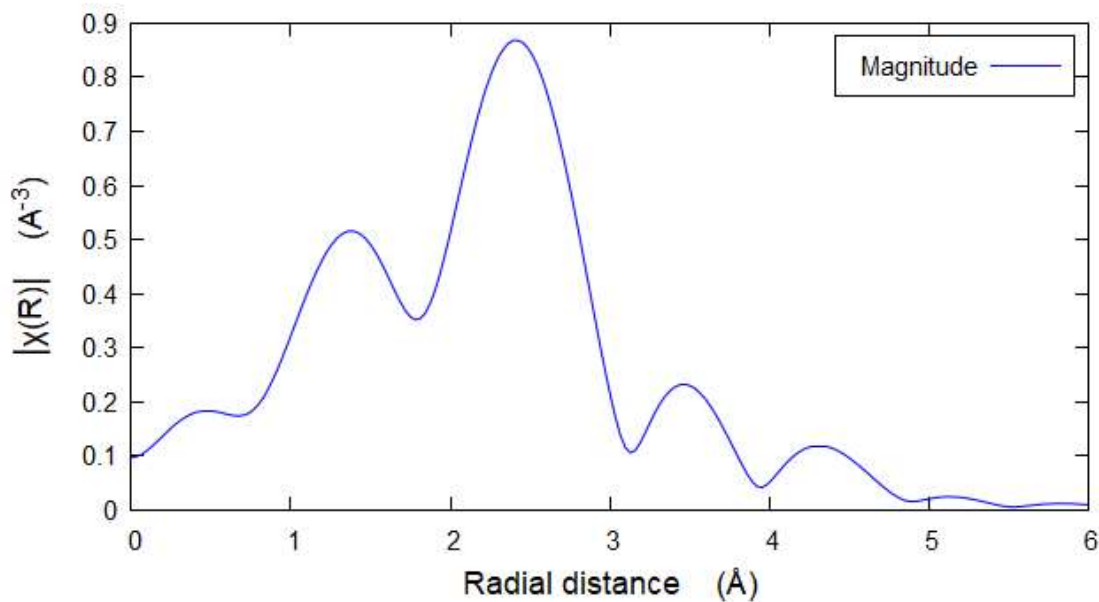


Figure 4.13: R-space projection of EXAFS of CpRe(CO)<sub>3</sub> in neat triethyl silane.

In Figure 4.13 an example R-space plot of CpRe(CO)<sub>3</sub> data is shown. This data can be used to compare to a theoretical model, which is generated by computationally fitting the theoretical parameters for the bond lengths and Debye-Waller factors to match the experimental data.

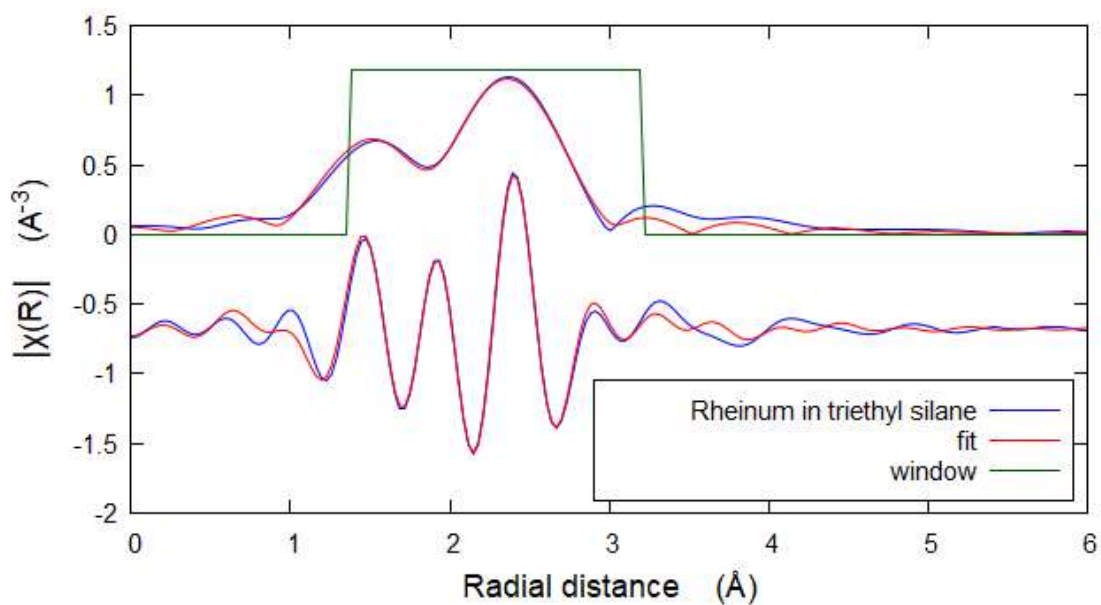


Figure 4.14: Fit of crystallography-determined geometry of  $\text{CpRe}(\text{CO})_3$  to experimental data for the EXAFS of  $\text{CpRe}(\text{CO})_3$  in triethyl silane, plotted in  $R$ -space. Figure includes magnitude (upper) and real component (lower) of the data.

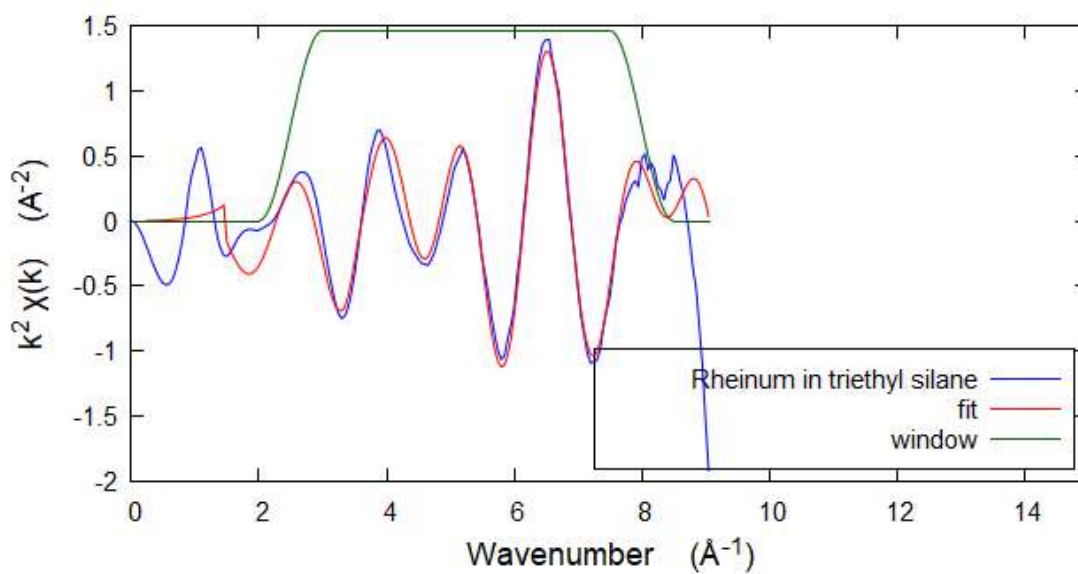


Figure 4.15:  $k$ -space plot of fit of  $\text{CpRe}(\text{CO})_3$  cif parameters to APS data for  $\text{CpRe}(\text{CO})_3$  in neat triethyl silane

Geometric data of the crystallographic structure of CpRe(CO)<sub>3</sub> (Cpf = formyl cyclopentadienyl)<sup>27</sup> was used as a first approximation to evaluate what paths needed to be fitted. Those paths were then used as an initial guess and the fit optimised until the minimisation of R was achieved while showing a good fit to crystallographic structure. The result is shown in Figures 4.14 and 4.15. The fit maps tightly to the experimental spectrum from 1.2 to 3.2 Å, which is the area of interest to the work.

Table 4.2: Derived parameters from fit to CpRe(CO)<sub>3</sub> in triethyl silane.

N Path	Distance	Crystallographic Distance	ΔR	Debye-Waller
3 Re-C <sub>CO</sub>	1.90±0.04	1.92	0.02±0.04	0.005±0.006
5 Re-C <sub>C5H5</sub>	2.30±0.02	2.30	0.00±0.01	0.001±0.003
10 Re-C-C <sub>C5H5</sub>	3.01±0.01	3.01	0.00±0.01	0.003±0.002
3 Re-O <sub>CO</sub>	3.05±0.04	3.05	0.02±0.04	0.005±0.006
6 Re-C-O <sub>CO</sub>	3.05±0.04	3.05	0.02±0.04	0.003±0.002
3 Re-C-O-C <sub>CO</sub>	3.05±0.04	3.05	0.02±0.04	0.003±0.002

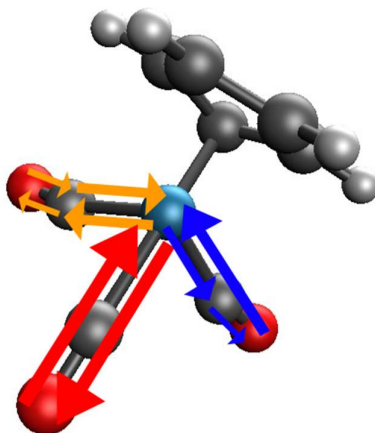
$E_0 = 8.5 \pm 3.9$ ,  $S\sigma^2 = 1$ ,  $k$  weight for fit: 2 ;  $k_{min} = 2.5$ ;  $k_{max} = 8$  ;  $R_{min} = 1.35$  ;  $R_{max} = 3.2$ ;  $R$ -factor: 0.00322. Window type: Hanning.

Table 4.2 shows the resulting parameters from this fit; the bond lengths and Debye-Waller factors for each scattering pathway contributing to the spectrum in that region. The difference between the estimated path lengths and crystallographic lengths is small and within the error margin of the fitting process, and the Debye-Waller factors are consistent and reasonable in size. These values also compare favourably to previous EXAFS measurements of CpRe(CO)<sub>3</sub>.<sup>28</sup>

In using IFEFFIT to calculate the scattering contributions of CpRe(CO)<sub>3</sub>, the Cp ring scattering was equated to 2 different scattering paths with degeneracies of 4 and 1 respectively. For the fitting itself only one path was used with a degeneracy of 5, as the Cp ring states are expected to be in flux as the ring can rotate about the metal bond<sup>29</sup>, and the accuracy of the measurement is not likely to be able to resolve the difference between the two similar contributions, and making this approximation simplifies the fitting process.

The computed distance given in the fitting table is similarly an average of the Re-C lengths calculated for the parent complex's structure, which likewise models some variation

between the bonds. This methodology has been applied to the Cp ring fit for the rest of the structures studied in this chapter, which is assumed to behave similarly for intermediate species. Previous studies show that distance remains between 2.20 and 2.40 Å even when the ring is heavily substituted.<sup>30</sup>



*Figure 4.16: Scattering paths of Re-C-O bonds in  $\text{CpRe}(\text{CO})_3$ , showing Re-O scatter (red), Re-C-O scatter (blue), and Re-C-O-C scatter (orange). The Re-C-O scatter is degenerate with Re-O-C scatter, leading to a doubling of the effective paths.*

While multiple scattering effects are not often significant components of the EXAFS regime, the near-linearity of the Re-C-O structure leads to a set of scattering paths that accrue to a sizable contribution. These paths are displayed in Figure 4.16 and included for completeness in the other EXAFS fitting tables in this Chapter.

To generate difference data, the EXAFS signal for the unphotolyzed solution was subtracted from the signal averaged across a set time interval after photolysis. This time interval was set for 10  $\mu\text{s}$  just before the next laser pulse to ensure good normalisation. The difference data was filtered using the method described in Chapter 2 to remove anomalous scans before averaging.

To fit difference spectra, the initial fit of the parent described above was taken and applied as a set of fixed paths and Debye-Waller factors, applying a negative  $S_0^2$  to them to model the effect of parent depletion in combination with the formation of new species.

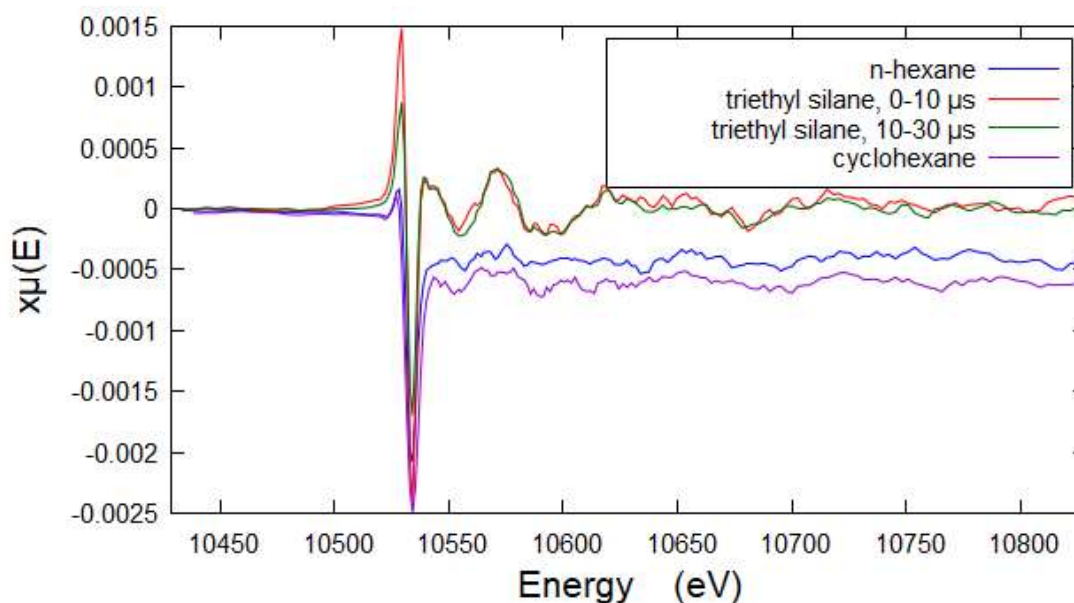


Figure 4.17: Difference data for EXAFS of  $\text{CpRe}(\text{CO})_3$  in various solvents. Data for *n*-hexane and cyclohexane is an average from 0 to 30  $\mu\text{s}$ .

As the addition of the weakly-bonding ligand is less electron-withdrawing than the carbonyl it replaces, the electron density at the metal centre is increased. This leads to the red-shift of the edge to lower energy. This produces a profile of the type seen in Figure 4.17, with the red-shifted product and negative parent edge overlapping to form the sharp rise and fall that precedes the oscillations of the difference XAFS.

#### 4.3.3.1 – XANES Difference Analysis

While in-depth XANES analysis has not been undertaken, it is possible to identify some key features of the difference data with a brief inspection of the XANES region, which is displayed for selected timeframes for each solvent in Figure 4.18.

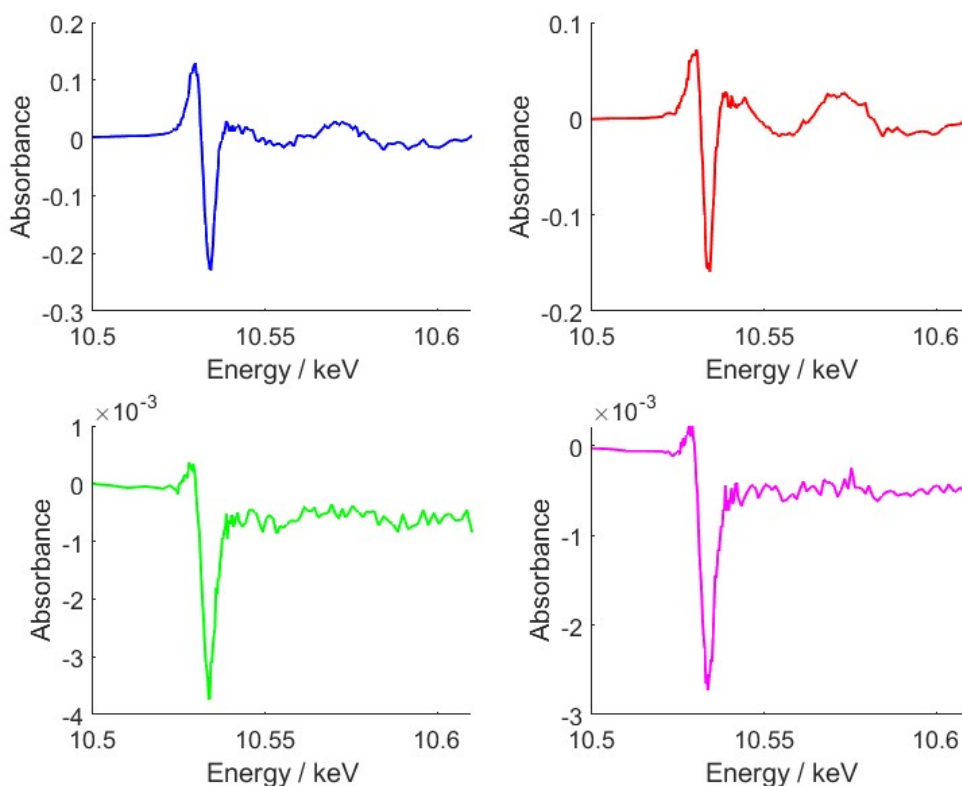


Figure 4.18: XANES difference spectra of Re  $L_{III}$  edge at; 0-10  $\mu$ s in triethyl silane (red), 10-30  $\mu$ s in triethyl silane (blue), in cyclohexane (green), and in n-hexane (magenta).

We see a clear difference between the XAFS found in a silane (upper two spectra) and an alkane (lower two spectra) solvent environment. There is a significant drop in the absorbance for the alkane differences past the edge, while the silane difference spectra exhibit no or a very small drop. This is consistent with previous TRXAS investigation of alkyl and silyl metal centre bonding<sup>25</sup>, but does not yet have a defined origin in literature.

The other major difference between the alkane and silane XANES is that the silane difference shows a strong oscillatory pattern past the edge, which is exaggerated at the later timeframe, while cyclohexane and n-hexane exhibit much smaller oscillations. This is within expectations, as we anticipate formation of a significant population of rhenium-silyl complex within the first microsecond of photolysis, with the remainder rhenium-alkyl complex converting to the silyl complex in the subsequent timeframe.

With silicon being a substantially heavier atom than carbon, it induces a significantly larger scattering effect, which goes some way to explaining the difference in feature intensity between the alkane and silane XANES.

#### 4.3.3.2 – EXAFS of $\text{CpRe}(\text{CO})_3$ in *n*-hexane

The photolysis of  $\text{CpRe}(\text{CO})_3$  in *n*-hexane is expected to be analogous to its behaviour in *n*-heptane, forming a metal-alkane complex that persists with a lifetime of several milliseconds. In the bonding of linear alkanes to the metal centre, chain walking may lead to the formation of distinct species, as the metal centre could be connected to a tertiary or a secondary carbon. Evidence for this process occurring was found for the photolysis of  $\text{W}(\text{CO})_6$  in *n*-heptane, with the path lengths of the  $(\text{CO})_5\text{W-C}_{\text{heptane}}$  scattering being calculated as a numeric average of the expected value for binding to the terminal or secondary carbons<sup>25</sup>, and the observation via NMR of alkane binding to a rhenium complex via various C-H moieties within the chain.<sup>26</sup>

Therefore, it is anticipated that there may be up to three different isomers of  $\text{CpRe}(\text{CO})_2(\text{n-hexane})$  in existence in the photolyzed solution. While resolving distinct contributions from different product species is beyond the capabilities of the technique at present, discrepancies in the fitting for the Re-alkane bond length compared to theory could indicate that alkane chain-walking occurs for the rhenium intermediate as well.

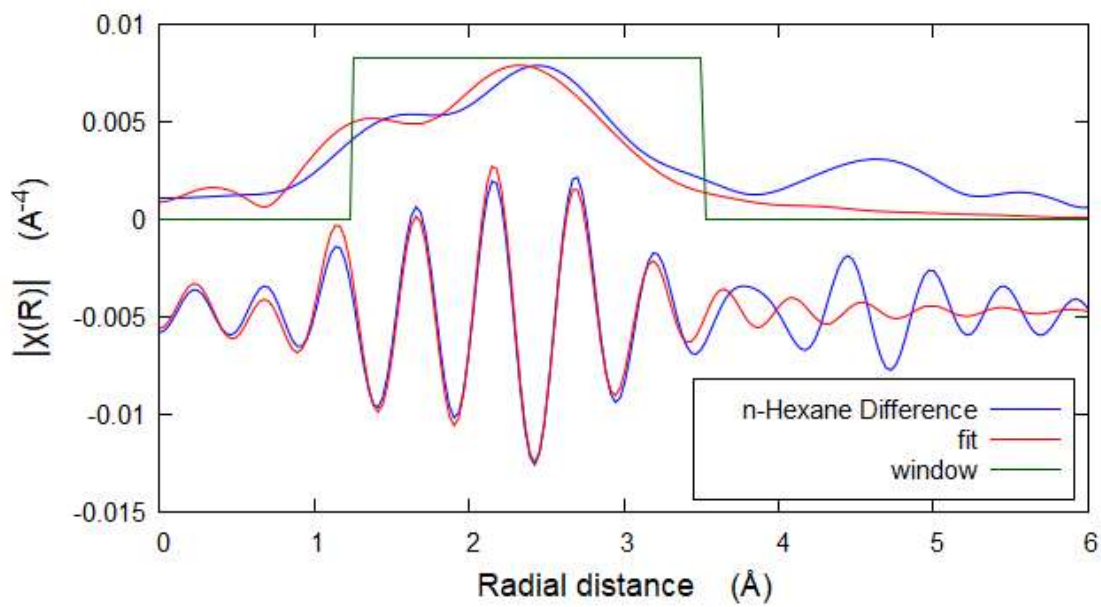


Figure 4.19: R-space fit of the first 30  $\mu\text{s}$  of difference data following photolysis of  $\text{CpRe}(\text{CO})_3$  in neat n-hexane.

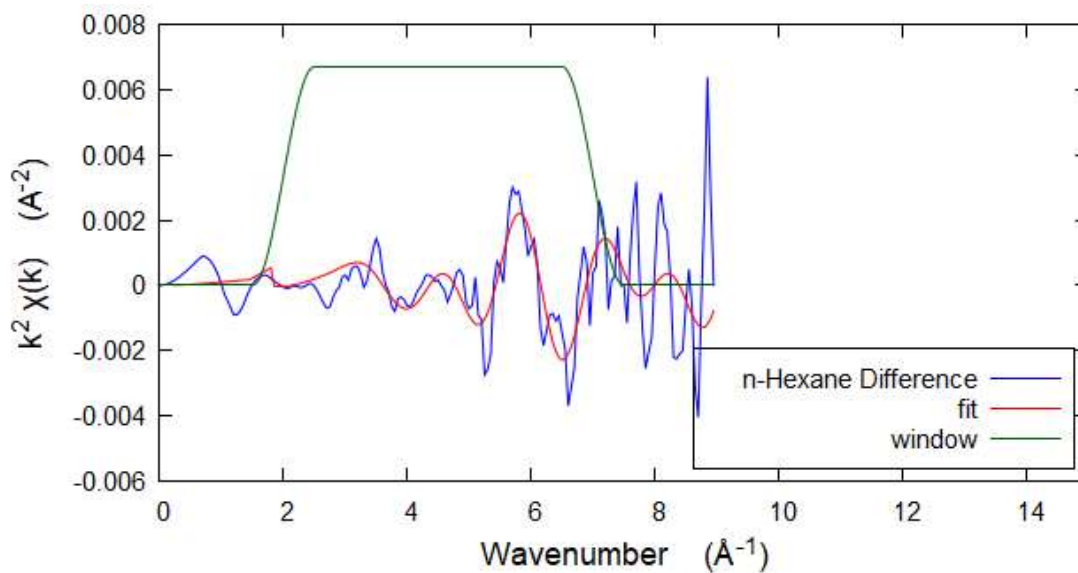


Figure 4.20: k-space spectrum of smoothed n-hexane difference data (blue) and computed fit (red).

Figure 4.19 shows the fit to the derived R-space spectrum of the experiment for  $\text{CpRe}(\text{CO})_3$  photolyzed in n-hexane, observing the 0 to 30  $\mu\text{s}$  timeframe. The quality of the fit is reasonable, although much less accurate than for the parent spectrum fit. This is expected with the vastly reduced signal to noise ratio inherent to the difference data. The shape is

superficially similar to the unexcited state, which is reasonable considering the degree of similarity in the structures of parent and product.

Table 4.3: Derived parameters from fit to difference data for  $\text{CpRe}(\text{CO})_3$  in *n*-hexane for 0 to 30  $\mu\text{s}$ .

Path	Fitted Distance	Computed Distance (M06)	$\Delta R$	Debye-Waller
2 Re-C <sub>CO</sub>	1.94±0.01	1.91	0.03±0.01	0.011±0.027
5 Re-C <sub>C5H5</sub>	2.30±0.17	2.27	0.03±0.17	0.020±0.002
2 Re-O <sub>CO</sub>	3.10±0.01	3.07	0.03±0.01	0.003±0.002
4 Re-C-O <sub>CO</sub>	3.10±0.01	3.07	0.03±0.01	0.003±0.002
2 Re-C-O-C <sub>CO</sub>	3.10±0.01	3.07	0.03±0.01	0.003±0.002
1 Re-C <sub>Hex</sub>	2.61±0.37	2.80/2.84	-0.19/-0.23 ±0.37	0.003±0.002

$E_0 = 18.44$ ,  $S_0^2 = 0.0167$ ,  $k$  weight for fit: 2 ;  $k_{min} = 2.0$ ;  $k_{max} = 7.0$  ;  $R_{min} = 1.35$  ;  $R_{max} = 3.5$ ;  $R$ -factor 0.0133

In Figure 4.20 we can see the smoothed *k*-space data aligns reasonably with the fit. There are significant oscillations in the 5 to 7  $\text{\AA}^{-1}$  region not described by the fit, and a few factors are considered which could explain this.

First is the degree of noise in the system. While this has been mitigated as much as possible by averaging multiple scans collected in sequence and employing other experimental techniques described in chapter 2, noise remains an observably large factor.

As a another possible contribution, while variation in the bond lengths should be accounted for by the Debye Waller factors, but there may be a set of bond length distortions not encapsulated by that factor. However if there were extended C-O bond lengths it would be visible in the IR spectra for the solution, which is not found to be the case, and the fitted Debye Waller factors have tended to smaller values.

As the window these oscillations are seen in is past 5  $\text{\AA}^{-1}$ , i.e. at high frequencies, they would correspond to longer *R*-values beyond the second shell which are beyond the probe limits of our experiment. Thus we can safely attribute them to noise.

Table 4.4: Predicted and experimentally determined bond lengths for Re-alkane bond in  $\text{CpRe}(\text{CO})_2(\text{n-alkane})$ .

Re-C <sub>n-alkane</sub> Length / Å	Alkane / binding carbon	Source
2.61	n-hexane	EXAFS (this work)
2.80	n-hexane / primary	Theory (this work)
2.84	n-hexane / secondary	Theory (this work)
2.60	methane	Ref <sup>31</sup>
2.67	methane	Ref <sup>12</sup>
2.79	ethane	Ref <sup>12</sup>
2.77	propane / primary	Ref <sup>12</sup>
2.77	n-butane / primary	Ref <sup>12</sup>
2.76	n-hexane / primary	Ref <sup>12</sup>
2.76	n-heptane / primary	Ref <sup>12</sup>
2.62	methane	Ref <sup>32</sup>
2.63	n-pentane / primary	Ref <sup>32</sup>
2.68	n-pentane / tertiary	Ref <sup>32</sup>
2.63	n-heptane / primary	Ref <sup>32</sup>
2.70	n-heptane / quaternary	Ref <sup>32</sup>
2.28	Activated n-pentane / primary	Ref <sup>32</sup>
2.30	Activated n-pentane / tertiary	Ref <sup>32</sup>

The fitting results for the Re-C<sub>alkane</sub> bond are compared with both our own calculations and literature computations in Table 4.4. Models from cited literature<sup>12, 31, 32</sup> are all for unactivated bonding, where the C-H moiety remains whole. Cobar et al.<sup>12</sup> describe their predictions as asymmetric  $\eta^2$  bindings. The literature values are consistently longer than our experimental fit, but within error of that value, and we see the best agreement with experiment with a model from Chan et al.<sup>31</sup>, which is for  $\text{CpRe}(\text{CO})_2(\text{methane})$  but performed to a high level of theory. The quoted value is for the derived optimal length from calculations using composite-CCSD(T)/def2-QZVPP, but their work included geometry

optimisations using various DFT basis set method combinations. These results ranged from 2.57 Å to 2.63 Å.

Lu et al. also report Re-C distances for the activated structure of  $\text{CpRe}(\text{CO})_2(\text{H})(\text{n-pentyl})$ , with calculations providing a distance of 2.28 Å for primary-bound and 2.30 Å for tertiary-bound pentane. These values are also within error of our EXAFS fit, but are substantially shorter than them, where other calculated lengths have been found to be longer than our observed distances. This difference is attributed in large part to the lack of dispersion factors included in our own calculations, which are modelled in detail by literature calculations.

Following the observations of Dr Garwood of early-time peak shifts in the TRIR of  $\text{CpRe}(\text{CO})_3$  in n-heptane, the first microsecond of the n-hexane difference data was averaged, processed, and investigated. The reduction in fit quality is attributable to the increased noise from averaging across a smaller time window, but a coherent fit can still be made.

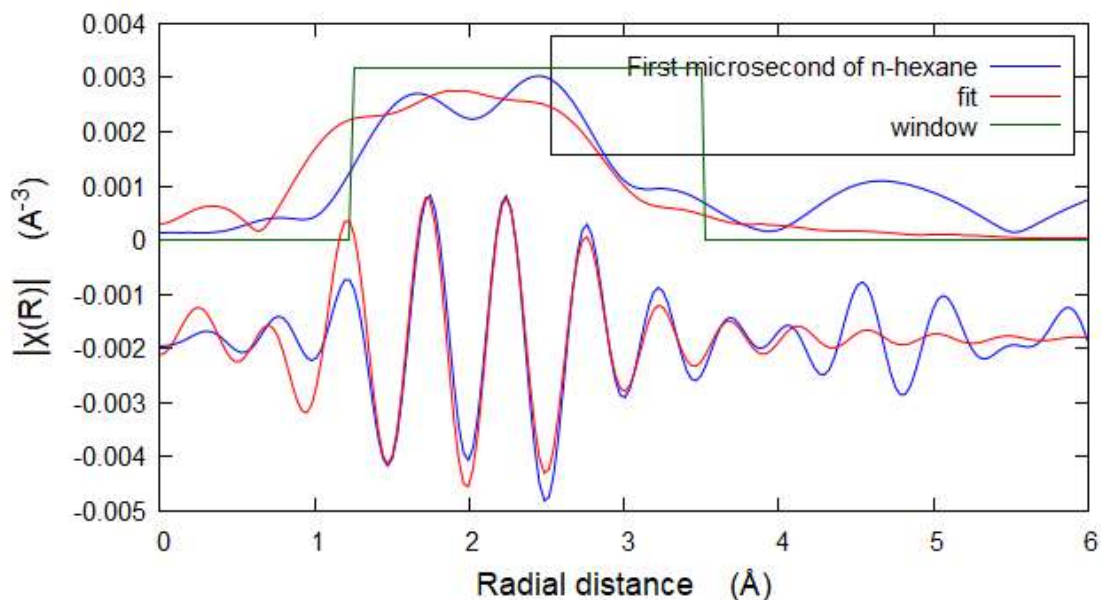


Figure 4.21: R-space difference of  $\text{CpRe}(\text{CO})_3$  in n-hexane for 0 to 1  $\mu\text{s}$  after photolysis.

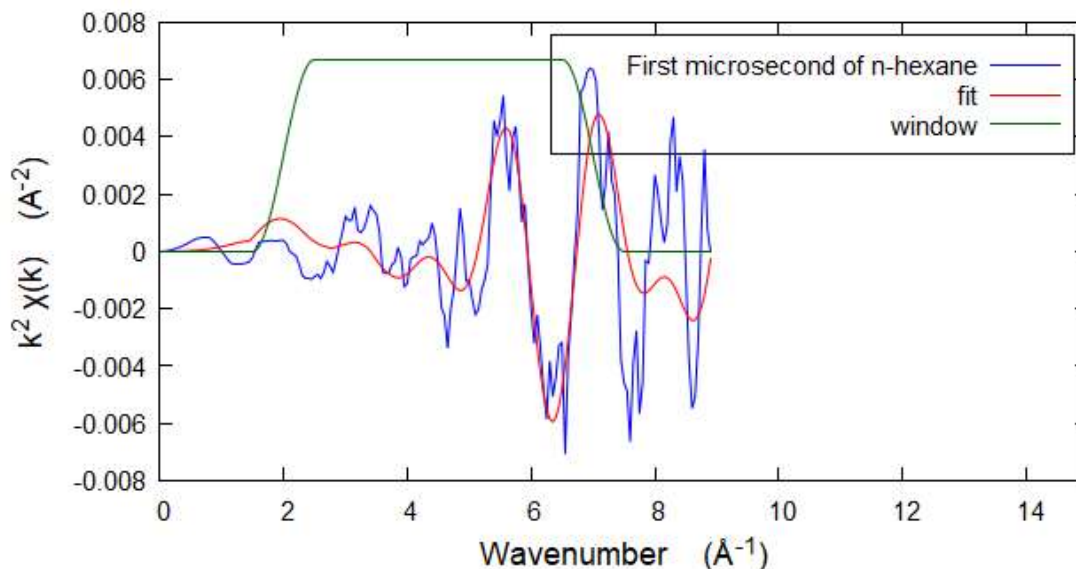


Figure 4.22:  $k$ -space difference spectrum of 0 to 1  $\mu$ s of  $\text{CpRe}(\text{CO})_3$  in  $n$ -hexane.

On visual inspection there is a pronounced difference between the first microsecond in  $R$ -space and the first 10 microseconds seen previously. The double peak feature is still resolved in the  $R$ -space magnitude plot, but shows a significant amount of broadening. This could be attributed to the presence of multiple isomers coexisting in solution in the 0 to 1  $\mu$ s window, but the evidence from TRIR shows no sign of this. Therefore, we cautiously attribute this change to a decrease in the signal to noise ratio for the smaller time window.

Table 4.5: Derived parameters from fit to difference data for  $\text{CpRe}(\text{CO})_3$  in  $n$ -hexane.

Path	Fitted Distance	Computed Distance (M06)	$\Delta R$	Debye-Waller
2 Re-C <sub>CO</sub>	1.96	1.91	0.05	0.002±0.003
5 Re-C <sub>C5H5</sub>	2.33±0.02	2.27	0.06±0.02	0.015±0.005
2 Re-O <sub>CO</sub>	3.03±0.05	3.07	-0.04±0.05	0.002±0.060
4 Re-C-O <sub>CO</sub>	3.03±0.05	3.07	-0.04±0.05	0.002±0.060
2 Re-C-O-C <sub>CO</sub>	3.03±0.05	3.07	-0.04±0.05	0.002±0.060
1 Re-C <sub>Hex</sub>	3.21±1.78	2.80/2.84	0.40/0.44 ±1.78	0.001±0.001

$E_0 = -11.00$ ,  $S_0^2 = 0.00313$ ,  $k$  weight for fit: 2;  $k_{min} = 2.0$ ;  $k_{max} = 7.0$ ;  $R_{min} = 1.35$ ;  $R_{max} = 3.5$ ;  $R$ -factor 0.0421

Table 4.5 shows a fit with a much longer Re-alkane bond length both in comparison to the 0-10  $\mu\text{s}$  fit and the calculated structure, which is in strong agreement with the theory that the rhenium centre is initially approached end-on by the C-H moiety of the alkane before transitioning from this  $\eta^1$  bonding scheme to a more stable  $\eta^2$  3-centre-2-electron configuration.

An improved R-value can be obtained by removing the limit on the rhenium-carbonyl bond length, but this results in a fitted distance of 2.05 Å. Other characterised rhenium carbonyl systems show no distances of this length<sup>33, 34</sup>, so it has been restricted to a more realistic length.

Unfortunately this fit is not of good quality. With error margins too high to be useful and an observably poor fit in Figure 4.21. The observed trend matches well to TRIR observations of the lifetime of the theoretical  $\eta^1$  intermediate at 0.88  $\mu\text{s}$ , but the quality of fit is insufficient to draw any conclusions from this.

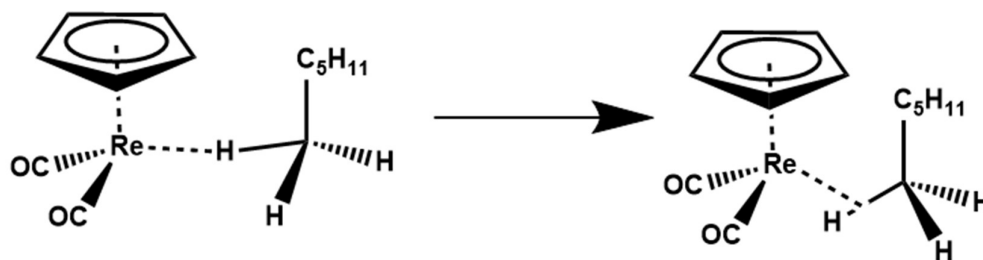


Figure 4.23: Scheme for reconfiguration of  $\text{CpRe}(\text{CO})_2(\text{n-hexane})$  from  $\eta^1$  binding to  $\eta^2$  binding.

#### 4.3.3.3 – EXAFS of $\text{CpRe}(\text{CO})_3$ in cyclohexane

In the photolysis of  $\text{CpRe}(\text{CO})_3$  in cyclohexane we expect to observe the formation of  $\text{CpRe}(\text{CO})_2(\text{cyclohexane})$ . With a cyclic alkane, each carbon is secondary and so any chain-walking effects should not have a significant impact the bond lengths derived from the EXAFS analysis.

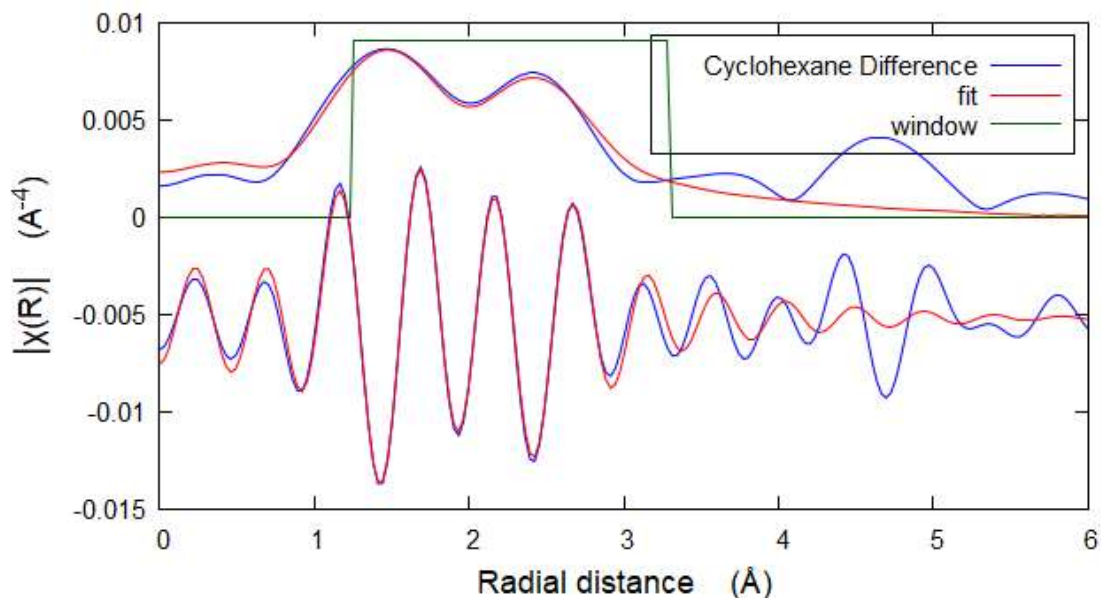


Figure 4.24: R-space fit of computed  $\text{CpRe}(\text{CO})_2(\text{cyclohexane})$  and  $\text{CpRe}(\text{CO})_3$  structures (red) to difference data of  $\text{CpRe}(\text{CO})_3$  photolyzed in neat cyclohexane (blue).

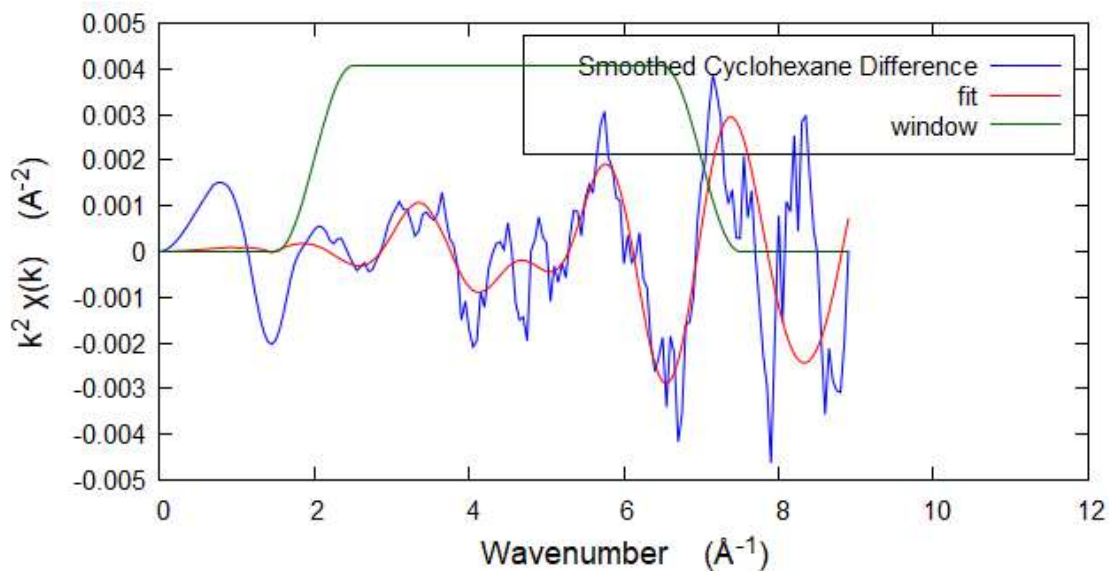


Figure 4.25: k-space fit of computed  $\text{CpRe}(\text{CO})_2(\text{cyclohexane})$  difference (red) overlaid on experimental data (blue).

The R-space and k-space projections of the fit for 0 to 30  $\mu\text{s}$  are shown in Figures 4.24 and 4.25 respectively, and show good qualitative agreement with the experimental data. In the k-space data major oscillations can be seen just above and below 6  $\text{\AA}^{-1}$ . These oscillations

are adhered to by the fit, but the impact of noise is visible, especially at 4-5 Å<sup>-1</sup>. The small oscillation at ~4.7 Å<sup>-1</sup> could be a product of noise or a real structural contribution that the current fit is failing to describe, but as it occurs at high frequency is once again attributed to noise. Given the confidence in the presence of unactivated CpRe(CO)<sub>2</sub>(cyclohexane) only provided by the TRIR data, it seems very likely that this is residual noise.

Table 4.6: Derived parameters from fit to difference data for CpRe(CO)<sub>3</sub> in cyclohexane.

Path	Fitted Distance	Computed Distance (M06)	ΔR	Debye-Waller
2 Re-C <sub>CO</sub>	1.94±0.06	1.90	0.04±0.06	0.005±0.005
5 Re-C <sub>C5H5</sub>	2.22±0.05	2.27	-0.05±0.05	0.005±0.005
2 Re-O <sub>CO</sub>	3.10±0.06	3.07	0.03±0.06	0.000±0.001
4 Re-C-O <sub>CO</sub>	3.10±0.06	3.07	0.03±0.06	0.005±0.005
2 Re-C-O-C <sub>CO</sub>	3.10±0.06	3.07	0.03±0.06	0.005±0.005
1 Re-C <sub>Cy</sub>	2.52±0.11	2.78	-0.26±0.11	0.000±0.001

$E_0 = 16.79$ ,  $S_0^2 = 0.00297$ ,  $k$  weight for fit: 2 ;  $k_{min} = 2.0$ ;  $k_{max} = 7.0$  ;  $R_{min} = 1.35$  ;  $R_{max} = 3.3$ ;  $R$ -factor 0.0105

The fit parameters of the cyclohexane-bound model to the experimental difference data are shown in Table 4.6. The derived path lengths for the carbonyl groups are consistent with computed values and have not changed much compared to the parent species, as expected. The Cp path length is predicted to be longer by the computational prediction, but the experimental value is consistent with lower bounds for bond lengths in similar structures.<sup>30</sup>

Similarly, the fit value of the rhenium-carbon distance for the cyclohexane is smaller than the computed distance. This is less egregious than the difference for the Cp ring as the bond is expected to be less stable and less accurately modelled (especially in light of the importance of the dispersion factor). It is also possible that the path length is shorter than expected as the geometry is conforming more tightly than expected to an η<sup>2</sup> bonding mode rather than η<sup>1</sup>. In this case the C-H bond would rotate to bring the carbon closer to the metal centre than is seen in our computational models. The computed structure shown in

Figure 4.26 displays a Re-H-C configuration that is much closer to a linear arrangement, with a bond angle of  $128.2^\circ$ .

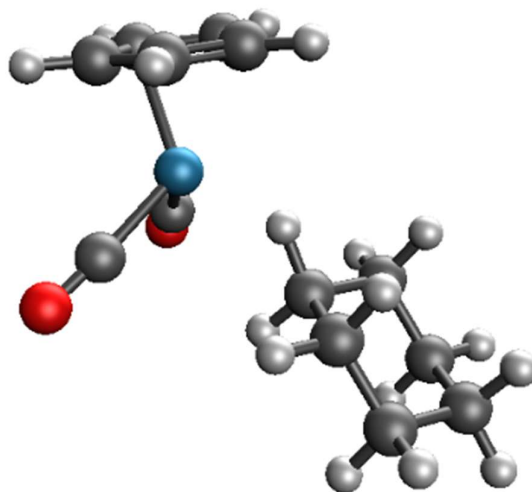


*Figure 4.26: Image of computed geometry of  $\text{CpRe}(\text{CO})_2(\text{cyclohexane})$*

These discrepancies might also be due to noise in the difference data, which is much more significant than in the base EXAFS, which has a much higher signal to noise ratio. This is supported by the R-factor of the fit being an order of magnitude greater compared to the fit of the unphotolyzed spectrum.

Incorrectness from the computational prediction is a given, as the Hamiltonian cannot be solved exactly, but the error is expected to be small with the use of the M06 level of theory, which is reported to be of good quality for evaluating organometallic systems.<sup>35</sup>

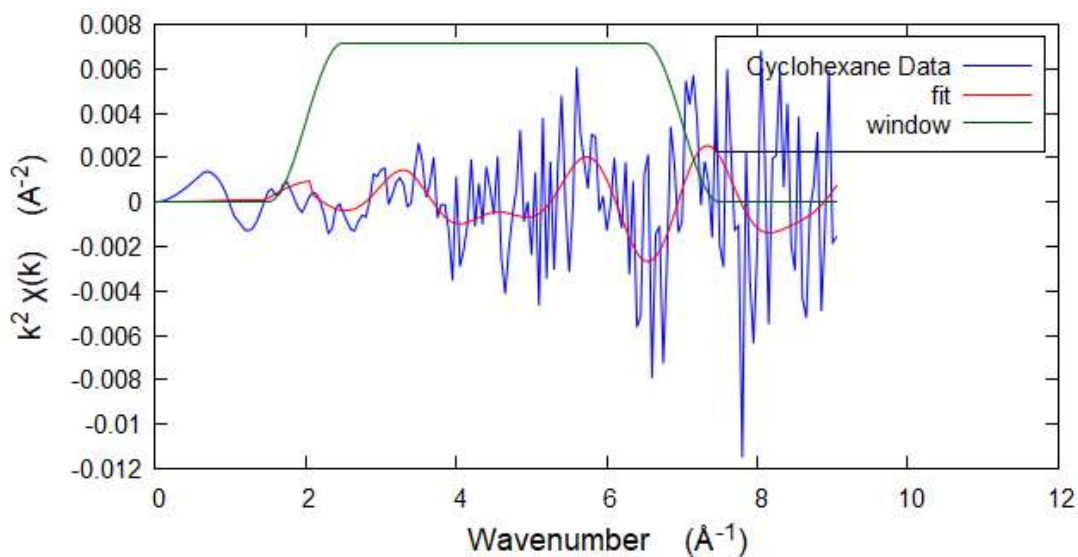


Figure 4.27: Plot of unsmoothed cyclohexane difference data (blue) shown with fit from smoothed data (red).

Figure 4.27 displays the equivalent k-space comparison for the fitting to unsmoothed difference data. The overall trend described by the fit is still visibly similar to the data through the noise, but individual features become much less apparent than in the smoothed version. This gives us confidence that the smoothing process has not led to an unreal fit. Further unsmoothed data figures are provided in Appendix I for comparison.

In a trend consistent with the fit of linear hexane, cyclohexane also shows a drastically shorter  $\text{Re-C}_{\text{alkane}}$  distance than expected when compared to literature predictions.

Table 4.7: Predicted and experimentally determined bond lengths for Re-alkane bond in  $\text{CpRe}(\text{CO})_2(\text{cycloalkane})$ .

Re- $\text{C}_{\text{cycloalkane}}$ Length / Å	Alkane	Source
2.52	cyclohexane	EXAFS (this work)
2.78	cyclohexane	Theory (this work)
2.67	cyclopropane	Ref. <sup>12</sup>
2.77	cyclobutane	Ref. <sup>12</sup>
2.80	cyclopentane	Ref. <sup>12</sup>
2.80	cyclohexane	Ref. <sup>12</sup>

Table 4.7 shows literature computed values are within 0.3 Å of our fitted bond length, although like with the linear fit are consistently longer than the experimental value. As with linear hexane bonding, some of the difference in our calculations appears to be attributable to dispersion factors. Additionally, this bond length is within 0.1 Å compared to its linear alkane equivalent, for experimental results and each set of theoretical calculations. Despite our anticipation of a shorter bond length in the cycloalkane complex, there is insufficient resolution in the data to verify that this is the case.

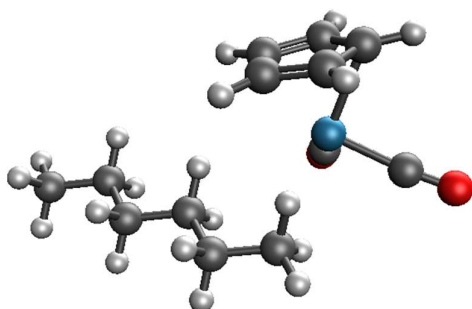


*Figure 4.28: Computed structure of  $\text{CpRe}(\text{CO})_2(\text{n-hexane})$  without dispersion.*

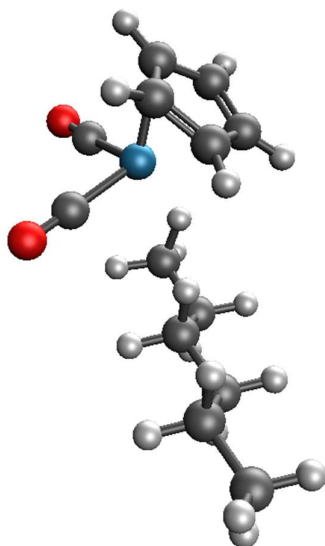


*Figure 4.29: Computed structure of  $\text{CpRe}(\text{CO})_2(\text{n-hexane})$  with dispersion*

We performed new calculations for  $\text{CpRe}(\text{CO})_2(n\text{-hexane})$  with an empirical correction for dispersion and obtained a  $\text{Re-C}_{\text{alkane}}$  bond length of 2.80 Å for primary carbon bonding and 2.81 Å for secondary bonding. Equivalent calculations for  $\text{CpRe}(\text{CO})_2(\text{cyclohexane})$  gave a length of 2.78 Å. These minor to negligible improvements over previous results suggest that computational accuracy in our calculations is not stemming from lack of dispersion corrections, and may require the use of expensive functionals to improve significantly.

#### 4.3.3.4 – EXAFS of $\text{CpRe}(\text{CO})_3$ in triethyl silane

In the photolysis of  $\text{CpRe}(\text{CO})_3$  in triethyl silane, we expect to see a transition from the alkyl-bound product  $\text{CpRe}(\text{CO})_2\text{EtSiH}(\text{Et})_2$  to the silyl-bound product  $\text{CpRe}(\text{CO})_2(\text{HSiEt}_3)$ , as proposed by Yang et al<sup>22</sup> and supported by further investigations described in Section 4.3.1, above. The activation of the Si-H bond in the product is not well-defined, but may be elucidated by EXAFS analysis.

As previous work in this chapter has shown, there are two timescales on which this transition occurs; a direct solvation of the unsaturated  $\text{CpRe}(\text{CO})_2$  complex via the Si-H moiety with a lifetime of 11.7 microseconds, and a solvation by the ethyl chain which reforms to the silyl-bound isomer with a lifetime of 1.4 microseconds. In order to extract difference spectra showing the presence of both alkyl-bound and silyl-bound product, the difference data was averaged in 2 separate sections: an early difference taking data from 0 to 10 μs post photolysis, and a late difference taking data from 10 to 30 μs post photolysis.

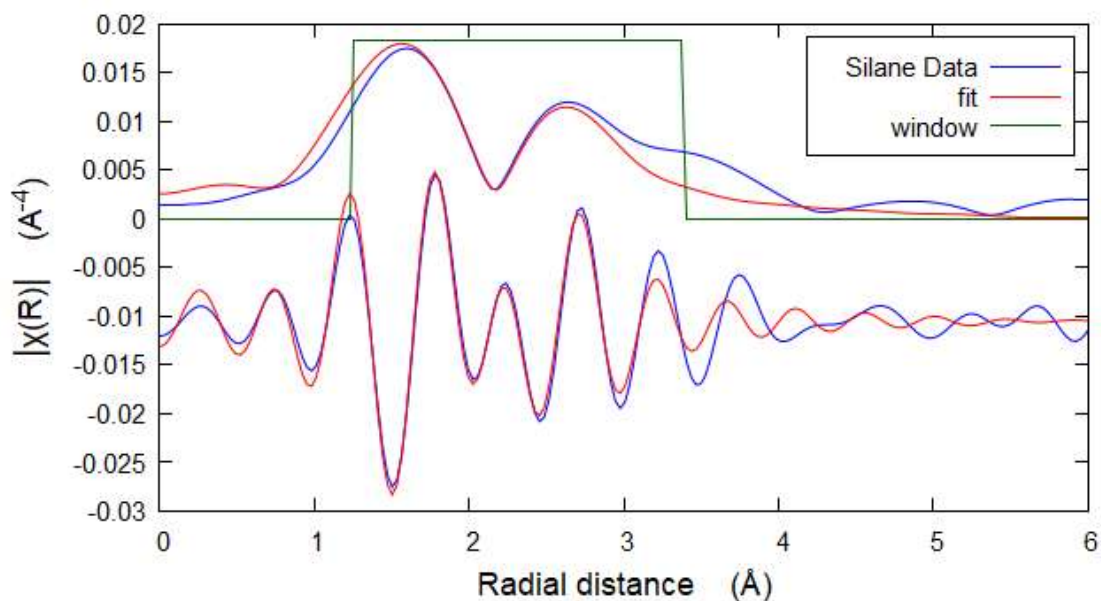


Figure 4.30: R-space plot showing fit of  $\text{CpRe}(\text{CO})_2(\text{Et}_3\text{SiH})$  paths (red) to experimental data from 0 to 10  $\mu\text{s}$  post photolysis (blue). Fitting was optimised for the region of 1.25 to 3.50  $\text{\AA}$  shown as the window (green).

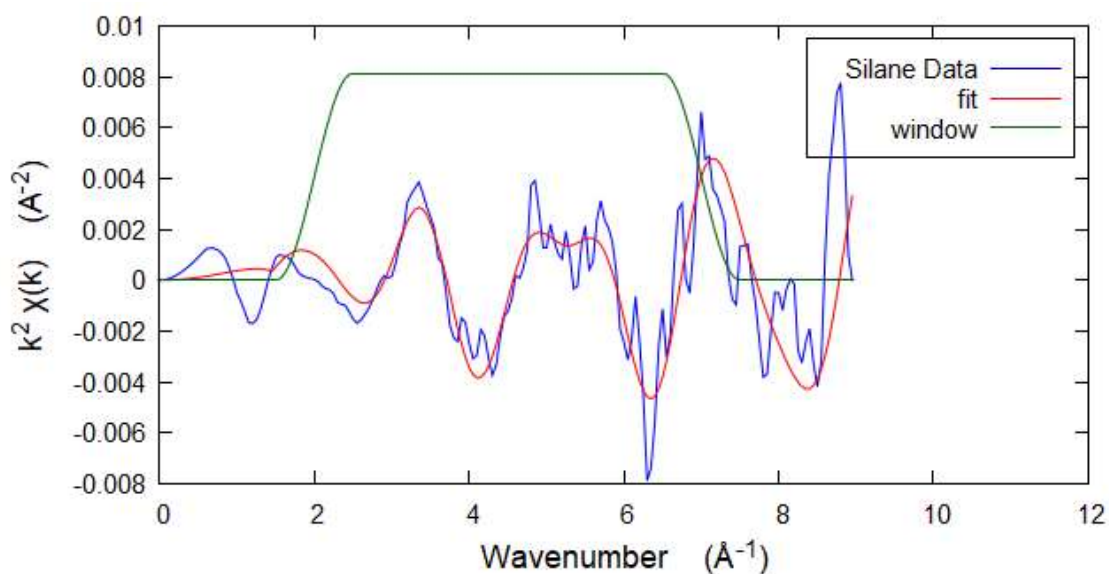


Figure 4.31: k-space spectrum of fit of  $\text{CpRe}(\text{CO})_2(\text{Et}_3\text{SiH})$  paths (red) to experimental data from 0 to 10  $\mu\text{s}$  post photolysis (blue).

The fitting of the 0 to 10  $\mu\text{s}$  data to an ethyl-bound structure is shown in Figures 4.30 and 4.31, with associated parameters in Table 4.8. The scattering of the secondary carbon from the ethyl chain is included as a factor due to its proximity to the edge of the fit window, and

the Re-C<sub>CO</sub> distance has been fixed to prevent adjustment to an unreasonable length, as has been explained in the fitting of n-hexane.

Table 4.8: Derived parameters from fit to difference data for CpRe(CO)<sub>3</sub> in triethyl silane for 0 to 10 μs post photolysis.

Path	Fitted Distance	Computed Distance	ΔR	Debye-Waller
2 Re-C <sub>CO</sub>	1.96	1.90	0.05	0.005±0.004
5 Re-C <sub>C5H5</sub>	2.30±0.04	2.31	0.01±0.04	0.017±0.006
1 Re-C <sub>Et</sub>	2.81±0.14	2.72	0.09±0.14	0.001±0.001
2 Re-O <sub>CO</sub>	3.04±0.03	3.07	0.03±0.03	0.005±0.004
4 Re-C-O <sub>CO</sub>	3.04±0.03	3.07	0.03±0.03	0.005±0.004
2 Re-C-O-C <sub>CO</sub>	3.05±0.03	3.07	0.02±0.03	0.005±0.004
1 Re-C <sub>Et'</sub>	3.58±0.14	3.51	0.07±0.14	0.001±0.001

$E_0 = -25.11$ ,  $S_0^2 = 0.00659$ ,  $k$  weight for fit: 2;  $k_{min} = 2$ ;  $k_{max} = 7.5$ ;  $R_{min} = 1.25$ ;  $R_{max} = 3.5$ ;  $R$ -factor 0.0196

In this case we see good agreement between the computed values and the experimental fit, with the R-factor being higher than previous fits but not entirely unreasonable. The computed values are consistently lower than fitted values, with the deviations being less than 0.15 Å. Of significant interest is the deviation in the rhenium-triethyl silane distances, which are slightly larger than for the more established carbonyl and Cp distances. This is in contrast to the comparisons of other rhenium-alkyl lengths, which have been shorter than expected from our own calculations.

There are a few potential explanations for this discrepancy. Firstly, the presence of the silane-bound species has a noticeable effect on the XANES, and so the signal from the alkyl bound species may be distorted by the similar structure of the silyl-bound complex, with the determination of the Re-C<sub>alkane</sub> bond being affected by the Re-Si bond.

Secondly, there could be a difference in the alkyl binding mode, where the Re-ethyl configuration is strictly  $\eta^1$  in nature, with the reconfiguration to a silyl-bound complex happening in place of any shift to an  $\eta^2$  configuration. This seems unlikely as evidence for

the  $\eta^1$  to  $\eta^2$  shift implies that it occurs within a couple of microseconds, and is a transition with almost no barrier to overcome.

Finally it is possible that the silane data's higher quality allows for a more accurate assignment of the bond length. While the silane and n-hexane results have overlapping errors, the cyclohexane error is much smaller and does not overlap with the silane result. Overall the first possibility, that the silyl-bound signal is already great enough in this window to distort the signal, seems like the most likely explanation.

The 0 to 10  $\mu\text{s}$  data was also fitted to the silane-bound geometry, to compare to the expected primary ethyl-bound product. The resulting fit is shown in Figures 4.32 and 4.33, with associated parameters for the fit presented in Table 4.9.

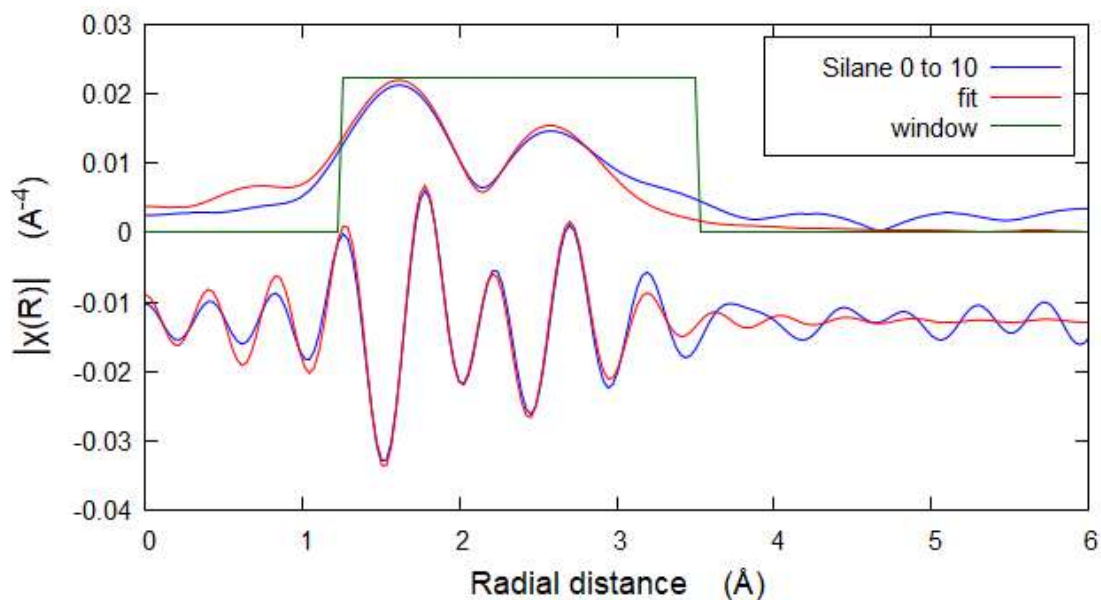


Figure 4.32: R-space plot showing fit of  $\text{CpRe}(\text{CO})_2(\text{HSiEt}_3)$  paths (red) to experimental data from 0 to 10  $\mu\text{s}$  post photolysis (blue).

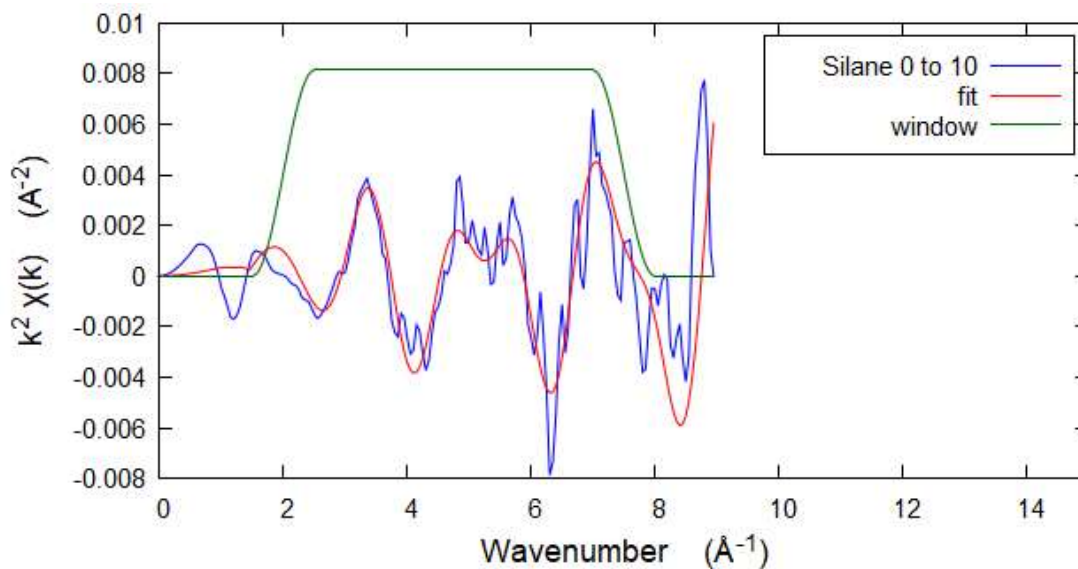


Figure 4.33: *k*-space plot showing fit of  $\text{CpRe}(\text{CO})_2(\text{HSiEt}_3)$  paths (red) to experimental data from 0 to 10  $\mu\text{s}$  post photolysis (blue).

Table 4.9: Derived parameters from fit to difference data for  $\text{CpRe}(\text{CO})_3$  in triethyl silane for 0 to 10  $\mu\text{s}$  post photolysis.

Path	Fitted Distance	Computed Distance	$\Delta R$	Debye-Waller
2 Re-C <sub>CO</sub>	1.97	1.91	0.06	0.001±0.005
5 Re-C <sub>C5H5</sub>	2.27±0.01	2.33	0.06±0.01	0.008±0.005
1 Re-Si	2.45±0.05	2.47	0.02±0.05	0.002±0.009
2 Re-O <sub>CO</sub>	3.01±0.01	3.07	0.06±0.01	0.003±0.002
4 Re-C-O <sub>CO</sub>	3.01±0.01	3.07	0.06±0.01	0.003±0.002
2 Re-C-O-C <sub>CO</sub>	3.01±0.01	3.07	0.06±0.01	0.003±0.002
3 Re-C <sub>Si</sub>	3.57±0.05	3.59	0.02±0.05	0.002±0.009

$E_0 = -28.86$ ,  $S_0^2 = 0.00683$ , *k* weight for fit: 2 ;  $k_{min} = 2$ ;  $k_{max} = 7.5$  ;  $R_{min} = 1.25$  ;  $R_{max} = 3.5$  ; *R*-factor 0.0257

In this case the theoretical calculations show decent agreement with the fit, although the errors on the Cp ring and CO lengths are smaller than the calculations' divergence from the fit. In this case restrictions have been placed on the lengths to prevent unfeasible results, as without them the Cp ring distance tends to 2.20 and the Re-O lengths to 2.97, both far smaller than is reasonable for such a bond length.

The computed Re-silane lengths are almost entirely accurate to the fitted values however, which provides more evidence that the silane signal is a heavy influence in this early timeframe.

The first microsecond of the data was investigated to see if it offered more insight into the early timeframe bonding in the solution, with a fit to the alkyl-bound isomer calculated.

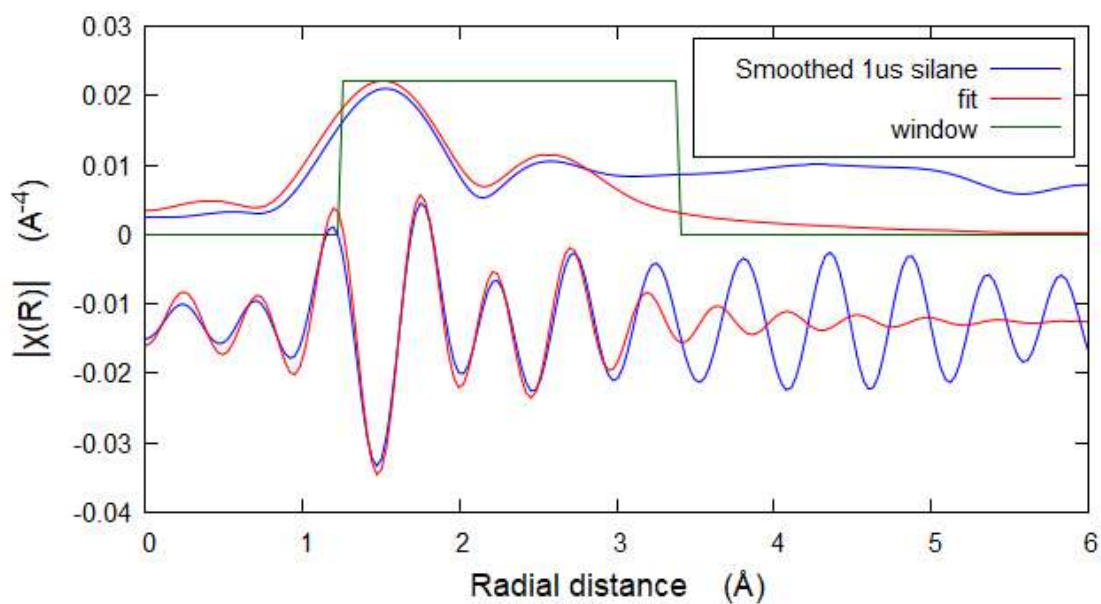


Figure 4.34: R-space fit of computed  $\text{CpRe}(\text{CO})_2(\text{Et}_3\text{SiH})$  and  $\text{CpRe}(\text{CO})_3$  structures (red) to difference data of  $\text{CpRe}(\text{CO})_3$  photolyzed in neat triethyl silane from 0 to 1  $\mu\text{s}$  (blue).

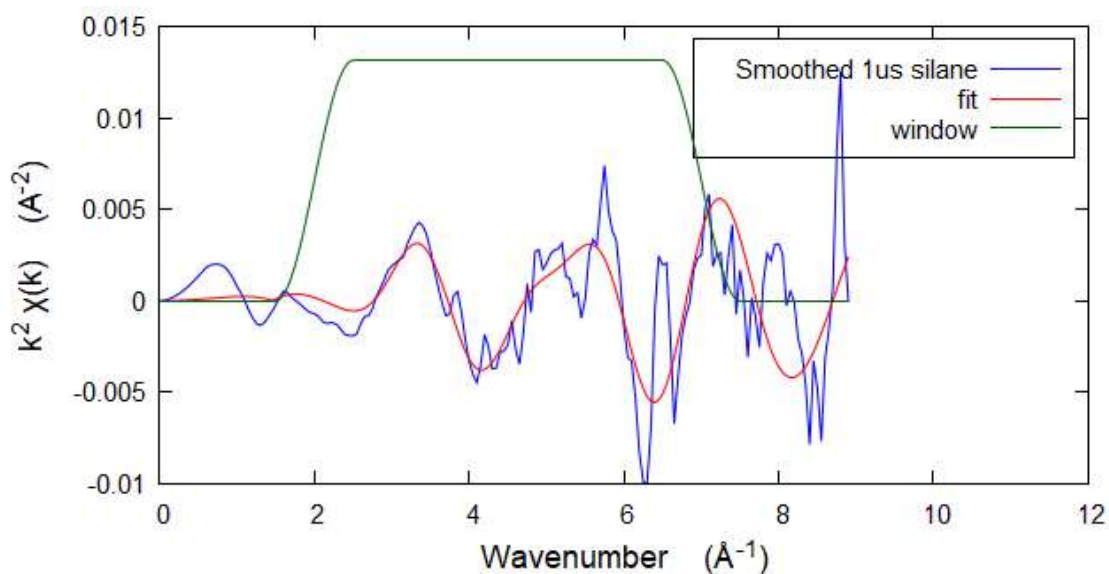


Figure 4.35: *k*-space fit of computed  $\text{CpRe}(\text{CO})_2(\text{Et}_3\text{SiH})$  and  $\text{CpRe}(\text{CO})_3$  structures (red) to difference data of  $\text{CpRe}(\text{CO})_3$  photolyzed in neat triethyl silane from 0 to 1  $\mu\text{s}$  (blue).

The fit shows reasonable correctness to the experimental data in the region of interest, which is appreciable given it comes from a data sample an order of magnitude smaller than for the 0 to 10  $\mu\text{s}$  fit.

Table 4.10: Derived parameters from fit to difference data for  $\text{CpRe}(\text{CO})_3$  in triethyl silane for 0 to 1  $\mu\text{s}$  post photolysis.

Path	Fitted Distance	Computed Distance	$\Delta R$	Debye-Waller
2 Re-C <sub>CO</sub>	1.96±0.00	1.90	0.06±0.00	0.008±0.009
5 Re-C <sub>C5H5</sub>	2.29±0.05	2.31	0.02±0.05	0.006±0.007
1 Re-C <sub>Et</sub>	2.86±0.32	2.72	0.14±0.32	0.001±0.001
2 Re-O <sub>CO</sub>	3.12±0.00	3.07	0.05±0.00	0.001±0.001
4 Re-C-O <sub>CO</sub>	3.12±0.00	3.07	0.05±0.00	0.008±0.001
2 Re-C-O-C <sub>CO</sub>	3.12±0.00	3.07	0.05±0.00	0.008±0.001
1 Re-C <sub>Et'</sub>	3.63±0.32	3.51	0.12±0.32	0.001±0.001

$E_0 = -24.14$ ,  $S_0^2 = 0.00457$ , *k* weight for fit: 2;  $k_{\min} = 2$ ;  $k_{\max} = 7.5$ ;  $R_{\min} = 1.25$ ;  $R_{\max} = 3.5$ ; *R*-factor 0.0484

There is a notable difference in the Re-C<sub>alkyl</sub> bond length arising from the silane data compared to the n-hexane and cyclohexane data. In order to investigate this the silane data was refitted with the Re-C<sub>alkyl</sub> length fixed at 2.57 Å and the n-hexane data was refitted with the equivalent bond length fixed at 2.86 Å.

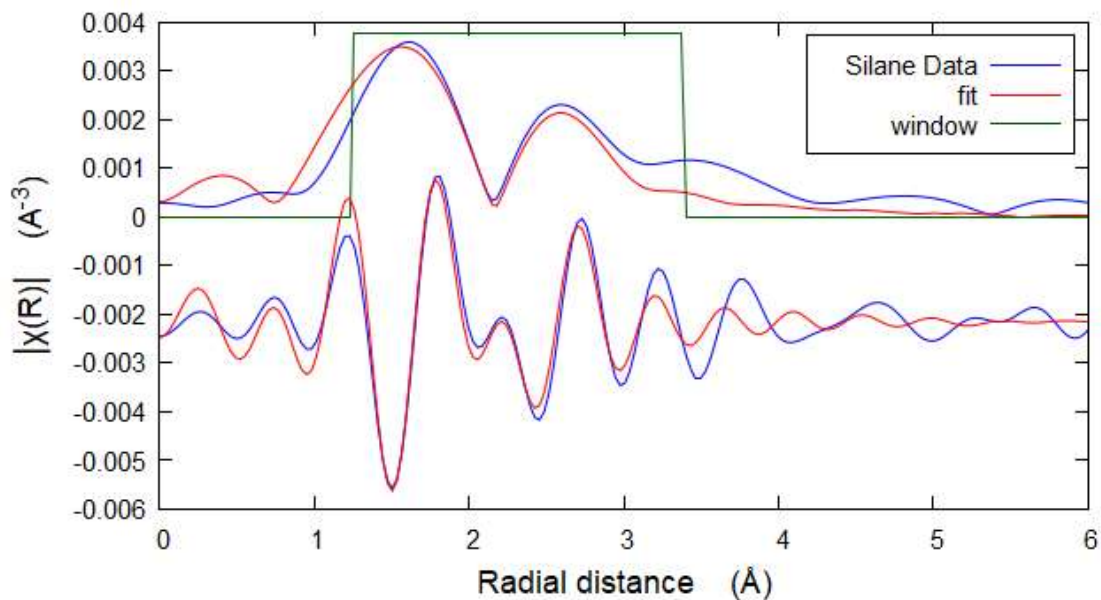


Figure 4.36: Fit of 0 to 10  $\mu$ s data for  $\text{CpRe}(\text{CO})_3$  in triethyl silane with Re-C distance fixed to 2.57 Å

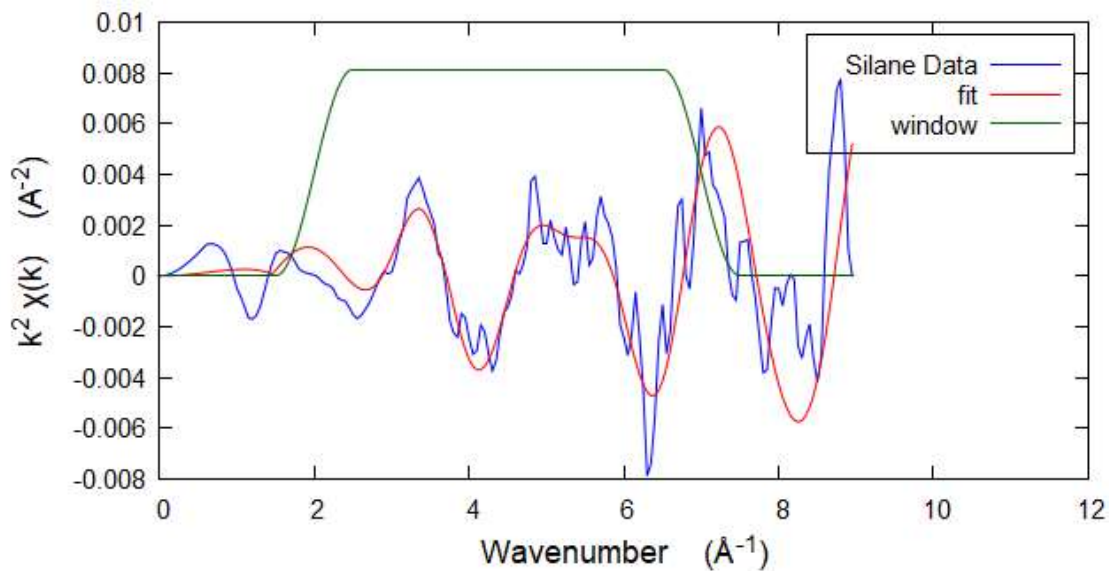


Figure 4.37: : Fit of 0 to 10  $\mu$ s data for  $\text{CpRe}(\text{CO})_3$  in triethyl silane with Re-C distance fixed to 2.57 Å

Table 4.11: Derived parameters from fit to difference data for  $\text{CpRe}(\text{CO})_3$  in triethyl silane for 0 to 10  $\mu\text{s}$  post photolysis with fixed  $\text{Re-C}_{\text{ethyl}}$  length.

Path	Fitted Distance	Computed Distance	$\Delta R$	Debye-Waller
2 Re-C <sub>CO</sub>	1.96	1.90	0.06	0.003±0.002
5 Re-C <sub>C<sub>5</sub>H<sub>5</sub></sub>	2.29±0.04	2.31	0.02±0.04	0.012±0.005
1 Re-C <sub>Et</sub>	2.57	2.72	0.14	0.020±0.001
2 Re-O <sub>CO</sub>	3.05±0.01	3.07	0.02±0.01	0.001±0.001
4 Re-C-O <sub>CO</sub>	3.05±0.01	3.07	0.02±0.01	0.003±0.002
2 Re-C-O-C <sub>CO</sub>	3.05±0.01	3.07	0.02±0.01	0.003±0.002
1 Re-C <sub>Et'</sub>	3.35	3.51	0.16	0.020±0.001

$E_0 = -25.13$ ,  $S_0^2 = 0.0391$ ,  $k$  weight for fit: 2 ;  $k_{\text{min}} = 2$ ;  $k_{\text{max}} = 7.5$ ;  $R_{\text{min}} = 1.25$ ;  $R_{\text{max}} = 3.5$ ;  $R$ -factor 0.0391

The fit is substantially worsened by this restriction, with the  $R$  value increasing from 0.0159 to 0.0391.

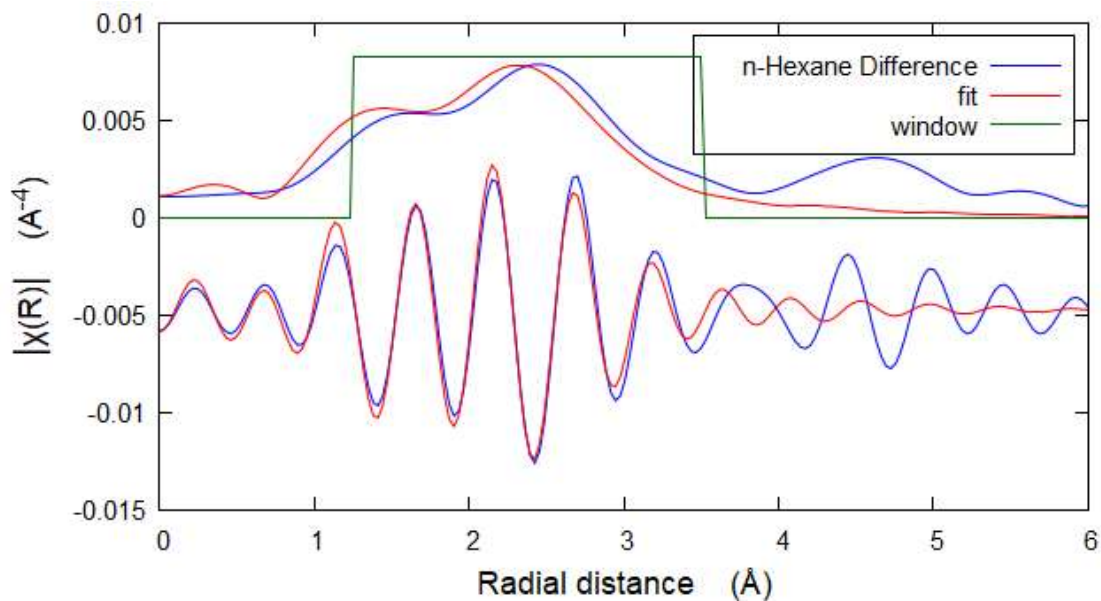


Figure 4.38:  $R$ -space fit of computed  $\text{CpRe}(\text{CO})_2(\text{n-hexane})$  and  $\text{CpRe}(\text{CO})_3$  structures with fixed  $\text{Re-C}_{\text{cyhex}}$  bond length (red) to difference data of  $\text{CpRe}(\text{CO})_3$  photolyzed in neat  $n$ -hexane from 0 to 30  $\mu\text{s}$  (blue).

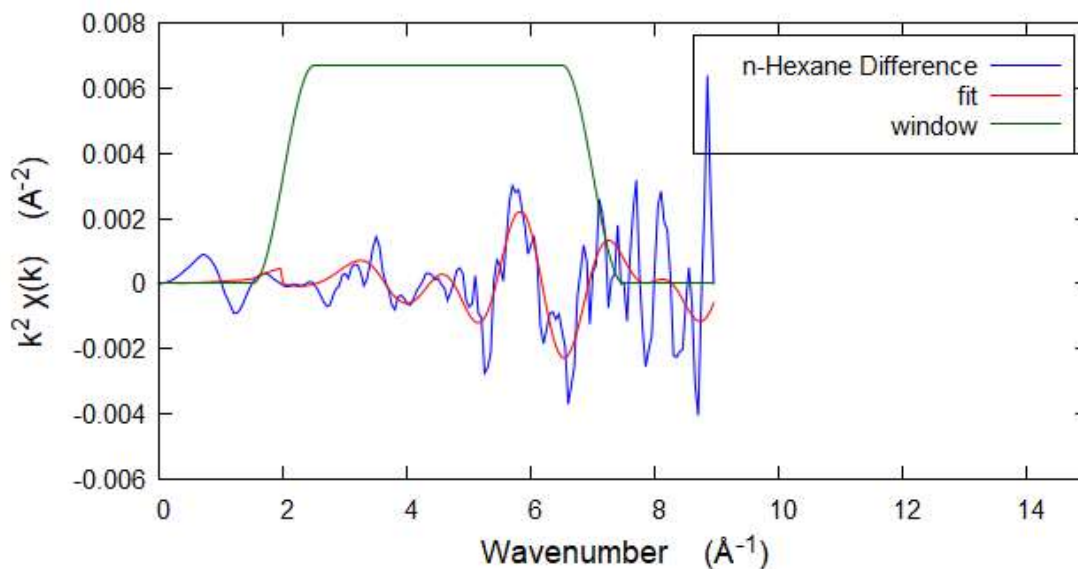


Figure 4.39: *k*-space fit of computed  $\text{CpRe}(\text{CO})_2(\text{n-hexane})$  and  $\text{CpRe}(\text{CO})_3$  structures with fixed  $\text{Re-C}_{\text{cyhex}}$  bond length (red) to difference data of  $\text{CpRe}(\text{CO})_3$  photolyzed in neat *n*-hexane from 0 to 30  $\mu\text{s}$  (blue).

Table 4.12: Derived parameters from fit to difference data for  $\text{CpRe}(\text{CO})_3$  in *n*-hexane with fixed  $\text{Re-C}_{\text{hex}}$  length.

Path	Fitted Distance	Computed Distance (M06)	$\Delta R$	Debye-Waller
2 Re-C <sub>CO</sub>	1.94±0.00	1.91	0.03	0.004±0.026
5 Re-C <sub>C5H5</sub>	2.33±0.22	2.27	0.06	0.020±0.003
2 Re-O <sub>CO</sub>	3.12±0.00	3.07	0.05	0.002±0.003
4 Re-C-O <sub>CO</sub>	3.12±0.00	3.07	0.05	0.002±0.003
2 Re-C-O-C <sub>CO</sub>	3.12±0.00	3.07	0.05	0.002±0.003
1 Re-C <sub>Hex</sub>	2.85	2.80/2.84	0.05/0.09	0.011±0.189

$E_0 = 14.72$ ,  $S_0^2 = 0.00123$ , *k* weight for fit: 2 ;  $k_{\text{min}} = 2.0$ ;  $k_{\text{max}} = 7.0$  ;  $R_{\text{min}} = 1.35$  ;  $R_{\text{max}} = 3.5$ ; *R*-factor 0.0378

Similarly attempting to force the *n*-hexane data to conform to a longer Re-C bond length results in a poorer fit, increasing *R* from 0.0133 to 0.0378.

The 10 to 30 microsecond window was fitted in order to determine the late timeframe behaviour of the solution, in which the silane bound complex was expected to be the dominant intermediate.

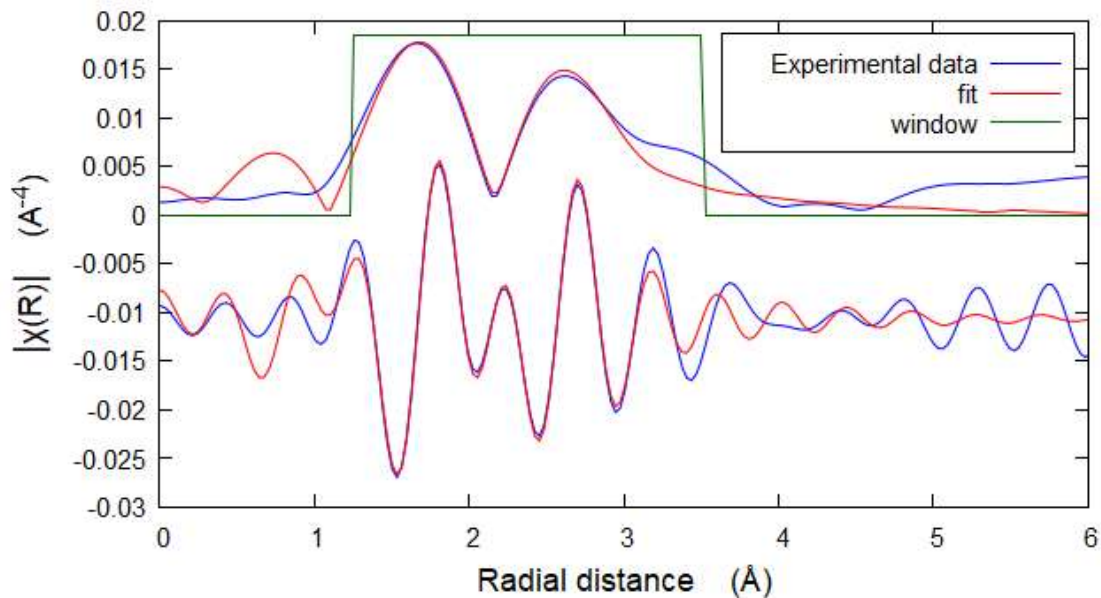


Figure 4.40: R-space plot of fit of  $\text{CpRe}(\text{CO})_2(\text{HSiEt}_3)$  computed paths to difference data for 10 to 30  $\mu\text{s}$  post photolysis of  $\text{CpRe}(\text{CO})_3$  in triethyl silane.

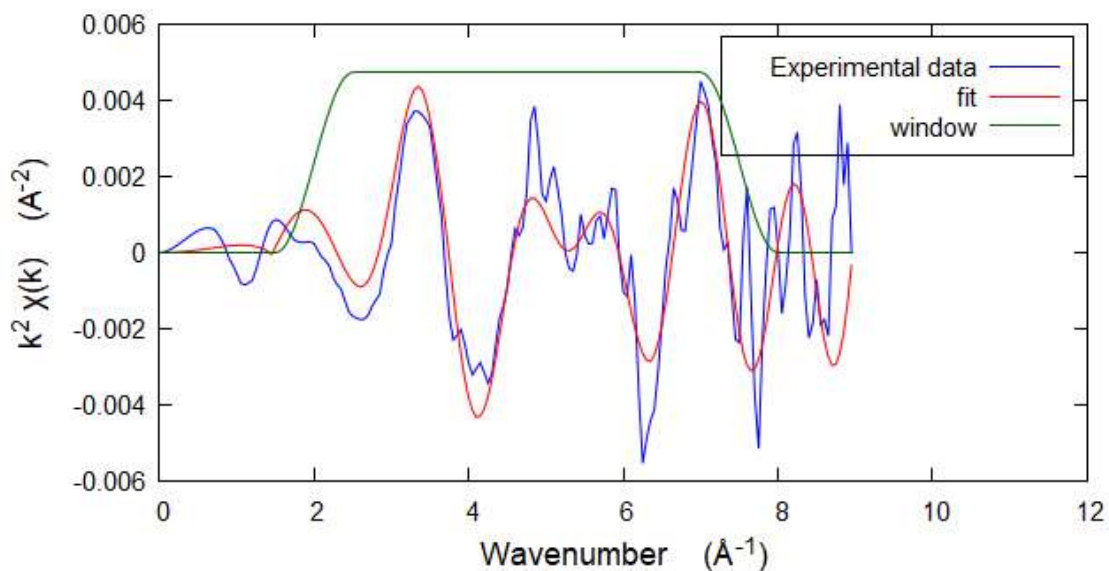


Figure 4.41: k-space plot of fit of  $\text{CpRe}(\text{CO})_2(\text{HSiEt}_3)$  computed paths to difference data for 10 to 30  $\mu\text{s}$  post photolysis of  $\text{CpRe}(\text{CO})_3$  in triethyl silane.

Figures 4.40 and 4.41 show the fitting for the later post-photolysis difference. In this case the transform from the experimental data is very similar to the earlier difference, with some change in the relative intensities of the peaks.

Table 4.13: Derived parameters from fit to difference data for  $\text{CpRe}(\text{CO})_3$  in triethyl silane for 10 to 30  $\mu\text{s}$  post photolysis.

Path	Fitted Distance	Computed Distance	$\Delta R$	Debye-Waller
<b>2 Re-C<sub>CO</sub></b>	1.97	1.91	0.06	0.002±0.005
<b>5 Re-C<sub>C5H5</sub></b>	2.27±0.01	2.33	0.06±0.01	0.010±0.005
<b>1 Re-Si</b>	2.42±0.05	2.47	0.05±0.05	0.001±0.002
<b>2 Re-O<sub>CO</sub></b>	3.01±0.01	3.07	0.06±0.01	0.002±0.002
<b>4 Re-C-O<sub>CO</sub></b>	3.01±0.01	3.07	0.06±0.01	0.002±0.002
<b>2 Re-C-O-C<sub>CO</sub></b>	3.01±0.01	3.07	0.06±0.01	0.002±0.002
<b>3 Re-C<sub>Si</sub></b>	3.55±0.05	3.59	0.04±0.05	0.001±0.002

$E_0 = -28.86$ ,  $S_0^2 = 0.00683$ ,  $k$  weight for fit: 2 ;  $k_{min} = 2$ ;  $k_{max} = 7.5$  ;  $R_{min} = 1.25$  ;  $R_{max} = 3.5$ ; R-factor 0.0316

While the R-factor is improved compared to the early time fit, there is a significant difference between the computed distances of the triethyl silane atoms and the fitted distances, shown in Table 4.13. The difference between the model and experiment might be attributable to  $\eta^2$  bonding, as is theorised to be a factor in the analysis of cyclohexane.

The signal to noise as a factor in both silane fits is supported by the improvement in R-factor from the early average, which covers a smaller time period and thus less data than the later average. However, in each case the fitting has been performed by assuming a single product species is the majority contributor to the difference. In reality each time interval is expected to contain a proportion of both silyl-bound and alkyl-bound  $\text{CpRe}(\text{CO})_2(\text{triethyl silane})$ .

Table 4.14: Predicted and experimentally determined bond lengths for Re-Si bond in  $\text{CpRe}(\text{CO})_2(\text{SiHEt}_3)$ .

Re-Si Length / Å	Details	Source
2.45	0 to 10 $\mu\text{s}$	EXAFS (this work)
2.42	10 to 30 $\mu\text{s}$	EXAFS (this work)
3.00	Unactivated	Theory (this work)
2.57	Activated	Theory (this work)
2.58	Unactivated	Ref <sup>23</sup>
2.56	Partially Activated	Ref <sup>23</sup>
2.51	Activated	Ref <sup>23</sup>

Our experimental results are consistent with the CAS(14,13)/Def2-SVPD geometries computed by Zhang and Su, although the relative accuracy of the measurements is not great enough to determine the activation of the complex. The experimentally determined Re-Si bond length appears to be significantly shorter than predictions for the unactivated structure and closer to the prediction for the activated complex, indicating that some degree of activation is occurring. Consistently with our results for Re-C<sub>alkane</sub> bonding in *n*-hexane and cyclohexane, the lengths from computed values seem to be consistently longer than the experimental results. Determining any change in Re-Si length with time is complicated by the presence of the alkyl-bound isomer.

#### 4.3.3.5 – Linear Combination Fitting of $\text{CpRe}(\text{CO})_3$ in triethyl silane

Athena was used to generate a linear combination fit of a late-time silane curve and the alkane-bound data for cyclohexane to try and establish a progression from alkane-bound to silane-bound. The results are shown below in Figures 4.42 and 4.43. A 35 to 45  $\mu\text{s}$  average of the silane difference data was used as a base silane-bound spectrum. The cyclohexane data was shifted manually to align its post edge structure with the baseline observed in silane. The fit was performed in the range of 0 to 70 eV above the edge.

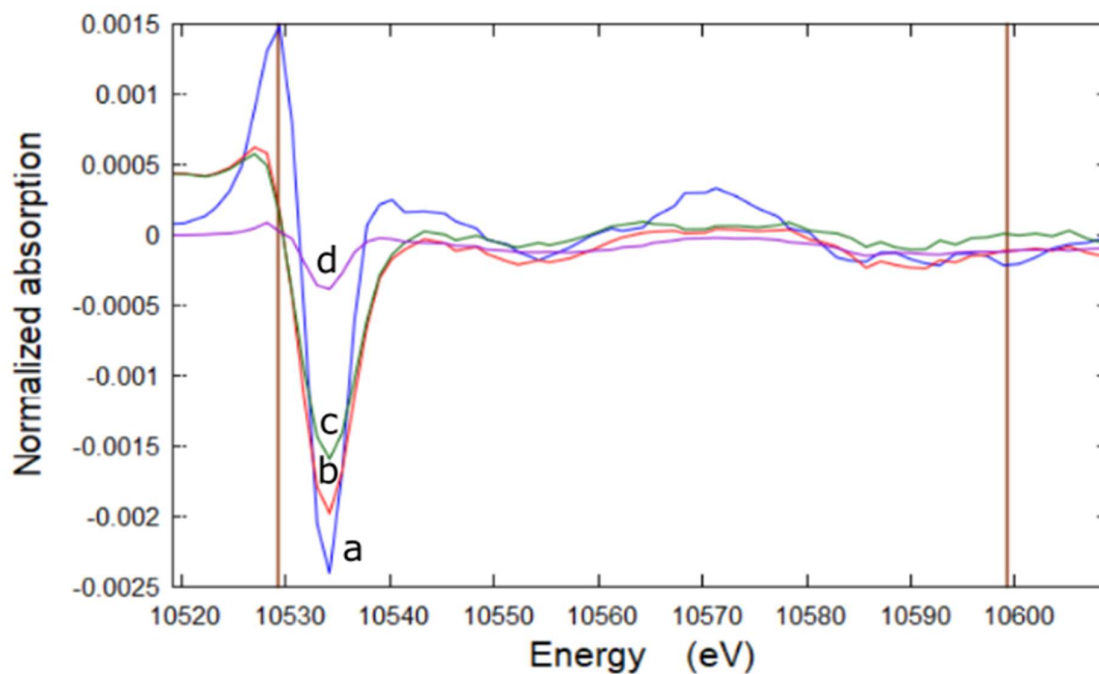


Figure 4.42: Linear combination of fits for difference data from 0 to 10  $\mu$ s in triethyl silane, showing 0-10  $\mu$ s triethyl silane data (a, blue), the LCF fit (b, red), the cyclohexane data (c, green), and the 35-45  $\mu$ s triethyl silane data (d, purple).

For the 0 to 10 microsecond window, a ratio of 0.165 silane to 0.835 alkane was calculated. This is in decent agreement with the prediction of a 0.25 to 0.75 initial ratio of silane to alkane photoproduct, although we can see in Figure 4.40 that the resulting spectrum is not similar to the experimental data.

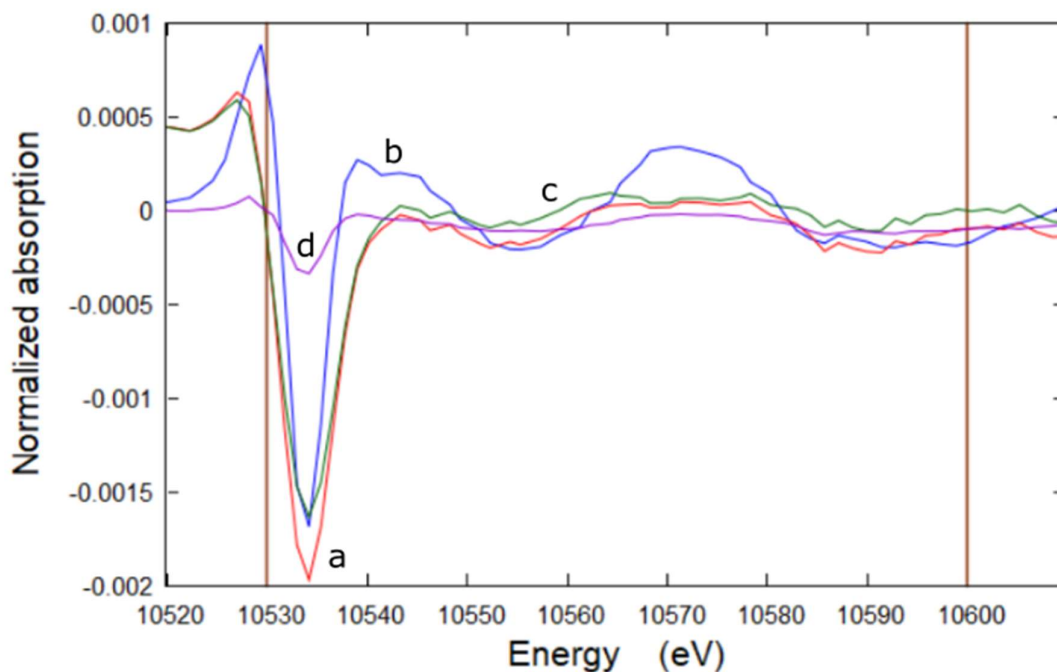


Figure 4.43: Linear combination of fits for difference data from 10 to 30  $\mu$ s in triethyl silane, showing 10-30  $\mu$ s triethyl silane data (a, red), the LCF fit (b, blue), the cyclohexane data (c, green), and the 35-45  $\mu$ s triethyl silane data (d, purple).

For 10 to 30 microseconds, a ratio of 0.143 silane to 0.857 alkane is calculated. This is in poor agreement with the rate of silane complex formation predicted by TRIR. As with EXAFS analysis, it appears that the triethyl silane signal obscures the cyclohexane signal from the earliest timeframes, preventing effective time-resolved analysis. Nonetheless it seems likely that a system with more comparable photoproducts could be analysed more effectively with this method.

#### 4.4 – Conclusions

The kinetics of the reaction of  $\text{CpRe}(\text{CO})_3$  with triethyl silane following photolysis of the solution have been investigated in *n*-heptane doped with triethyl silane and neat triethyl silane. TRIR investigation has shown that for  $\text{CpRe}(\text{CO})_3$  in *n*-heptane doped with triethyl silane there is formation of at least two distinct species, and has allowed us to chart the

dependence of the rate of formation of  $\text{CpRe}(\text{CO})_2(\text{HSiEt}_3)$  on the concentration of triethyl silane.

TRXAS investigations have determined the length of the rhenium-carbon bond in  $\text{CpRe}(\text{CO})_2(\text{n-hexane})$  as  $2.61 \pm 0.37 \text{ \AA}$ , and the equivalent bond length in  $\text{CpRe}(\text{CO})_2(\text{cyclohexane})$  as  $2.52 \pm 0.11 \text{ \AA}$ . These values are within error of theoretical models and constitute some of the first experimentally determined values for rhenium-alkane bond lengths.

TRXAS investigations of  $\text{CpRe}(\text{CO})_3$  in neat triethyl silane were used to determine the Re-Si bond length, with a length of  $2.45 \pm 0.05 \text{ \AA}$  for the 0 to 10  $\mu\text{s}$  timeframe and a length of  $2.42 \pm 0.05 \text{ \AA}$  at the 10 to 30  $\mu\text{s}$  timeframe. This gives evidence for a degree of activation of the Si-H bond, although error margins are too large to say whether this is full activation. The limits of TRXAS have been explored, with the difference signal of a mixed system of alkane-bound and silane-bound rhenium showing significantly more silane character than is expected for its proportional presence in the system. I therefore recommend future experiments in EXAFS focus on systems with a single significant photoproduct and advance our understanding of the XAS behaviour of those species before trying to track transitions between chemically distinct species again. Measuring detail sufficient to conclusively determine the activation of C-H or Si-H bonds will require both more extensive calculations and higher quality data than have been obtained in this Thesis.

## 4.5 – References

1. R. N. Perutz, S. Sabo-Etienne and A. S. Weller, *Angewandte Chemie International Edition*, 2022, 61, e202111462.
2. G. J. Kubas, *Chemical Reviews*, 2007, 107, 4152-4205.
3. R. N. Perutz and J. J. Turner, *Journal of the American Chemical Society*, 1975, 97, 4791-4800.

4. A. J. Cowan and M. W. George, *Coordination Chemistry Reviews*, 2008, 252, 2504-2511.
5. S. Geftakis and G. E. Ball, *Journal of the American Chemical Society*, 1998, 120, 9953-9954.
6. S. D. Pike, A. L. Thompson, A. G. Algarra, D. C. Apperley, S. A. Macgregor and A. S. Weller, *Science*, 2012, 337, 1648-1651.
7. A. G. Algarra, A. L. Burnage, M. Iannuzzi, T. Krämer, S. A. Macgregor, R. E. M. Pirie, B. Tegner and A. S. Weller, in *21st Century Challenges in Chemical Crystallography II: Structural Correlations and Data Interpretation*, eds. D. Michael P. Mingos and P. R. Raithby, Springer International Publishing, Cham, 2020, pp. 183-228.
8. J. A. Calladine, K. Q. Vuong, X. Z. Sun and M. W. George, *Pure and Applied Chemistry*, 2009, 81, 1667-1675.
9. X.-Z. Sun, D. C. Grills, S. M. Nikiforov, M. Poliakoff and M. W. George, *Journal of the American Chemical Society*, 1997, 119, 7521-7525.
10. S. B. Duckett, M. W. George, O. S. Jina, S. L. Matthews, R. N. Perutz, X.-Z. Sun and K. Q. Vuong, *Chemical Communications*, 2009, 1401 - 1403.
11. G. E. Ball, T. A. Darwish, S. Geftakis, M. W. George, D. J. Lawes, P. Portius and J. P. Rourke, *Proceedings of the National Academy of Sciences of the United States of America*, 2005, 102, 1853-1858.
12. E. A. Cobar, R. Z. Khaliullin, R. G. Bergman and M. Head-Gordon, *Proceedings of the National Academy of Sciences of the United States of America*, 2007, 104, 6963-6968.
13. R. H. Crabtree, E. M. Holt, M. Lavin and S. M. Morehouse, *Inorganic Chemistry*, 1985, 24, 1986-1992.
14. D. Astruc, *New Journal of Chemistry*, 2005, 29, 42-56.
15. M. A. Graham, J. J. Turner, M. Poliakoff and R. N. Perutz, *Journal of Organometallic Chemistry*, 1972, 34, C34-+.

16. D. M. Roe, P. M. Bailey, K. Moseley and P. M. Maitlis, *Journal of the Chemical Society, Chemical Communications*, 1972, 1273-1274.
17. S. E. Bromberg, H. Yang, M. C. Asplund, T. Lian, B. K. McNamara, K. T. Kotz, J. S. Yeston, M. Wilkens, H. Frei, R. G. Bergman and C. B. Harris, *Science*, 1997, 278, 260-263.
18. S. Tabassum, A. F. Zahoor, K. G. Ali, M. Irfan, S. M. Hussain and R. Akhtar, *Journal of the Iranian Chemical Society*, 2022, 19, 3285-3315.
19. G. I. Childs, C. S. Colley, J. Dyer, D. C. Grills, X. Z. Sun, J. X. Yang and M. W. George, *Journal of the Chemical Society-Dalton Transactions*, 2000, 1901-1906.
20. A. J. Cowan, P. Portius, H. K. Kawanami, O. S. Jina, D. C. Grills, X.-Z. Sun, J. McMaster and M. W. George, *Proceedings of the National Academy of Sciences*, 2007, 104, 6933-6938.
21. W. Jetz and W. A. G. Graham, *Inorganic Chemistry*, 1971, 10, 4-&.
22. H. Yang, M. C. Asplund, K. T. Kotz, M. J. Wilkens, H. Frei and C. B. Harris, *Journal of the American Chemical Society*, 1998, 120, 10154-10165.
23. Z. F. Zhang and M. D. Su, *Rsc Advances*, 2018, 8, 10987-10998.
24. G. Garwood, Doctor of Philosophy, University of Nottingham, 2022.
25. S. A. Bartlett, N. A. Besley, A. J. Dent, S. Diaz-Moreno, J. Evans, M. L. Hamilton, M. W. D. Hanson-Heine, R. Horvath, V. Manici, X. Z. Sun, M. Towrie, L. J. Wu, X. Y. Zhang and M. W. George, *Journal of the American Chemical Society*, 2019, 141, 11471-11480.
26. D. J. Lawes, S. Geftakis and G. E. Ball, *Journal of the American Chemical Society*, 2005, 127, 4134-4135.
27. A. S. Romanov, G. F. Angles, M. Y. Antipin and T. V. Timofeeva, *Acta Crystallographica Section C-Structural Chemistry*, 2012, 68, M69-M72.
28. R. Crüsemann, V. Fritzsche, S. Hückmann and H. Bertagnolli, *Japanese Journal of Applied Physics*, 1993, 32, 41.

29. J. S. Waugh, J. H. Loehlin, F. A. Cotton and D. P. Shoemaker, *Journal of Chemical Physics*, 1959, 31, 1434-1435.
30. N. W. Alcock, *Journal of the Chemical Society a -Inorganic Physical Theoretical*, 1967, 2001-&.
31. B. Chan and G. E. Ball, *Journal of Chemical Theory and Computation*, 2013, 9, 2199-2208.
32. Q. Lu, F. Neese and G. Bistoni, *Physical Chemistry Chemical Physics*, 2019, 21, 11569-11577.
33. N. Masciocchi, G. D'Alfonso, L. Garavaglia and A. Sironi, *Angewandte Chemie International Edition*, 2000, 39, 4477-4480.
34. Y. Otero, A. Arce, Y. D. Sanctis, R. Machado, M. C. Goite, T. Gonzalez and A. Briceño, *Inorganica Chimica Acta*, 2013, 404, 77-81.
35. Y. Zhao and D. G. Truhlar, *Theoretical Chemistry Accounts*, 2008, 120, 215-241.

# Chapter 5 – Manganese-solvent interactions

## 5.1 – Introduction

This Chapter discusses the investigation of bonding in organometallic manganese-alkane and manganese-silane complexes via TRIR and TRXAS methods using a similar methodology to that used in Chapter 4. Manganese carbonyls make up an extensively investigated branch of organometallic complexes.<sup>1,2</sup> Manganese is a useful transition metal to investigate; as a first-row transition metal it lacks some of the complex factors of heavier metals, i.e. relativistic factors that can be modelled in computations as a scalar contribution rather than a more complex shift, and it provides a useful benchmark for then comparing behaviours with those heavier elements.<sup>3</sup> It is also more abundant and cheaper than rhenium and other heavier metals, and  $\text{CpMn}(\text{CO})_3$  has been used to generate  $\text{H}_2$  in a hexane/water system.<sup>4</sup>

Manganese systems have been previously investigated by XAS, probing both solid state<sup>5</sup> and solution phase systems.<sup>6</sup> Sigma complexes of manganese<sup>7</sup> are an extensively investigated subset of sigma-alkane complexes. They have been described in previous studies characterising  $\text{CpMn}(\text{CO})_2(\text{alkane})$  and related systems, which have used techniques such as TRIR and NMR.<sup>8</sup> These studies are discussed in more detail below.

This Thesis has previously explored utilising TRIR alongside EXAFS analysis in Chapter 4. In this Chapter the focus of XAFS analysis is instead on the XANES. The XAFS measurements were performed at Diamond Light source, which due to instrument limitations could only scan far enough to extract XANES data. Therefore, there is no EXAFS analysis in this Chapter. The XANES offers less quantitative insight than EXAFS analysis, but it occurs over a smaller energy window, allowing for faster scanning, and can still be used to examine the electronic and molecular structure of metal complexes.<sup>9,10</sup>

### 5.1.1 – Manganese-Alkane Complexes

Manganese is among many metals that have been investigated for use in C-H activation, from as early as 1973.<sup>11</sup> Early carbonyl-based manganese alkane complexes were discovered shortly after the initial explorations of group VI carbonyl metal alkane complexes<sup>12</sup>, and have been characterised for a variety of alkanes.<sup>8</sup>

As a specific example, manganese-propane and manganese-butane complexes investigated by TRIR and NMR showed evidence of  $\sigma$ -bonding to both the primary and secondary carbons of the alkane ligand, as can be seen in Figure 5.1.<sup>13</sup>

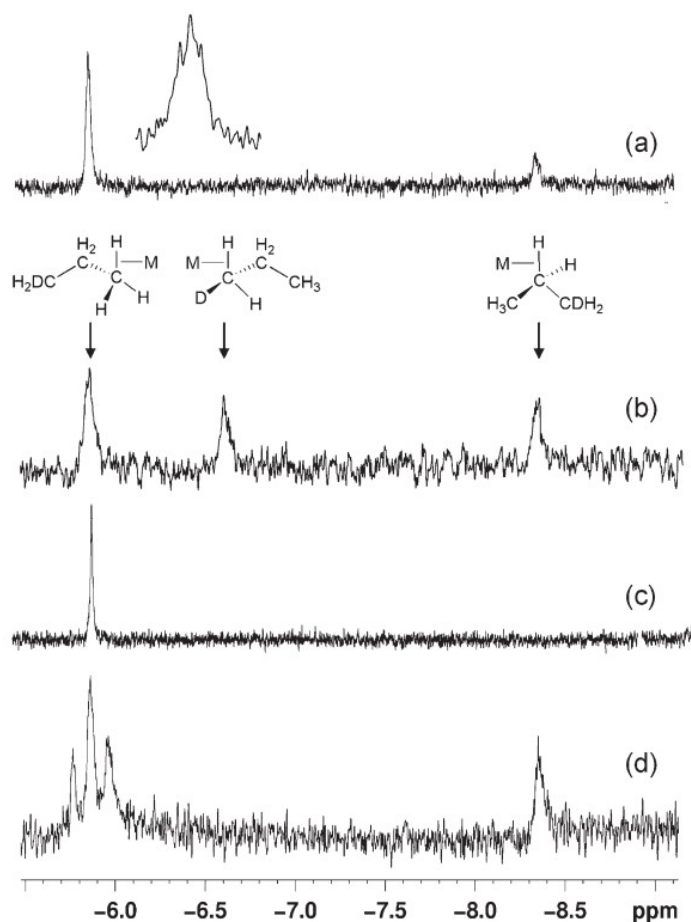


Figure 5.1:  $^1\text{H}$  NMR spectrum of  $\text{CpMn}(\text{CO})_3$  photolyzed in a) propane; b) propane-1- $\text{d}_1$ ; c) propane-2,2- $\text{d}_2$ ; and d) propane- $^{13}\text{C}_1$ . Replicated from ref.<sup>13</sup>

On photolysis,  $\text{CpMn(CO)}_3$  solvated in n-heptane forms  $\text{CpMn(CO)}_2(\text{n-heptane})$  within a few hundred picoseconds.<sup>1</sup> Figure 5.2 shows selected FTIR and TRIR spectra of this process, with the parent species decaying within 1 picosecond and giving rise to bands attributed to  $^3\text{CpMn(CO)}_2$  before being replaced by the bands attributed to  $\text{CpMn(CO)}_2(\text{n-heptane})$  over the next few hundred picoseconds.

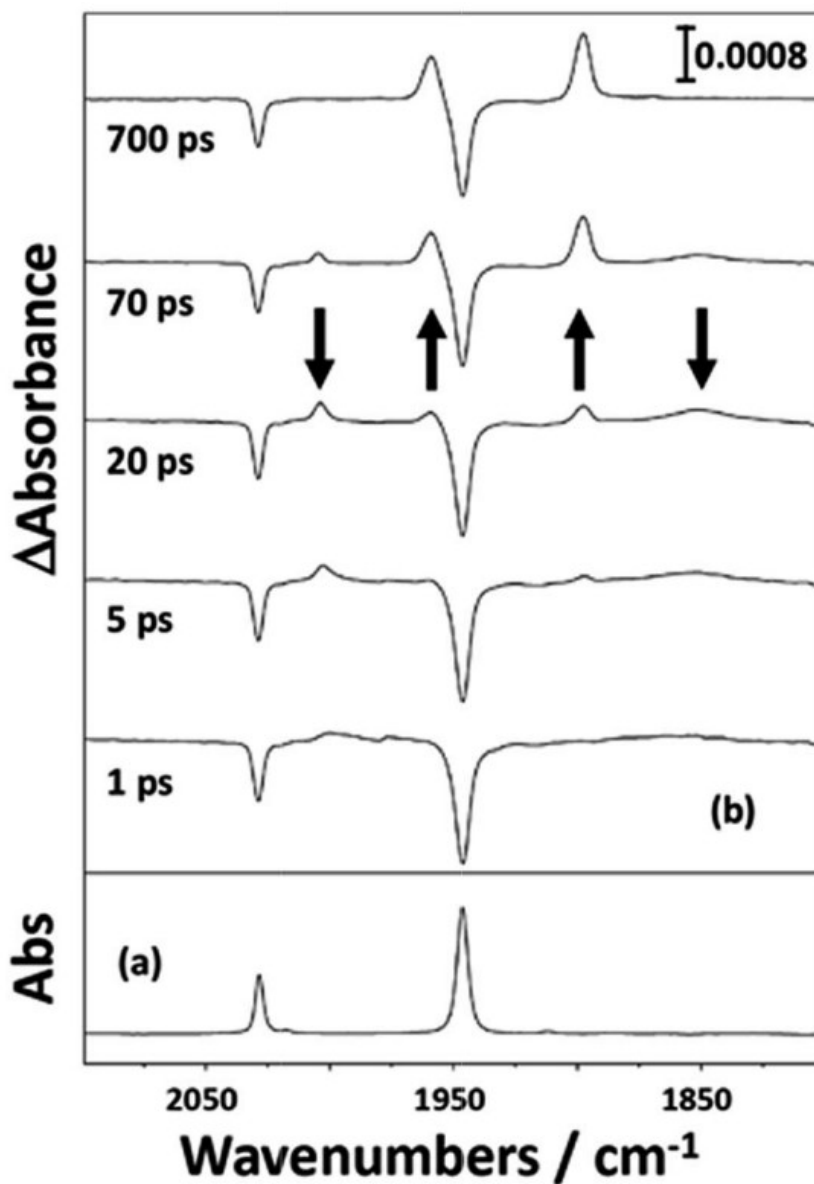


Figure 5.2: IR spectra of  $\text{CpMn(CO)}_3$  in n-heptane including a) FTIR of the solution and b) TRIR at selected intervals post photolysis. Replicated from ref.<sup>1</sup>

Manganese complexes tend to be less inclined to activate C-H bonds compared to their rhenium analogues, as the oxidative addition processes tend to occur more favourably with the heavier transition metals.<sup>14</sup> Nonetheless there have been consistent efforts to exploit manganese complexes as catalysts for C-H activation.<sup>15</sup>

### 5.1.2 – Manganese-Silane Complexes

An example of a transition metal-silane bond was first synthesised in 1956<sup>16</sup>, and since then manganese-silane complexes have been a popular subject of study.<sup>17, 18</sup> As with rhenium-silane complexes, there is a wealth of opportunity for developing selective catalysts for silicon-based synthesis.<sup>19</sup>

Komuro et al. investigated silyl activation with manganese carbonyls and found evidence that as the number of CO ligands decreases, the Mn-Si bond strength increases<sup>20</sup>, and recent studies have developed selective Mn-Si reactions that employ  $\text{Mn}_2(\text{CO})_{10}$  as a catalyst to produce allylsilanes, as shown in Figure 5.3.<sup>21</sup>

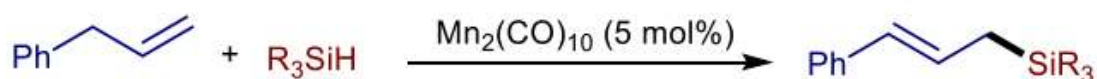


Figure 5.3: Reaction scheme developed by Wu et al.<sup>21</sup>

While the interactions of rhenium are very similar to those of manganese in the  $\text{CpM}(\text{CO})_3$  system, there are distinct differences. As discussed in chapter 4, Yang *et al.* made investigations into manganese and rhenium and where they observed that the rhenium complex appears to cleave the Si-H bond when photolyzed in the presence of  $\text{HSi}(\text{Et})_3$ , they found the manganese complex appears to activate the bond only partially, elongating the Si-H bond but not fully cleaving it.<sup>22</sup>

In addition, they proposed a significantly more complex reaction pathway for the manganese process, which is shown below in Figure 5.4. In short, the manganese complex can arrive at a

triplet or singlet state following photolysis, but either of these states can still bond to the triethyl silane solvent molecule via the ethyl tail or directly via the Si-H moiety.

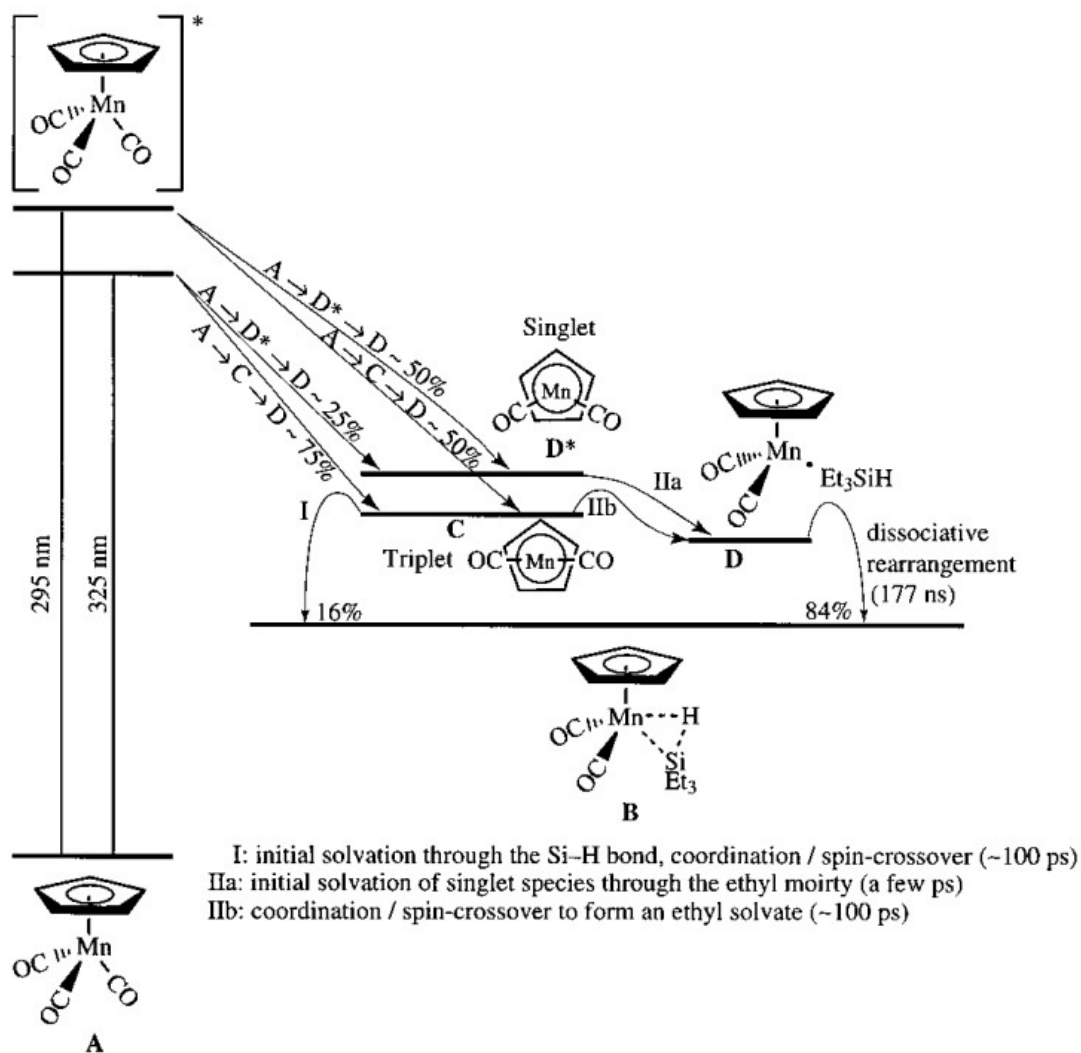


Figure 5.4: Proposed mechanism for reaction pathway of  $\text{CpMn}(\text{CO})_3$ , reproduced from Yang et al.<sup>22</sup>

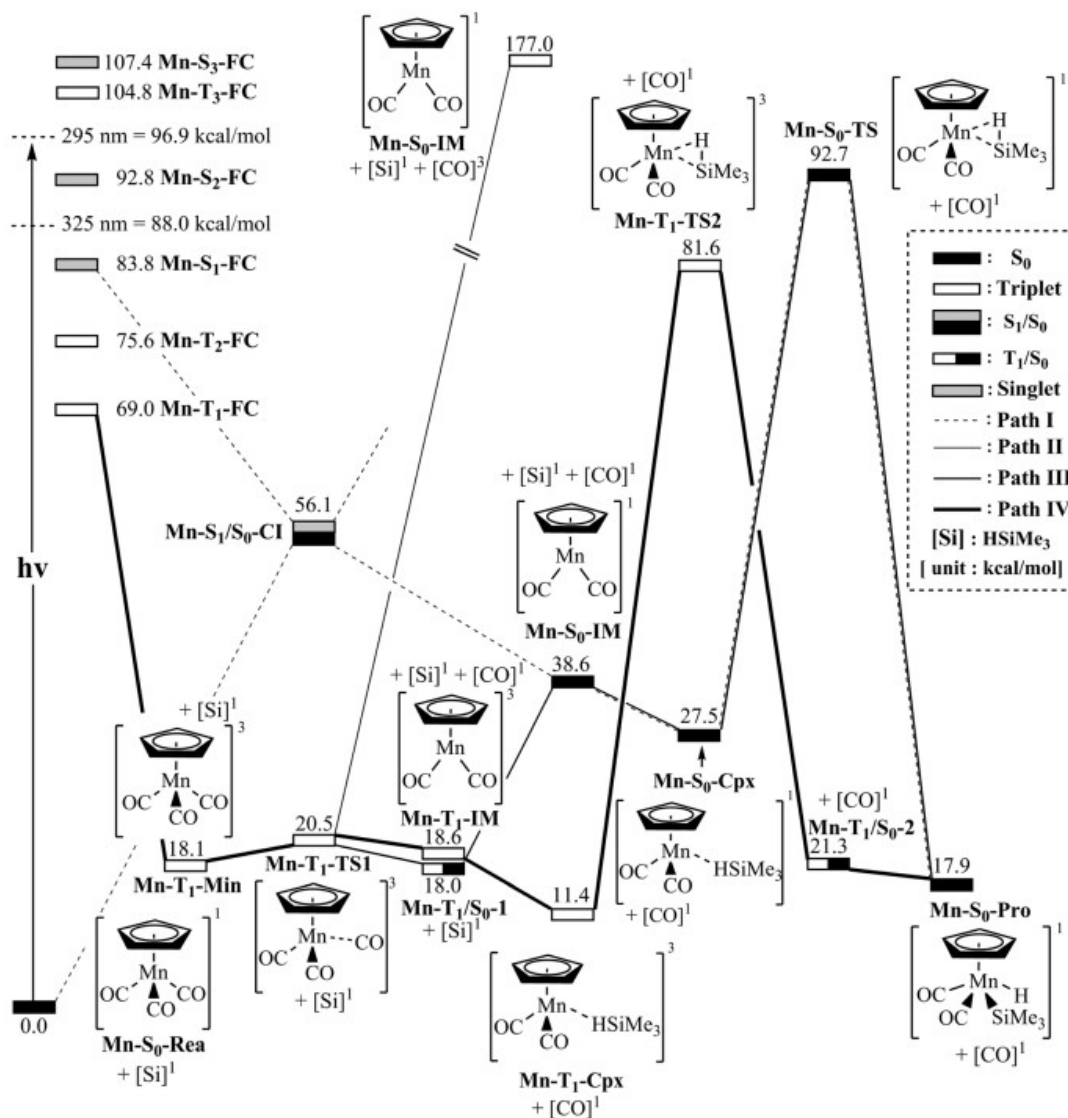


Figure 5.5: Calculated energy profiles for the photoexcitation reactions of  $\text{CpMn(CO)}_3$  with energies given in  $\text{kcal mol}^{-1}$ . Reproduced from Zhang and Su<sup>23</sup>.

The work of Zhang and Su in mapping the energy states of the photolysis of  $\text{CpMn(CO)}_3$  and subsequent reaction with triethyl silane is shown in Figure 5.5 and, as with Yang et al.'s findings, is significantly more complex than the rhenium analogue. Their calculations agree that the parent complex can be excited to both a triplet and singlet state, which leads to a branching array of pathways by which CO loss is followed by bonding of the triethyl silane solvent molecule. While this can occur via the triplet or singlet state, in both cases there is a steep energy barrier between the silane binding and progression to the activated state.

## 5.2 – Aims

While the solvent systems of  $\text{CpMn}(\text{CO})_3$  do not produce intermediate complexes with lifetimes as long as those of  $\text{CpRe}(\text{CO})_3$ , the x-ray energies available at Diamond Light Source enabled probing of the K-edge of manganese, allowing for the opportunity to computationally model the XANES of the parent and products and develop on existing theories of the reaction of  $\text{CpMn}(\text{CO})_3$  in alkanes and silanes. In looking at these alkyl and silyl systems, we can investigate how the electronic structure of the metal centre changes with the formation of alkyl or silyl sigma complexes, and how that variance arises from the different binding modes.

It also provided an occasion to test the effectiveness of modelling the XANES with QChem for a system where the relativistic component could be modelled as a scalar contribution.

The aims of this chapter are as follows:

- (i) To investigate the photolysis of  $\text{CpMn}(\text{CO})_3$  in alkane and silane solvents with TRIR in order to obtain the correct kinetic profiles required for TRXAS measurements.
- (ii) To investigate the photolysis of  $\text{CpMn}(\text{CO})_3$  in both neat alkane and silane solvents with TRXAS, building upon and supplementing the findings of TRIR investigation focusing identifying intermediates by using the XANES data rather than the XAFS.
- (iii) To determine changes in the electronic structure of the photoproducts from analysis of TRXAS XANES data.
- (iv) To compare and contrast analysis methods of XANES data on these weakly bound organometallic complexes in order to test the limits of modelling the XANES with both QChem and FDMNES.

As mentioned in Chapter 4, TRIR studies were undertaken at Nottingham to investigate  $\text{CpM}(\text{CO})_3$  ( $M = \text{Re}, \text{Mn}$ ) in n-heptane and triethyl silane in an extension of the work by Yang *et al.*<sup>22</sup>, for which the results for manganese are presented below.

Undertaking TRXAS measurements on manganese at the APS was not possible, as the beamline monochromator could not produce a stable output at the low energy of the

manganese K-edge. This investigation was therefore restricted to experiments at Diamond. While some suitable data for the pursuit of aims (iii) to (iv) was obtained at Diamond in 2020, the majority of viable data was obtained in July 2023, and therefore analysis has not been extensive given the time available. A longer run of beamtime was provided in 2020, but the setup had issues that were not overcome in the allotted time. The 2023 experiment was performed with a vastly improved setup but was conducted in a shorter run.

## 5.3 – Results

As outlined in Chapter 4, TRIR investigations were carried out at the University of Nottingham on  $\text{CpRe}(\text{CO})_3$  and  $\text{CpMn}(\text{CO})_3$  in alkane and silane solution and were performed in collaboration with Genevieve Garwood.<sup>24</sup> The results for the manganese are presented below in Sections 5.3.1 and 5.3.2.

XANES data was collected at Diamond Light Source and is presented and discussed in relation to the TRIR findings in sections 5.3.3, 5.3.4, and 5.3.5.

### 5.3.1 – TRIR of $\text{CpMn}(\text{CO})_3$ in neat triethyl silane

The reaction of  $\text{CpMn}(\text{CO})_3$  in neat triethyl silane proceeds in a similar fashion to the analogous rhenium species described in Chapter 4. It can be seen in Figure 5.6 that there are two parent depletion peaks at  $2029\text{ cm}^{-1}$  and  $1946\text{ cm}^{-1}$ , corresponding to the loss of the  $\nu(\text{C-O})$  stretches from  $\text{CpMn}(\text{CO})_3$ , which persist for the entire timescale of the experiment as expected.

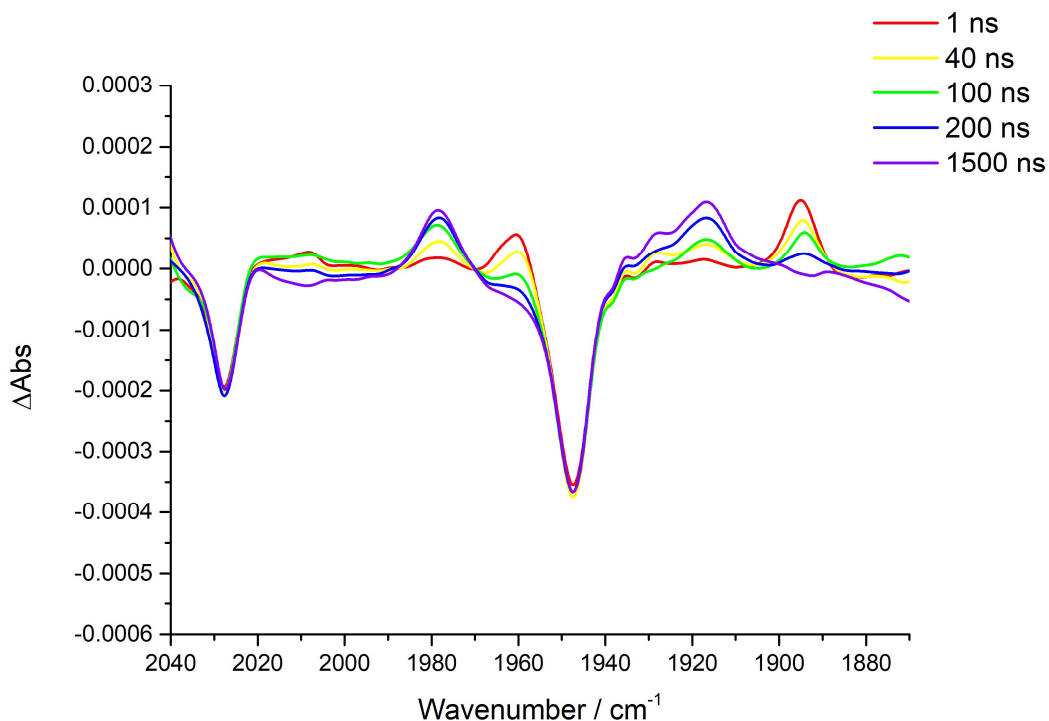


Figure 5.6: Selected TRIR spectra of  $\text{CpMn}(\text{CO})_3$  in neat triethyl silane, photolyzed at 266 nm and observed out to 200  $\mu\text{s}$ . No significant decay was observed after circa 2  $\mu\text{s}$ , so only spectra from before that point are displayed.

There are two sets of two growth peaks, the first set occurring at 1960  $\text{cm}^{-1}$  and 1894  $\text{cm}^{-1}$ , appearing within 1 ns alongside the parent depletion bands at 2028  $\text{cm}^{-1}$  and 1946  $\text{cm}^{-1}$  and decaying away over the next several hundred nanoseconds. These peaks are in good agreement with previous observations assigned to the  $\text{CpMn}(\text{CO})_2(\text{Et}_3\text{SiH})$  intermediate<sup>22</sup>, and occur at lower wavenumbers indicative of a more weakly-bound species interacting with the metal centre, and so we assign these peaks to the ethyl-bound intermediate.

The second set of product peaks emerges over the next 2  $\mu\text{s}$ , at 1978  $\text{cm}^{-1}$  and 1917  $\text{cm}^{-1}$ . They grow in with a rate commensurate to the decay of the initial photoproducts. These peaks are again within 2  $\text{cm}^{-1}$  of assignments by Yang et al., this time to the silane-bound complex  $\text{CpMn}(\text{CO})_2(\text{HSiEt}_3)$ .

This assignment derives from the peak positions moving from lower to higher wavenumbers with the transition from primary to secondary product, which is indicative of a stronger bonding to the metal centre that increases the stability of the attached carbonyl groups.

We can see that the shift in wavenumber between the alkane-bound species and the silane-bound species is much smaller than for the equivalent process in rhenium explored in Chapter 4: in this case the silyl-assigned peaks are 18 and 23  $\text{cm}^{-1}$  greater than their alkyl-assigned equivalents, while for rhenium we see a 36 to 37  $\text{cm}^{-1}$  shift. This suggests the carbonyl bonds are significantly weaker than for the parent species, which indicates a reduced degree of electron density on the metal centre, an observation which is consistent with the theory that the manganese system does not activate the Si-H bond as much as the rhenium does.

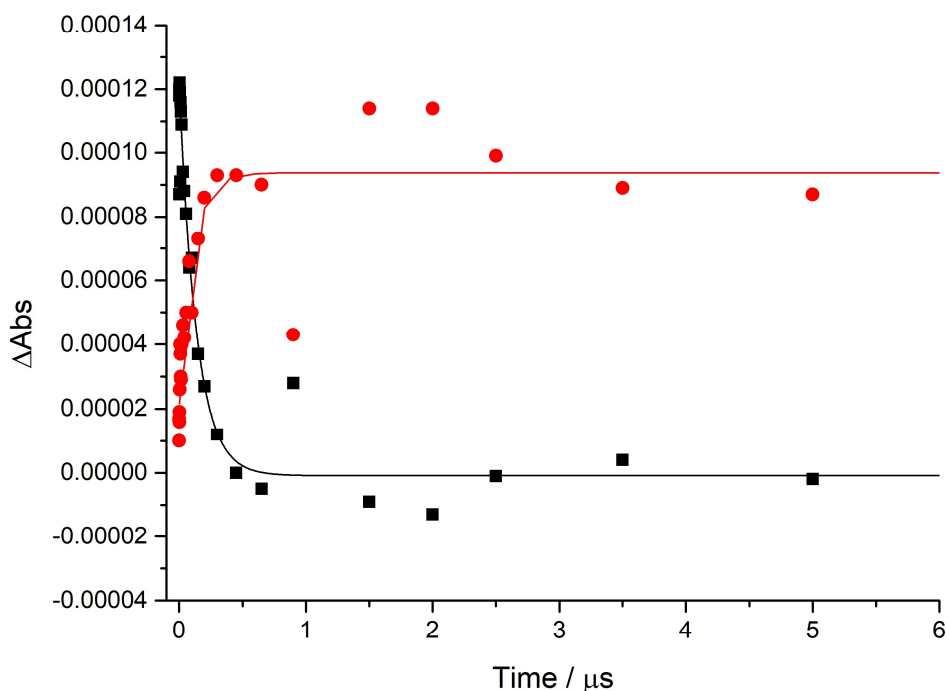


Figure 5.7: Graph of decay of absorption peak at 1894  $\text{cm}^{-1}$  (black) and growth at 1917  $\text{cm}^{-1}$  (red) for  $\text{CpMn}(\text{CO})_3$  photolyzed at 266 nm.

The half-life of this reaction was derived from the peaks at 1894, 1917 and 1978  $\text{cm}^{-1}$  via an exponential decay fit, for which the fits for 1894 and 1917  $\text{cm}^{-1}$  are displayed in Figure 5.7. The peak at 1960  $\text{cm}^{-1}$  was excluded due to its proximity to a parent depletion peak. The resulting rate was calculated as  $121 \pm 18 \text{ ns}$ , which is not in good agreement with Yang et al.'s reported value of 180 ns. This difference might be attributable to temperature variation,

or from their use of 325 nm radiation to initiate photolysis. This lower-energy radiation could lead to reduced reactivity of photoproducts and thus an extended lifetime before overcoming the barrier to further reformation.

### 5.3.2 – TRIR of $\text{CpMn}(\text{CO})_3$ in n-heptane doped with triethyl silane

A set of solutions with a concentration of  $\text{CpMn}(\text{CO})_3$  of 1 mM were excited at 266 nm with a laser pulse energy of 1  $\mu\text{J}$ . The solutions tested were doped with 30, 60, 120, 180, and 240 mM of triethyl silane.

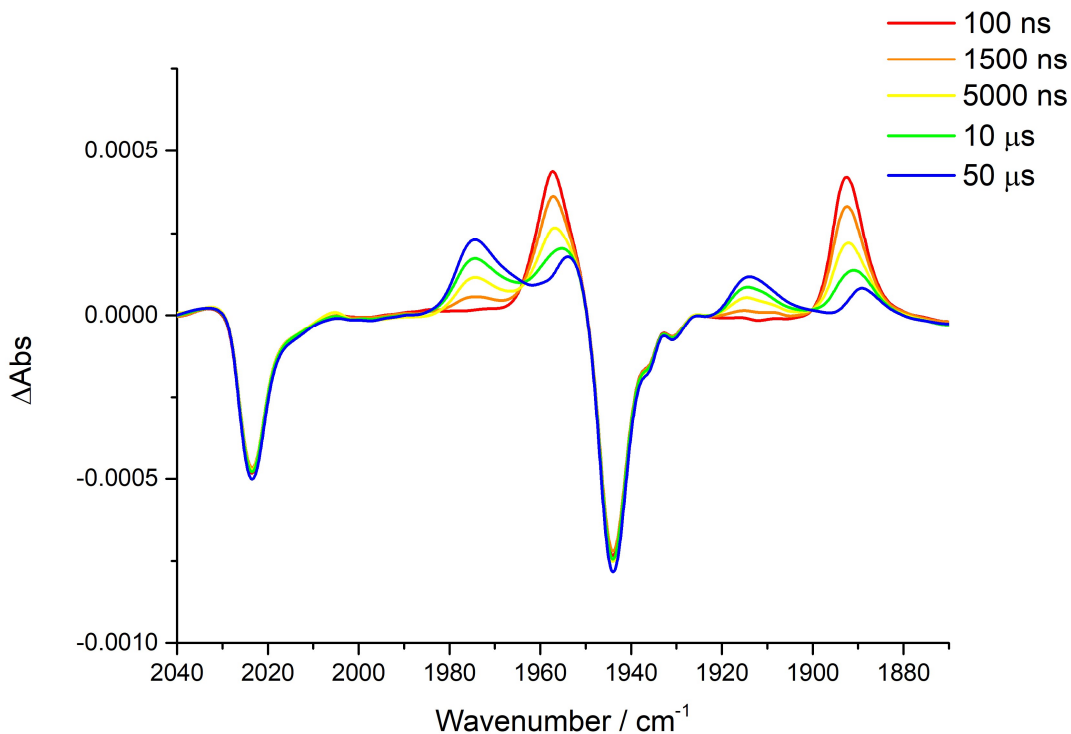


Figure 5.8: TRIR spectra of  $\text{CpMn}(\text{CO})_3$  in n-heptane doped with 30 mM of triethyl silane.

We can see in Figure 5.8 that on photolysis, both carbonyl bands of the parent (seen at 2023 and 1944  $\text{cm}^{-1}$ ) are bleached, with no reformation observed on the experiment's timescale. These parent positions are slightly lower (by about 3  $\text{cm}^{-1}$ ) than previously observed for

$\text{CpMn(CO)}_3$  in n-heptane or triethyl silane<sup>1</sup>, which we attribute to a slight energy miscalibration. Within 100 ns we see a pair of product bands appear at 1957 and 1892  $\text{cm}^{-1}$ , which proceed to decay on the microsecond timescale. Another 2 product bands are seen to form at 1975 and 1914  $\text{cm}^{-1}$ , with a growth rate commensurate with the decay of the initial product bands. Figure 5.8 shows the relevant TRIR spectra for a 30 mM concentration of triethyl silane and is representative of the behaviour seen at other tested concentrations.

Data from previous investigations<sup>22, 25</sup> gives the peak positions for the  $\nu(\text{CO})$  bands of  $\text{CpMn(CO)}_2(\text{Et}_3\text{SiH})$  as 1960 and 1892  $\text{cm}^{-1}$  in neat  $\text{HSiEt}_3$ , and the positions for  $\text{CpMn(CO)}_2(\text{n-heptane})$  in neat heptane as 1960 and 1897  $\text{cm}^{-1}$ . These values both align reasonably with the position of the primary photoproduct, accounting for the energy difference observed in the parent. We do see a shift to lower wavenumbers of those peaks on the timescale of the experiment. This could be explained by the formation of 2 overlapping photoproducts, which react to form the secondary product at different rates. After 50  $\mu\text{s}$  these peaks are at 1954 and 1889  $\text{cm}^{-1}$ , and given the favourability of rearrangement for the ethyl-bound triethyl silane complex it seems more likely that these later time positions correspond to the heptane-bound species.

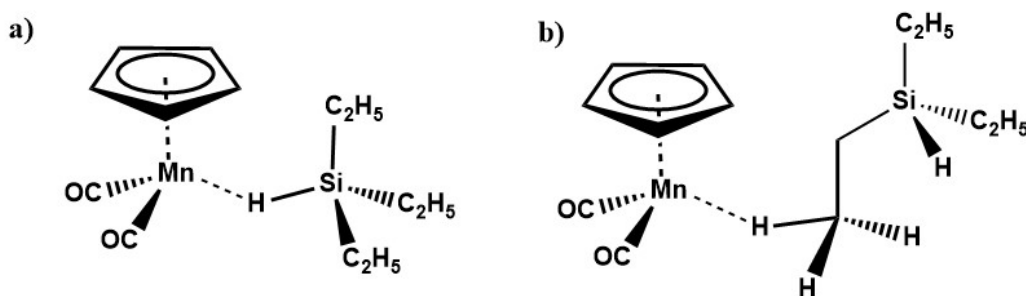


Figure 5.9: illustration of the two complexes formed by triethyl silane binding to  $\text{CpMn(CO)}_2$ , showing a)  $\text{CpMn(CO)}_2(\text{HSiEt}_3)$ , and b)  $\text{CpMn(CO)}_2(\text{EtSiHEt}_2)$

The bands for the primary product are thus tentatively attributed to the formation of  $\text{CpMn(CO)}_2(\text{n-heptane})$  as well as  $\text{CpMn(CO)}_2(\text{EtSiHEt}_2)$ , while the secondary product is assigned as  $\text{CpMn(CO)}_2(\text{SiHEt}_3)$ . The expected structures of these two silane-based photoproducts are shown in Figure 5.9. We can propose that on photolysis  $\text{CpMn(CO)}_2(\text{n-heptane})$  is formed within the first 100 ns, with a subsequent reaction to form a silane-bound complex. The decay of those peaks being tightly matched to the growth of the metal-silyl complex is indicative of the silane molecule solvating directly with the Si-H bond, or

there being a very fast transition between the ethyl-bound complex and the silyl-bound version. Yang et. al. reports such a mechanism as having a time constant of  $\sim 180$  ns in neat triethyl silane, suggesting the latter possibility is occurring in the heptane solution.

We therefore describe the reaction of  $\text{CpMn}(\text{CO})_3$  in this system as:

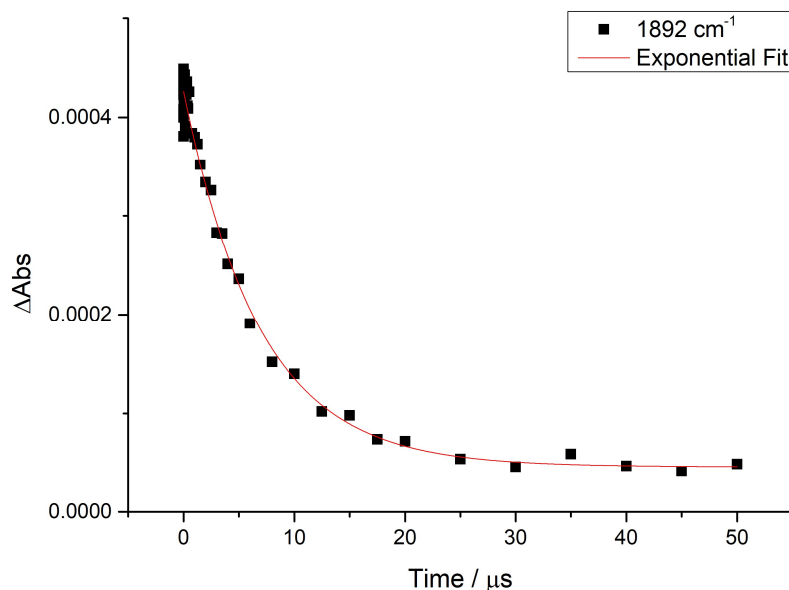
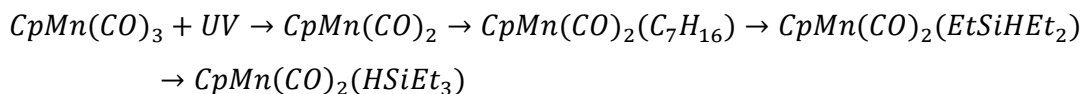


Figure 5.10: Plot of change in absorbance at  $1892\text{ cm}^{-1}$  against time for the photolysis of  $\text{CpMn}(\text{CO})_3$  in *n*-heptane doped with 30 mM of triethyl silane. The experimental data are fitted to a first-order exponential decay.

The decay and growth of each product peak on the microsecond timescale was fitted to an exponential (with a selected example shown in Figure 5.9), which was then averaged for each concentration of silane investigated to produce an observed rate constant. These were plotted and fit as shown in Figure 5.10 and can be seen to show a strong linear trend.

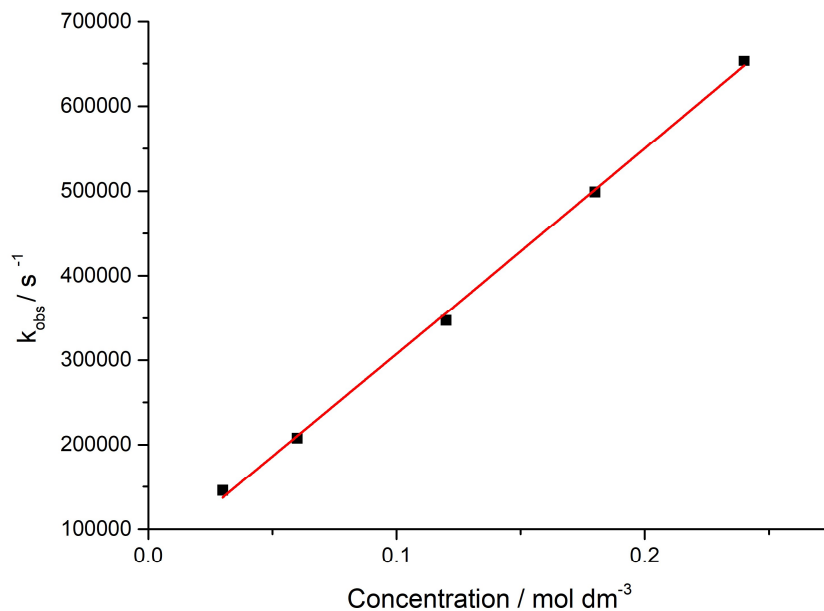


Figure 5.11: Plot of relationship between observed rate constant and silane concentration for  $\text{CpMn}(\text{CO})_3$  and triethyl silane in *n*-heptane.

This linear relationship illustrates the increase in rate of interconversion as the concentration of doped triethyl silane increases. We can make the following relation using the pseudo-first order rate equation:

$$k_{obs} = k[\text{HSiEt}_3]$$

Which we employ due to the vast excess of triethyl silane relative to  $\text{CpMn}(\text{CO})_3$ . From this we can determine the pseudo-first order rate constant to be  $k = 2.429 \pm 0.047 \times 10^6 \text{ mol}^{-1} \text{ dm}^3 \text{ s}^{-1}$ .

Table 5.1: Observed rates of reaction in selected concentrations of triethyl silane for 5 mM CpMn(CO)<sub>3</sub> in *n*-heptane.

Silane Concentration / M	Rate, $k_{\text{obs}} / \text{s}^{-1}$
0.03	$1.45 \times 10^5$
0.06	$2.07 \times 10^5$
0.12	$3.47 \times 10^5$
0.18	$4.99 \times 10^5$
0.24	$6.54 \times 10^5$

This gives a rate of interconversion that is on the microsecond timescale, suitable for observing the transition in the available time window for TRXAS.

### 5.3.3 – XANES of CpMn(CO)<sub>3</sub> in neat *n*-heptane

TRXAS experiments conducted in July 2023 used triethyl silane in place of tributyl silane (which was used in earlier experiments described below in Section 5.3.5) due to the difficulty of obtaining and preparing a large volume of CpMn(CO)<sub>3</sub> in neat tributyl silane.

Data was collected for 7 hours for CpMn(CO)<sub>3</sub> in neat *n*-heptane. For each energy point measured, the last 4  $\mu\text{s}$  of the data was averaged as the ‘laser off’ value, while the first 4  $\mu\text{s}$  were similarly averaged as the initial ‘laser on’ value. For each such data set, the difference between these 2 values were taken and used to plot a difference curve. Anomalies and unusable data were filtered algorithmically by analysing the formation of a depletion profile as described in Chapter 2. The filtered data sets were then combined and averaged to produce a single curve. The initial ‘laser off’ spectra are compared to the results of the FDMNES and QChem generated models, are presented below in Figures 5.11 and 5.12.

The difference data are then discussed below. In this case we expect the only photoproduct to be CpMn(CO)<sub>2</sub>(n-heptane), although evidence from analogous systems suggests that this binding could be via primary or secondary carbons in the alkane.<sup>13, 26</sup>

Theoretical XANES models were generated using QChem by performing an excited states calculation. For each species, a geometry optimised with the B3LYP functional and the Jorge-ADZP basis set and then an excited state calculation to converge 250 roots (except where otherwise noted) was performed with that geometry.

FDMNES simulations were performed with either a crystallographic structure from literature or a DFT-optimised geometry as per the QChem modelling method. These structures were used to generate a XANES spectrum first with a radius of 3 Å, then with a radius of 7 Å using the previous iteration as a starting point.

It should be noted that FDMNES calculates absorption at energies relative to the main metal edge, which is defined as 0 eV, thus when comparing FDMNES predictions to real data a manual energy shift has been applied to align it with the real data edge.

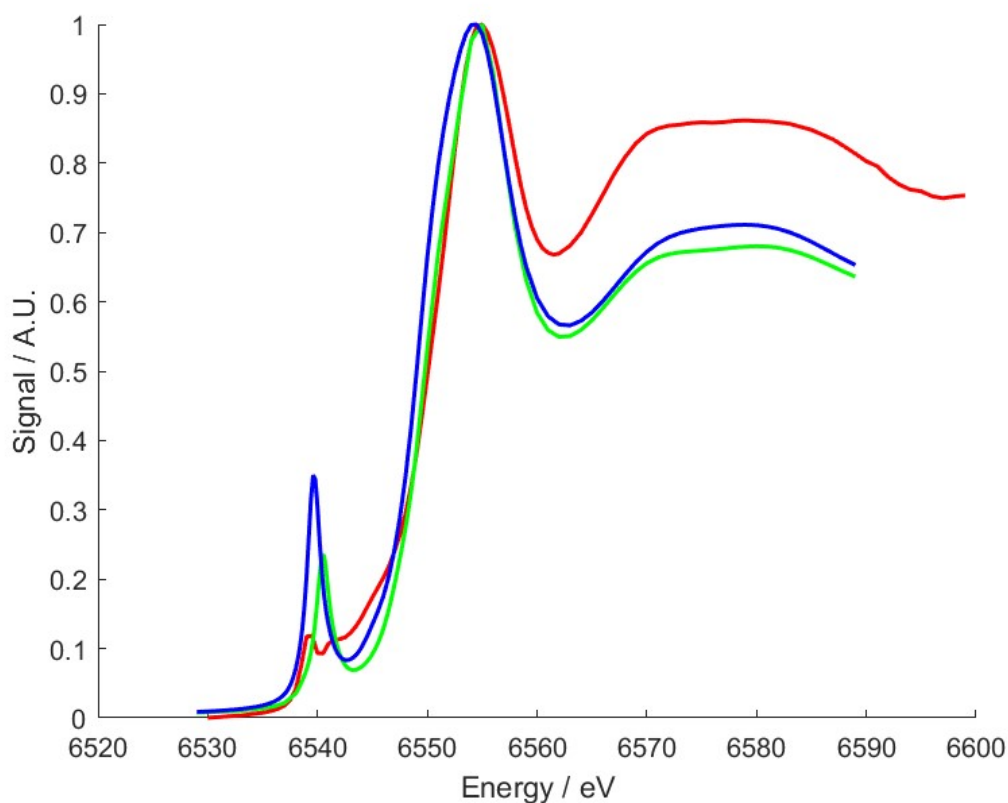


Figure 5.12: Comparison of experimental XANES data (red) for  $\text{CpMn}(\text{CO})_3$  to FDMNES computed edge with DFT geometry (green) and crystallographic geometry (blue)

Figure 5.11 shows the difference between experimental data for  $\text{CpMn}(\text{CO})_3$  in n-heptane and the FDMNES predictions produced via a DFT-optimised geometry and a geometry from crystallographic data.<sup>27</sup> While FDMNES clearly captures the main features of the pre-edge and the shape of the post-edge, there are sizable differences in the relative intensities of those features, and it does not capture the pre-edge convolution beyond that primary rise.

Compared to the CIF based prediction, the DFT-based prediction is less apt in describing the character of the main edge but is generally a little more accurate in describing the pre-edge and post-edge regions. This is however a matter of minor variations: both spectra are qualitatively similar to experiment while differing in in magnitude the same areas by similar degrees.

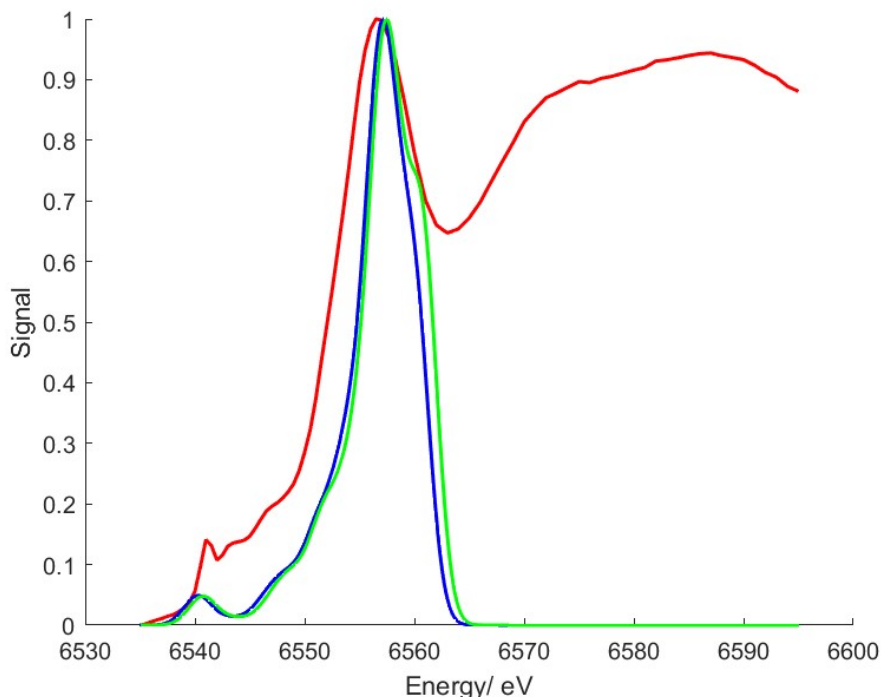


Figure 5.13: Comparison of QChem simulations with 150 roots of the XANES of  $\text{CpMn}(\text{CO})_3$  to experimental data (red). Notably the CIF-derived version (green) seems to pronounce a shoulder just past the main edge more than the DFT variant (blue).

In Figure 5.12, the equivalent simulations from QChem are compared with the edge. It can be observed that QChem has obvious limitations; while it expresses features of the pre-edge, including both the initial peak at 6541 eV and the convoluted structure between it and the main edge at 6556 eV, the limitation on the number of states computed means it cuts off at  $\sim 6560$  eV, and the relative intensity of the pre-edge is underestimated when the spectra have been normalised with respect to the main edge peak.

Although both geometries have been computed with 150 roots for this figure, we can see that the crystallographic structure projects a shoulder slightly further than the DFT-computed model. This illustrates an important detail for comparing structures, especially in difference spectra: converging the same number of roots for different structures can lead to different ranges of energies in the states computed.

Unlike FDMNES, QChem makes a prediction of the edge energy, including a scalar shift of 44.68 eV to account for relativistic effects. This correction is broadly correct but miscalculates the edge position by approximately 4 eV compared to experimental data, which is made

evident below in Figure 5.13. For other comparison figures this shift has been accounted for by applying a manual correction to align the main edge of the theoretical data to the experimental position. The figure also shows another limitation of the use of QChem spectra, in that there is no intrinsic calculation of broadening in the program.

To enable comparisons to real data the QChem-computed data (which consists of an energy value and intensity for each state) is interpreted via a further calculation which models each excited state as a Lorentzian curve of fixed width. This modelling of broadening is largely sufficient to make qualitative comparisons but fails to account for the increase in the degree of broadening that occurs with increasing energy across the XANES. This is visible in the reduced height of the pre-edge rise and the clear resolution of peaks in the post-edge.

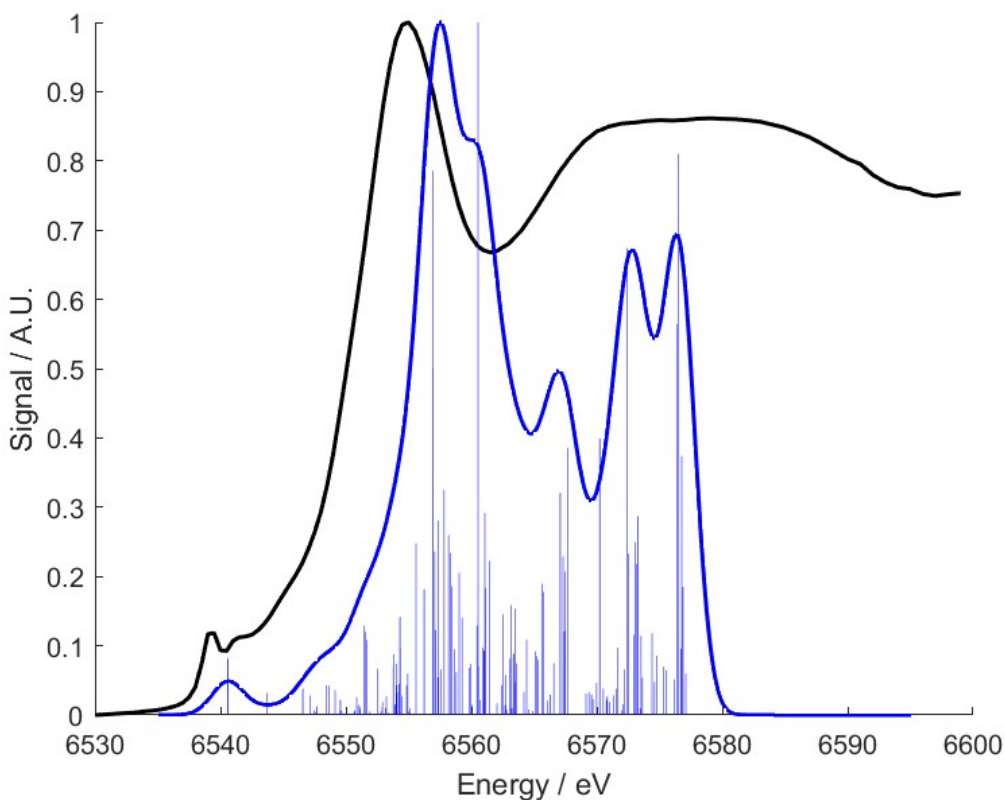


Figure 5.14: Experimental K-edge spectrum of Mn for  $\text{CpMn}(\text{CO})_3$  in *n*-heptane (black) and theoretical XANES for  $\text{CpMn}(\text{CO})_3$  generated via QChem (blue). Individual excited states are shown as bars alongside the artificially broadened curve.

Previous work has analysed the excited states of  $\text{CpMn}(\text{CO})_3$  for UV/vis spectroscopy<sup>28</sup>, which observes the same end states through excitation from a valence orbital, rather than a core orbital. While not tailored to our needs, comparison with UV/visible simulations might be useful in assigning low-lying excited states and contextualising those transitions. For this comparison it is important to note that the equivalent UV/vis transitions are not affected by identical factors: excitations from inner shells of heavy elements are shifted by relativistic effects as well as being on a much larger energy scale. Full et al. calculated the first set of transitions to be at 3.22 and 3.80 eV, corresponding to  $3d_{\text{Mn}}$ -to- $3d_{\text{Mn}}$  excitations. These would correspond to the 2 lowest excited states we observe at 6540.59 and 6540.62 eV in our simulations, visible in Figure 5.13.

This allows us to identify the origin of these first pre-edge features as excitations to d orbitals, but little else. It is not of particular use in distinguishing characteristic in the difference data.

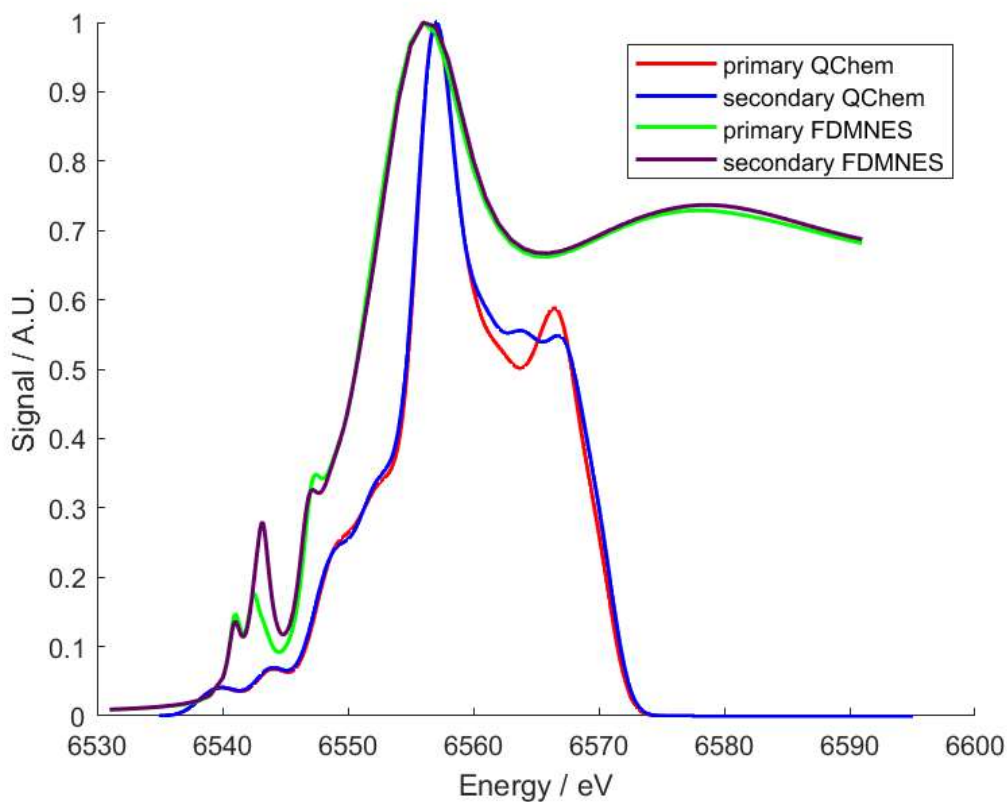


Figure 5.15: Simulated XANES spectra of  $\text{CpMn}(\text{CO})_2(n\text{-heptane})$  bound via primary and secondary carbons evaluated via FDMNES and QChem.

Figure 5.14 shows the static simulation spectra from both QChem and FDMNES of the two binding modes of n-heptane considered, and it can be seen that there is very little differentiation between them. FDMNES predicts a similar set of 3 distinct peaks in the pre-edge with differing intensities and virtually no difference in the rest of the spectrum, while QChem predicts almost no difference between the two binding modes in the pre-edge and a minor difference in the post-edge.

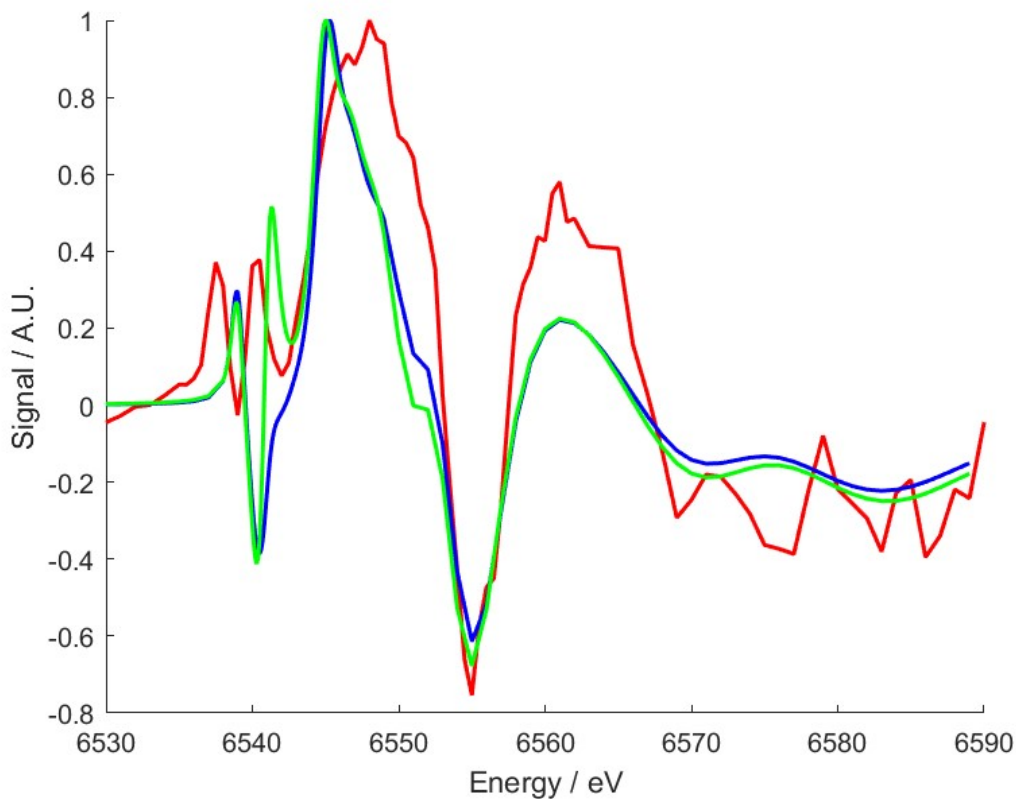


Figure 5.16: Experimental difference for  $\text{CpMn}(\text{CO})_3$  photolyzed in n-heptane (red) compared with difference spectra computed with FDMNES  $\text{CpMn}(\text{CO})_2(\text{n-heptane})$  intermediate. The primary bound isomer (green) and secondary bound isomer (blue) are both shown.

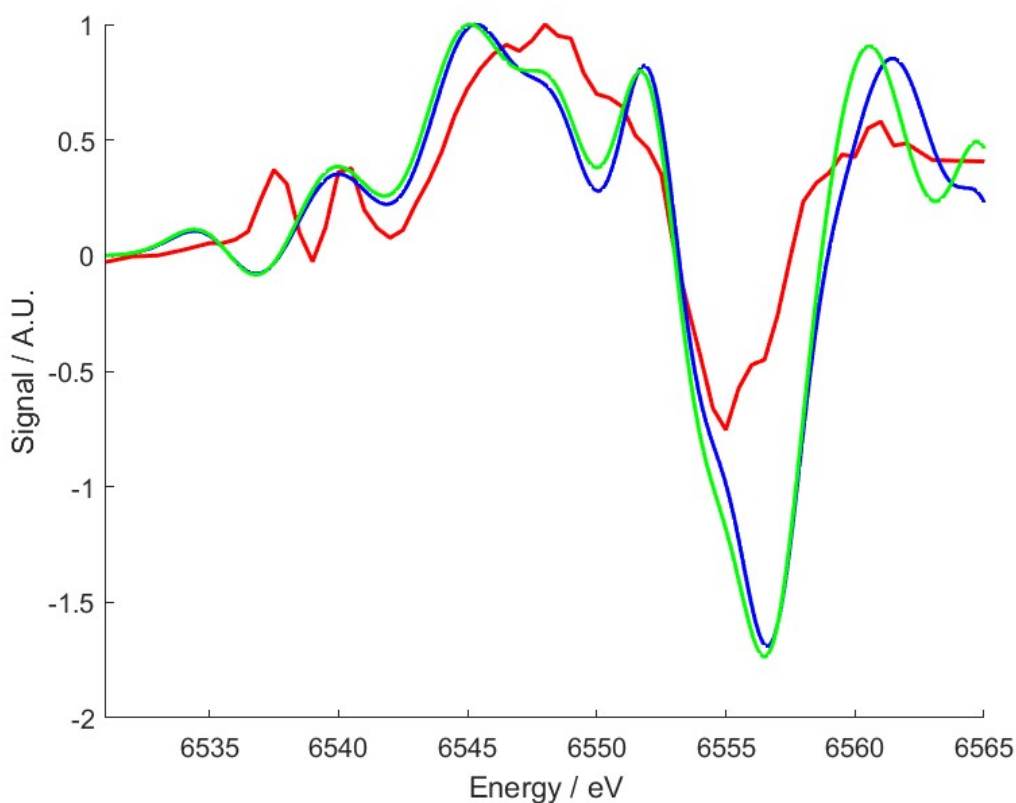


Figure 5.17: Experimental difference for  $\text{CpMn}(\text{CO})_3$  photolyzed in *n*-heptane (red) compared with difference spectra computed with QChem for the  $\text{CpMn}(\text{CO})_2(\textit{n}\text{-heptane})$  intermediate. The primary bound isomer (green) and secondary bound isomer (blue) are both shown.

In Figures 5.15 and 5.16, showing the experimental difference data compared to the computed difference spectra for FDMNES and QChem respectively, we can see there is a strong resemblance between the experimental difference and the computed difference from both QChem and FDMNES. In each case there are clear peaks visible in the pre-edge followed by a rise at approximately 6549 eV, and a valley at around 6557 eV, matching the doped *n*-heptane data qualitatively. However, the valley from depletion of the parent is much shallower. This might be attributable to reduced noise in the experimental data, but other sections of the spectrum have not been affected in the same way. A more likely explanation is that the percentage conversion of photolyzed parent to alkane complex may be significantly less than 100%, or a ‘replenishment’ of parent from the jet flow if the x-ray laser overlap is near the upper edge of the laser spot.

In the FDMNES simulations we see a generally good fit to the depletion valley in both width and intensity, and a pre-edge that maps better to the primary binding prediction than the secondary binding prediction. The primary binding simulation models 2 distinct pre-edge positive features where the secondary binding prediction does not. Neither captures the rise either side of the edge depletion particularly well.

For both QChem predictions there is a characteristic peak in between the rise and depletion valley that is not present in the experimental data. This feature might be removed by more comprehensive broadening but could also be attributed to differences in the energies of states in the region, which could also explain mismatch in the depletion region directly after it. Given the shoulder we can see in Figure 5.13, it seems likely that this arises at least partially from broadening variance.

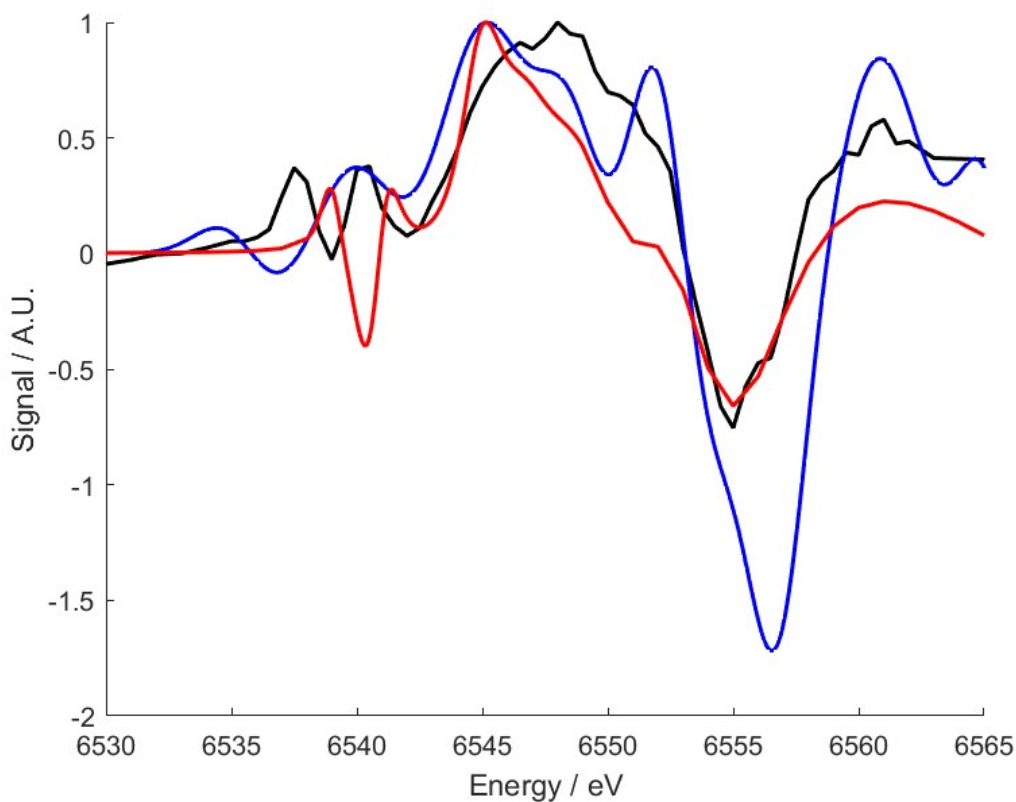


Figure 5.18: Experimental data for  $\text{CpMn}(\text{CO})_3$  photolyzed in *n*-heptane (black) compared to weighted average difference data from FDMNES (red) and QChem (blue).

From previous studies we have strong evidence that alkane binding to metal centres results in a mixed system of primary and secondary bound alkanes, so a weighted average based on the number of available primary and secondary binding sites available in *n*-heptane was calculated. Figure 5.17 shows the results of a weighted average difference anticipating a ratio of 3:5 for primary bound to secondary bound  $\text{CpMn(CO)}_2(n\text{-heptane})$ , and it can be seen that there is a vast improvement in the accuracy of the pre-edge prediction for FDMNES.

The main difference that remains is the growth/loss pattern at the edge, with the experimental data showing a broad rise with no individually resolved peaks while FDMNES predicts a shallower decline to the loss region, and QChem anticipates a second peak resolved just before the loss region. The high similarity between the QChem predictions for the binding modes mean there are no major distinguishing changes in the weighted average.

There is a slight improvement in the post-depletion region, but as this is towards the upper limit of the excited states energy range computed, it could easily be influenced by uncalculated transitions, and so no significant inferences can be made.

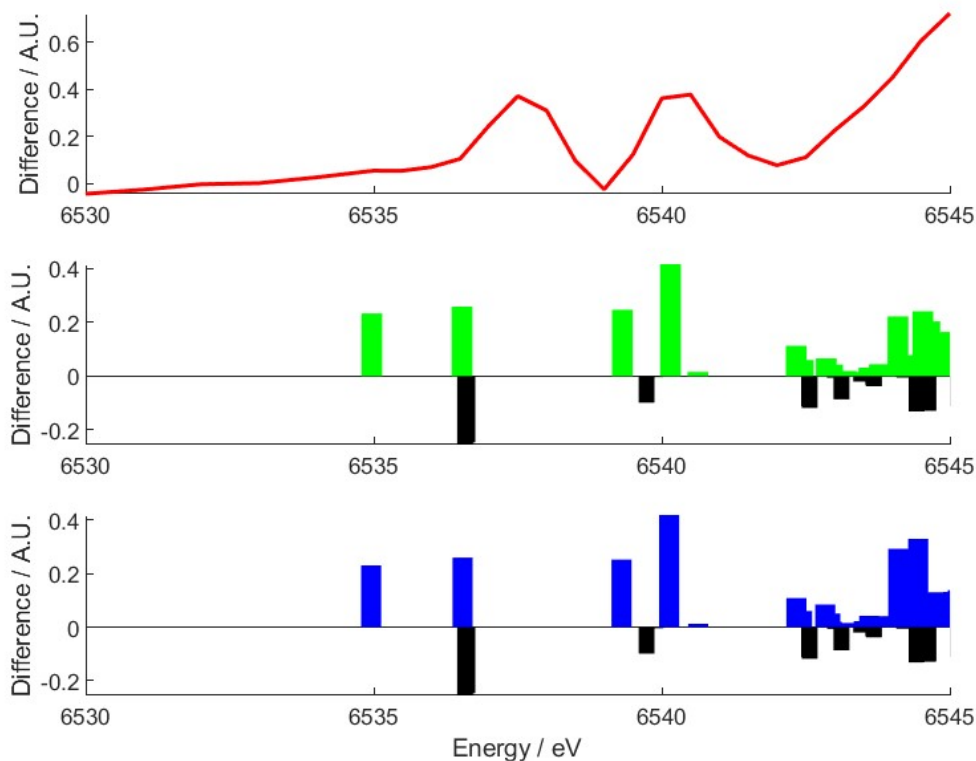


Figure 5.19: Excited states of  $\text{CpMn}(\text{CO})_2(n\text{-heptane})$  computed for QChem for primary bound (green) and secondary bound (blue) compared with difference data for  $\text{CpMn}(\text{CO})_3$  photolyzed in neat  $n\text{-heptane}$ . Excited states for  $\text{CpMn}(\text{CO})_3$  are shown as negative contributions (black), and all excited states are normalised via a single value for comparison.

In Figure 5.18 we can see that there is little difference between the predicted positions of the pre-edge excited states for the primary and secondary bound isomers. These transitions should correspond to low-lying excited states.

The primary bound structure is predicted to almost identical transitions in this region to the secondary bound structure, with major transitions at 6535, 6537, 6539, and 6540 eV. These are arrayed similarly to the predicted states for  $\text{CpMn}(\text{CO})_3$ , which shows significant states at 6537 and 6540 eV. Observations of an experimental peak at 6540 eV align well with theory, with the parent species transition in that region being much weaker. The other experimental peak is at 6538 eV however, indicating the theoretical transitions from the 6535 to 6537 eV region are being underestimated.

This is consistent with calculations of the parent as shown in Figure 5.12, where it can be seen the pre-edge is higher in experiment than theory.

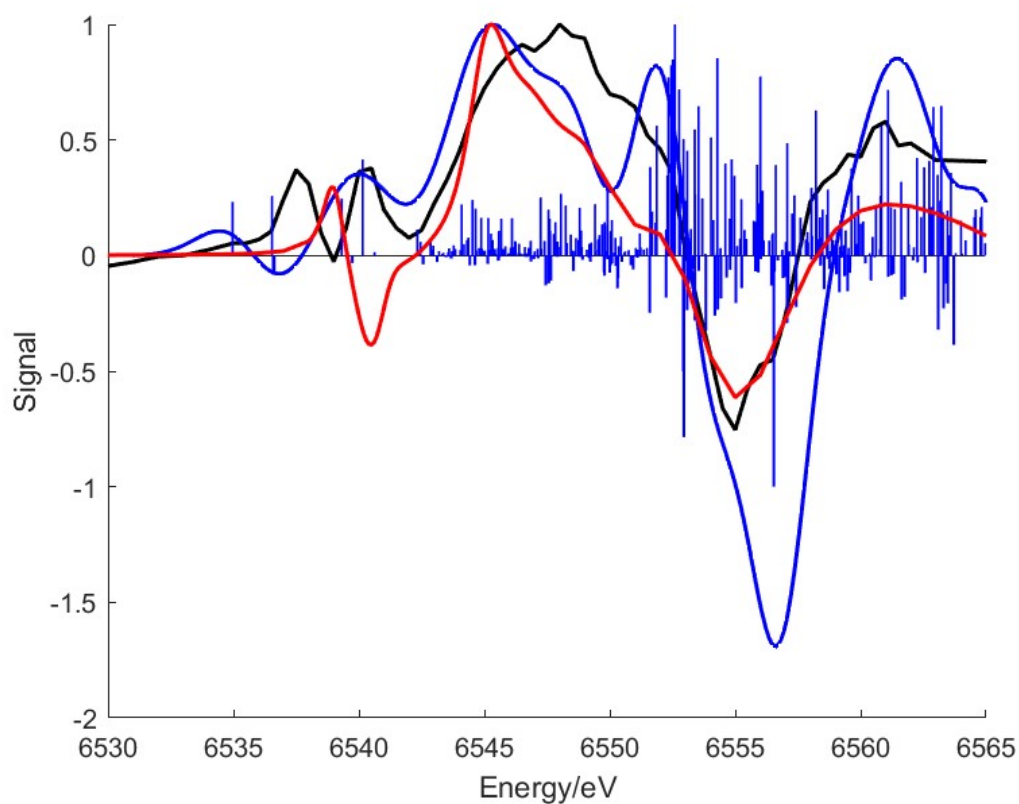


Figure 5.20: Difference data (black) compared with secondary bound FDMNES of  $\text{CpMn}(\text{CO})_2(n\text{-heptane})$  (red), and excited states for  $\text{CpMn}(\text{CO})_2(n\text{-heptane})$  and  $\text{CpMn}(\text{CO})_3$  shown as positive and negative lines respectively (blue)

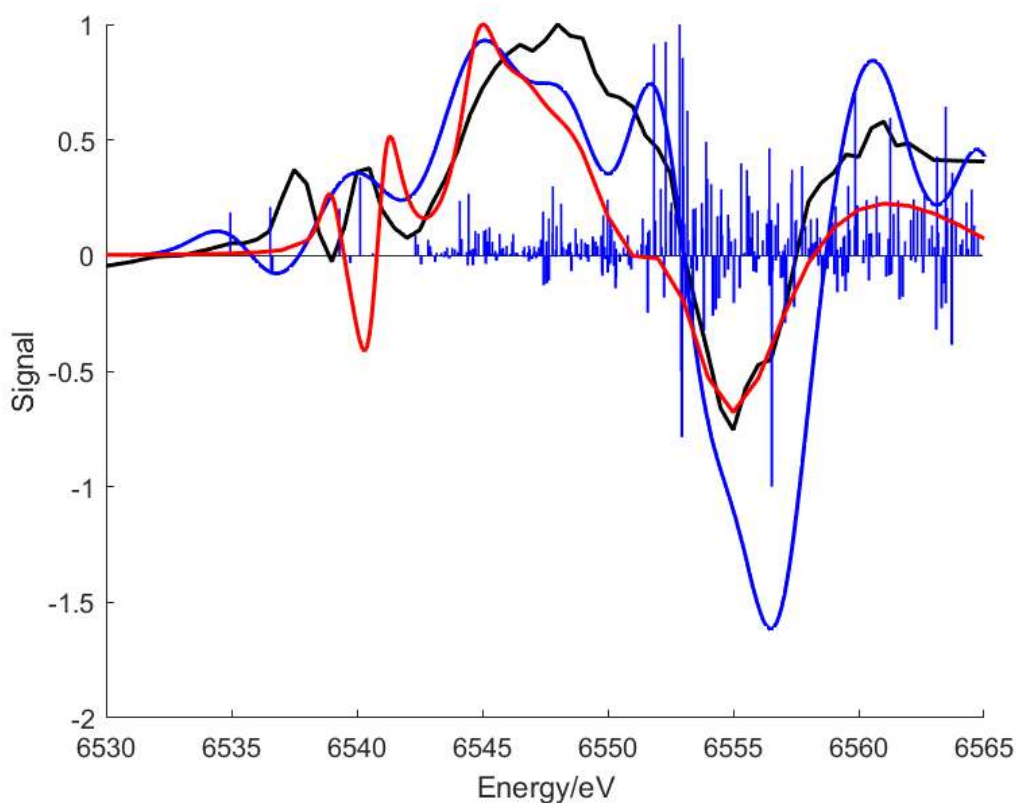


Figure 5.21: Difference data (black) compared with primary bound FDMNES of  $\text{CpMn}(\text{CO})_2(\text{n-heptane})$  (red), and excited states for  $\text{CpMn}(\text{CO})_2(\text{n-heptane})$  and  $\text{CpMn}(\text{CO})_3$  shown as positive and negative lines respectively (blue)

Figures 5.19 and 5.20 illustrate the emergence of the difference data's key features from the excited states of the parent and product species. In both cases we can see that the valley from 6552 eV to 6558 eV arises from 2 very strong transitions in the parent and several less intense transitions, while the rise before 6552 eV is induced by a dense run of strong transitions in the product species that is not offset by the sparser transitions in the parent.

#### 5.3.4 – XANES of $\text{CpMn}(\text{CO})_3$ in neat triethyl silane

Data was collected for 8 hours for  $\text{CpMn}(\text{CO})_3$  in neat triethyl silane. In this case for the 4 microsecond long window studied, we expect to see a majority photoproduct of silyl-bound

$\text{CpMn(CO)}_2(\text{HSiEt}_3)$ , as TRIR investigation in Section 5.3.1 shows formation of this product and depletion of the ethyl-bound isomer within 1.5  $\mu\text{s}$ .

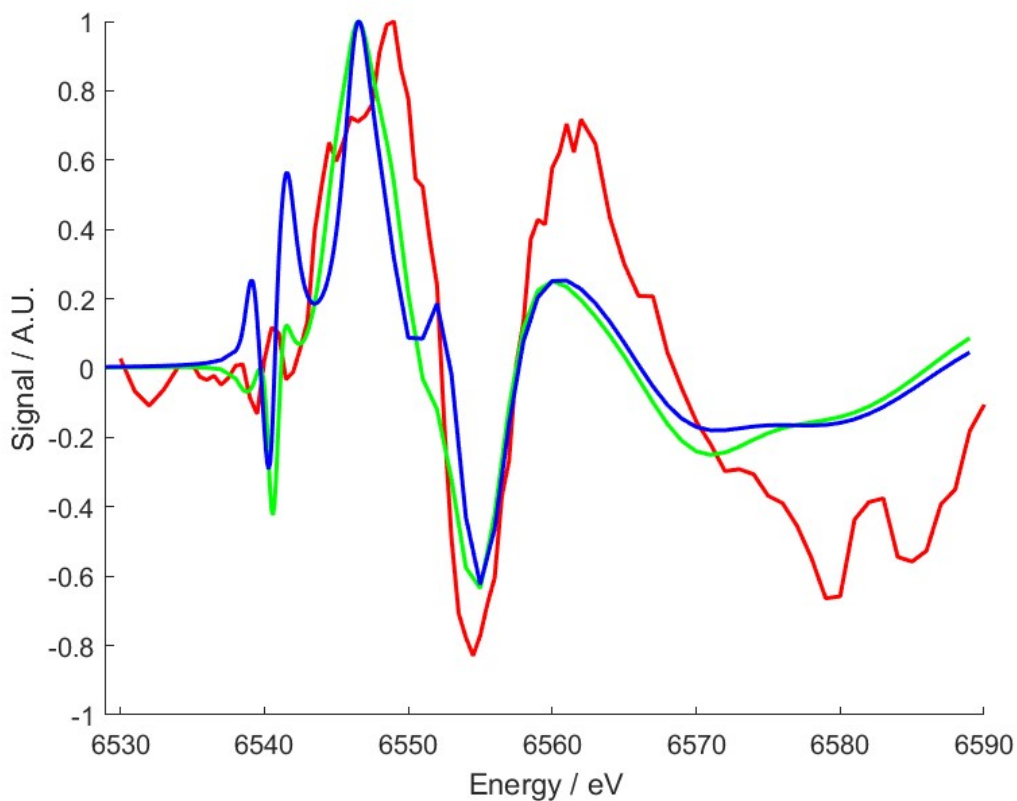


Figure 5.22: Difference data for  $\text{CpMn(CO)}_3$  photolyzed in neat triethyl silane from both experimental (red) and theoretical methods. Includes FDMNES computations for  $\text{CpMn(CO)}_2(\text{HSiEt}_3)$  (green) and  $\text{CpMn(CO)}_2(\text{Et}_3\text{SiH})$  (blue).

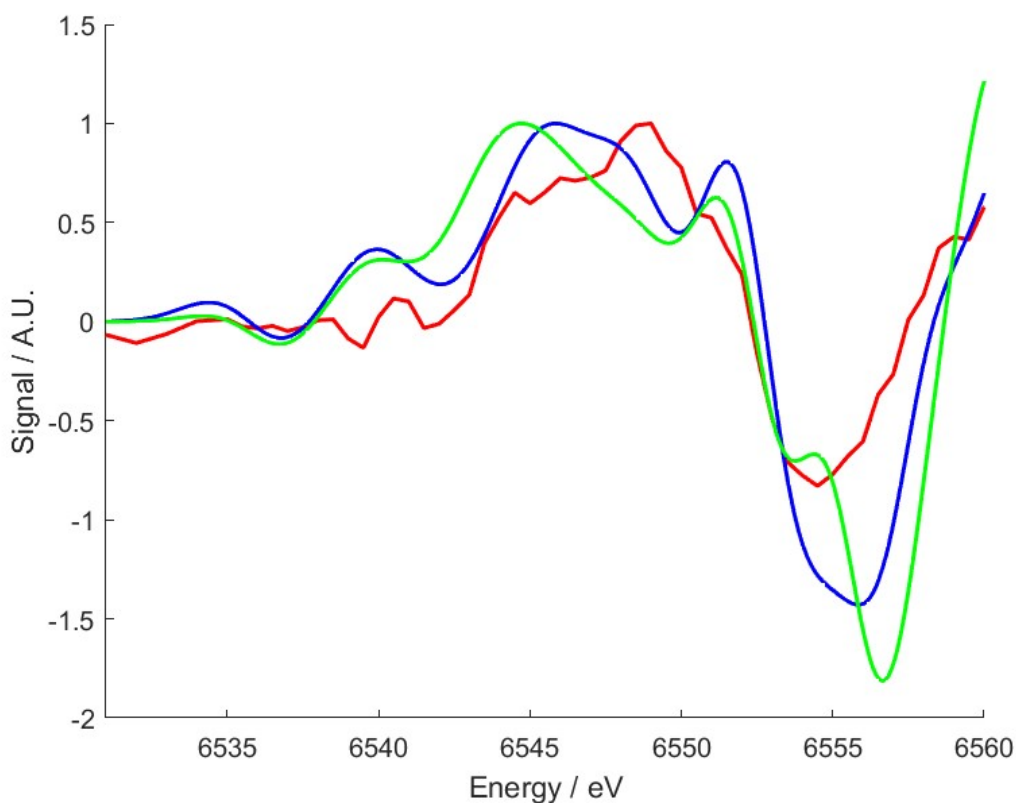


Figure 5.23: Difference data for  $\text{CpMn(CO)}_3$  photolyzed in neat triethyl silane from both experimental (red) and theoretical methods. Includes QChem computations for  $\text{CpMn(CO)}_2(\text{HSiEt}_3)$  (green) and  $\text{CpMn(CO)}_2(\text{Et}_3\text{SiH})$  (blue).

As with  $\text{CpMn(CO)}_3$  in *n*-heptane, we see a series of pre-edge peaks before a sharp rise and fall from the growth of a broader-edged species and depletion of the narrower edge of the parent. before 6550 eV and a steep valley past 6550 eV, in experimental and theoretical spectra. Further in the experimental data, we can see that there are much smaller features in the pre-edge than there were for *n*-heptane, while the edge and post-edge regions are relatively similar.

In this case the intensity of pre-edge features matching to experiment in Figure 5.21 shows a much stronger match to the silane-bound prediction than the carbon-bound for FDMNES. The silane-bound features are much closer to the experimental data in magnitude, and where the ethyl-bound simulation predicts a resolved peak between the main rise and fall at the edge, the silane-bound model and the experimental data do not express this feature.

In the predictions of QChem we see a distinct peak between the main rise and fall around the edge, although much less pronounced in the silane-bound model, which also includes a second peak in the valley region. In this case the carbon-bound intermediate seems to match the experimental feature intensities more accurately than the silane bound intermediate. It is hard to make any meaningful statements on the pre-edge beyond the carbon-bound mode predicting an earlier feature not expressed significantly in the experimental data.

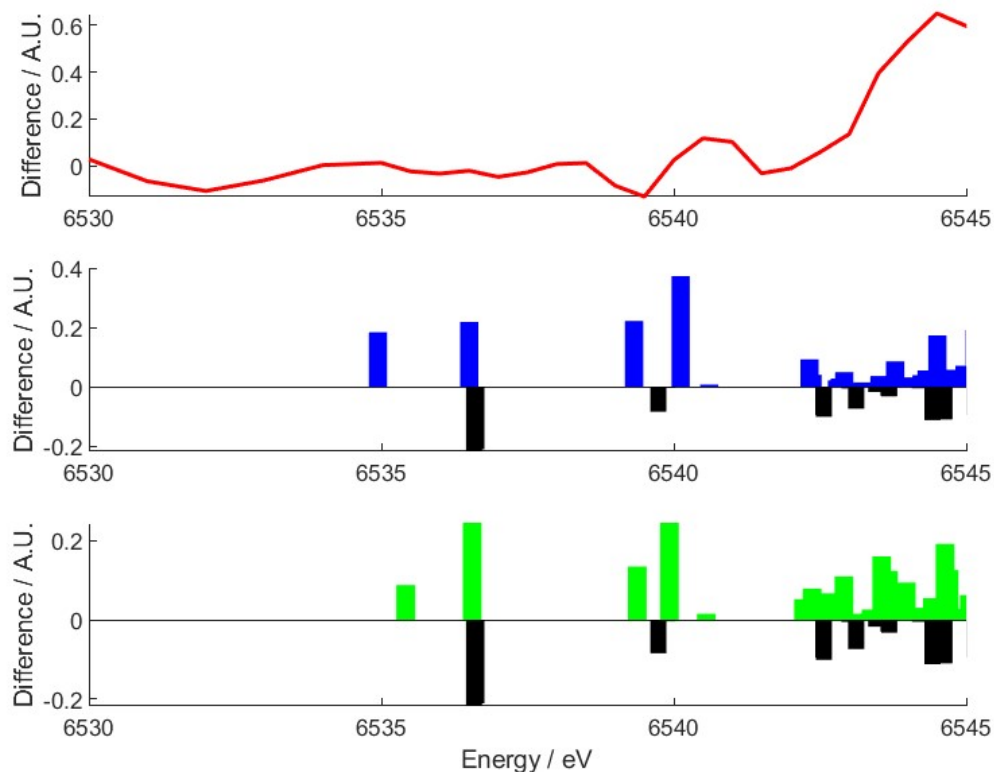


Figure 5.24: Excited states of  $\text{CpMn(CO)}_2(\text{Et}_3\text{SiH})$  (blue),  $\text{CpMn(CO)}_2(\text{HSiEt}_3)$  (green) and  $\text{CpMn(CO)}_3$  (black) with pre-edge energy range of data for  $\text{CpMn(CO)}_3$  photolyzed in neat triethyl silane.

Examining the excited states of the photoproducts as shown in Figure 5.23, we can see more clear differences between the silane-bound and ethyl-bound isomers. We can see noise in the 6531 to 6533 eV region which makes it hard to confirm the resemblance between later

pre-edge features around 6540 eV. However, we can also see the pattern by which the carbon-bound intermediate exhibits a larger pre-edge difference than the silane-bound, with the silane variant having significantly weaker transitions. With comparison to our previously discussed measurements in *n*-heptane we can say that the features we can see suggest a silane-bound structure more than a carbon-bound variant.

### 5.3.5 – XANES of $\text{CpMn}(\text{CO})_3$ in *n*-heptane doped with tributyl silane

Measurements were taken at Diamond Light Source to observe the XANES of  $\text{CpMn}(\text{CO})_3$  in *n*-heptane doped with 0.05 M of tributyl silane in 2020.

The collected experimental data consisted of around 6 hours of observation, consisting of 15  $\mu\text{s}$  segments for each pump-probe cycle. As with previously described studies, a 4  $\mu\text{s}$  window was used for the laser on and laser off spectra, with the difference taken to produce the spectrum shown in Figure 5.24.

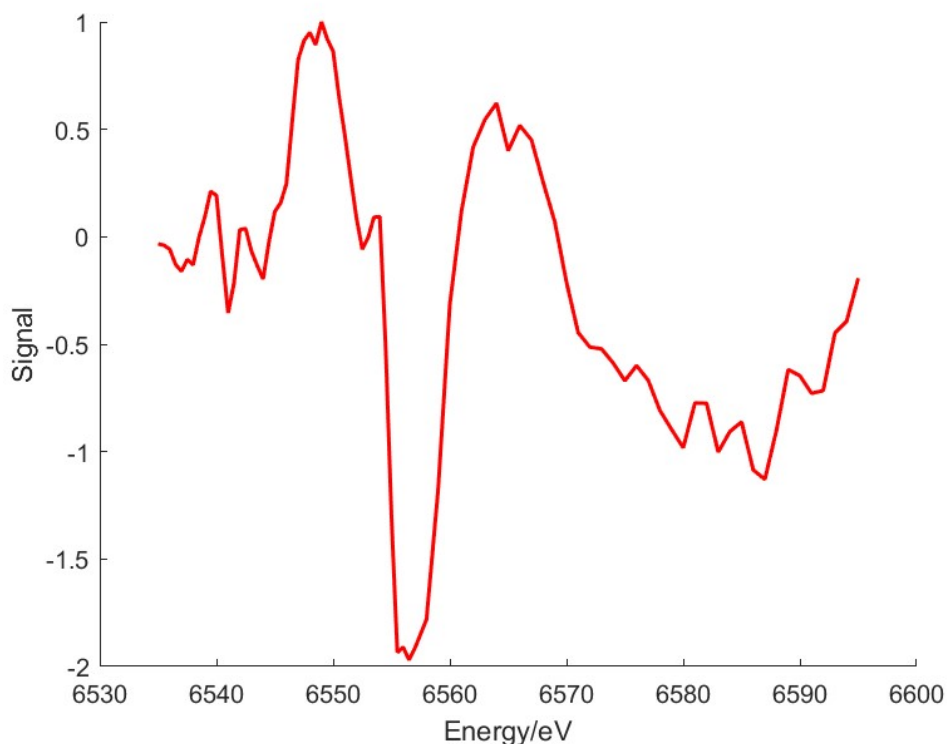


*Figure 5.25: Experimental difference data for photolysis of  $\text{CpMn}(\text{CO})_3$  in *n*-heptane doped with tributyl silane.*

In this data we can see the same characteristic profile as is visible in the XANES data discussed in Chapter 4: a large valley at the original edge position with a large positive shift just before it, indicating the depletion of the parent species and growth of a new species with a slightly lower edge position.

Further analysis was attempted using the time region of 6 to 10  $\mu\text{s}$ , but these data were found to have insufficient signal to noise. This was speculated to be due to inaccuracies in the alignment process, which was confirmed when later experiments (described above) performed with an improved method of alignment produced much higher quality data in a shorter timeframe of collection.

When comparing experimental data to theoretical predictions, it has been assumed that there is one child product that will make up the majority of the product species present, and not a statistically significant combination of 2 or more child species. Previous investigation of  $\text{CpMn}(\text{CO})_3$  in neat triethyl silane estimates that about 84% of the photolyzed parent binds

to the solvent by the ethyl chain before rearranging to bind via the Si-H bond, with the remainder solvating directly via the silane moiety.<sup>22</sup> Our own TRIR work predicts that for  $\text{CpMn}(\text{CO})_3$  in *n*-heptane doped with triethyl silane, the *n*-heptane co-ordinates to the vacant site first before being replaced by the triethyl silane, which binds via the Si-H moiety. Work by Lingjun Wu provides results for the analogous procedure in *n*-heptane doped with 0.25M tributyl silane, both  $\text{CpMn}(\text{CO})_2(\textit{n}\text{-heptane})$  and  $\text{CpMn}(\text{CO})_2(\text{HSiBu}_3)$  are formed within a nanosecond of photolysis. However  $\text{CpMn}(\text{CO})_2(\textit{n}\text{-heptane})$  remains the majority photoproduct, with the tributyl silane substituting for it later giving it a lifetime of circa  $4.5\mu\text{s}$ .<sup>29</sup>

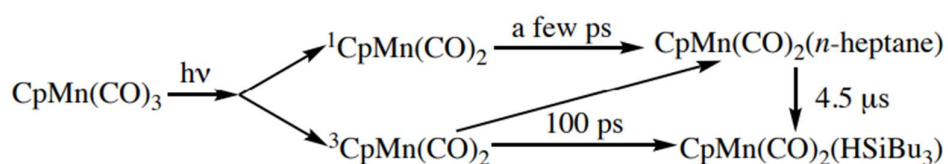


Figure 5.26: Reaction pathways for the photolysis of  $\text{CpMn}(\text{CO})_3$  in heptane doped with 0.25M tributyl silane. Replicated from Ref.<sup>29</sup>

With a much lower concentration of tributyl silane used in the XANES investigation, the anticipated lifetime of the alkane-bound intermediate is significantly longer, and so it is expected that the main photoproduct visible in the data will be the alkane-bound intermediate. Wu's experiments evaluated the lifetime to be  $9.3 \pm 0.4 \mu\text{s}$ , in significant excess of the  $4 \mu\text{s}$  timeframe we have observed.

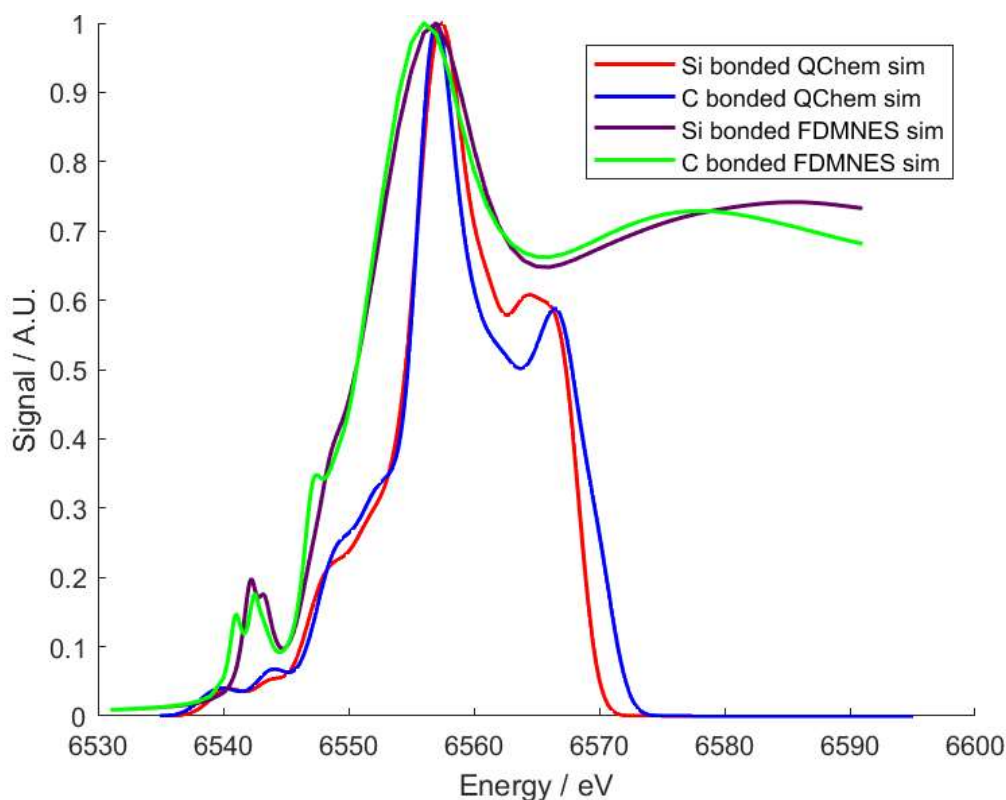


Figure 5.27: Simulated XANES spectra of  $\text{CpMn}(\text{CO})_2(n\text{-heptane})$  and  $\text{CpMn}(\text{CO})_2(\text{HSiEt}_3)$  evaluated via both FDMNES and QChem.

Figure 5.26 shows simulations of the XANES of potential photoproducts produced with both FDMNES and QChem. Both the Si-H bound silane complex and primary C-H bound *n*-heptane complex have been compared to experimental data in previous sections, and it is apparent that there are spectral differences between the two species.

In the FDMNES spectra there is a substantial difference in the pre-edge, but little variation in the post-edge. QChem simulations likewise show a more convoluted pre-edge. The computations' highest computed states are at 6567.9 eV and 6567.6 eV, so analysis of the difference calculated with these models cannot be reasonably extended past 6564 eV, where unaccounted for states may have a significant effect on the spectrum.

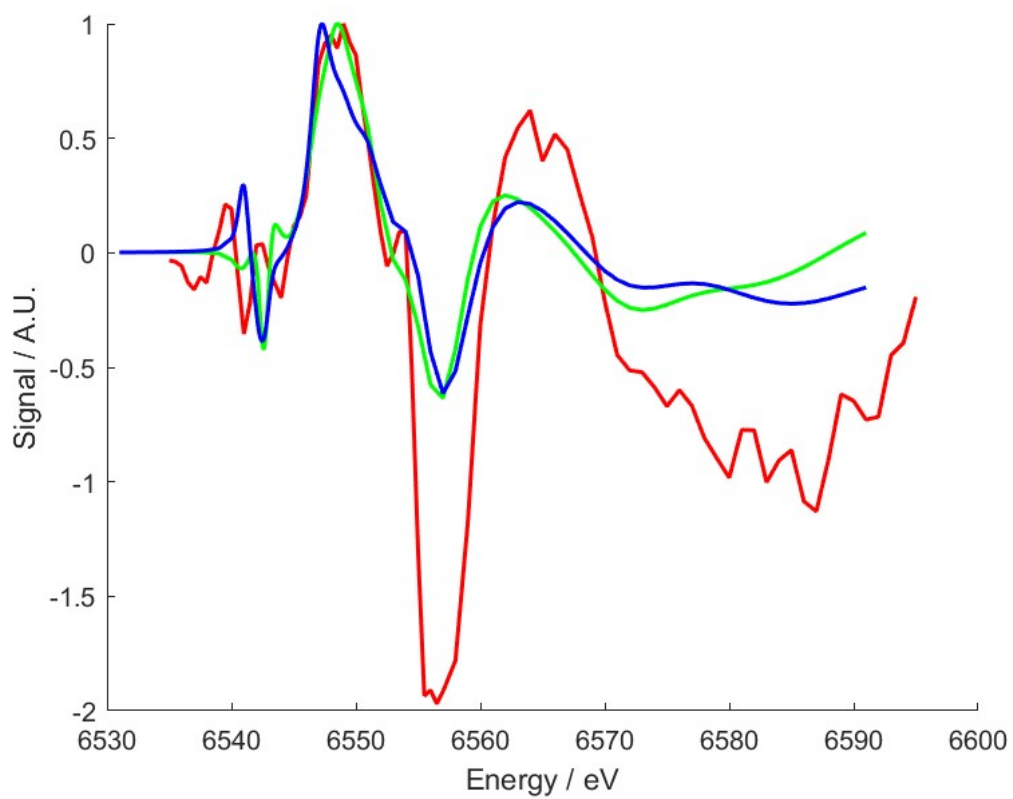


Figure 5.28: Comparison of difference spectra from experimental data (red) to  $\text{CpMn(CO)}_2(\text{HSiEt}_3)$  (green) and  $\text{CpMn(CO)}_2(n\text{-heptane})$  (blue) difference spectra produced using FDMNES.

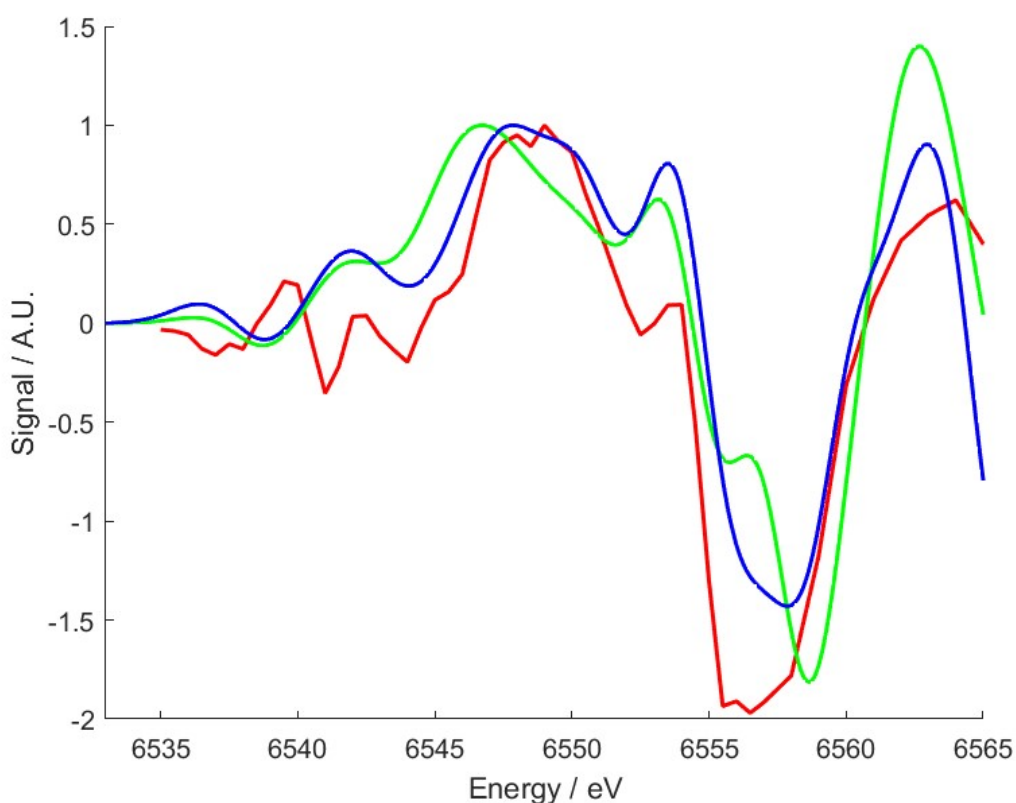


Figure 5.29: Comparison of difference spectra from experimental data (red) to  $\text{CpMn}(\text{CO})_2(\text{HSiEt}_3)$  (green) and  $\text{CpMn}(\text{CO})_2(n\text{-heptane})$  (blue) difference spectra produced using QChem.

Figures 5.27 and 5.28, displayed above, show how the experimentally determined difference spectrum compares to the theoretical simulations for a triethyl silane molecule bonded to the metal centre by the Si-H bond and for *n*-heptane bound via a primary C-H bond. Both experimental and theoretical spectra are normalised to their highest positive value, although in each case the largest difference arises from the negative peak associated with the loss of  $\text{CpMn}(\text{CO})_3$ .

This negative feature is consistently underestimated by FDMNES and QChem for each considered isomer, although it is more closely matched in intensity by the QChem calculations. This is in contrast to findings for neat *n*-heptane and triethyl silane solutions, where the 'loss' feature is well-modelled in magnitude by FDMNES and overestimated by QChem.

In isolation, this difference could be attributed to inaccuracies in the signal strength estimated by either piece of software, but the quality of that estimate for neat solvent measurements suggests otherwise.

One possibility is that there has been more loss of parent than formation of product. Given that such a disparity is not observed in neat triethyl silane or *n*-heptane, and TRIR provides no evidence for the formation of radicals or dimers to explain this difference, such a change is unlikely to be a product of the chemical system. Depending on the quality of the jet, it is possible that the difference arises from the base spectrum coming from a thicker portion of the jet than the post-photolysis data. This would be consistent with the discrepancy being reduced in the newer data, which implemented an improved nozzle and pumping system. However, given the data are collected over several hours of pumping, to have such a consistent distortion to increase pre-photolysis signal would be highly unlikely. The use of a higher laser power in this experiment may also be a contributing factor.

This may also be attributed to noise but is a high degree of difference to explain with signal variation (with the relative intensity of the depletion at about 1 for other solutions and 2 for *n*-heptane doped with tributyl silane). Overall, it seems likely that this difference arises from the less well tuned setup used for this earlier experiment.

The edge region itself holds the strongest indicator of what species might be present with a distinct peak at 6553 eV, between the main edge peak and trough. The FDMNES carbon bound simulation predicts its magnitude quite well, while the silicon variant predicts a much smaller shoulder. The QChem spectra each predict a distinct peak, with the heptane-bound variant showing a much larger peak than the silane-bound species.

In the post-edge region from  $\sim 6560$  eV onwards, the FDMNES simulations show a qualitative match to the general curve of the experimental data. There is a slightly better match in the trend of the *n*-heptane bound complex in this region compared to the triethyl silane bound complex, but there is significant mismatch in the intensity and no fine detail is resolved through the noise in the experimental data to make a useful comparison. The heptane-bound prediction from QChem adheres more closely to experiment than the silane-bound prediction at the limit of modelling.

In the pre-edge region, there is again no clear match to indicate one isomer is definitively present compared to the other. The experimental curve shows a trough-peak-trough-peak-trough pattern before rising into the main edge, and none of the produced theoretical spectra match this exact pattern. The carbon variants in both the FDMNES and QChem prediction have a peak-trough-peak-trough pattern, but that is about the extent of the qualitative similarity. FDMNES also predicts the silane-bound version to have a similar feature in the pre-edge, but both of the FDMNES simulations fail to accurately describe the intensities of both pre-edge features.

As was observed in simulation of the parent in Figure 5.12, the parent's pre-edge peaks are overestimated in intensity as well as energy. Given that precedent, a 3 eV shift could be applied to align the pre-edge features, but that still leaves a large disparity between the first peak for the silicon bound complex and a similar mismatch with the second peak for the carbon bound complex.

By comparing the pre-edge to our data for neat *n*-heptane and triethyl silane, we can see the same primary difference peak in the pre-edge for *n*-heptane but not with triethyl silane, adding further evidence that we are seeing a carbon-bound species.

Taken together we have experimental evidence of a carbon-bound complex and more accurate modelling of the experimental data for those carbon-bound structures in both QChem and FDMNES. Mismatch in the FDMNES prediction appears as though it would be well-explained by a small proportion of silane-bound isomer in solution, which is expected from the TRIR data.

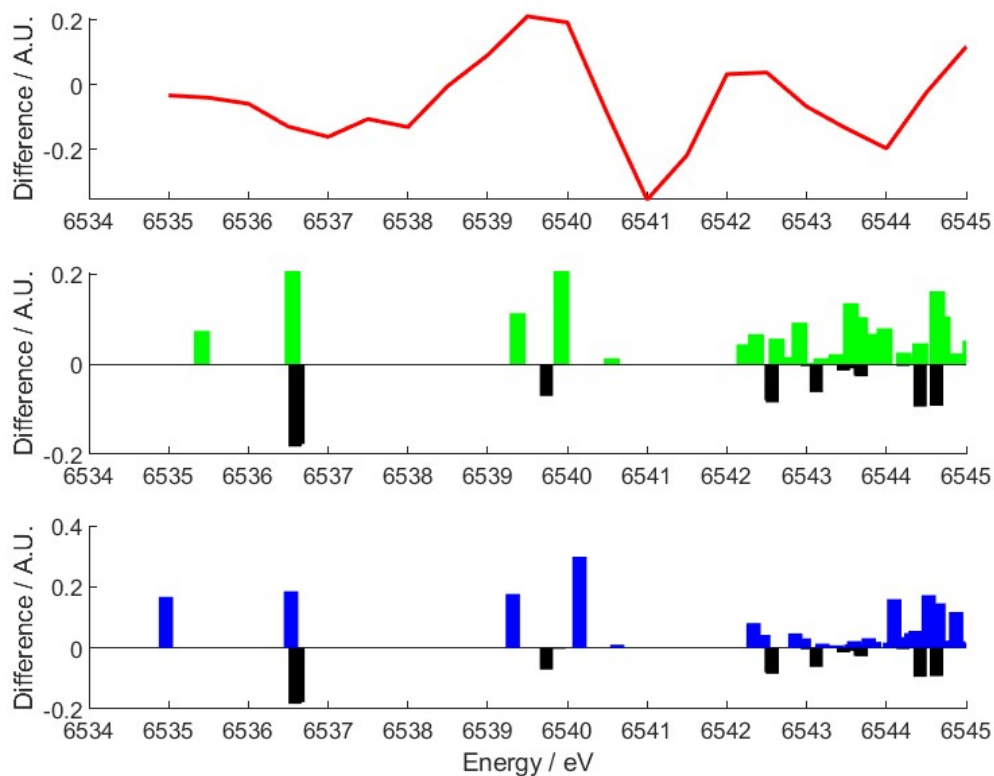


Figure 5.30: QChem excited states predictions for  $\text{CpMn}(\text{CO})_3$  (black),  $\text{CpMn}(\text{CO})_2(\text{Et}_3\text{SiH})$  (blue) and  $\text{CpMn}(\text{CO})_2(\text{HSiEt}_3)$  (green) compared with experimental data (red) for the pre-edge region.

Figure 5.29 shows a closer view of the pre-edge region with excited states for the parent and two potential product species overlaid. We can see that there is a shift in the two pre-edge peaks compared to those of *n*-heptane (6540 and 6542 eV compared to 6538 and 6540 eV), one which is not described by a change in the excited states predictions. If found to be a replicable phenomenon, this might indicate that there is a significant difference in the electronic character of  $\text{CpMn}(\text{CO})_2(\text{Et}_3\text{SiH})$  and  $\text{CpMn}(\text{CO})_2(n\text{-heptane})$ , despite their very similar carbon-bound structures. At present it is unclear whether the shift is attributable to noise or a contribution from silane-bound isomer.

## 5.4 – Conclusions

We have for the first time performed TRXAS experiments on metal-alkane and metal-silane complexes at Diamond. TRIR has been used to identify the photoproducts of  $\text{CpMn}(\text{CO})_3$  photolyzed in *n*-heptane, triethyl silane, and *n*-heptane doped in triethyl silane. By comparison to TRXAS measurements we have found evidence that  $\text{CpMn}(\text{CO})_2(\textit{n}\text{-heptane})$  exists in both the primary carbon bound and secondary carbon bound isomers.

Comparison of TRXAS spectra has also let us assign a silane-bound structure for  $\text{CpMn}(\text{CO})_2(\text{HSiEt}_3)$  and differentiate between silane and alkane binding. In comparisons to data for  $\text{CpMn}(\text{CO})_3$  in *n*-heptane doped with triethyl silane we found spectral variation allowing us to identify the majority photoproduct as a carbon-bound species.

We have also demonstrated the effectiveness of FDMNES as a qualitative tool for assigning difference spectra. As FDMNES is a software package with a low access barrier, the fact that it can be used to evaluate XANES difference data with significant accuracy is an important part of advancing the accessibility and wider use of the TRXAS technique.

## 5.5 – References

1. X. Wu, Z. Liu, T. S. Murphy, X. Z. Sun, M. W. D. Hanson-Heine, M. Towrie, J. N. Harvey and M. W. George, *Faraday Discussions*, 2019, 220, 86-104.
2. C. R. Kemnitz, E. S. Ball and R. J. McMahon, *Organometallics*, 2012, 31, 70-84.
3. G. I. Childs, C. S. Colley, J. Dyer, D. C. Grills, X.-Z. Sun, J. Yang and M. W. George, *Journal of the Chemical Society, Dalton Transactions*, 2000, 1901-1906.
4. J. W. Kee, Y. Y. Tan, B. H. G. Swennenhuis, A. A. Bengali and W. Y. Fan, *Organometallics*, 2011, 30, 2154-2159.

5. M. M. Syrokvashin, E. V. Korotaev, I. Y. Filatova, S. V. Trubina and S. B. Erenburg, *Spectrochimica Acta Part a-Molecular and Biomolecular Spectroscopy*, 2018, 205, 593-596.
6. R. Chatterjee, C. Weninger, A. Loukianov, S. Gul, F. D. Fuller, M. H. Cheah, T. Fransson, C. C. Pham, S. Nelson, S. Song, A. Britz, J. Messinger, U. Bergmann, R. Alonso-Mori, V. K. Yachandra, J. Kern and J. Yano, *Journal of Synchrotron Radiation*, 2019, 26, 1716-1724.
7. G. J. Kubas, *Journal of Organometallic Chemistry*, 2001, 635, 37-68.
8. O. Torres, J. A. Calladine, S. B. Duckett, M. W. George and R. N. Perutz, *Chemical Science*, 2015, 6, 418-424.
9. J. D. Bourke, M. T. Islam, S. P. Best, C. Q. Tran, F. Wang and C. T. Chantler, *Journal of Physical Chemistry Letters*, 2016, 7, 2792-2796.
10. L. N. Nchari, G. A. Hembury, A. M. Beesley, D. J. Meehan, N. Tsapatsaris, M. Hudson, M. Thomason and S. L. M. Schroeder, Camerino, ITALY, 2009.
11. R. H. Crabtree, *Chemical Reviews*, 1995, 95, 987-1007.
12. C. Hall and R. N. Perutz, *Chemical Reviews*, 1996, 96, 3125-3146.
13. J. A. Calladine, S. B. Duckett, M. W. George, S. L. Matthews, R. N. Perutz, O. Torres and Q. V. Khuong, *Journal of the American Chemical Society*, 2011, 133, 2303-2310.
14. J. A. Labinger and J. E. Bercaw, *Nature*, 2002, 417, 507-514.
15. W. F. Wang, D. Q. Xu, Q. S. Sun and W. Sun, *Chemistry-an Asian Journal*, 2018, 13, 2458-2464.
16. T. S. Piper, D. Lemal and G. Wilkinson, *Naturwissenschaften*, 1956, 43, 129-129.
17. R. H. Crabtree, *Angewandte Chemie International Edition in English*, 1993, 32, 789-805.
18. N. Almutairi, S. Vijjamarri and G. D. Du, *Catalysts*, 2023, 13, 12.
19. I. Fleming, A. Barbero and D. Walter, *Chemical Reviews*, 1997, 97, 2063-2192.

20. T. Komuro, S. Okawara, K. Furuyama and H. Tobita, *Chemistry Letters*, 2012, 41, 774-776.
21. S. Wu, Y. Zhang, H. Y. Jiang, N. Ding, Y. B. Wang, Q. Su, H. Zhang, L. Wu and Q. L. Yang, *Tetrahedron Letters*, 2020, 61, 4.
22. H. Yang, M. C. Asplund, K. T. Kotz, M. J. Wilkens, H. Frei and C. B. Harris, *Journal of the American Chemical Society*, 1998, 120, 10154-10165.
23. Z. F. Zhang and M. D. Su, *Rsc Advances*, 2018, 8, 10987-10998.
24. G. Garwood, Doctor of Philosophy, University of Nottingham, 2022.
25. T. S. Murphy, Doctor of Philosophy, University of Nottingham, 2015.
26. S. A. Bartlett, N. A. Besley, A. J. Dent, S. Diaz-Moreno, J. Evans, M. L. Hamilton, M. W. D. Hanson-Heine, R. Horvath, V. Manici, X. Z. Sun, M. Towrie, L. J. Wu, X. Y. Zhang and M. W. George, *Journal of the American Chemical Society*, 2019, 141, 11471-11480.
27. A. O. Borissova, M. Y. Antipin and K. A. Lyssenko, *The Journal of Physical Chemistry A*, 2009, 113, 10845-10851.
28. J. Full, L. González and C. Daniel, *The Journal of Physical Chemistry A*, 2001, 105, 184-189.
29. L. Wu, Doctor of Philosophy, University of Nottingham, 2018.

# Appendix I – Unsmoothed Rhenium

## Difference Data

Comparison figures between the smoothed and unsmoothed k-space data obtained for rhenium complexes are given below. In these Figures we can see that smoothing did not remove all noise from the spectra; further smoothing was not performed to avoid destroying actual features of the data.

With the level of smoothing applied significant noise is visible past the 5 Å threshold and becomes overwhelming at about 7 Å, so windows of fitting applied in Chapter 4 have been limited to 7 Å and below.

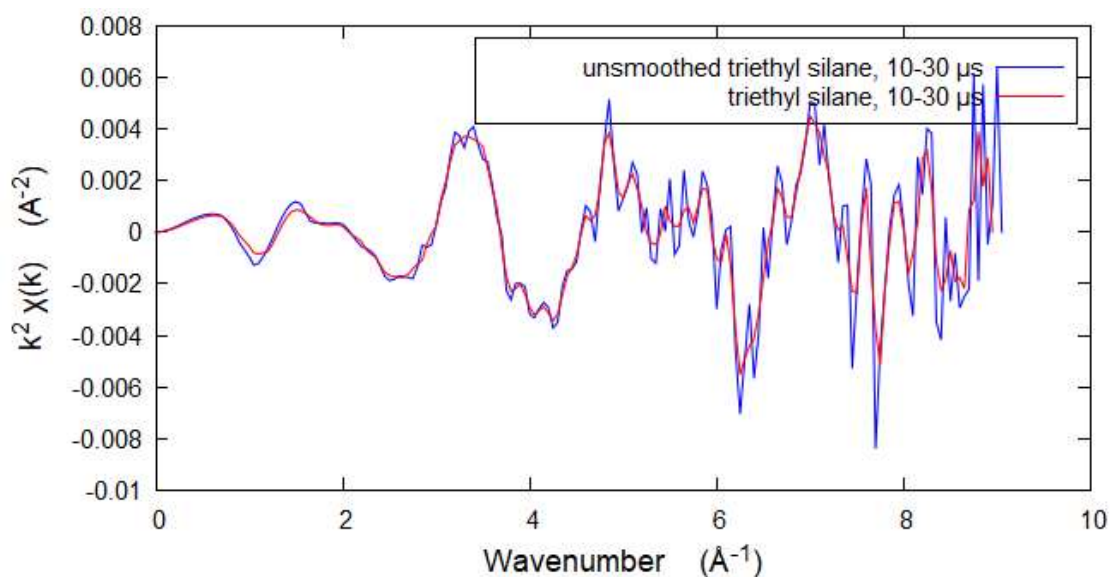


Figure I.1: Smoothed and unsmoothed k-space difference data for the photolysis of  $\text{CpRe}(\text{CO})_3$  in neat triethyl silane in the 10 to 30  $\mu\text{s}$  window.

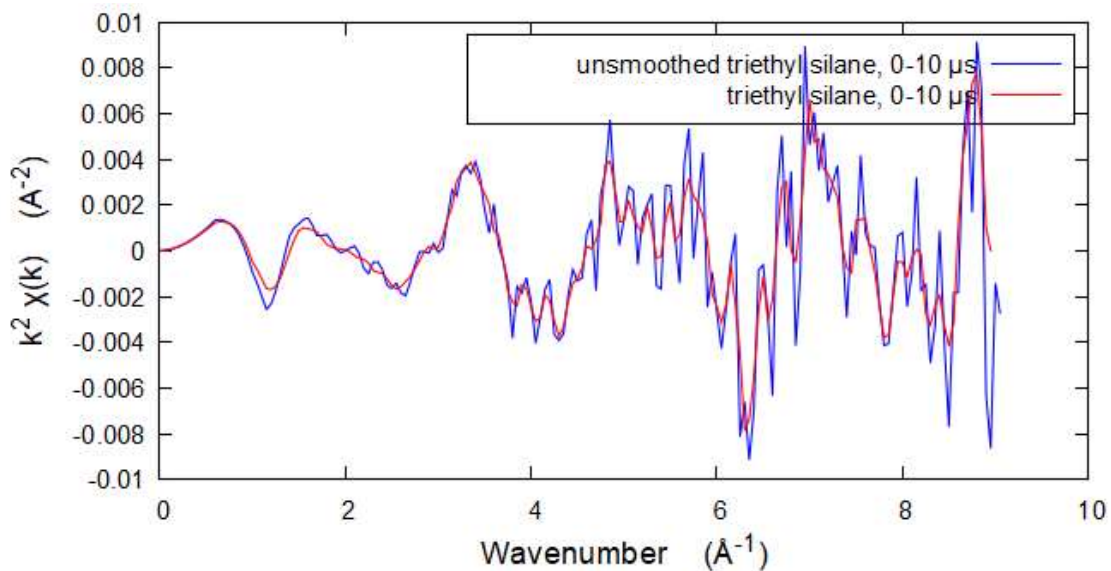


Figure 1.2: Smoothed and unsmoothed  $k$ -space difference data for the photolysis of  $\text{CpRe}(\text{CO})_3$  in neat triethyl silane in the 0 to 10  $\mu\text{s}$  window.

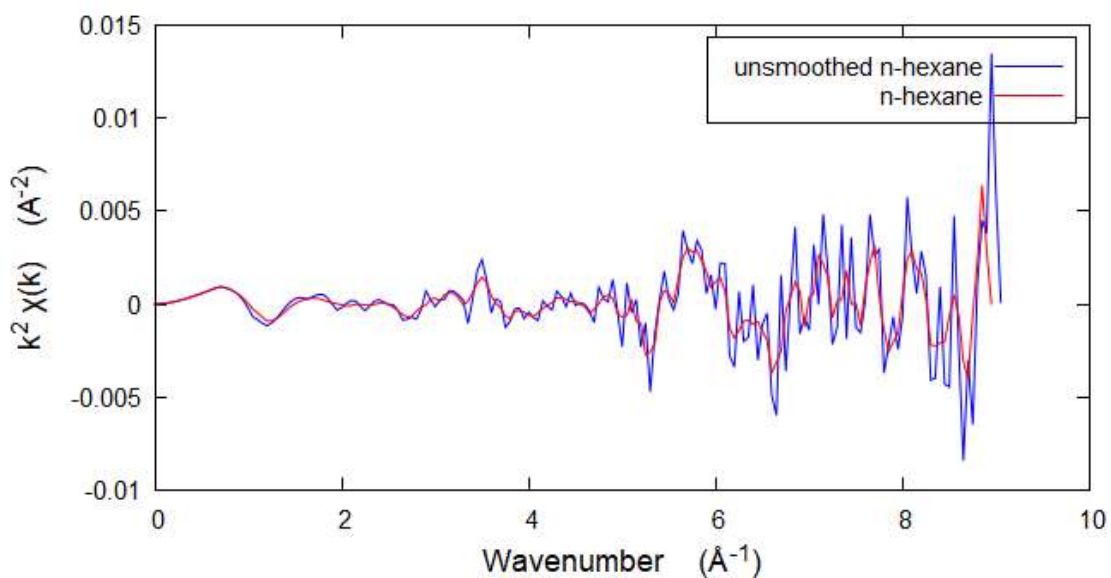


Figure 1.3: Smoothed and unsmoothed  $k$ -space difference data for the photolysis of  $\text{CpRe}(\text{CO})_3$  in neat  $n$ -hexane in the 0 to 30  $\mu\text{s}$  window.

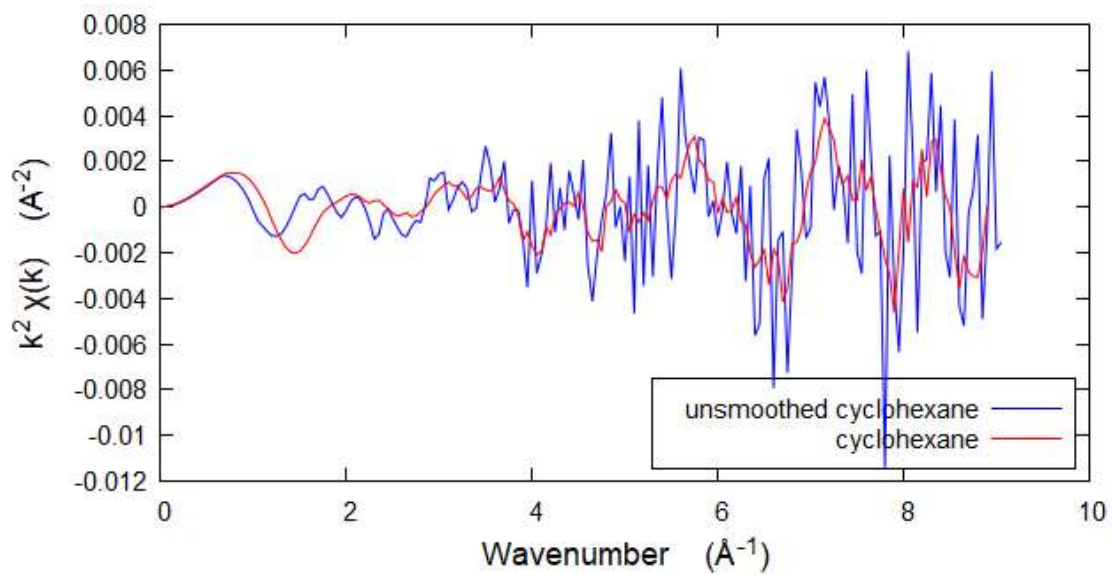


Figure I.4: Smoothed and unsmoothed  $k$ -space difference data for the photolysis of  $\text{CpRe}(\text{CO})_3$  in neat cyclohexane in the 0 to 30  $\mu\text{s}$  window.